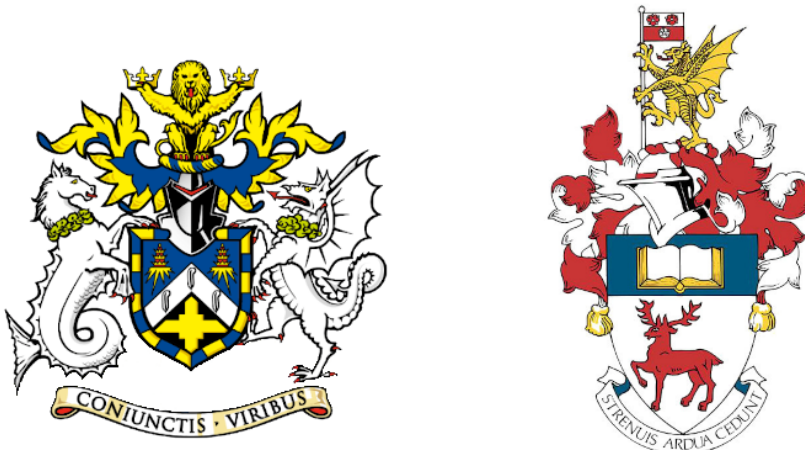


¹ ADVANCING NEUTRINO
² DETECTION AND TRIGGERING IN
³ DUNE



⁴
⁵ Francisco Martínez López

⁶ Submitted in partial fulfillment of the requirements
⁷ of the Degree of Doctor of Philosophy

⁸ School of Physical and Chemical Sciences
⁹ Queen Mary University of London

¹⁰ School of Physics and Astronomy
¹¹ University of Southampton

¹² December 2024

Statement of originality

- 14 I, Francisco Martínez López, confirm that the research included within this thesis is my
15 own work or that where it has been carried out in collaboration with, or supported by
16 others, that this is duly acknowledged below and my contribution indicated. Previously
17 published material is also acknowledged below.
- 18 I attest that I have exercised reasonable care to ensure that the work is original, and
19 does not to the best of my knowledge break any UK law, infringe any third party's
20 copyright or other Intellectual Property Right, or contain any confidential material.
- 21 I accept that the University has the right to use plagiarism detection software to check
22 the electronic version of the thesis.
- 23 I confirm that this thesis has not been previously submitted for the award of a degree
24 by this or any other university.
- 25 The copyright of this thesis rests with the author and no quotation from it or information
26 derived from it may be published without the prior written consent of the author.
- 27 Signature: [can be digital signature]
- 28 Date:
- 29 Details of collaboration and publications:
30 [insert details here if applicable]

Abstract

31

32 Work in progress ...

¡Oh memoria, enemiga mortal de mi descanso!

El ingenioso hidalgo don Quijote de la Mancha

MIGUEL DE CERVANTES SAAVEDRA

Acknowledgements

34 Work in progress ...

Contents

Statement of originality	3
Abstract	5
Acknowledgements	9
Contents	14
List of Figures	15
List of Tables	33
List of Abbreviations	35
1 Introduction	37
2 Neutrino physics	39
2.1 Neutrinos in the SM	39
2.2 Trouble in the neutrino sector	43
2.2.1 The solar neutrino problem	43
2.2.2 The atmospheric neutrino problem	45
2.3 Massive neutrinos	47
2.4 Neutrino oscillation formalism	49
2.4.1 Oscillations in vacuum	51
2.4.2 Oscillations in matter	54
2.4.3 Current status of neutrino oscillations	56
2.5 Open questions in the neutrino sector	57
2.6 Neutrino interactions	58

CONTENTS

3 The Deep Underground Neutrino Experiment	63
3.1 Overview	63
3.2 Physics goals of DUNE	65
3.3 LBNF beamline	67
3.4 Near Detector	69
3.4.1 ND-LAr	71
3.4.2 TMS/ND-GAr	72
3.4.3 PRISM	73
3.4.4 SAND	74
3.5 A More Capable Near Detector	74
3.5.1 Requirements	75
3.5.2 Reference design	75
3.5.3 R&D efforts	78
3.6 Far Detector	81
3.6.1 Horizontal Drift	82
3.6.2 Vertical Drift	84
3.6.3 FD Data Acquisition System	86
4 Matched Filter approach to Trigger Primitives	89
4.1 Motivation	89
4.2 Signal-to-noise ratio definition	91
4.3 Low-pass FIR filter design	93
4.4 Matched filters	96
4.5 Using simulated samples	103
4.5.1 Angular dependence	109
4.5.2 Distortion and peak asymmetry	110
4.5.3 Hit sensitivity	114
5 DM searches with neutrinos from the Sun	123
5.1 Gravitational capture of DM by the Sun	123

CONTENTS

5.2	Neutrino flux from DM annihilations	130
5.3	Computing limits from solar neutrino fluxes	131
5.4	Example: Kaluza-Klein Dark Matter	135
5.5	High energy DM neutrino signals	138
5.5.1	DIS events	141
5.5.2	Single proton QEL events	145
5.5.3	Results	149
5.6	Example: Leptophilic Dark Matter	151
5.7	Systematic uncertainties	155
5.7.1	Systematic uncertainties in the solar WIMP signal	156
5.7.2	Systematic uncertainties in the atmospheric background	157
5.7.3	Common systematic uncertainties	157
6	Particle ID in ND-GAr	159
6.1	GArSoft	160
6.1.1	Event generation	160
6.1.2	Detector simulation	161
6.1.3	Reconstruction	162
6.2	dE/dx measurement in the TPC	165
6.2.1	Energy calibration	167
6.2.2	Truncated dE/dx mean	177
6.2.3	Mean dE/dx parametrisation	180
6.2.4	Particle identification	184
6.3	Muon and pion separation in the ECal and MuID	184
6.3.1	Track-ECal matching	187
6.3.2	Classification strategy	191
6.3.3	Feature selection and importance	195
6.3.4	Hyperparameter optimisation	206
6.3.5	Probability calibration	210

CONTENTS

6.3.6	Performance	212
6.4	ECal time-of-flight	212
6.4.1	Arrival time estimations	214
6.4.2	Proton and pion separation	216
6.5	Charged pion decay in flight	216
6.5.1	Track breakpoints	219
6.6	Neutral particle identification	226
6.6.1	ECal clustering	226
6.6.2	π^0 reconstruction	229
6.7	Integration in GArSoft	231
7	Event selection in ND-GAr	235
7.1	Data sample	235
7.2	ν_μ CC selection	236
7.2.1	Selection optimisation	239
7.2.2	Selection performance	245
7.2.3	Primary muon kinematics	247
7.3	Charged pion identification	251
7.3.1	ν_μ CC $1\pi^\pm$ selection	258
7.4	Neutral pion identification	258
7.5	Systematic uncertainties	258
7.5.1	Flux uncertainties	258
7.5.2	Cross section uncertainties	260
7.5.3	Detector uncertainties	260
8	Conclusion and outlook	261
A	An appendix	263
Bibliography		265

List of Figures

2.1	Solar neutrino fluxes for the solar model BS05(OP).	44
2.2	Zenith angle distributions for the selected ν_e and ν_μ events in the SK detector.	46
2.3	$K^0 \rightleftharpoons \bar{K}^0$ mixing through W^\pm exchange.	50
2.4	Feynman diagrams of the four most relevant CC interactions to long baseline neutrino oscillation experiments.	59
2.5	Total muon neutrino CC cross section per nucleon as a function of the neutrino energy.	60
2.6	Schematic representation of a ν_μ CCQE interaction with a neutron inside a nucleus.	61
3.1	Schematic diagram of the DUNE experiment and the LBNF beamline. .	64
3.2	Schematic longitudinal section of the LBNF beamline at Fermilab. . .	67
3.3	Predicted neutrino fluxes at the FD in FHC mode and RHC mode. . .	68
3.4	Representation of the ND hall in Phase II, showing the different subcomponents.	69
3.5	Schematic representation of the external components of ND-LAr, including the cryostat and the PRISM movable system and detailed drawing of one ArgonCube module.	70
3.6	Schematic view of the TMS detector, highlighting its main parts. . . .	71
3.7	Cross section of the ND-GAr geometry, showing the HPgTPC, ECal and magnet.	72
3.8	Predicted beam muon neutrino flux at the ND location for different off-axis positions.	73

LIST OF FIGURES

3.9	Diagram of the ALICE TPC, showing the two drift chambers, inner and outer field cages and readout chambers.	76
3.10	Diagram of the ALICE TPC, showing the two drift chambers, inner and outer field cages and readout chambers.	77
3.11	Photographs of the TOAD pressure vessel at RHUL.	79
3.12	Electron microscope image and schematic diagram of a GEM electrode.	80
3.13	Schematic diagram showing the operating principle of a LArTPC with wire readout.	81
3.14	Proposed design for the FD-1 and FD-2 modules following the HD principle.	82
3.15	Schematic representation of an APA frames showing the U, V, X and G wires.	83
3.16	A PDS module containing 24 X-ARAPUCAs and the location of the modules on the APAs.	84
3.17	Proposed design for the FD-3 module following the VD principle.	85
3.18	Schematic representation of the electrode strip configuration for a top and bottom CRU.	86
3.19	Detailed diagram of the DUNE FD DAQ system.	87
4.1	<i>Schematic representation of an APA. The black lines represent the APA steel frame. The green and magenta lines correspond to the direction of the U and V induction wires respectively. The blue lines indicate the direction of the X collection wires and the wire shielding G.</i>	90
4.2	<i>Left panel: Zoomed unfiltered waveform corresponding to channel 7840 from the ProtoDUNE-SP raw data capture <code>felix-2020-07-17-21:31:44</code> (blue line). The green dashed lines mark the region $\pm 3\sigma_{\text{raw}}$. The resulting noise waveform is also shown (red line). Top right panel: ADC distribution for channel 7840, where the green shaded region represents $\pm \sigma_{\text{raw}}$. Bottom right panel: noise ADC distribution for channel 7840, where the green shaded region represents $\pm \sigma_{\text{noise}}$.</i>	91

LIST OF FIGURES

- 4.3 *Left panel:* Zoomed filtered waveform corresponding to channel 7840 from the ProtoDUNE-SP raw data capture `felix-2020-07-17-21:31:44` (blue line). The filter used was the current implementation of the low-pass FIR filter in `dtp-firmware`. The green dashed lines mark the region $\pm 3\sigma_{\text{raw}}$. The resulting noise waveform is also shown (red line). *Top right panel:* ADC distribution for channel 7840 after filtering, where the green shaded region represents $\pm \sigma_{\text{raw}}$. *Bottom right panel:* noise ADC distribution for channel 7840 after filtering, where the green shaded region represents $\pm \sigma_{\text{noise}}$ 93
-
- 4.4 Power spectrum in decibels for the current implementation of the low-pass FIR filter in `dtp-firmware` (blue line), compared to the response of an optimal filter obtained using the Parks-McClellan algorithm for the same pass-band (red line). Also for comparison I include the spectrum of the optimal filter when taking only the integer part of the coefficients (red dashed line). 94
-
- 4.5 Relative change in the S/N for the ProtoDUNE-SP raw data capture `felix-2020-07-17-21:31:44`, using different values of the cutoff frequency f_c and the transition width δf . The optimal Chebyshev filters were applied using just the integer part of the coefficients given by the Parks-McClellan algorithm. 95
-
- 4.6 Distribution of the relative change of the S/N on the different wire planes from the ProtoDUNE-SP raw data capture `felix-2020-07-17-21:31:44` after the optimal Chebyshev filter was applied. The filter was computed with the Parks-McClellan algorithm using a cutoff of $f_c = 0.068 \text{ ticks}^{-1}$ and a transition width $\delta f = 0.010 \text{ ticks}^{-1}$ 96

LIST OF FIGURES

- 4.7 *Left panel: Zoomed match filtered waveform corresponding to channel 7840 from the ProtoDUNE-SP raw data capture `felix-2020-07-17-21:31:44` (blue line). The filter used was directly extracted from the data, being the 32 values around the first peak in the original waveform. The green dashed lines mark the region $\pm 3\sigma_{\text{raw}}$. The resulting noise waveform is also shown (red line). Top right panel: ADC distribution for channel 7840 after match filtering, where the green shaded region represents $\pm \sigma_{\text{raw}}$. Bottom right panel: noise ADC distribution for channel 7840 after match filtering, where the green shaded region represents $\pm \sigma_{\text{noise}}$* 97
- 4.8 *Relative improvement in the S/N for the raw data capture `felix-2020-07-17-21:31:44`, using the matched filter following the parametrisation in Eq. (4.17). The black crosses in both panels denote the location of the maximum ratio value.* 100
- 4.9 *Left panel: Optimal matched filter coefficients for the U (blue line) and V (red line) planes. The filters were computed with our parametrisation in Eq. (4.17) for the parameter values $\delta = 0.035$, $\sigma = 0.191$ and $\delta = 0.018$, $\sigma = 0.191$ respectively. Right panel: Distribution of the relative change of the S/N on the two induction wire planes from the ProtoDUNE-SP raw data capture `felix-2020-07-17-21:31:44` after their respective optimal matched filters were applied.* 103
- 4.10 *Left panel: distributions of the particles track length in the liquid argon for the generated $E_k = 100$ MeV monoenergetic samples, electrons (blue), muons (red), protons (green) and neutral pions (purple). Right panel: distribution of the length of the longest photon in the neutral pion sample after the decay process $\pi^0 \rightarrow \gamma\gamma$.* 104

LIST OF FIGURES

- 4.11 *Left panel: schematic representation of the two new rotated reference frames used in this analysis (denoted as prime and double prime), viewed from the yz plane. The magenta stack of lines represent the wires in the U plane, whereas the green lines correspond to the wires in the V plane. Right panel: 3D representation of the momentum of one of the generated monoenergetic muons (red arrow) in the original reference frame (black lines), along with the new reference frame used for the U plane waveforms (blue lines). In the yz plane I added the projection of these three.* 106
- 4.12 *Distributions of the mean S/N improvement per event for the corresponding sample after applying the matched filters. Here I separated the change in the U plane (blue) and the V plane (red) channels. From top left to the right: muon, electron, proton and neutral pion. All the events have a fixed kinetic energy of $E_k = 100$ MeV.* 107
- 4.13 Angular dependence of the mean S/N and the S/N improvement, for the different monoenergetic samples considered (from top to bottom: electrons, muons, protons and neutral pions). The two columns on the left represent the values for the U plane waveforms. The top subplots show the mean S/N for raw (green) and filtered (red) waveforms whereas the bottom subplots depict the averaged S/N improvement (black). 108
- 4.14 Angular dependence of the mean S/N and the S/N improvement, for the different monoenergetic samples considered (from top to bottom: electrons, muons, protons and neutral pions). The two columns on the left represent the values for the U plane waveforms. The top subplots show the mean S/N for raw (green) and filtered (red) waveforms whereas the bottom subplots depict the averaged S/N improvement (black). 109

LIST OF FIGURES

4.15 Selected consecutive waveforms corresponding to two monoenergetic $E_k = 100$ MeV muon events, one is parallel to the APA and to the wires in the U plane (left panel) and the other is normal to the APA plane and perpendicular to the U plane wires (right panel). The solid lines represent the raw waveforms whereas the dashed lines correspond to the waveforms after the matched filter was applied. The waveforms on the left panel have been scaled by a factor of 0.15 to have similar amplitude to the ones on the right panel.	111
4.16 Left panel: peak asymmetry distribution for the case of the monoenergetic $E_k = 100$ MeV muon sample. Each value corresponds to a single bipolar signal peak from a channel in any event. The blue distribution represents the peaks on U plane channels, whereas the red corresponds to signal peaks in V wires. Right panel: relation between the mean peak asymmetry per event with the S/N for U channel waveforms from the $E_k = 100$ MeV muon sample. The top subplot shows the decimal logarithm of the mean S/N for the raw (red) and the matched filtered (blue) waveforms. The bottom subplot contains the mean S/N improvement ratio after the matched filter was applied.	112
4.17 Raw data display in the plane time (in firmware ticks) vs. offline channel number for an $E_k = 100$ MeV electron event. The produced true hits are superimposed (black boxes) as well as the hits comming from the standard hit finder chain (blue circles) and the hit finder using the matched filter (green triangles).	114

LIST OF FIGURES

- 4.18 Dependence of the precision (blue), sensitivity (red) and F_1 (green) scores on the threshold values used in the hit finder, for the FIR (left panel) and matched filter (right panel) cases. The results were obtained after matching the hits to the true hits in the case of the isotropic muon sample with kinetic energy in the range 5 to 100 MeV, taking only into account the induction plane channels. The points represent the mean value while the error bars indicate one standard deviation around that mean value. . . 117
- 4.19 Dependence of the averaged hit sensitivity on the kinetic energy of the events for the matched filter (blue) and standard (red) hits, for the case of the muon (left panel) and electron (right panel) samples, separated between U (top plots) and V (bottom plots) induction wire planes. The top subplots contain the hit sensitivities for the two hit finder alternatives, while the bottom subplots show the ratio between the two. The horizontal lines sit at the mean value and represent the size of the energy bins, while the vertical error bars indicate one standard deviation around that mean value. . . . 118
- 4.20 Distributions of the hit sensitivity in the U (top panels) and V (bottom panels) planes versus the hit sensitivity in the X plane, both for the standard hits (left panels) and the matched filter hits (right panels), in the case of the electron sample and a threshold of 30 ADC. 120
- 4.21 Top panels: standard residual plots of the hit sensitivities between the X and U planes. Bottom panels: quantile-quantile plots of the hit sensitivity standard residuals between the X and U planes. In all cases, the left panel corresponds to the standard hits while the right panel represents the matched filter case, all from the electron sample with a 30 ADC threshold. 121

LIST OF FIGURES

5.1	<i>Input solar parameters used in our capture rate computation as functions of the Sun's radius, from left to right: temperature (with respect to the temperature at the core), mass (in solar masses) and electron number density (with respect to the electron density at the core). All quantities shown correspond to the standard solar model BS2005-OP [1].</i>	126
5.2	<i>Capture rates as a function of the DM mass for the DM-electron interactions (red lines), SD DM-nucleons interactions (green lines) and SI DM-nucleons interactions (blue lines). Solid lines represent the values computed in this work while the dashed lines are the one given in Ref. [2]. All the rates are shown for a choice of scattering cross section of $\sigma_i = 10^{-40} \text{ cm}^2$. . .</i>	128
5.3	<i>NuWro computed $\nu_\mu - {}^{40}\text{Ar}$ charged-current scattering cross section as a function of the neutrino energy E_μ. The black line shows to the total cross section, whereas the others correspond to the different contributions (in red quasi-elastic scattering, in green resonant pion exchange, in blue deep inelastic scattering and in purple meson exchange current).</i>	131
5.4	<i>Expected atmospheric neutrino flux as a function of the neutrino energy E_ν at Homestake at solar minimum, taken from Ref. [3]. The blue solid (dashed) line correspond to muon neutrinos (antineutrinos) and the red solid (dashed) line correspond to electron neutrinos (antineutrinos). . . .</i>	133
5.5	Feynman diagrams for B^1B^1 annihilation into SM fermions.	135
5.6	Feynman diagrams for B^1B^1 annihilation into a Higgs boson pair. . . .	136
5.7	<i>Computed spectra of muon neutrinos at the DUNE FD site from B^1 annihilations in the Sun for three different values of M_{LKP}, plotted in relative energy units for legibility.</i>	137

LIST OF FIGURES

5.8 Projected 90% confidence level upper limit for DUNE (400 kT yr) on the spin- dependent B^1 -proton scattering cross section as a function of M_{LKP} (green dots). I also show the previous limits from IceCube [4] (blue line) and Antares [5] (red line) on the LKP cross section. The shaded area represents the disfavoured region (at 95% confidence level) on the mass of the LKP from LHC data [6].	138
5.9 Computed spectra of muon neutrinos at the DUNE FD site from $\tau^+\tau^-$ (left panel) and $b\bar{b}$ (right panel) annihilations in the Sun for the DM masses $m_{\text{DM}} = 10$ GeV (red line), 50 GeV (green line) and 100 GeV (blue line), plotted in relative energy units.	139
5.10 Distribution of the muon neutrino energies from the $\tau^+\tau^-$ (left panel) and $b\bar{b}$ (right panel) annihilation channels, for $m_{\text{DM}} = 10$ GeV, separated by CC interaction type: QEL (blue), MEC (orange), RES (green) and DIS (red).	140
5.11 Distributions of θ_μ (left panel), θ_j (central panel) and θ_{plane} (right panel) for the $b\bar{b}$ sample with $m_{\text{DM}} = 10$ GeV (blue) and the atmospheric background (red).	141
5.12 Left panel: signal efficiencies (blue lines) and background rejections (red lines) for events passing the cuts $\theta < \theta_{\text{cut}}$ for the jet (solid lines) and muon (dashed lines) angles. Right panel: signal efficiency (blue line) and background rejection (red line) for events passing the cut $\theta_{\text{plane}} < \theta_{\text{cut}}$ for the momentum conservation plane deviation.	143
5.13 Signal efficiencies for the $\tau^+\tau^-$ (blue line) and $b\bar{b}$ (red line) DIS samples as functions of the DM mass, m_{DM} , obtained by applying the optimal angular cuts $\theta_\mu < 27^\circ$, $4^\circ < \theta_j < 26^\circ$ and $\theta_{\text{plane}} < 3.5^\circ$	144
5.14 Distributions of $\cos \theta_\mu$ (left panel), $\cos \theta_p$ (central panel) and $\cos \theta_N$ (right panel) for the $\tau^+\tau^-$ QEL sample with $m_{\text{DM}} = 5$ GeV (blue) and the atmospheric background (red).	145

LIST OF FIGURES

5.15 <i>Left panel: value of the loss function for the training sample (blue line) and accuracy for the validation sample (red line) versus the number of iterations for the MLP classifier training. Right panel: distributions of the predicted probabilities assigned by the MLP classifier to the test sample for the $\tau^+\tau^-$ QEL signal with $m_{\text{DM}} = 5 \text{ GeV}$ (blue) and the atmospheric background (red).</i>	146
5.16 <i>Signal efficiencies for the $\tau^+\tau^-$ (blue line) and $b\bar{b}$ (red line) single proton QEL samples as functions of the DM mass, m_{DM}, obtained by requiring a minimum predicted probability from the MLP classifier of 0.97 in order to achieve a background rejection greater than 99.8%.</i>	148
5.17 <i>Projected 90% confidence level upper limit for DUNE (400 kT yr) on the spin-dependent DM-nucleon scattering cross section as a function of m_{DM}, for the annihilation channels $\tau^+\tau^-$ (blue) and $b\bar{b}$ (red) separated by interaction type (up triangles denote DIS interactions whereas down triangles represent QEL interactions). I also show the previous limits from IceCube [7] (solid lines) and the projected sensitivities for Pingu [8] (dashed lines) and Hyper-Kamiokande [9] (dash-dotted lines), as well as the direct detection limits from PICASSO [10] (solid green line) and PICO-60 C₃F₈ [11] (dashed green line).</i>	149
5.18 <i>Left panel: Projected 90% confidence level sensitivity of DUNE (400 kT yr) to the scale Λ of an EFT containing only leptophilic DM axial-axial interactions (blue line). Right panel: . In both cases the corresponding limits from DarkSide-50 [12] (dotted green line) and XENON1T [13] (dashed red line) are also shown, together with the configurations for which the correct relic density is achieved (black line), all for the coupling values $c_A^e = 10^3$ and $c_A^\nu = 10^{-2}$.</i>	154
6.1 Schematic diagram showing the different modules involved in the ND-GAr production.	164

LIST OF FIGURES

6.2 Distribution of the fraction of energy deposits with residual range less than 20% of the total track length, and distribution of the ionisation per unit length after removing the tracks with less than 30% of their energy deposits in the last 20% of the track.	168
6.3 Distribution of the reconstructed ionisation charge per unit length for different reclustering values, and distribution of the median change in dQ/dx per track for the $N_{group} = 4$ reclustering.	169
6.4 Distribution of the Geant4-simulated energy losses per unit length versus residual range for the stopping proton sample.	171
6.5 Fitted most probable dQ/dx values for each dE/dx bin, together with best fit to the logarithmic calibration function.	172
6.6 Fitted most probable dQ/dx values for each dE/dx bin for three different ADC bit limits.	174
6.7 Area normalised dE/dx distributions for the true and the reconstructed energy deposits in the stopping proton sample, both after applying the calibration and the calibration and the normalisation correction.	175
6.8 Fractional residuals between the true and the corrected dE/dx means and the 60% truncated means, and fractional residuals between the true and the uncorrected, corrected and uncalibrated dE/dx 60% truncated means.	177
6.9 Estimated values of the mean dE/dx bias and resolution for the stopping proton sample at different values of the truncation factor.	178
6.10 Examples of the truncated mean dE/dx LanGauss fits for various $\beta\gamma$ bins, from a simulated FHC neutrino sample.	180
6.11 Resulting one and two dimensional projections of the posterior probability distributions of the ALEPH $\langle dE/dx \rangle$ parameters obtained by fitting the 60% truncated mean dE/dx values from a FHC neutrino sample.	181

LIST OF FIGURES

6.12 Truncated mean dE/dx obtained for the FHC neutrino sample as a function of the $\beta\gamma$ product, together with the fitted most probable values for each $\beta\gamma$ bin and the best fit obtained using the ALEPH parametrisation.	182
6.13 Distribution of the 60% truncated mean dE/dx versus reconstructed momentum for the FHC neutrino sample.	183
6.14 Estimated values of the mean dE/dx bias and resolution obtained for the true protons in a FHC neutrino sample.	184
6.15 True momentum distribution for the primary muon in ν_μ CC $N\pi^\pm$ interactions inside the fiducial volume of ND-GAr, compared to the post FSI charged pion spectrum.	185
6.16 Distributions of energy deposits in the ECal for a muon and a charged pion with similar momenta.	186
6.17 Left panel: comparison between the precision (blue), sensitivity (yellow) and F_1 score (red) obtained for the default (horizontal lines) and new algorithms, both with the χ^2 -based direction estimator (squares) and cheating the directions (circles), for different values of the χ^2 cut. Right panel: comparison of the performance of the new algorithm when applying the cluster t_0 correction (squares) and when (circles).	188
6.18 Schematics of a possible option to deal with track-ECal associations in non-zero t_0 neutrino interaction events, trying to correct for the drift direction uncertainty in a cluster-by-cluster basis using the cluster time, $t_{cluster}$	190
6.19 Momentum distribution for the reconstructed muons (top panel) and charged pions (bottom panel) in a FHC neutrino sample, together with the fraction of them reaching the ECal (red) and MuID (blue). Each entry corresponds to a reconstructed track, backtracked to a true muon or pion which has not produced any other reconstructed track.	192

LIST OF FIGURES

6.20 Predicted truncated mean dE/dx versus momentum, for electrons, muons, charged pions and protons, obtained using the ALEPH parametrisation. The vertical dashed lines represent the boundaries of the six regions used for the muon and pion classification training.	193
6.21 Example ECal feature distributions for muons and charged pions in the five different momentum ranges considered.	197
6.22 Example MuID feature distributions for muons and charged pions in the three different momentum ranges considered.	198
6.23 Left panel: cumulative explained variance for the first three principal components (top panel) and contribution of the different features to the principal axes in feature space (bottom panel). Right panel: Shapley (blue) and Gini (red) feature importances for the different input features. Both figures correspond to the samples in the momentum range $0.3 \leq p < 0.8 \text{ GeV}/c$	200
6.24 Left panel: cumulative explained variance for the first three principal components (top panel) and contribution of the different features to the principal axes in feature space (bottom panel). Right panel: Shapley (blue) and Gini (red) feature importances for the different input features. Both figures correspond to the samples in the momentum range $0.8 \leq p < 1.5 \text{ GeV}/c$	201
6.25 Evolution of the SHAP importance for the top six most important features across all five momentum ranges.	203
6.26 Permutation importances for the ten most important features in the different momentum ranges (from left to right, top to bottom, in increasing momentum order). The bars indicate the effect that permutations of each feature have on the purity (blue) and the sensitivity (yellow), the translucent regions representing one standard deviation around the central value.	205

LIST OF FIGURES

6.27 Values of the precision and sensitivity obtained for 10000 BDT hyperparameter configurations, for the momentum regions I, III and V.	208
6.28 Reliability diagrams for the BDT classifier used in the momentum range $0.3 \leq p < 0.8 \text{ GeV}/c$, both for the original (blue circles) and calibrated (yellow squares) responses. For reference, the response of a perfectly calibrated classifier is also shown (black dashed line).	210
6.29 Uncalibrated (left panel) and calibrated (right panel) predicted probabilities assigned by the BDT classifiers for true muons (blue) and charged pions (red) in the momentum range $0.3 \leq p < 0.8 \text{ GeV}/c$	211
6.30 Schematic of the hit selection used for the ToF measurement. The grid represents the layers of the inner ECal, with coloured squares indicating the tiles with hits. Green squares indicate the selected hits.	213
6.31 Particle velocity versus momentum measured with different ECal arrival time estimations. From left to right: earliest hit time, average hit time, and fitted hit time. In all cases the time resolution is $\Delta\tau = 0.1 \text{ ns}$	215
6.32 Mass spectra for p (blue) and π^\pm (yellow) particles, using different ECal time resolution values (from top to bottom, in ascending order), and arrival time estimates. From left to right: earliest hit time, average hit time, and fitted hit time. The dashed lines indicate the true masses of the particles.	217
6.33 Efficiency (top panel) and purity (bottom panel) for the proton selection as a function of the momentum, for $\Delta\tau = 0.10 \text{ ns}$	218
6.34 Distributions of the velocities measured by ToF with the inner ECal, for different momentum bins, in a FHC neutrino interaction sample. The Gaussian fits are performed around the maxima for each particle species.	219

LIST OF FIGURES

6.35 Left panel: number of non-decaying, decaying and decaying in the fiducial volume pions for a MC sample of 100000, $p = 500$ MeV/ c isotropic positively charged pions inside the TPC. Right panel: event display for a positive pion decaying inside the fiducial volume, with a single reconstructed track for the pion and muon system.	220
6.36 Values of $\chi_k^{2(FB)}$ (top left panel), F_k (top right panel), $D_k^{1/R}$ (bottom left panel) and D_k^ϕ (bottom right panel) versus position along the drift direction for a reconstructed track in a positive pion decay event. The vertical red dashed line indicates the true location of the decay point. . .	221
6.37 Fractional residual distributions of the true and reconstructed decay position along the drift coordinate, using the position of the maximum of $\chi_k^{2(FB)}$ (left panel) and F_k (right panel) as estimates of the decay position. Also shown are double Gaussian fits to these points (red lines). . .	222
6.38 Distributions of the extreme values of $\chi_k^{2(FB)}$ (top left panel), F_k (top right panel), $D_k^{1/R}$ (bottom left panel) and D_k^ϕ (bottom right panel) for non-decaying reconstructed pion tracks (blue) and tracks which include the decay inside the fiducial volume (red).	224
6.39 Left panel: distributions of the predicted probabilities assigned by the BDT classifier to a test sample of decaying pion+muon tracks (blue) and non-decaying pion tracks (red). Left: signal efficiency versus background acceptance (ROC curve) obtained from the BDT for the test sample. . .	225
6.40 Left panel: dependence of the decay position finding resolution on the true value of the decay angle for the $\chi_k^{2(FB)}$ (red) and F_k (blue) methods. Right panel: signal efficiency (blue line) and background rejection (red line) from the BDT classifier versus true decay angle.	225

LIST OF FIGURES

6.41 Mean values of the F_1 -score marginal distributions for the different free parameters of the new clustering algorithm, with the error bars representing one standard deviation around the mean. The F_1 -score values were computed for the 6561 possible parameter configurations using 1000 ν_μ CC interaction events.	228
6.42 Left panel: distributions of the number of ECal clusters per photon from π^0 decays for the standard (red) and new (blue) clustering algorithms. Right panel: reconstructed invariant mass distributions for photon pairs from single π^0 events using the standard (red) and new (blue) ECal clustering algorithms.	230
6.43 Distributions of proton dE/dx and ToF scores for a sample of 100000 FHC neutrino interactions in the HPgTPC.	232
7.1 Schematic diagram of the HPgTPC including the fiducial volume.	238
7.2 True positive, false positive, and false negative true neutrino energy distributions for a ν_μ CC selection.	239
7.3 Efficiency and purity for the ν_μ CC selection as a function of the different cuts.	241
7.4 Significance for the ν_μ CC selection as a function of the different cuts. .	241
7.5 Normalised 2D distributions of efficiency, purity and significance for the ν_μ CC selection. The $S/\sqrt{S+B}$ is normalised to the highest value achieved. The vertical dashed line indicates a purity value of 0.85, whereas the horizontal one corresponds to an efficiency of 0.80.	242
7.6 Cumulative efficiency and purity for the ν_μ CC selection.	243
7.7 True neutrino energy spectra for the ν_μ CC selection.	244
7.8 True neutrino energy spectra for the ν_μ CC selection.	245

LIST OF FIGURES

7.9 True neutrino energy spectra for the ν_μ CC selection with (blue) and without (red) sign selection. The selected events are broken down by true positives (signal) and false positives (background). The true distribution is also shown (black data points). The bottom panel shows the ratios between the number of false positives and total selected events per bin. . .	246
7.10 Efficiency 2D distributions for the ν_μ CC selection given the true position of the interaction vertex.	247
7.11 Distributions for the reconstructed versus truth generated primary muon momentum (top left panel), longitudinal momentum (top right panel), transverse momentum (bottom left panel), and beam angle (bottom right panel). The reconstructed values correspond to the selected primary muon candidate, whereas the truth values come from the true primary muon in the event.	248
7.12 Efficiency and purity of the ν_μ CC selection as a function of the primary muon true momentum and beam angle.	249
7.13 Fractional residual distributions for the position of the primary vertex in the ν_μ CC selection.	250
7.14 Distribution of events given their true and reconstructed π^\pm multiplicity, for a given selection.	252
7.15 Efficiency and purity for the ν_μ CC $0\pi^\pm$ selection as a function of the different cuts.	254
7.16 Efficiency and purity for the ν_μ CC $1\pi^\pm$ selection as a function of the different cuts.	255
7.17 Row and column normalised distributions of events given their true and reconstructed π^\pm multiplicity, for the selection that maximises the significance of the ν_μ CC $1\pi^\pm$ selection.	257
7.18 Purity versus efficiency achieved for the different cut configurations explored separated by the various ν_μ CC $N\pi^\pm$ selections.	258

LIST OF FIGURES

- 7.19 Invariant mass distribution obtained for the unassociated ECal cluster pair in the event with the value closest to the true π^0 mass. 259

List of Tables

2.1	Values of T_3 and $Y/2$ assigned to the first generation of fermions.	41
2.2	Neutral current couplings.	42
2.3	Summary of neutrino oscillation parameters determined in the Neutrino Global Fit of 2020 [14].	57
3.1	Summary of the two-phased plan for DUNE.	65
3.2	Exposure and time required to achieve the different physics milestones of the two phases.	66
4.1	<i>Characteristic parameters of the two monoenergetic muon events selected, relative to the U plane: projected angles in the xz' and $y'z'$ planes, S/N values for the raw and filtered waveforms, mean improvement of the S/N and peak asymmetry.</i>	111
5.1	Systematic uncertainties for the solar WIMP signal events.	156
5.2	Systematic uncertainties for the solar WIMP atmospheric background events.	157
6.1	Calibration parameters obtained from the fit of the ND-GAr simulated stopping proton sample to the calibration function, for different ADC limits.	173
6.2	Momentum ranges and description of the PID approach assumed for the muon and pion classification task.	194
6.3	Optimal values of the hyperparameters used by the BDT, for each momentum range.	209

LIST OF TABLES

6.4	Performance metrics of the BDTs with optimal hyperparameters, for the different momentum ranges.	209
6.5	Summary of parameters and sampled values used in the optimisation of the clustering algorithm.	228
7.1	Event rates in ND-GAr.	236
7.2	Step-by-step ν_μ CC selection cuts and cumulative passing rates.	243

List of Abbreviations

ADC	Analog to Digital Converter	HPgTPC	High Pressure gaseous Time Projection Chamber
ALEPH	Apparatus for LEP PHysics		
ALICE	A Large Ion Collider Experiment	LBL	Long BaseLine
BDT	Boosted Decision Tree	MuID	Muon IDentification system
CC	Charged Current	NC	Neutral Current
DM	Dark Matter	ND	Near Detector
DUNE	Deep Underground Neutrino Experiment	ND-GAr	Near Detector Gaseous Argon
ECal	Electromagnetic Calorimeter	ND-LAr	Near Detector Liquid Argon
FD	Far Detector	PDG	Particle Data Group
FHC	Forward Horn Current	RHC	Reverse Horn Current

1

35

Introduction

36

2

37

Neutrino physics

38
39 *Little particles of inspiration sleet through the universe all the time traveling*
40 *through the densest matter in the same way that a neutrino passes through a*
41 *candyfloss haystack, and most of them miss.*

42 – Terry Pratchett, *Sourcery*

43 Ever since they were postulated in 1930 by Wolfgang Pauli to explain the continuous
44 β decay spectrum [15] and later found by F. Reines and C. Cowan at the Savannah
45 River reactor in 1953 [16], neutrinos have had a special place among all other elementary
46 particles. They provide a unique way to probe a wide range of quite different physics,
47 from nuclear physics to cosmology, from astrophysics to colliders. Moreover, there is
48 compelling evidence to believe that the study of neutrinos may be key to unveil different
49 aspects of physics beyond the SM, difficult to test elsewhere.

50 In this Chapter, I will review the basics of neutrino physics, from its role within the
51 SM to the main open questions related to the neutrino sector, paying special attention
52 to the phenomenology of neutrino oscillations.

53 2.1 Neutrinos in the SM

54 The SM of fundamental interactions was initially proposed in 1967 by S. Glashow, S.
55 Weinberg and A. Salam[17–19]. This theoretical framework describes the dynamics
56 of leptons and quarks, by introducing a collection of mediating gauge vector bosons
57 and one scalar particle, known as the Higgs boson. It assumes that the local $SU(3) \times$

CHAPTER 2. NEUTRINO PHYSICS

58 SU(2)_L × U(1)_Y gauge symmetry is an internal symmetry of the system, with SU(3)
 59 describing quantum chromodynamics, and SU(2)_L × U(1)_Y being the gauge groups of
 60 the electroweak sector. For a detailed overview of the SM of electroweak interactions,
 61 see Ref. [20].

62 In the SM, neutrinos appear in three flavours, namely ν_e , ν_μ , and ν_τ . These are
 63 associated with the corresponding charged leptons, e , μ , and τ . Neutrinos exist only
 64 as left-handed particles, grouped in doublets with the charged leptons, while the later
 65 come in both chirality states:

$$\begin{pmatrix} \nu_e \\ e_L^- \end{pmatrix}, \quad \begin{pmatrix} \nu_\mu \\ \mu_L^- \end{pmatrix}, \quad \begin{pmatrix} \nu_\tau \\ \tau_L^- \end{pmatrix}, \quad e_R^-, \quad \mu_R^-, \quad \tau_R^-. \quad (2.1)$$

66 Similarly, quarks also exist in both chirality states, and are grouped as:

$$\begin{pmatrix} u_L \\ d_L \end{pmatrix}, \quad \begin{pmatrix} s_L \\ c_L \end{pmatrix}, \quad \begin{pmatrix} t_L \\ b_L \end{pmatrix}, \quad u_R, \quad d_R, \quad s_R, \quad c_R, \quad t_R, \quad b_R. \quad (2.2)$$

67 The fact that there are no right-handed neutrino fields implies that neutrinos are
 68 strictly massless within the SM. This restriction follows from the experimental observation
 69 that all neutrinos produced via weak interactions are pure left-handed helicity states
 70 (and similarly antineutrinos are pure right-handed states). The hypothetical existence
 71 of right-handed neutrinos could be indirectly inferred from the observation of non-zero
 72 neutrino masses, nevertheless the existence of neutrino masses is not a sufficient condition
 73 for the existence of such fields.

74 Left and right-handed fermions transform differently under SU(2)_L × U(1)_Y rotations,
 75 as the right-handed particles are singlets under SU(2)_L. Applying a local transformation,
 76 they change as:

$$\begin{aligned} \psi_L &\longrightarrow e^{-iY\beta(x)/2} e^{-iT_a\alpha_a(x)} \psi_L, \\ \psi_R &\longrightarrow e^{-iY\beta(x)/2} \psi_R, \end{aligned} \quad (2.3)$$

77 where $Y/2$ and T_a are the generators of SU(2)_L and U(1)_Y, respectively, and $\beta(x)$ and

2.1. NEUTRINOS IN THE SM

Table 2.1: Values of T_3 and $Y/2$ assigned to the first generation of fermions.

	e_L	ν_e	e_R	u_L	d_L	u_R	d_R
T_3	-1/2	1/2	0	1/2	-1/2	0	0
$Y/2$	-1/2	-1/2	-1	1/6	1/6	2/3	-1/3

78 $\alpha_a(x)$ are the parameters of the rotation.

79 The values of the quantum numbers $Y/2$ and T_3 , the third component of the weak
80 isospin, have to be assigned to the different particles. The values of T_3 follow from the
81 commutation relations of the generators of $SU(2)$. After the spontaneous symmetry
82 breaking $SU(2)_L \times U(1)_Y \rightarrow U(1)_{EM}$, one finds the relation which determines the electric
83 charge:

$$Q = T_3 + \frac{Y}{2}, \quad (2.4)$$

84 Setting the electric charge to -1 for electrons, we can find the values of the hypercharge
85 for the rest of the fermions. The resulting values for the first generation of leptons and
86 quarks are shown in Tab. 2.1.

87 It is clear that the free Lagrangian of the theory is not be invariant under the gauge
88 transformations, as the kinetic terms contain derivatives. Therefore, to make it invariant,
89 one needs to introduce a set of gauge bosons. They appear in the so-called covariant
90 derivative, which replaces the common derivative and transforms in the same way as the
91 fermion fields under local rotations. This constrain fixes completely the transformations
92 of the spin-1 fields. For left and right-handed particles, the covariant derivatives are
93 given by:

$$\begin{aligned} D_\mu \psi_L &= \left(\partial_\mu + ig' \frac{Y}{2} B_\mu + ig T_a W_\mu^a \right) \psi_L, \\ D_\mu \psi_R &= \left(\partial_\mu + ig' \frac{Y}{2} B_\mu \right) \psi_R, \end{aligned} \quad (2.5)$$

94 where W_μ^i , $i = 1, 2, 3$ and B_μ are the gauge bosons for the $SU(2)_L$ and $U(1)_Y$ factors,
95 respectively, and g and g' are the corresponding gauge couplings. It can be shown that
96 these fields transform in the adjoint representation of the gauge group.

CHAPTER 2. NEUTRINO PHYSICS

Table 2.2: Neutral current couplings.

	u	d	ν_e	e
$2v_f$	$1 - \frac{8}{3}\sin^2\theta_W$	$-1 + \frac{4}{3}\sin^2\theta_W$	1	$-1 + 4\sin^2\theta_W$
$2a_f$	1	-1	1	-1

97 So far, the theory only contains massless particles, as adding bare mass terms to
 98 the Lagrangian would spoil the gauge symmetry. Therefore, the mass terms need to
 99 be induced by a spontaneous violation of the symmetries. In the SM, the responsible
 100 for this is the Higgs mechanism. The Higgs doublet is coupled to the gauge bosons
 101 through the covariant derivative, and to the fermions through the Yukawa couplings.
 102 Upon spontaneous symmetry breaking, the vacuum expectation value of the Higgs field
 103 generate the mass terms of the particles.

104 In order to obtain the physical intermediate vector boson states, we need to perform
 105 the following redefinitions:

$$\begin{aligned} A_\mu &= \sin \theta_W W_\mu^3 + \cos \theta_W B_\mu, \\ Z_\mu &= \cos \theta_W W_\mu^3 - \sin \theta_W B_\mu, \\ W_\mu^\pm &= \frac{1}{\sqrt{2}} (W_\mu^1 \mp iW_\mu^2), \end{aligned} \tag{2.6}$$

106 where A_μ is the photon field, and Z_μ and W_μ^\pm are the neutral and the charged weak
 107 boson fields, respectively. The Weinberg angle, θ_W , relates the weak coupling constants
 108 and the electric charge:

$$e = g' \cos \theta_W = g \sin \theta_W. \tag{2.7}$$

109 At this point, the interacting part of the electroweak Lagrangian can be re-written
 110 as the sum of three contributions: the electromagnetic (EM), charged-current (CC) and
 111 neutral-current (NC) components:

$$\begin{aligned} \mathcal{L}_{\text{EW}}^{\text{int}} &= \mathcal{L}_{\text{EM}} + \mathcal{L}_{\text{CC}} + \mathcal{L}_{\text{NC}} \\ &= -eA_\mu J_{\text{EM}}^\mu - \frac{g}{2\sqrt{2}} (W_\mu^+ J_{\text{CC}}^\mu + \text{h.c.}) - \frac{g}{2\cos\theta_W} Z_\mu J_{\text{NC}}^\mu, \end{aligned} \tag{2.8}$$

2.2. TROUBLE IN THE NEUTRINO SECTOR

112 with the currents defined as:

$$\begin{aligned} J_{\text{EM}}^\mu &= \sum_f Q_f \bar{f} \gamma^\mu f, \\ J_{\text{CC}}^\mu &= \sum_\ell \bar{\nu}_\ell \gamma^\mu (1 - \gamma_5) \ell + \sum_f \bar{u}_f \gamma^\mu (1 - \gamma_5) d_f, \\ J_{\text{NC}}^\mu &= \sum_f \bar{f} \gamma^\mu (v_f - a_f \gamma_5) f, \end{aligned} \quad (2.9)$$

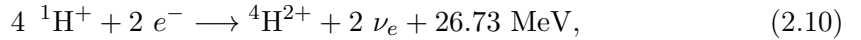
113 where f denotes any SM fermion, ℓ and ν_ℓ a charged lepton and a neutrino of any flavour,
114 and u_f and d_f an up-like and a down-like quarks of any flavour. For the NC case, the
115 values of the v_f and a_f couplings are given in Tab. 2.2.

116 As seen in Eq. (5.8), in the electroweak theory neutrinos are coupled to the Z boson
117 in a universal way. Therefore, by measuring the so-called invisible decay width of the Z
118 boson we have an estimate of the number of light (i.e. lighter than the Z boson) neutrino
119 flavours. This number was measured by LEP in a combined analysis of $e^+ e^- \rightarrow \mu^+ \mu^-$
120 and $e^+ e^- \rightarrow$ hadrons to be $N_\nu = 2.9840 \pm 0.0082$ [21].

121 2.2 Trouble in the neutrino sector

122 2.2.1 The solar neutrino problem

123 Neutrinos are produced everywhere in vast amounts. One of the most prominent sources
124 of neutrinos in our vicinity is our Sun. The Sun is powered mainly by two nuclear fusion
125 reactions, the p – p chain and the CNO cycle. In both cases, the overall reaction is:



126 where part of the released energy is lost to the neutrinos. The electron neutrinos
127 produced are often labelled after the processes that generate them. Figure 2.1 shows the
128 solar neutrino flux as a function of the neutrino energy, broken down by the production
129 process.

CHAPTER 2. NEUTRINO PHYSICS

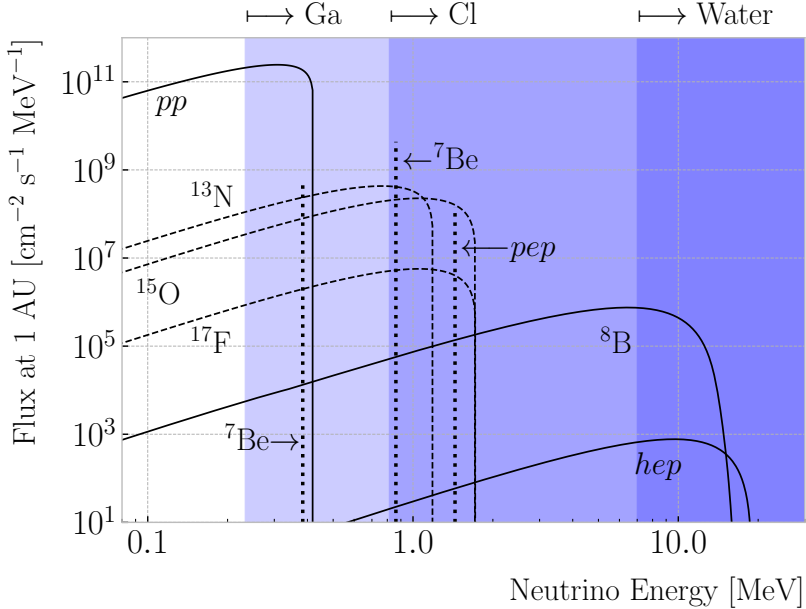


Figure 2.1: Solar neutrino fluxes for the solar model BS05(OP). The detection thresholds for Gallium, Chlorine and water-based experiments are also shown. Figure adapted from Ref. [1].

In the late 1960s, the Brookhaven Solar Neutrino Experiment, led by R. Davis, started

data taking with the goal of measuring the solar neutrino flux [22]. The experiment

used a tank containing 380 m^3 of tetrachloroethene (C_2Cl_4), a liquid commonly used

in dry-cleaning, located 1.5 km underground in the Homestake mine, in Lead, South

Dakota. The incoming neutrinos would get captured following the reaction:

$$\nu_e + {}^{37}\text{Cl} \longrightarrow {}^{37}\text{Ar} + e^-, \quad (2.11)$$

therefore allowing to measure the neutrino flux by counting the ${}^{37}\text{Ar}$ isotopes. The

threshold for this reaction is 0.814 MeV, just below the 0.862 MeV line from the ${}^7\text{Be}$

ground state transition.

The results of the experiment were compared to the theoretical predictions made by

J. Bahcall [23]. During its operation from 1968 to 2002, the experiment observed a solar

ν_e flux that was approximately a third of the total prediction [24].

In the early 1990s, the SAGE [25] and GALLEX [26] experiments started operations.

2.2. TROUBLE IN THE NEUTRINO SECTOR

142 The detection principle used for both experiments was similar to that of the Homestake
143 experiment, but using ^{71}Ga instead of C_2Cl_4 . With a detection threshold of 0.233 MeV,
144 the Gallium-based experiments were able to observe the pp neutrino flux. Both
145 experiments measured a solar electron neutrino flux that was a factor of two lower
146 than the predictions, demonstrating that this deficit was energy-dependent.

147 In the early 2000s, the SNO experiment put an end to the solar neutrino puzzle
148 [27, 28]. Thanks to its directionality capabilities, being a Cherenkov light detector, as
149 well as to its heavy water target, SNO measured the total solar neutrino flux through
150 the NC process:

$$\nu_\alpha + d \longrightarrow n + p + \nu_\alpha, \quad (2.12)$$

151 where $\alpha = e, \mu, \tau$. This measurement agreed with the solar model predictions. Then,
152 measuring the CC reaction:

$$\nu_e + d \longrightarrow p + p + e^-, \quad (2.13)$$

153 they were able to establish that the ν_μ and ν_τ solar fluxes are in fact non-zero, revealing
154 that electron neutrinos were transitioning into different flavours.

155 2.2.2 The atmospheric neutrino problem

156 When cosmic-rays interact with the atoms in the upper atmosphere, a plethora of
157 hadrons, mainly π and K mesons, are produced. In particular, for the charged pions,
158 we have the following decay chain dominates:

$$\begin{aligned} \pi^+ &\longrightarrow \mu^+ + \nu_\mu, \\ \mu^+ &\longrightarrow e^+ + \bar{\nu}_\mu + \nu_e, \end{aligned} \quad (2.14)$$

159 and similar for the antiparticles. For neutrino energies < 1 GeV, the ratio:

$$\frac{N(\nu_\mu + \bar{\nu}_\mu)}{N(\nu_e + \bar{\nu}_e)}, \quad (2.15)$$

160 of produced neutrinos and antineutrinos is, in good approximation, equal to two [29].

CHAPTER 2. NEUTRINO PHYSICS

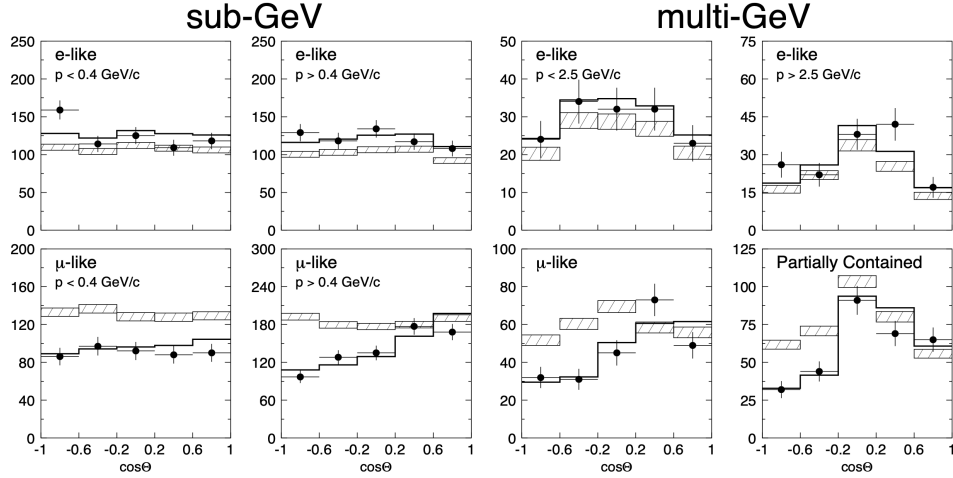


Figure 2.2: Zenith angle distributions for the selected ν_e (top row) and ν_μ (bottom row) events in the SK detector. The hatched region corresponds to the expectation in the case of no oscillations, whereas the solid line indicates the best-fit in the case of $\nu_\mu \rightarrow \nu_\tau$ oscillations. Figure taken from Ref. [34].

161 During the 1980s, several proton decay experiments, like Kamiokande [30], IMB [31],

162 MACRO [32], and Soudan-2 [33], measured the flux of atmospheric neutrinos. This was

163 an important part of their research programme, as the atmospheric neutrinos constitute

164 their main background. All these experiments reported an atmospheric neutrino ratio

165 lower than the predictions.

166 A few years before the SNO discovery, in 1998, Super-Kamiokande (SK) collaboration

167 measured the atmospheric ν_e and ν_μ spectra as a function of the zenith angle [34].

168 Upward-going particles have negative zenith angle, $\cos \Theta < 0$, indicating that they

169 entered from the bottom of the detector. These upward-going neutrinos had to travel

170 through the Earth in order to reach the detector, allowing SK to probe a broad range

171 of baselines. Figure 2.2 shows the reported distributions (black dots), compared to the

172 no oscillations prediction (hatched region). This measurement confirmed that muon

173 neutrinos transition to other flavours, and that this phenomenon depends both on the

174 energy and the path length of the neutrino.

175 The SK and SNO findings provided definitive evidence for the existence of neutrino

176 oscillations, and therefore non-zero neutrino masses. This constitutes one of the

177 groundbreaking discoveries of modern physics and has acted as driving force for beyond

2.3. MASSIVE NEUTRINOS

the Standard Model (BSM) physics. The minimal extension of the SM we can do to address these phenomena is introducing different masses for at least two of the neutrinos. This way, we are left with three neutrino mass eigenstates ν_1 , ν_2 , and ν_3 , with masses m_1 , m_2 , and m_3 respectively, which in general will not coincide with the flavour eigenstates, ν_e , ν_μ , and ν_τ .

2.3 Massive neutrinos

The existence of neutrino oscillations imply that neutrinos are massive particles. However, as we have seen before, within the SM neutrinos are massless, as they do not have a mass term in the Lagrangian. If one wants to give neutrinos a mass, the particle content of the SM needs to be expanded.

A way of generating massive neutrinos while maintaining gauge invariance is by introducing an arbitrary number of sterile neutrinos N_i , $i = 1, \dots, m$. These allow for two different types of neutrino mass terms:

$$-\mathcal{L}_{M_\nu} = \sum_{i=1}^m \sum_{j=1}^3 M_D^{ij} \bar{N}_i \nu_{Lj} + \frac{1}{2} \sum_{i=1}^m \sum_{j=1}^m M_N^{ij} \bar{N}_i N_j^c + \text{h.c.}, \quad (2.16)$$

where M_D is a complex $m \times 3$ matrix and M_N a complex and symmetric $m \times m$ matrix. The first term, often referred to as the Dirac mass term, arises from the corresponding Yukawa interaction after the spontaneous electroweak symmetry breaking, similar to the other fermions. The second term, called the Majorana mass term, is allowed in the Lagrangian, as it is a singlet of the gauge group. However, it violates lepton number conservation by two units.

If one imposes lepton number symmetry conservation, the Majorana term must banish, $M_N = 0$. In this case, if $m = 3$ we can identify the sterile neutrinos as the right-handed component of the neutrino field. The Dirac mass matrix can be diagonalised using two unitary matrices, V_R^ν and V_L^ν , as:

$$M_D = V_R^\nu \text{ diag}(m_1, m_2, m_3) V_L^{\nu\dagger}, \quad (2.17)$$

CHAPTER 2. NEUTRINO PHYSICS

201 where m_i , $i = 1, 2, 3$ are the masses of the three neutrino mass eigenstates.

202 The neutrino mass term can be written in term of the resulting eigenstates as:

$$-\mathcal{L}_{M_\nu} = \sum_{i=1}^3 m_i \bar{\nu}_{Di} \nu_{Di}, \quad (2.18)$$

203 with:

$$\nu_{Di} = \left(V_L^{\nu\dagger} \nu_L \right)_i + \left(V_R^{\nu\dagger} N \right)_i. \quad (2.19)$$

204 In this scenario, both the low energy particle budget and the symmetries of the SM
 205 have to be modified. Moreover, the masses of the neutrinos are generated exclusively
 206 through the Higgs mechanism, which does not explain why they are much smaller than
 207 those of the charged leptons.

208 Going back to the general case, we can re-write Eq. (2.16) in matrix form as:

$$-\mathcal{L}_{M_\nu} = \frac{1}{2} \begin{pmatrix} \bar{\nu}_L^c & \bar{N} \end{pmatrix} \begin{pmatrix} 0 & M_D^T \\ M_D & M_N \end{pmatrix} \begin{pmatrix} \nu_L \\ N^c \end{pmatrix} + \text{h.c.} = \bar{\nu}^c M_\nu \nu + \text{h.c.}, \quad (2.20)$$

209 with $\nu = (\nu_L, N^c)^T$ being a $(3+m)$ -dimensional vector grouping the active and the
 210 sterile neutrinos. The matrix M_ν , which is a complex $(3+m) \times (3+m)$ symmetric
 211 matrix, can be diagonalised by means of a unitary matrix V^ν , yielding:

$$M_\nu = V^\nu \text{ diag}(m_1, m_2, \dots, m_{3+m}) V^{\nu T}. \quad (2.21)$$

212 Using this eigendecomposition, the neutrino mass term can be expressed as:

$$-\mathcal{L}_{M_\nu} = \frac{1}{2} \sum_{i=1}^{3+m} m_i \bar{\nu}_{Mi} \nu_{Mi}, \quad (2.22)$$

213 where the states ν_{Mi} , commonly referred to as Majorana neutrinos, are defined as:

$$\nu_{Mi} = \left(V^{\nu\dagger} \nu \right)_i + \left(V^{\nu\dagger} \nu \right)_i^c, \quad (2.23)$$

214 in such a way that the Majorana condition, $\nu_M^c = \nu_M$, holds true.

2.4. NEUTRINO OSCILLATION FORMALISM

215 As a consequence of the Majorana condition, the neutrino and the antineutrino states
 216 can be described in terms of a single field. As opposed to the charged leptons, which
 217 need to be represented by a four-component or Dirac spinor, the Majorana neutrino is
 218 described by a two-component or Weyl spinor.

219 If the eigenvalues of the Majorana mass matrix, M_N , are much larger than the
 220 electroweak symmetry breaking scale, the diagonalisation of M_ν leads to 3 light and m
 221 heavy neutrino states:

$$-\mathcal{L}_{M_\nu} = \frac{1}{2}\bar{\nu}_l M_l \nu_l + \frac{1}{2}\bar{\nu}_h M_h \nu_h, \quad (2.24)$$

222 where the two mass matrices are given by:

$$\begin{aligned} M_l &\simeq -V_l^T M_D^T M_N^{-1} M_D V_l, \\ M_h &\simeq V_h^T M_N V_h, \end{aligned} \quad (2.25)$$

223 with V_l and V_h two unitary matrices.

224 This scenario represents the so-called see-saw mechanism [35–39]. The name comes
 225 from the fact that the masses of the heavy states are proportional to M_N , whereas for
 226 the light states they are proportional to M_N^{-1} . While both the heavy and the light
 227 neutrinos are Majorana particles, it can be shown that the heavy states are mainly
 228 right-handed, whereas the light ones are mostly left-handed.

2.4 Neutrino oscillation formalism

230 Neutrino oscillations were first proposed in 1958 by B. Pontecorvo [40], inspired by the
 231 neutral kaon oscillation phenomenon [41]. Neutral kaons, K^0 and \bar{K}^0 , have opposite
 232 strangeness (± 1) and are produced in strong processes. It was observed that, when
 233 having a beam initially pure of neutral kaons of one type, these would transition into
 234 their antiparticles while propagating. Because the weak interaction does not conserve
 235 strangeness, neutral kaons can change their identity via the processes shown in Fig. 2.3.

236 The mixing considered initially by Pontecorvo was between the neutrino and the

CHAPTER 2. NEUTRINO PHYSICS

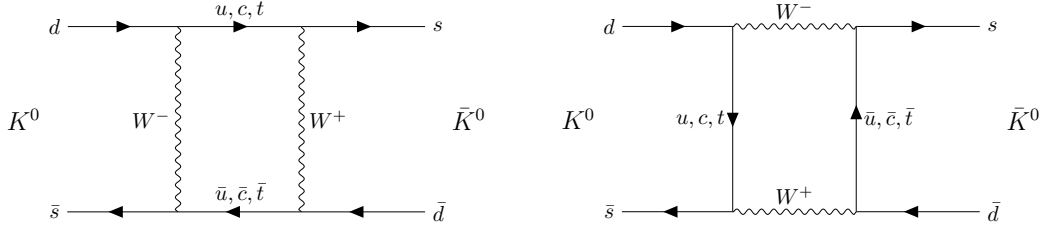


Figure 2.3: $K^0 \rightleftharpoons \bar{K}^0$ mixing through W^\pm exchange.

237 antineutrino states, as only one neutrino flavour was known at the time. After the
238 discovery of the muon neutrino, the mixing between flavours was also explored [42].

239 In the general case, we have 3 active and m sterile neutrinos, resulting in $3 + m$
240 neutrino mass eigenstates. Working in the mass basis, the leptonic charged-current
241 Lagrangian can be written as:

$$-\mathcal{L}_{CC}^{lep} = \frac{g}{\sqrt{2}} (\bar{e}_L, \bar{\mu}_L, \bar{\tau}_L) \gamma^\mu U \begin{pmatrix} \nu_1 \\ \nu_2 \\ \vdots \\ \nu_{3+m} \end{pmatrix} W_\mu^+ + \text{h.c.}, \quad (2.26)$$

242 where U is a $3 \times (3 + m)$ matrix which obeys $UU^\dagger = I_{3 \times 3}$, but in general will not be
243 unitary, $U^\dagger U \neq I_{(3+m) \times (3+m)}$.

244 The leptonic mixing matrix, U , establishes how the neutrino mass states couple to
245 the charged leptons. In general, a complex $n \times n$ matrix can be fully specified by $2n^2$ real
246 parameters. If the matrix is unitary, then the number of independent parameters reduces
247 to n^2 , as one has to impose n normalisation and $n(n - 1)$ orthogonality constraints.
248 In our case, we can further reduce the number of parameters by performing a phase
249 redefinition of the charged lepton fields, without affecting the physics. This is not true
250 for the neutrinos. As they may be their own antiparticles, one is not allowed to remove
251 any physically relevant phases. If we consider n generations of leptons, the total number
252 of parameters in the mixing matrix is $n^2 - n$. Out of these, half of them are mixing
253 angles, while the other half are complex phase factors.

254 Considering the extended SM without any additional sterile neutrino states, the
255 resulting 3×3 mixing matrix is unitary. This matrix, often called the Pontecorvo-Maki-

2.4. NEUTRINO OSCILLATION FORMALISM

256 Nakagawa-Sakata (PMNS) matrix [43, 44], relates the set of active neutrinos and the
257 three mass eigenstates as:

$$|\nu_\alpha\rangle = \sum_{i=1}^3 U_{\alpha i}^* |\nu_i\rangle, \quad (2.27)$$

258 where the Greek index α denotes the flavour $\{e, \mu, \tau\}$ and the Latin index i the mass state
259 $\{1, 2, 3\}$. This leptonic mixing matrix may be parametrized in terms of 6 parameters, 3
260 of which are mixing angles θ_{12} , θ_{13} and θ_{23} , one CP-violating phase δ_{CP} and 2 Majorana
261 phases α and β :

$$U = \begin{pmatrix} 1 & 0 & 0 \\ 0 & c_{23} & s_{23} \\ 0 & -s_{23} & c_{23} \end{pmatrix} \begin{pmatrix} c_{13} & 0 & s_{13} e^{-i\delta_{CP}} \\ 0 & 1 & 0 \\ -s_{13} e^{i\delta_{CP}} & 0 & c_{13} \end{pmatrix} \begin{pmatrix} c_{12} & s_{12} & 0 \\ -s_{12} & c_{12} & 0 \\ 0 & 0 & 1 \end{pmatrix} \begin{pmatrix} 1 & 0 & 0 \\ 0 & e^{i\alpha} & 0 \\ 0 & 0 & e^{i\beta} \end{pmatrix}, \quad (2.28)$$

262 where $c_{ij} \equiv \cos \theta_{ij}$ and $s_{ij} \equiv \sin \theta_{ij}$. This matrix is analogous to the Cabibbo-Kobayashi-
263 Maskawa (CKM) matrix in the quark sector. If neutrinos are Dirac fermions, we can
264 drop the Majorana phases in the PMNS matrix, as in this case we can perform the
265 phase redefinitions. However, these phases play no role on the neutrino oscillation
266 phenomenology.

267 In the case that additional sterile neutrinos states are present, the full leptonic mixing
268 matrix would not be unitary in general. For instance, in the see-saw scenario, the 3×3
269 submatrix for the three light Majorana neutrinos is not unitary. However, the deviations
270 from unitarity are of the order $\mathcal{O}(M_D/M_N)$, and therefore expected to be negligible.

271 2.4.1 Oscillations in vacuum

272 Consider the case where a neutrino of flavour α is produced at $t = 0$, and then it
273 propagates through vacuum. Such a state will evolve in time according to the relation:

$$|\nu_\alpha(\vec{x}, t)\rangle = \sum_{i=1}^3 U_{\alpha i}^* e^{-i(E_i t - \vec{p}_i \cdot \vec{x})} |\nu_i(\vec{x} = \vec{0}, t = 0)\rangle, \quad (2.29)$$

274 in the plane wave approximation, as the mass eigenstates are also eigenstates of the free
275 Hamiltonian.

CHAPTER 2. NEUTRINO PHYSICS

276 This way, the probability for the neutrino to transition from flavour α to flavour β
277 will be given by:

$$P(\nu_\alpha \rightarrow \nu_\beta) = |\langle \nu_\beta | \nu_\alpha(\vec{x}, t) \rangle|^2 = \left| \sum_{i=1}^3 \sum_{j=1}^3 U_{\alpha i}^* U_{\beta j} e^{-i(E_i t - \vec{p}_i \cdot \vec{x})} \langle \nu_j | \nu_i \rangle \right|^2 \\ = \left| \sum_{i=1}^3 U_{\alpha i}^* U_{\beta i} e^{-i(E_i t - \vec{p}_i \cdot \vec{x})} \right|^2, \quad (2.30)$$

278 where we have used the orthogonality relation $\langle \nu_i | \nu_j \rangle = \delta_{ij}$. A usual approximation to
279 take at this point is to consider ultra-relativistic neutrinos, i.e. $p_i \simeq E$, so we can write
280 the dispersion relations as:

$$E_i = \sqrt{p_i^2 + m_i^2} \approx E + \frac{m_i^2}{2E}. \quad (2.31)$$

281 In the end, assuming $t \approx L$ where L is the distance between the production and the
282 detection points, the probability for the $\nu_\alpha \rightarrow \nu_\beta$ transition becomes:

$$P(\nu_\alpha \rightarrow \nu_\beta) = \sum_{i,j} U_{\alpha i}^* U_{\beta i} U_{\alpha j} U_{\beta j} e^{-i \frac{\Delta m_{ij}^2}{2E} L} \\ = \delta_{\alpha\beta} - 4 \sum_{i < j} \Re e [U_{\alpha i}^* U_{\beta i} U_{\alpha j} U_{\beta j}^*] \sin^2 \left(\frac{\Delta m_{ij}^2}{4E} L \right) \\ + 2 \sum_{i < j} \Im m [U_{\alpha i}^* U_{\beta i} U_{\alpha j} U_{\beta j}^*] \sin \left(\frac{\Delta m_{ij}^2}{2E} L \right), \quad (2.32)$$

283 where Δm_{ij}^2 is the difference of the squared masses of the j th and i th neutrino mass
284 eigenvalues. At this point, it is usual to write the phase responsible for the oscillations
285 as:

$$\Delta_{ij} \equiv \frac{\Delta m_{ij}^2}{4E} L \simeq 1.27 \frac{\Delta m_{ij}^2}{(\text{eV}^2)} \frac{L}{(\text{km})} \frac{(\text{GeV})}{E}. \quad (2.33)$$

286 Notice that, in the case of antineutrinos, the only difference would be the sign of the
287 last term in the oscillation probability. As the process $\bar{\nu}_\alpha \rightarrow \bar{\nu}_\beta$ is the CP-mirror image
288 of $\nu_\alpha \rightarrow \nu_\beta$, the differences between their oscillation probabilities would be a measure of

2.4. NEUTRINO OSCILLATION FORMALISM

289 CP symmetry violation:

$$\begin{aligned} A_{CP}^{\alpha\beta} &= P(\nu_\alpha \rightarrow \nu_\beta) - P(\bar{\nu}_\alpha \rightarrow \bar{\nu}_\beta) \\ &= 4 \sum_{i<j} \Im \left[U_{\alpha i}^* U_{\beta i} U_{\alpha j} U_{\beta j}^* \right] \sin 2\Delta_{ij}. \end{aligned} \quad (2.34)$$

290 Assuming that CPT invariance holds, then the following relation must be true:

$$P(\nu_\alpha \rightarrow \nu_\beta) = P(\bar{\nu}_\beta \rightarrow \bar{\nu}_\alpha), \quad (2.35)$$

291 as these two process are related by the CPT symmetry. From the definition of probability,
292 we also must have:

$$\sum_{\beta} P(\nu_\alpha \rightarrow \nu_\beta) = \sum_{\beta} P(\bar{\nu}_\alpha \rightarrow \bar{\nu}_\beta) = 1, \quad (2.36)$$

293 where the sum includes all flavours, including α . From these two constraints, one can
294 probe that:

$$A_{CP}^{\alpha\beta} = -A_{CP}^{\beta\alpha}, \quad (2.37)$$

295 and in particular:

$$A_{CP}^{\alpha\alpha} = 0. \quad (2.38)$$

296 A direct consequence of this last relation is that there are no observable CP-violating
297 effects in the so-called disappearance experiments. One needs to perform appearance
298 experiments, where the flavour detected is different from the original flavour, in order
299 to measure the CP asymmetry. Neutrino experiments often report the amount of CP-
300 violation through the Jarlskog invariant. In terms of the parametrisation typically used
301 to write the PMNS matrix, it is given by:

$$J = \frac{1}{8} \cos \theta_{13} \sin 2\theta_{12} \sin 2\theta_{13} \sin 2\theta_{23} \sin \delta_{CP}. \quad (2.39)$$

302 The Jarlskog invariant can be used to compare the amount of CP-violation in the lepton
303 and the quark sectors, where $J = 3.12^{+0.13}_{-0.12} \times 10^{-5}$ in the latter [45].

CHAPTER 2. NEUTRINO PHYSICS

304 2.4.2 Oscillations in matter

305 When neutrinos propagate through matter, their oscillation can be affected in mainly
 306 two ways. First, neutrinos can inelastically scatter with nuclei, thus destroying the
 307 coherent propagation of their quantum state. Nevertheless, in most cases this effect is
 308 negligible (even in very dense mediums like the core of the Sun). Second, neutrinos can
 309 also experience coherent or forward scatterings, that can affect their oscillation but not
 310 lose the coherent propagation of the state.

311 The first proposed model to account for neutrino oscillations in matter was proposed
 312 by Mikhaev, Smirnov and Wolfenstein (MSW) [46]. It relies on the fact that, as the
 313 only charged lepton present in ordinary matter is the electron, electron neutrinos can
 314 undergo both charged and neutral-current interactions with matter whereas for muon
 315 and tau neutrinos just neutral currents are possible.

316 An illustrative way to introduce the MSW mechanism is by considering the two
 317 flavours case. It can be shown that the evolution of the two flavour eigenstates in vacuum
 318 is given by the following time-dependent Schrödinger equation:

$$i \frac{d}{dt} \begin{pmatrix} \nu_e \\ \nu_\mu \end{pmatrix} = H_V \begin{pmatrix} \nu_e \\ \nu_\mu \end{pmatrix}, \quad (2.40)$$

319 with a vacuum Hamiltonian given by:

$$H_V = \frac{\Delta m^2}{4E} \begin{pmatrix} -\cos 2\theta & \sin 2\theta \\ \sin 2\theta & \cos 2\theta \end{pmatrix}, \quad (2.41)$$

320 where Δm^2 is the mass splitting between the two neutrino states and θ the only mixing
 321 angle. For simplicity, I omit the terms of the Hamiltonian that are proportional to the
 322 identity, as they do not affect the oscillation phenomenology.

323 The NC contribution to the matter potential is identical for all the flavours, and has
 324 the form:

$$V_{NC} = -\frac{G_F}{\sqrt{2}} N_n(x), \quad (2.42)$$

2.4. NEUTRINO OSCILLATION FORMALISM

325 where G_F is the Fermi constant and $N_n(x)$ the local neutron density. Because it is
 326 common to all flavours, I do not take it into account in the effective Hamiltonian, as it
 327 would appear as a term proportional to the identity. The CC component only affects
 328 the electron neutrino (and antineutrino). It can be written as:

$$V_{\text{CC}} = \pm \sqrt{2} G_F N_e(x), \quad (2.43)$$

329 with $N_e(x)$ being the local electron density in the material. In the end, the effective
 330 Hamiltonian which describes the propagation of the flavour eigenstates in matter only
 331 contains an extra $\nu_e - \nu_e$ element:

$$H_M = H_V + \begin{pmatrix} V_{\text{CC}} & 0 \\ 0 & 0 \end{pmatrix}. \quad (2.44)$$

332 The solution to the Schrödinger equation greatly simplifies if one considers the case
 333 of a constant matter density. In that case, the effective Hamiltonian can be diagonalised,
 334 obtaining the effective neutrino mass eigenstates in matter. It can be re-written in the
 335 same form as the vacuum Hamiltonian:

$$H_M = \frac{\Delta m_m^2}{4E} \begin{pmatrix} -\cos 2\theta_m & \sin 2\theta_m \\ \sin 2\theta_m & \cos 2\theta_m \end{pmatrix}, \quad (2.45)$$

336 where the effective mass splitting and the effective mixing angle are given by:

$$\begin{aligned} \Delta m_m^2 &= \lambda \Delta m_m^2, \\ \sin 2\theta_m &= \frac{\sin 2\theta_m}{\lambda} \end{aligned} \quad (2.46)$$

337 with:

$$\begin{aligned} \lambda &= \sqrt{(\cos 2\theta - A)^2 + \sin^2 2\theta}, \\ A &= \pm \frac{2\sqrt{2} G_F N_e E}{\Delta m^2}. \end{aligned} \quad (2.47)$$

338 In terms of the effective matter oscillation parameters, the transition probability

CHAPTER 2. NEUTRINO PHYSICS

339 $\nu_e \rightarrow \nu_\mu$ (in the two flavour approximation) reads:

$$P(\nu_e \rightarrow \nu_\mu) = \sin^2 2\theta_m \sin^2 \left(\frac{\Delta m_m^2}{2E} L \right) \quad (2.48)$$

340 From this last equation one can see that, when $\cos 2\theta = A > 0$ the oscillations are
341 greatly enhanced. This effect is known as the MSW resonance. For the neutrinos, this
342 resonant condition is only satisfied if $\Delta m^2 > 0$ (the opposite is true for antineutrinos).
343 This is can be exploited by long baseline experiments, which can gain sensitivity to the
344 neutrino mass hierarchy through matter effects.

345 2.4.3 Current status of neutrino oscillations

346 A wide range of neutrino experiments provide experimental input to the neutrino
347 oscillation framework, both using natural or synthetic neutrino sources. The results
348 from one of the neutrino global fit analyses, shown in Tab. 2.3¹, summarise well our
349 current understanding of the different oscillation parameters.

350 **Solar neutrino experiments** detect neutrinos produced in thermonuclear reactions
351 inside the Sun, mainly from the so-called *pp* chain and the CNO cycle. These neutrinos
352 have a typical energy in the range from 0.1 to 20 MeV. These experiments (Homestake
353 [47], GALLEX [26], SAGE [25], Borexino [48], Super-Kamiokande [49] and SNO [50])
354 provide the best sensitivities to θ_{12} and Δm_{21}^2 .

355 **Atmospheric neutrino experiments** detect the neutrino flux produced when
356 cosmic rays scatter with particles in Earth's atmosphere. These collisions generate particle
357 showers that eventually produce electron and muon neutrinos (and antineutrinos). Their
358 energies range from few MeV to about 10^9 GeV. Experiments, like Super-Kamiokande
359 [51] and IceCube [52] use atmospheric neutrinos to measure oscillations and are specially
360 sensitive to θ_{23} and Δm_{32}^2 .

361 **Reactor neutrino experiments** look for the $\bar{\nu}_e$ spectrum produced by nuclear
362 reactors, with energies in the MeV scale. Depending on the distance to the source,

¹These are the results reported during M. Tórtola's talk at Neutrino 2024 (see this link). I need to keep an eye and see if they publish these or other updated results in the near future.

2.5. OPEN QUESTIONS IN THE NEUTRINO SECTOR

Table 2.3: Summary of neutrino oscillation parameters determined in the Neutrino Global Fit of 2020 [14].

Parameter	Best fit $\pm 1\sigma$	3σ range
Δm_{21}^2 [eV $^2 \times 10^{-5}$]	$7.55^{+0.22}_{-0.20}$	6.98 – 8.19
$ \Delta m_{31}^2 $ [eV $^2 \times 10^{-3}$] (NO)	$2.51^{+0.02}_{-0.03}$	2.43 – 2.58
$ \Delta m_{31}^2 $ [eV $^2 \times 10^{-3}$] (IO)	$2.41^{+0.03}_{-0.02}$	2.34 – 2.49
$\sin^2 \theta_{12}/10^{-1}$	3.04 ± 0.16	2.57 – 3.55
$\sin^2 \theta_{23}/10^{-1}$ (NO)	$5.64^{+0.15}_{-0.21}$	4.23 – 6.04
$\sin^2 \theta_{23}/10^{-1}$ (IO)	$5.64^{+0.15}_{-0.18}$	4.27 – 6.03
$\sin^2 \theta_{13}/10^{-2}$ (NO)	$2.20^{+0.05}_{-0.06}$	2.03 – 2.38
$\sin^2 \theta_{13}/10^{-2}$ (IO)	$2.20^{+0.07}_{-0.04}$	2.04 – 2.38
δ_{CP}/π (NO)	$1.12^{+0.16}_{-0.12}$	0.76 – 2.00
δ_{CP}/π (IO)	$1.50^{+0.13}_{-0.14}$	1.11 – 1.87

363 long-baseline experiments like KamLAND [53] are sensitive to the solar mass splitting
364 Δm_{21}^2 whereas much shorter baseline experiment such as RENO [54] or DayaBay [55]
365 measure θ_{13} and Δm_{31}^2 .

366 **Accelerator experiments** measure neutrino fluxes generated in particle accelerators.
367 Usually mesons are produced in the accelerator to be focused into a beam, then some
368 decay to muon neutrinos and the rest are absorbed by a target. Depending on the
369 configuration one can obtain a beam made of mostly neutrinos or antineutrinos. The
370 typical energies of these neutrinos are in the GeV range. Experiments such as NOvA
371 [56], T2K [57], MINOS [58], OPERA [59] and K2K [60] (and in the future DUNE [61])
372 are primarily sensitive to θ_{13} , θ_{23} and Δm_{32}^2 . Also, in the coming years DUNE [61] and
373 Hyper-Kamiokande [62] will be sensitive to δ_{CP} .

374 2.5 Open questions in the neutrino sector

375 A crucial question that remains open these days, and is of vital importance for oscillation
376 phenomena, is whether the mass eigenvalue ν_3 is the heaviest (what we call normal
377 ordering) or the lightest (referred to as inverted ordering) of the mass eigenstates. In

CHAPTER 2. NEUTRINO PHYSICS

378 other words, this means that we do not know the sign of Δm_{32}^2 , so we can either have
379 $m_1 < m_2 < m_3$ (NO) or $m_3 < m_1 < m_2$ (IO).

380 Another big puzzle is related to the value of δ_{CP} . Nowadays it is poorly constrained,
381 with all values between π and 2π being consistent with data. A prospective measurement
382 different from $\delta_{CP} = 0, \pi$ will predict CP-violation in the leptonic sector, and thus
383 contribute along with the one measured in the quark sector to the total amount of
384 CP-violation. Although it is true that these two contributions by themselves are not
385 enough to explain the matter anti-matter asymmetry in our universe, the amount of
386 CP-violation in the leptonic sector can be key to explain such imbalance.

387 Both of these questions, because of their nature, could be understood thanks to
388 future oscillation experiments.

389 Notwithstanding, there are other mysteries that can not be unveiled just by conducting
390 oscillation experiments, as certain quantities do not influence these phenomena. Among
391 these there is the question of the absolute values of the neutrino masses. Depending
392 on the value of the lightest of the neutrino masses we can have different mass spectra,
393 from hierarchical $m_1 \ll m_2 < m_3$ (NO) or $m_3 \ll m_1 < m_2$ (IO) to quasi-degenerate
394 $m_1 \simeq m_2 \simeq m_3$.

395 Other open question concerns the nature itself of the neutrinos. If neutrinos are Dirac
396 particles then their mass term can be generated through the usual Higgs mechanism
397 by adding right-handed neutrino fields. However, if they are Majorana particles and
398 therefore their own antiparticles, there is no need to add extra fields to have the mass
399 term in the Lagrangian. Experiments like SuperNEMO [63], SNO+ [64] and NEXT
400 [65], which search for neutrino-less double beta decay, will be able to determine whether
401 neutrinos are Dirac or Majorana.

402 2.6 Neutrino interactions

403 The study of neutrino-nucleus interactions is of great importance for long baseline
404 neutrino oscillation experiments. The interaction model provides a mapping between

2.6. NEUTRINO INTERACTIONS

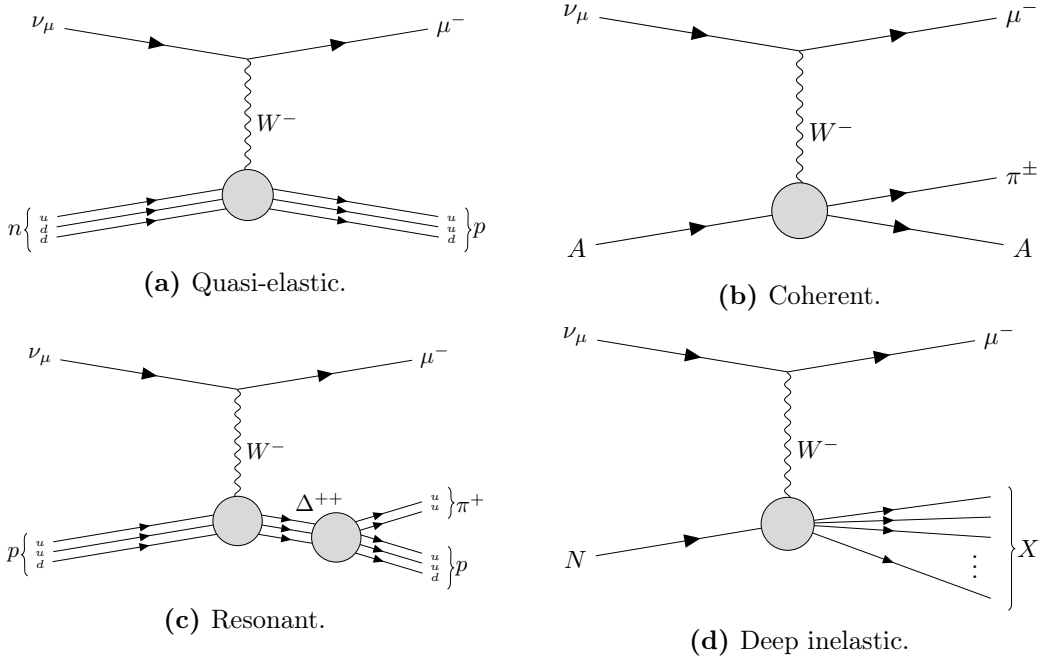


Figure 2.4: Feynman diagrams of the four most relevant CC interactions to long baseline neutrino oscillation experiments.

405 the energy of the incoming neutrino and the final state particles after the interaction.
 406 Because in this kind of experiments neutrinos are obtained as secondary decay products
 407 of mesons, typically charged pions and kaons, their energies are not known a priori. Not
 408 only that, but the kinematics of the interacting nucleon are also unknown. Therefore, we
 409 rely on the neutrino interaction models to provide this relation between the observables
 410 in the detector and the true kinematics of the neutrino. Interaction modelling is expected
 411 to be the one of the leading sources of systematic uncertainties in the next generation of
 412 long baseline experiments [66–68].

413 In the case of neutrino interactions with nuclei, at the energies relevant for long
 414 baseline oscillation experiments, around the GeV-scale, the process is dominated by
 415 the interaction between the neutrino and a single nucleon within the nuclear medium.
 416 Figure 2.4 shows examples of the four most common neutrino CC interactions. In this
 417 diagrams A indicated that the interaction happened with the nucleus as a whole, whereas
 418 N denotes a single nucleon.

419 At low energies, below 1 GeV, quasi-elastic (QE) interactions dominate. In a CCQE

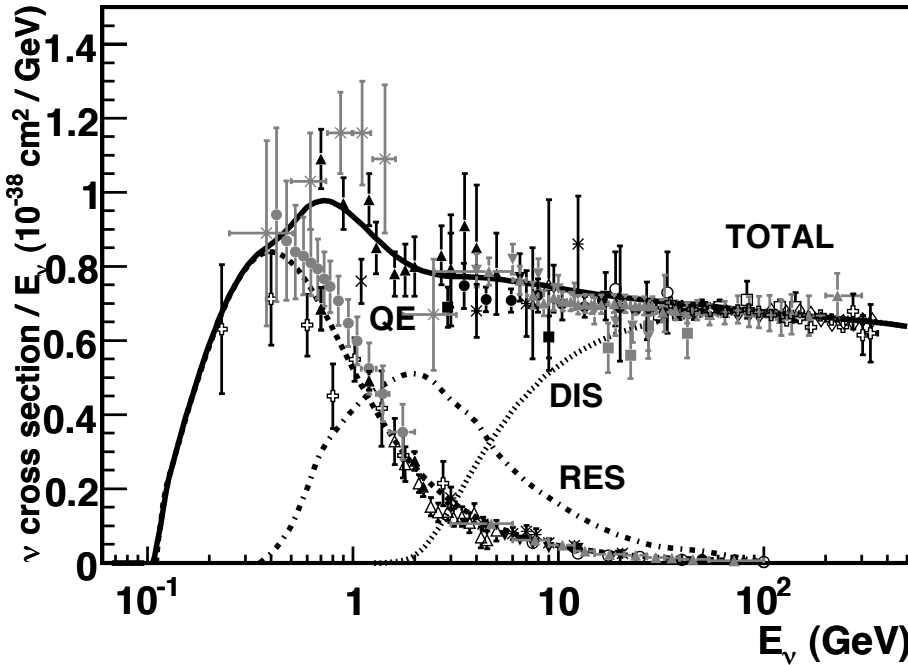


Figure 2.5: Total ν_μ CC cross section per nucleon as a function of the neutrino energy. The contributions from the different channels are shown. Figure taken from Ref. [69].

interaction a neutrino (antineutrino) interacts with a neutron (proton), converting it into a proton (neutron) which is then ejected from the nucleus together with the resulting charged lepton. At energies above 1 GeV the neutrino is able to excite the nucleon into a baryonic resonance, which promptly decays into a nucleon and a pion. These are the so-called resonant (RES) interactions. Neutrinos also interact with entire nucleus coherently, in the process known as coherent (COH) interaction. This kind of reactions also produce a single pion in the final state. At high neutrino energies, above 5 GeV, deep inelastic scattering (DIS) takes place. In these processes, the neutrino interacts with a single quark within the nucleon, breaking the nucleon and producing a hadronic shower.

Figure 2.5 shows a compilation of measurements of the total ν_μ CC cross section (see Ref. [69] for the details of the different experimental results). Also shown are the contributions from the different interaction modes. The contribution of the CCCOH interaction is omitted, as it is negligible compared to the others. This shows how the

2.6. NEUTRINO INTERACTIONS

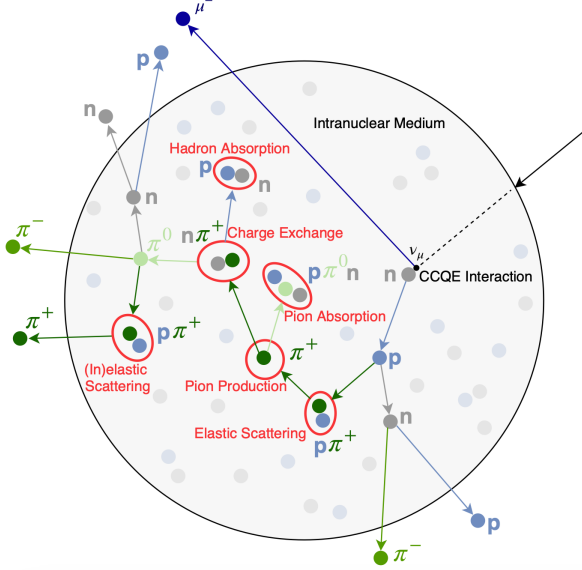


Figure 2.6: Schematic representation of a ν_μ CCQE interaction with a neutron inside a nucleus. The reaction produces a muon and a proton, which travel through the nuclear medium. The outgoing proton undergoes various kinds of hadronic FSIs on its way out. Figure taken from Ref. [70].

434 interaction model needs to accurately predict the neutrino-nucleon cross section for the
 435 different interaction modes across a broad energy range, to obtain the correct relative
 436 contributions.

437 Nuclear effects alter the neutrino cross section, as well as the multiplicities of the
 438 final state particles. Therefore, the interaction models need to account for the effects
 439 introduced by the nuclei. There are several models available to describe the initial state
 440 of the nucleus, like the relativistic Fermi gas model [71], spectral functions [72] or the
 441 random phase approximation [73]. The other main effect that interaction models have to
 442 deal with are the so-called final state interactions (FSI). These are the interactions of the
 443 particles produced in the neutrino-nucleon scattering as they travel through the nuclear
 444 medium. Typically, the lepton exits the nucleus without interacting. However, hadrons
 445 tend to get scattered, absorbed or re-emitted. These effects are usually described by
 446 means of intra-nuclear cascade models [74]. Figure 2.6 illustrates the effects of FSI on
 447 the observable particle content in the detector after a ν_μ CCQE interaction.

448 There exists a rich experimental programme dedicated to the measurement of neutrino

CHAPTER 2. NEUTRINO PHYSICS

449 cross sections. The list of such experiments in the recent years include MiniBooNE
450 [75], MINERvA [76], MicroBooNE [77] and SBND [78]. Additionally, thanks to their
451 near detectors, long baseline experiments can perform cross section measurements.
452 Some recent examples are NOvA [79] or T2K [80]. Future oscillation experiments
453 will greatly benefit from these measurements, as the measurement of the oscillation
454 parameters depends on the cross section modelling. However, there are alternative
455 data-driven approaches to extract the oscillation probabilities without relying on a
456 neutrino interaction model, which are planned to be explored in the next generation of
457 experiments [81, 82].

458

459

460

461

462

463

464

465

466

467

468

469

470

The Deep Underground Neutrino Experiment

Deep in the human unconscious is a pervasive need for a logical universe that makes sense. But the real universe is always one step beyond logic.

– Frank Herbert, *Dune*

The Deep Underground Neutrino Experiment (DUNE) is a next generation long-baseline neutrino experiment [83]. It will aim to address several questions in neutrino physics, study neutrinos from astrophysical sources and search for beyond the standard model physics.

This chapter reviews the main goals of the DUNE experiment, the design of the far detector modules and their data acquisition (DAQ) system, and the role that the near detector plays in the physics program of DUNE.

3.1 Overview

The main physics goals of DUNE are:

- measure the neutrino mass hierarchy, the amount of CP violation in the leptonic sector and the θ_{23} octant,
- detect rare low energy neutrino events, like neutrinos from supernova bursts, and
- search for proton decay and other beyond the standard model phenomena.

CHAPTER 3. THE DEEP UNDERGROUND NEUTRINO EXPERIMENT

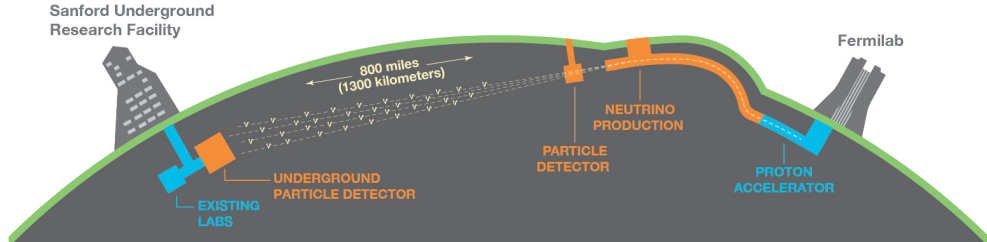


Figure 3.1: Schematic diagram of the DUNE experiment and the LBNF beamline [83].

The design of DUNE has been tailored with these goals in mind. It will consist of two neutrino detectors. A near detector (ND) complex will be placed at Fermilab, 574 m downstream of the neutrino production point, whereas a larger far detector (FD) will be built in the Sandford Underground Research Facility (SURF), South Dakota, approximately 1300 km away. Figure 3.1 shows a simplified view of the various components of DUNE (not to scale).

The beam neutrinos will be provided by the Long-Baseline Neutrino Facility (LBNF) beamline, the multi-megawatt wide-band neutrino beam planned for Fermilab. It will produce neutrinos travelling in the direction of SURF, with the capability to switch between neutrino and antineutrino mode.

Before arriving to the FD, the neutrino beam meets the ND complex, which serves as the experiment's control. The design of the DUNE ND is mainly driven by the needs of the oscillation physics program, as its main role is to measure the unoscillated neutrino energy spectra. From these we can predict the unoscillated spectra at the FD, which can be compared to the spectra measured at the FD to extract the oscillation parameters. Additionally, the ND has a physics programme of its own, including cross section measurements and BSM physics searches.

The technology chosen for the FD modules of DUNE is the liquid Argon time projection chamber (LArTPC). Its four modules will record neutrino interactions from the accelerator-produced beam arriving at predictable times. As it also aims at recording rare and low energy events, like supernovae and solar neutrinos, the FD requires trigger

3.2. PHYSICS GOALS OF DUNE

Table 3.1: Summary of the two-phased plan for DUNE. Adapted from Ref. [84].

Parameter	Phase I	Phase II	Benefit
FD mass	20 kt fiducial	40 kt fiducial	FD statistics
Beam power	up to 1.2 MW	2.4 MW	FD statistics
ND config.	ND-LAr, TMS, SAND	ND-LAr, ND-GAr, SAND	Systematic constraints

498 schemes which can deal with both kinds of physics, and also maximum uptime.

499 DUNE is planned to be built using a staged approach consisting on two phases,
500 which are summarised in Tab. 3.1. Phase I consists of a FD with 50% of the total
501 fiducial mass, a reduced version of the ND complex and a 1.2 MW proton beam. It will
502 be sufficient to achieve some early physics goals, like the determination of the neutrino
503 mass ordering. For its Phase II, DUNE will feature the full four FD modules, a more
504 capable ND and a 2.4 MW proton beam. The physics milestones for the two phases are
505 given in Tab. 3.2, in a staging scenario which assumes that Phase II is completed after
506 6 years of operation.

507 A summary of the DUNE science program can be found in the DUNE FD Technical
508 Design Report (TDR) Volume I [83]. For a detailed discussion on the two-phased
509 approach the reader is referred to the DUNE Snowmass 2021 report [84].

510 3.2 Physics goals of DUNE

511 As noted in the literature (see for instance Ref. [14] for a review), the parameter space of
512 the neutrino oscillation phenomena within the three-flavour picture is quite constrained
513 by current experimental data. However, there are still crucial open questions, like the
514 mass ordering, the value of δ_{CP} or the θ_{23} octant. One of the main goals of DUNE is to
515 determine precisely the values of these parameters [85].

516 To address these questions DUNE can look to the subdominant oscillation channel
517 $\nu_\mu \rightarrow \nu_e$ ($\bar{\nu}_\mu \rightarrow \bar{\nu}_e$) and study the energy dependence of the ν_e ($\bar{\nu}_e$) appearance probability.
518 When we focus on the antineutrino channel $\bar{\nu}_\mu \rightarrow \bar{\nu}_e$ there is a change in the sign of δ_{CP} ,
519 thus introducing CP-violation. Moreover, due to the fact that there are no positrons in

CHAPTER 3. THE DEEP UNDERGROUND NEUTRINO EXPERIMENT

Table 3.2: Exposure and time required to achieve the different physics milestones of the two phases. The predictions assume a Phase II staging scenario where FD modules 3 and 4 are deployed in years 4 and 6 and both the beam and ND are upgraded after 6 years. Adapted from Ref. [84].

Stage	Physics milestone	Exposure (kt-MW-years)	Years (staged)
Phase I	5σ MO ($\delta_{CP} = -\pi/2$)	16	1-2
	5σ MO (100% of the δ_{CP} values)	66	3-5
	3σ CPV ($\delta_{CP} = -\pi/2$)	100	4-6
Phase II	5σ CPV ($\delta_{CP} = -\pi/2$)	334	7-8
	δ_{CP} resolution of 10 degrees ($\delta_{CP} = 0$)	400	8-9
	5σ CPV (50% of the δ_{CP} values)	646	11
	3σ CPV (75% of the δ_{CP} values)	936	14
	$\sin^2(2\theta_{13})$ resolution of 0.004	1079	16

520 the composition of Earth, there is a sign difference for the matter effect contribution
 521 when looking to the antineutrino channel. This asymmetry is proportional to the baseline
 522 length L and is sensitive to the sign of Δm_{31}^2 , and thus to the neutrino mass ordering.

523 Another of the main physics goals of DUNE is the search for baryon-number violating
 524 processes. Specifically, it will try to answer the question of whether protons are stable
 525 or not. There is no symmetry argument that forbids protons from decaying, but its
 526 apparent stability seems to suggest that baryon number is conserved [86]. However,
 527 proton decay is a usual feature of grand-unified theories, where electromagnetic, weak
 528 and strong interactions are unified above a certain energy scale [87].

529 As the energy deposition scale for this kind of searches is nearly the same as the one
 530 for long-baseline neutrino oscillations, DUNE will be able to look for them. It has several
 531 advantages over other experiments, such as excellent imaging and particle identification,
 532 which can be translated to lower backgrounds.

533 The last of the main objectives of DUNE is the detection of neutrinos originated in
 534 supernovae explosions, what is called a supernova neutrino burst (SNB). These neutrinos
 535 carry with them information about the core-collapse process, from the progenitor to the
 536 explosion and the remnant; but also may have information about new exotic physics. So
 537 far, the only neutrino events ever recorded from such a process were a few dozens of $\bar{\nu}_e$

3.3. LBNF BEAMLINE

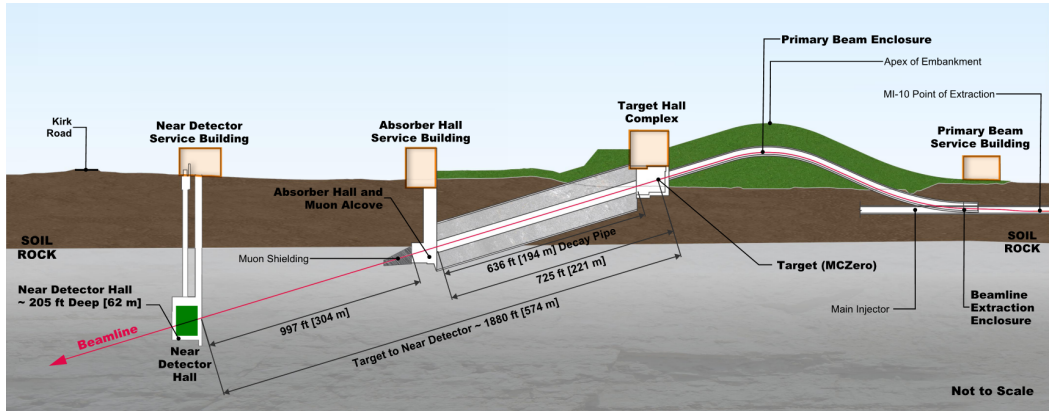


Figure 3.2: Schematic longitudinal section of the LBNF beamline at Fermilab (not to scale). Figure taken from Ref. [90].

538 events from the 1987A supernova located in the Magellanic Cloud, 50 kpc away from
 539 Earth [88,89].

540 DUNE aims to collect SNB events. Although these are quite rare, as the expected
 541 supernovae explosion events are about one every few decades for our galaxy and
 542 Andromeda, the long lifetime of the experiment (around a few decades as well) makes it
 543 reasonable to expect some. Nowadays the main sensitivity to SNB of most experiments
 544 is to the $\bar{\nu}_e$ through inverse beta decay. One of the advantages of DUNE is its expected
 545 sensitivity to ν_e , since the dominant channel will be ν_e CC scattering.

546 Moreover, due to the stringent requirements that the main physics goals set for
 547 DUNE, it will allow also to perform searches for all kind of BSM physics. Among
 548 others, DUNE will be able to look for: active-sterile neutrino mixing, non-unitarity of
 549 the PMNS matrix, non-standard interactions, Lorentz and CPT violations, neutrino
 550 trident production, light-mass DM, boosted DM and heavy neutral leptons. The reader
 551 is referred to the DUNE FD TDR Volume II [85] for a full discussion of the physics
 552 scope of DUNE.

553 3.3 LBNF beamline

554 The LBNF project is responsible for producing the neutrino beam for the DUNE detectors.
 555 A detailed discussion of the LBNF program can be found in the DUNE/LBNF CDR

CHAPTER 3. THE DEEP UNDERGROUND NEUTRINO EXPERIMENT

556 Volume III [90].

557 A schematic diagram of the longitudinal section of the LBNF beamline is shown in
 558 Fig. 3.2. First, a beam of 60 – 120 GeV protons is extracted from the Fermilab Main
 559 Injector. This beam is aimed towards the target area, where it collides with a cylindrical
 560 graphite target to produce pions and kaons.

561 The diffuse, secondary beam of particles is focused by a pair of magnetic horns.
 562 These select the positively charged particles when operated in Forward Horn Current
 563 (FHC) mode, or the negatively charged ones when the current is reversed, also known as
 564 Reverse Horn Current (RHC) mode. The focused secondary beam then enters a 194 m
 565 decay pipe where the pions and kaons will predominantly produce $\mu^+\nu_\mu$ pairs when in
 566 FHC mode (or $\mu^-\bar{\nu}_\mu$ in RHC mode).

567 At the end of the decay pipe a hadron absorber removes the undecayed hadrons and
 568 muons from the beam, which reduces the ν_e ($\bar{\nu}_e$) and $\bar{\nu}_\mu$ (ν_μ) contamination coming
 569 from the μ^+ (μ^-) decays. The resulting neutrino flux at the FD is shown in Fig. 3.3,
 570 both for FHC (left) and RHC (right) modes. These predictions show the intrinsic $(\bar{\nu})_e$
 571 contamination and wrong sign component from wrong sign and neutral meson decays,
 572 as well as muons decaying before reaching the absorber.

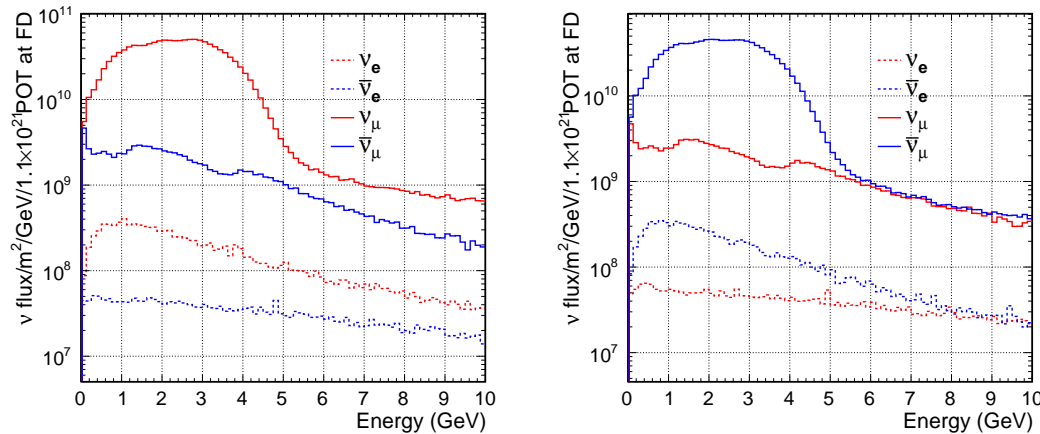


Figure 3.3: Predicted neutrino fluxes at the FD in FHC mode (left panel) and RHC mode (right panel). Figures taken from Ref. [85].

3.4. NEAR DETECTOR

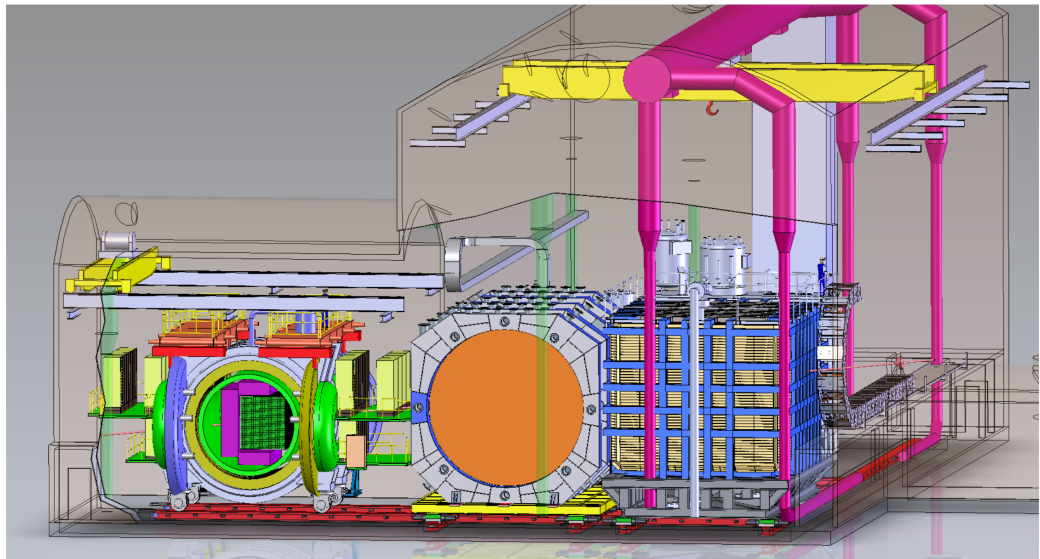


Figure 3.4: Representation of the ND hall in Phase II, showing the different subcomponents. From right to left, in the direction of the beam, we have ND-LAr, ND-GAr and SAND. Figure taken from Ref. [91].

573 3.4 Near Detector

574 To estimate the oscillation parameters we measure the neutrino energy spectra at the FD.
575 This reconstructed energy arises from a convolution of the neutrino flux, cross section,
576 detector response and the oscillation probability. Using theoretical and empirical models
577 to account for the other effects, one can extract the oscillation probability using the
578 measurement. However, these models have associated a number of uncertainties that
579 are then propagated to the oscillation parameters.

580 One of the main roles of the ND is to measure the neutrino interaction rates before
581 the oscillation effects become relevant, i.e. close to the production point. By measuring
582 the ν_μ and ν_e energy spectra, and that of their corresponding antineutrinos, at the ND
583 we can constrain the model uncertainties. A complete cancellation of the uncertainties
584 when taking the ratio between the FD and ND measurements is not possible, as that
585 would require both detectors to have identical designs and the neutrino fluxes to be
586 the same. Because of the distance, the flux probed by the FD will have a different
587 energy and flavour composition than that at the ND, as neutrinos oscillate and the beam

CHAPTER 3. THE DEEP UNDERGROUND NEUTRINO EXPERIMENT

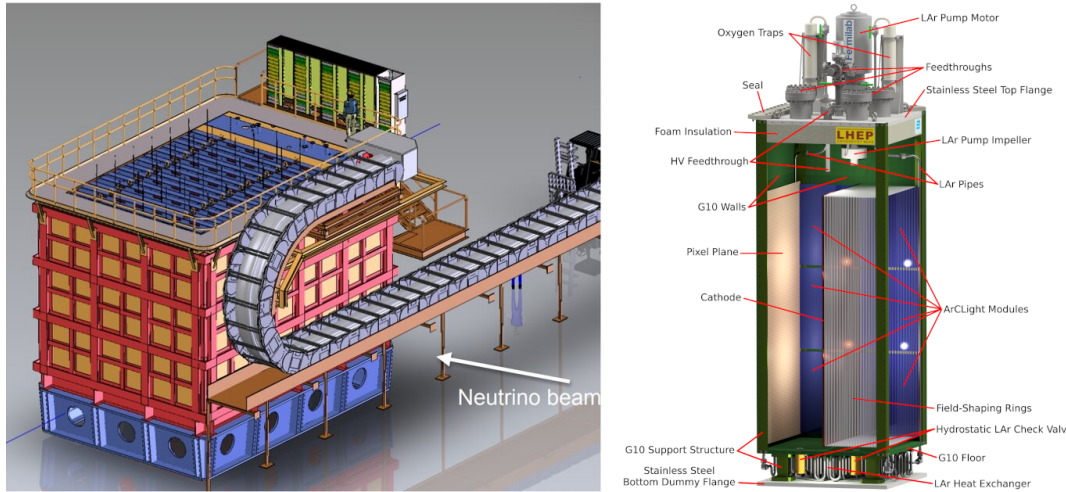


Figure 3.5: Schematic representation of the external components of ND-LAr, including the cryostat and the PRISM movable system (left) and detailed drawing of one ArgonCube module (right). Figure adapted from Ref. [83].

spreads. The differences in the flux also determine the design of the detectors, therefore the ND is limited in its capability to match the FD design.

Nevertheless, having a highly capable ND, DUNE can minimise the systematic uncertainties affecting the observed neutrino energy. The ND data can be used to tune the model parameters by comparison with the prediction. Then, one uses the tuned model to predict the unoscillated FD spectra. Comparing the prediction with the measured spectra it is possible to extract the oscillation parameters.

Additionally, the ND will have a physics program of its own. In particular, it will measure neutrino cross sections that will then be used to constrain the model used in the long-baseline oscillation analysis. It will also be used to search for BSM phenomena such as heavy neutral leptons, dark photons, millicharged particles, etc.

The DUNE ND can be divided in three main components, a LArTPC known as ND-LAr, a magnetised muon spectrometer, which will be the Temporary Muon Spectrometer (TMS) in Phase I and ND-GAr in Phase II, and the System for on-Axis Neutrino Detection (SAND). The layout of the Phase II DUNE ND can be seen in Fig. 3.4. The first two components of the ND will be able to move off-axis, in what is called the Precision Reaction-Independent Spectrum Measurement (PRISM) concept. More details

3.4. NEAR DETECTOR

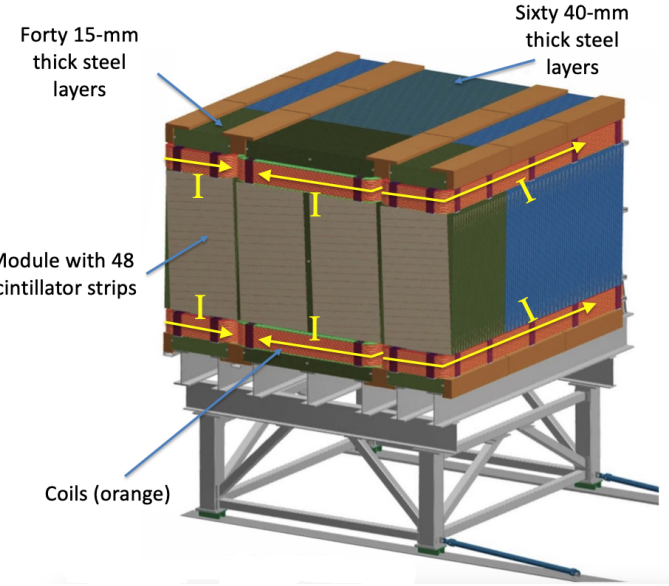


Figure 3.6: Schematic view of the TMS detector, highlighting its main parts. Figure adapted from Ref. [83].

605 on the purpose and design of the ND can be found in the DUNE ND Conceptual Design
 606 Report (CDR) [91].

607 **3.4.1 ND-LAr**

608 ND-LAr is a LArTPC, as the ND needs a LAr component to reduce cross section and
 609 detector systematic uncertainties in the oscillation analysis. However, its design differs
 610 significantly from those proposed for the FD modules. Because of the high event rates
 611 at the ND, approximately 55 neutrino interaction events per $10 \mu\text{s}$ spill, ND-LAr will be
 612 built in a modular way. Each of the modules, based on the ArgonCube technology, is a
 613 fully instrumented, optically isolated TPC with a pixelated readout. The pixelisation
 614 allows for a fully 3D reconstruction and the optical isolation reduces the problems due
 615 to overlapping interactions. Figure 3.5 shows a representation of the external parts of
 616 ND-LAr (left) and a detailed diagram of an ArgonCube module (right).

617 With a fiducial mass of 67 t and dimensions $7 \text{ m} (\text{w}) \times 3 \text{ m} (\text{h}) \times 5 \text{ m} (\text{l})$, ND-LAr
 618 will be able to provide high statistics and contain the hadronic systems from the beam
 619 neutrino interactions, but muons with a momentum higher than 0.7 GeV will exit the

CHAPTER 3. THE DEEP UNDERGROUND NEUTRINO EXPERIMENT

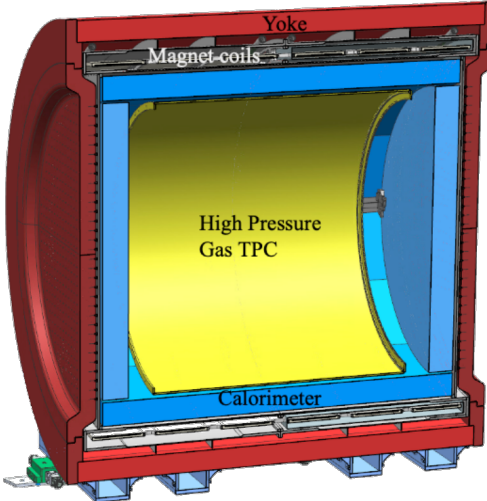


Figure 3.7: Cross section of the ND-GAr geometry, showing the HPgTPC, ECal and magnet. Figure adapted from Ref. [92].

620 detector.

621 3.4.2 TMS/ND-GAr

622 To accurately estimate the neutrino energy, the momentum of the outgoing muons needs
 623 to be determined. That is the reason why a muon spectrometer is needed downstream
 624 of ND-LAr.

625 In Phase I that role will be fulfilled by TMS. It is a magnetised sampling calorimeter,
 626 with alternating steel and plastic scintillator layers. Figure 3.6 shows a schematic view
 627 of the TMS detector. The magnetic field allows a precise measurement of the sign of the
 628 muon, so one can distinguish between neutrino and antineutrino interactions.

629 After the Phase II upgrade, TMS will be replaced with a more capable near detector.
 630 The current technology considered is ND-GAr. This detector is a magnetised, high-
 631 pressure GAr TPC (often denoted as HPgTPC) surrounded by an electromagnetic
 632 calorimeter (ECal) and a muon tagger. A cross section of its geometry can be seen
 633 in Fig. 3.7. ND-GAr will be able to measure the momenta of the outgoing muons
 634 while also detect neutrino interactions inside the GAr volume. This allows ND-GAr
 635 to constrain the systematic uncertainties even further, as it will be able to accurately

3.4. NEAR DETECTOR

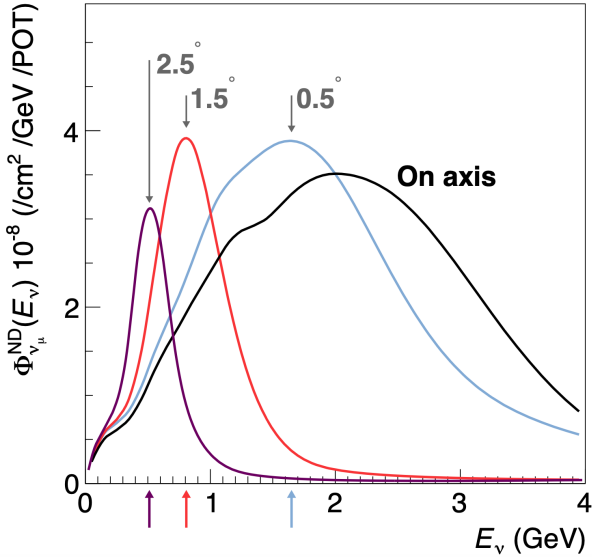


Figure 3.8: Predicted beam muon neutrino flux at the ND location for different off-axis positions. Figure taken from Ref. [91].

636 measure neutrino interactions at low energies thanks to the lower tracking thresholds of
 637 GAr.

638 3.4.3 PRISM

639 In general, the observed peak neutrino energy of a neutrino beam decreases as the
 640 observation angle with respect to the beam direction increases. This feature has been
 641 used in other long-baseline neutrino experiments, like T2K (2.5° off-axis) and NOvA
 642 (0.8° off-axis), to achieve narrower energy distributions. The DUNE PRISM concept
 643 exploits this effect using a movable ND. Within PRISM both ND-LAr and the muon
 644 spectrometer (TMS in Phase I and ND-GAr in Phase II) can be moved up to 3.2°
 645 off-axis, equivalent to move the detectors 30.5 m laterally through the ND hall.

646 This allows to record additional data samples with different energy compositions.
 647 Figure 3.8 compares the on-axis muon neutrino flux at the ND with the fluxes at different
 648 off-axis positions. As the off-axis position increases the neutrino flux becomes closer to
 649 a monoenergetic beam with a lower peak energy. These samples can be used to perform
 650 a data-driven determination of the relation between true and reconstructed neutrino

CHAPTER 3. THE DEEP UNDERGROUND NEUTRINO EXPERIMENT

651 energy, to reduce the dependence on the interaction model. The off-axis samples are
652 linearly combined to produce a narrow Gaussian energy distribution centered on a target
653 true energy. From the combination coefficients one can build a sample of reconstructed
654 neutrino events that will determine the energy mapping.

655 The PRISM samples will be used to form a flux at the ND location similar in shape
656 to the oscillated flux measured by the FD. This method can be used to extract the
657 oscillation parameters with minimal input from the neutrino interaction model.

658 3.4.4 SAND

659 The role of SAND is to monitor the beam stability by measuring the on-axis neutrino
660 energy spectra. As the PRISM program requires that ND-LAr and its downstream
661 muon spectrometer spend about half of the time in off-axis positions, it is not possible
662 to monitor the stability with the movable detectors. Moreover, for the success of PRISM
663 it is essential to have a stable beam configuration, or, at least, a quick assessment and
664 modeling of the distortions.

665 The SAND detector is magnetised, and features an inner low density tracker, a LAr
666 target with optical readout and surrounding sampling calorimeter.

667 3.5 A More Capable Near Detector

668 In DUNE Phase II, a more capable near detector is needed to achieve the ultimate physics
669 goals of the experiments. The current leading proposal for this detector is ND-GAr.
670 As mentioned previously, it will fulfill the role of TMS, measuring the momentum and
671 sign of the charged particles exiting ND-LAr. Additionally, it will be able to measure
672 neutrino interactions inside the HPgTPC, achieving lower energy thresholds than those
673 of the ND and FD LArTPCs. By doing so ND-GAr will allow to constrain the relevant
674 systematic uncertainties for the LBL analysis even further. A detailed discussion on the
675 requirements, design, performance and physics of ND-GAr can be found in the DUNE
676 ND CDR [91] and the ND-GAr white paper [93].

3.5. A MORE CAPABLE NEAR DETECTOR

677 3.5.1 Requirements

678 The primary requirement for ND-GAr is to measure the momentum and charge of
679 muons from ν_μ and $\bar{\nu}_\mu$ CC interactions in ND-LAr, in order to measure their energy
680 spectrum. To achieve the sensitivity to the neutrino oscillation parameters described
681 in the DUNE FD TDR Volume II [85], ND-GAr should be able to constrain the muon
682 energy within a 1% uncertainty or better. The main constraint will come from the
683 calibration of the magnetic field, which will be performed using neutral kaon decays in
684 the HPgTPC.

685 Another requirement for ND-GAr is the precise measurement of neutrino interactions
686 on argon for the energies relevant to the neutrino oscillation program. The goal is to
687 constrain the cross section systematic uncertainties in the regions of phase space that
688 are not accessible to ND-LAr. This requires the kinematic acceptance for muons in
689 ND-GAr to exceed that of ND-LAr, being comparable to the one observed in the FD.

690 ND-GAr should also be able to help establishing the relationship between true and
691 reconstructed energy from neutrino interactions on argon with low thresholds, being
692 sensitive to particles that are not observed or may be misidentified in ND-LAr. In
693 particular, ND-GAr needs to have low tracking thresholds in order to measure the
694 spectrum of pions and protons produced in final-state interactions (FSI). It also must
695 be able to accurately measure the pion multiplicity in 1, 2 and 3 pions final states, to
696 inform the pion mass correction in the LArTPCs.

697 3.5.2 Reference design

698 The final design of ND-GAr is still under preparation. However, a preliminary baseline
699 design was in place at the time of the ND CDR. This section summarises the main
700 features of that design, as it is also the one used for the default geometry in our simulation.
701 A DUNE Phase II white paper, discussing the different options under consideration for
702 the ND-GAr design, is in progress.

CHAPTER 3. THE DEEP UNDERGROUND NEUTRINO EXPERIMENT

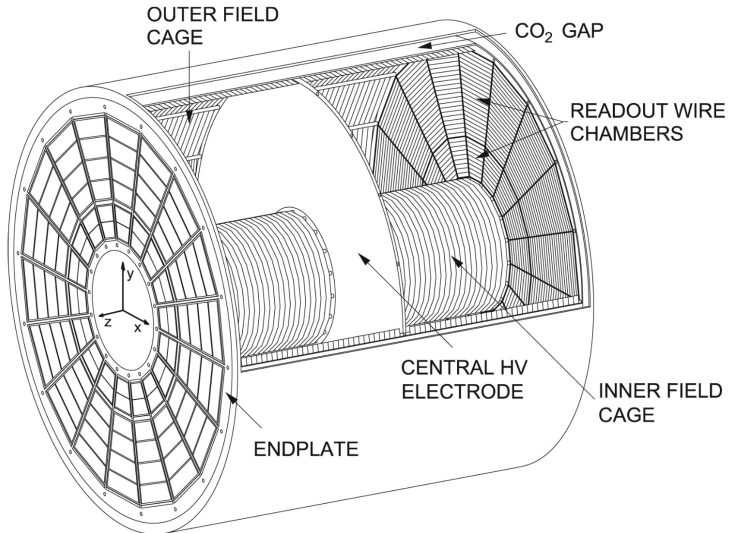


Figure 3.9: Diagram of the ALICE TPC, showing the two drift chambers, inner and outer field cages and readout chambers. Figure taken from Ref. [91].

703 HPgTPC

704 The reference design for the ND-GAr HPgTPC follow closely that of the ALICE TPC.
 705 It is a cylinder with a central high-voltage cathode, generating the electric field for
 706 the two drift volumes, with a maximum drift distance of 2.5 m each. The anodes will
 707 be instrumented with charge readout chambers. The original design repurposed the
 708 multi-wire proportional readout chambers (MWPCs) of ALICE, however some of the
 709 current R&D efforts focus on a gas electron multiplier (GEM) [94] option instead. Figure
 710 3.9 shows a schematic diagram of the ALICE TPC design. The basic ND-GAr geometry
 711 will resemble this, except for the inner field cage.

712 It will use a 90:10 molar fraction Ar: CH_4 mixture at 10 bar. With this baseline gas
 713 mixture light collection is not possible, as the quenching gas absorbs most of the VUV
 714 photons. Additional R&D efforts are underway, to understand if different mixtures allow
 715 for the light signal to be used to provide a t_0 while maintaining stable charge gain.

3.5. A MORE CAPABLE NEAR DETECTOR

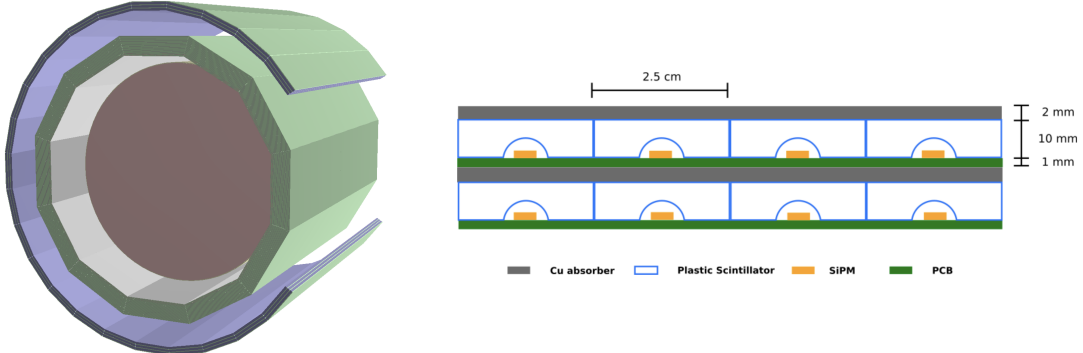


Figure 3.10: View of the 12-sided ECal barrel and outer muon tagger geometries (left) and layout of the ECal tile layers for the 2 mm Cu, 10 mm scintillator option (right). Figure adapted from Ref. [91].

716 ECal

717 The main role of the ND-GAr ECal is the calorimetric measurement of the electron
 718 energies and the reconstruction of photons, in particular those from neutral pion decays.
 719 Also, the ECal is able to provide a t_0 timestamp for neutrino interactions, by associating
 720 its activity to the tracks in the HPgTPC. The ECal will also be able to perform
 721 neutron reconstruction using time of flight and reject external backgrounds, thanks to
 722 its sub-nanosecond time resolution.

723 The ECal design features three independent subdetectors, two end caps at each side
 724 and a barrel surrounding the HPgTPC. Each of the detectors is divided in modules,
 725 which combine alternating layers of plastic scintillator and absorber material readout
 726 by SiPMs. The inner scintillator layers consist of $2.5 \times 2.5 \text{ cm}^2$ high-granularity tiles,
 727 whereas the outer ones are made out of 4 cm wide cross-strips spanning the whole
 728 module length. The current barrel geometry consists of 8 tile layers and 34 strip layers,
 729 while the end caps feature 6 and 36 respectively. The thickness of the scintillator layers
 730 is 7 mm and 5 mm for the Pb absorber layers. The 12-sided geometry of the ECal barrel
 731 (left) and the layout of the tile layers (left)¹ can be seen in Fig. 3.10.

¹The figure shows the layout of the tile layers for a previous design with 2 mm Cu absorber and 10 mm plastic scintillator, as mentioned in the text the current choice is 5 mm Pb absorber and 7 mm scintillator.

CHAPTER 3. THE DEEP UNDERGROUND NEUTRINO EXPERIMENT

732 Magnet

733 The ND-GAr magnet design, know as the Solenoid with Partial Yoke (SPY), consists of
734 two coupled solenoids with an iron return yoke. The idea behind the design is to have a
735 solenoid as thin as possible, as well as a return yoke mass distribution that minimises
736 the material budget between ND-LAr and ND-GAr. The magnet needs to provide a
737 0.5 T field in the direction perpendicular to the beam, parallel to the drift electric field.
738 It needs to host the pressure vessel and the surrounding ECal, which points to a inner
739 diameter of ~ 6.4 m.

740 The solenoid is a single layer coil, based on niobium titanium superconducting
741 Rutherford cable. The total length of the coil is 7.5 m. The bobbin will be split in four
742 segments grouped in pairs with two identical cryostats, connected in series. The iron
743 yoke features an aperture in the upstream side to allow the muons coming from ND-LAr.
744 Still, its material will be enough to reduce the magnetic field reaching SAND, and also
745 stop the charged pions produced inside the HPgTPC.

746 Muon system

747 The design of the ND-GAr muon system is still in a preliminary stage. Its role is to
748 distinguish between muons and pions punching through the ECal. This is especially
749 important for wrong-sign determination, to separate these from neutral current events.

750 In its current form, the muon system consists of three layers of longitudinal sampling
751 structures. It alternates 10 cm Fe absorber slabs with 2 cm plastic scintillator strips.
752 The transverse granularity required is still under study.

753 3.5.3 R&D efforts

754 There are several ND-GAr-related prototypes, mostly focused on the TPC charge
755 readout and electronics. The priority is to test the full readout chain, in a high-pressure
756 environment, using a gas mixture with high argon fraction. A detailed summary of these
757 can be found in the DUNE Phase II white paper [92].

3.5. A MORE CAPABLE NEAR DETECTOR

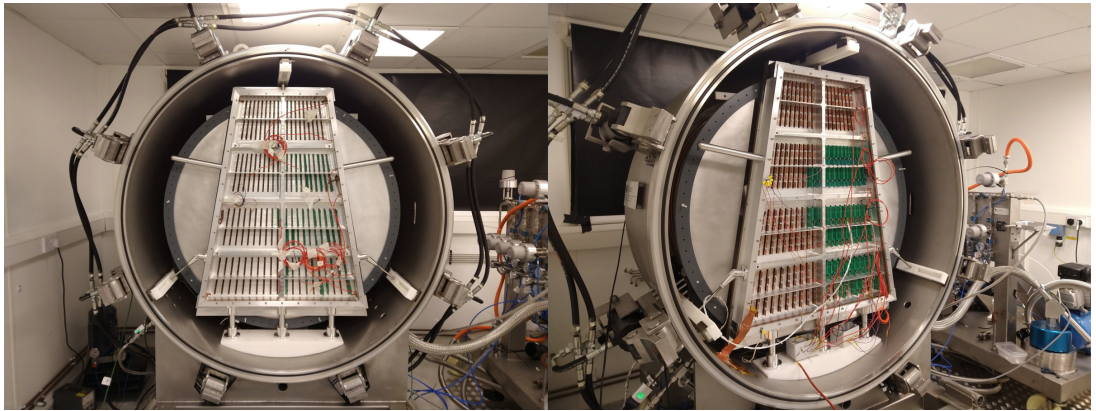


Figure 3.11: Photographs of the TOAD pressure vessel at RHUL. The TPC is mounted inside the vessel, and the OROC is supported by an aluminium frame. Figure taken from Ref. [95].

758 Multi-Wire Proportional Chambers

759 As mentioned before, the original ND-GAr design repurposes the MWPCs of the ALICE
760 TPC, which became available after the recent upgrade [96]. These were operated using
761 a 90:10:5 Ne:CO₂:N₂ gas mixture at 1 atm. Therefore, their performance needed to be
762 studied in an argon gas environment at high pressure.

763 The Gas-argon Operation of ALICE TPC (GOAT) test stand tested the ALICE
764 readout chambers at high pressure. In particular, it used one of the previously operated
765 ALICE inner MWPCs, also known as IROCs, in a pressure vessel rated to 10 atm. It
766 measured the gas gain at various pressure points, voltages and gas mixtures.

767 The Test stand of an Overpressure Argon Detector (TOAD) tested an ALICE outer
768 MWPC, also known as OROC, up to 5 atm. During its time at RHUL, it was used to
769 study the achievable gas gain of the OROC [95]. At the moment, it is being commissioned
770 at Fermilab for a full detector test of the readout electronics and the DAQ.

771 Figure 3.11 shows the interior of the TOAD pressure vessel. The TPC is mounted
772 inside the vessel on three rails. The back of the OROC, supported by an aluminium
773 frame, can be seen at the front.

CHAPTER 3. THE DEEP UNDERGROUND NEUTRINO EXPERIMENT

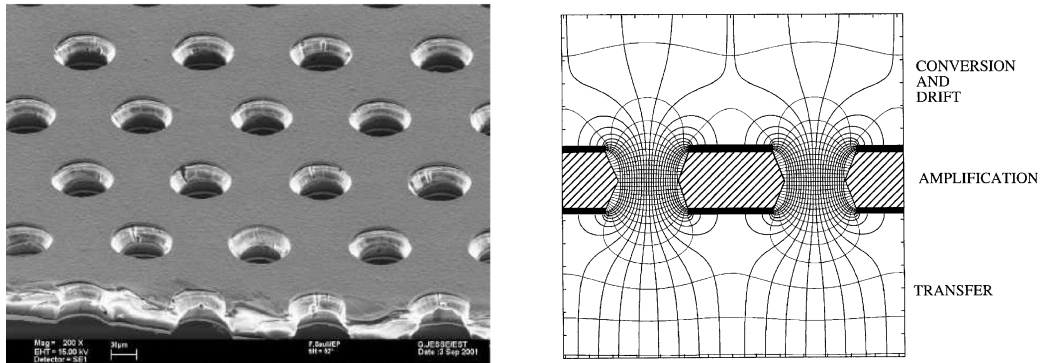


Figure 3.12: Left panel: electron microscope image of a 50 μm thick GEM electrode, with hole pitch and diameter of 140 and 70 μm , respectively. Right panel: Schematics of a GEM electrode cross section, showing the electric field lines around the holes. Figures taken from Ref. [97].

774 Gas Electron Multiplier

775 An alternative to the MWPC option is the use of GEMs. These are a type of micro-patter
 776 detector, where the ionisation electrons passing through the holes in the GEM layers
 777 are accelerated by a high intensity electric field. The acceleration causes the electrons
 778 to ionise the medium, resulting in an avalanche which increase the signal exponentially
 779 [94]. GEMs are used in numerous experiments that need a high spatial resolution, like
 780 ALICE [98] and CMS [99] after their upgrades.

781 Figure 3.12 (left panel) shows an electron microscope picture of a 50 μm thick GEM
 782 electrode, with a pitch between neighbouring holes of 140 μm and a hole diameter of
 783 70 μm . A schematic representation of the cross section of a GEM layer is shown in Fig.
 784 3.12 (left panel).

785 The Gaseous Argon T0 (GAT0²) prototype studies the use of thick GEMs made out
 786 of glass to achieve optical imaging of the primary ionisation. Using a 10 atm pressure
 787 vessel, the goal is to study different argon-based mixtures that allow for a precise t_0
 788 determination.

789 The GEM Over-pressurized with Reference Gases (GORG³) test stand is currently
 790 testing a GEM-based charge readout, using a triple-GEM stack.

²Spanish for cat.

³Persian for wolf.

3.6. FAR DETECTOR

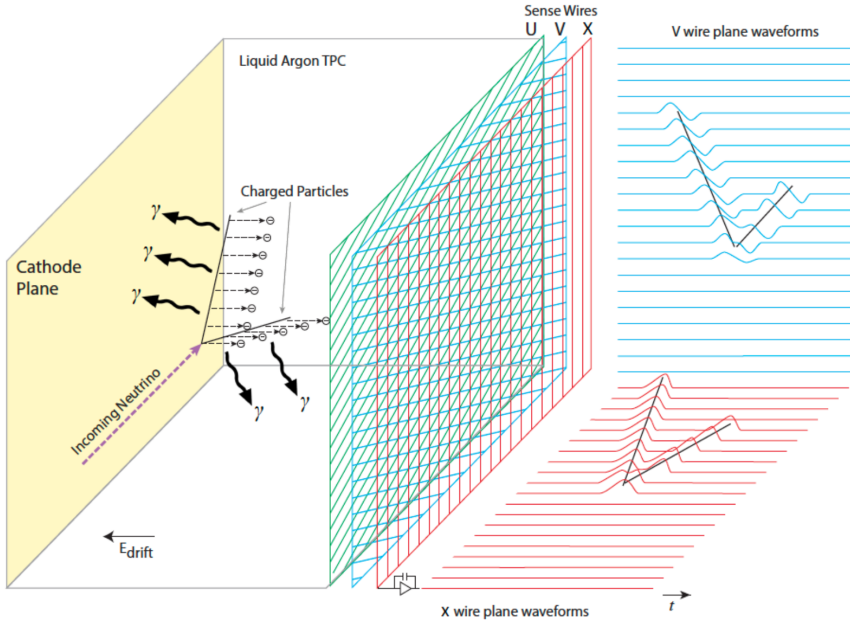


Figure 3.13: Schematic diagram showing the operating principle of a LArTPC with wire readout. Figure taken from Ref. [83].

791 3.6 Far Detector

792 The DUNE FD complex will sit 1300 km away from the beam target and 1.5 km
 793 underground at SURF, South Dakota. Two caverns will host the four FD modules, two
 794 of them per cavern, each embedded in cryostats of dimensions 18.9 m (w) \times 17.8 m (h) \times
 795 65.8 m (l). A central, smaller cavern will host the cryogenic system.

796 Three out of the four modules will be liquid argon (LAr) time projection chamber
 797 detectors, often refer to as LArTPCs, with a LAr fiducial mass of at least 10 kt each.
 798 The first and second FD modules, FD-1 and FD-2, will use a Horizontal Drift (HD)
 799 technology, whereas the third module, FD-3, will have a Vertical Drift (VD) direction.
 800 The technology for the fourth module is still to be decided,

801 For each event, with energies ranging from a few MeV to several GeV, these detectors
 802 collect both the scintillation light and the ionisation electrons created when the charged
 803 particles produced in neutrino-nucleus interactions ionise the argon nuclei. In both HD
 804 and VD designs the characteristic 128 nm scintillation light of argon is collected by a
 805 photon detection system (PDS). This light will indicate the time at which electrons

CHAPTER 3. THE DEEP UNDERGROUND NEUTRINO EXPERIMENT

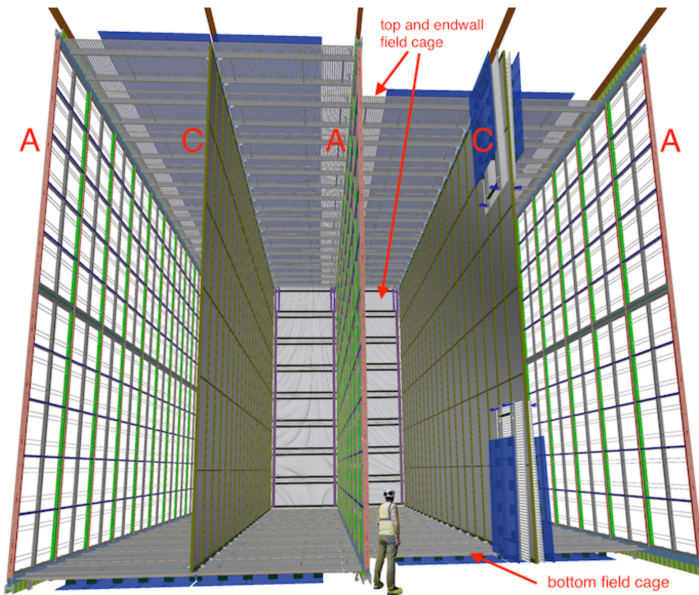


Figure 3.14: Proposed design for the FD-1 and FD-2 modules following the HD principle. Figure taken from Ref. [83].

806 start to drift, thus enabling reconstruction over the drift coordinate when compared
 807 to the time when the first ionisation electron arrives to the anode. Reconstruction of
 808 the topology in the transverse direction is achieved using the charge readout. Fig. 3.13
 809 illustrates the detection principle described, for the case of a HD detector with a wire
 810 readout.

811 3.6.1 Horizontal Drift

812 The HD design the ionisation electrons produced as charged particles traverse the LAr
 813 drift horizontally towards the anode planes, due to the effect of an electric field. These
 814 anode planes are made out of three layers of wire readout. This design, previously
 815 known as single-phase (SP), was tested by the ProtoDUNE-SP detector at CERN. The
 816 prototype collected data from a hadron beam and cosmic rays, providing high-quality
 817 data sets for calibration and performance studies.

818 Each FD HD detector module is divided in four drift regions, with a maximum drift
 819 length of 3.5 m, by alternating anode and cathode walls. The surrounding field cage
 820 ensures the uniformity of the 500 V/cm horizontal electric field across the drift volumes.

3.6. FAR DETECTOR

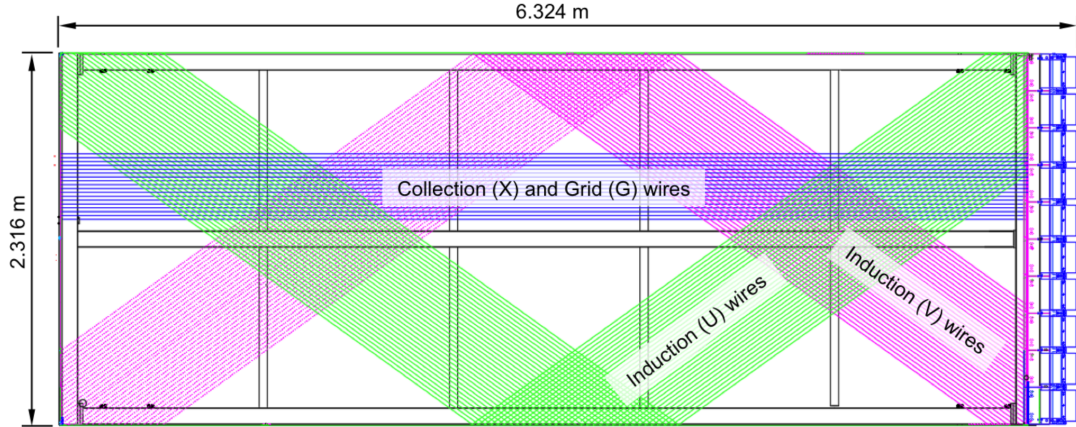


Figure 3.15: Schematic representation of an APA. The black lines represent the APA steel frame. The green and magenta lines correspond to the direction of the U and V induction wires respectively. The blue lines indicate the direction of the X collection wires and the wire shielding G. Figure taken from Ref. [83].

821 The three anode walls, which constitute the charge readout of the detector, are built by
 822 stacking anode plane assemblies (APAs), 2 high times 25 wide. The design of the HD
 823 modules is shown in Fig. 3.14.

824 Each APA is made of 2560 active wires arranged in three layers, plus an extra grid
 825 layer, wrapped around a metal frame. The two induction wire planes, U and V, sit at
 826 $\pm 35.7^\circ$ to the vertical on each side of the APA. The collection and shielding plane wires,
 827 X and G, run parallel to the vertical direction. The ionisation electrons drift past the
 828 induction planes, generating bipolar signals on those wires, and are collected by the
 829 collection plane, producing a monopolar positive signal. The spacing between the wires
 830 is ~ 5 mm, and it defines the spatial resolution of the APA.

831 The front-end readout electronics, or cold electronics as they are immerse in the LAr,
 832 are attached to the top of the up APAs and the bottom of the down APAs. Mounted on
 833 the front-end mother boards we have a series of ASICs that digitize the signals from the
 834 collection and induction planes. Each wire signal goes to a charge-sensitive amplifier,
 835 then there is a pulse-shaping circuit and this is followed by the analogue-to-digital
 836 converter. This part of the process happens inside the LAr to minimise the number of
 837 cables penetrating the cryostat. The digitised signals come out finally via a series of

CHAPTER 3. THE DEEP UNDERGROUND NEUTRINO EXPERIMENT

838 high-speed serial links to the warm interface boards (WIBs), from where the data is sent
839 to the back-end DAQ through optical fibers.

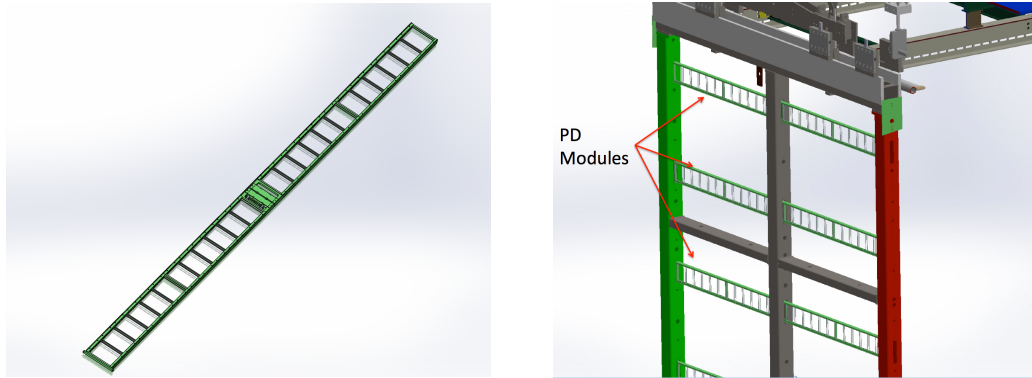


Figure 3.16: A PDS module containing 24 X-ARAPUCAs (left) and the location of the modules on the APAs (right). Figure taken from Ref. [83].

840 The PDS uses modules of X-ARAPUCA devices, mounted on the APA frames
841 between the wire planes. Each X-ARAPUCA consists of layers of dichroic filter and
842 wavelength-shifter. They shift the VUV scintillation light into the visible spectrum,
843 sending then the visible photons to silicon photomultiplier (SiPM) devices. The PDS
844 modules are 209 cm × 12 cm × 2 cm bars, containing 24 X-ARAPUCAs. There are 10
845 of these PDS modules per APA. Fig. 3.16 shows a PDS module (left) and the placement
846 of the modules on the APAs (right).

847 3.6.2 Vertical Drift

848 In the VD case the ionisation electrons will drift vertically until they meet a printed
849 circuit board-based (PCB) readout plane. It is based on the original dual-phase (DP)
850 design deployed at CERN, known as ProtoDUNE-DP, used a vertical drift design with
851 an additional amplification of the ionization electrons using a gaseous argon (GAr) layer
852 above the liquid phase. The VD module incorporates the positive features of the DP
853 design without the complications of having the LAr-GAr interface.

854 The current design of the FD VD module counts with two drift chambers with a
855 maximum drift distance of 6.5 cm. A cathode plane splits the detector volume along the
856 drift direction while the two anode planes are connected to the bottom and top walls

3.6. FAR DETECTOR

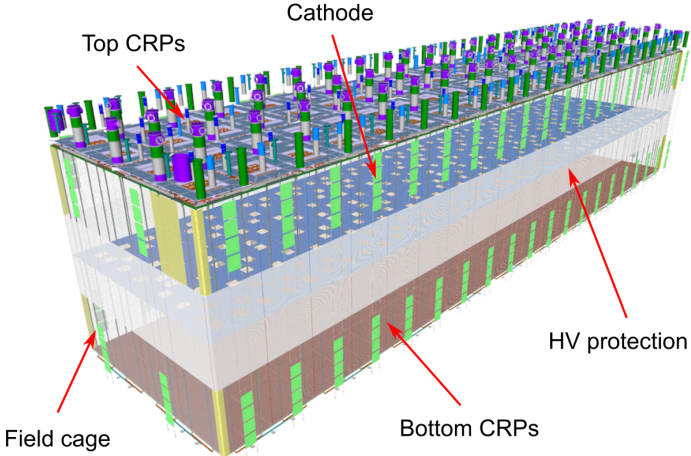


Figure 3.17: Proposed design for the FD-3 module following the VD principle. Figure adapted from Ref. [100].

857 of the detector. The layout of the VD module is shown in Fig. 3.17. Compared with
 858 the HD design, the VD option offers a slightly larger instrumented volume and a more
 859 cost-effective solution for the charge readout.

860 As in the HD design, each drift volume features a 500 V/cm electric field and a
 861 field cage that ensures its uniformity. The anode planes are arrays of 3.4 m × 3 m
 862 charge-readout planes (CRPs). These are formed by a pair of charge-readout units
 863 (CRUs), which are built from two double-sided perforated PCBs, with their perforations
 864 aligned. The perforations allow the drift electrons to pass between the layers.

865 The PCB face opposite to the cathode has a copper guard plane which acts as
 866 shielding, while its reverse face is etched with electrode strips forming the first induction
 867 plane. The outer PCB has electrode strips on both faces, the ones facing the inner PCB
 868 form the second induction plane while the outermost ones form the collection plane. Fig.
 869 3.18 shows the layout of the electrode strips for the top (left) and bottom (right) CRUs.
 870 The magenta and blue lines represent the first and second induction planes respectively,
 871 and the green lines correspond to the collection plane.

872 The PDS in the VD module will use the same X-ARAPUCA technology developed
 873 for the HD design. The plan is to place the PDS modules on the cryostat walls and on

CHAPTER 3. THE DEEP UNDERGROUND NEUTRINO EXPERIMENT

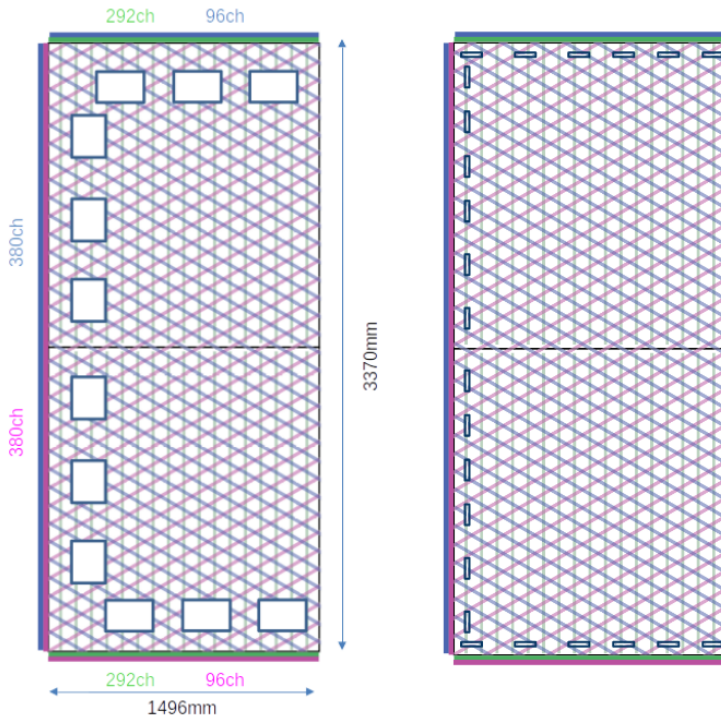


Figure 3.18: Schematic representation of the electrode strip configuration for a top (left) and bottom (right) CRU. Figure taken from Ref. [100].

874 the cathode, in order to maximise the photon yield.

875 **3.6.3 FD Data Acquisition System**

876 The data acquisition (DAQ) system receives, processes and stores data from the detector
877 modules. In the case of DUNE the DAQ architecture is designed to work for all FD
878 modules interchangeably, except some aspects of the upstream part which may depend
879 on the specific module technology.

880 The enormous sample rate and the number of channels in TPC and PD readouts
881 will produce a very large volume of data. These pose really strong requirements and
882 challenges to the DUNE FD DAQ architecture. It will be required to read out data of
883 the order of ten thousand or more channels at rates of a few MHz. To cope with the
884 huge data volume, segmented readouts and compression algorithms are used to reduce
885 the data rate to manageable levels.

886 The DAQ system of the DUNE FD is composed of five different subsystems. The

3.6. FAR DETECTOR

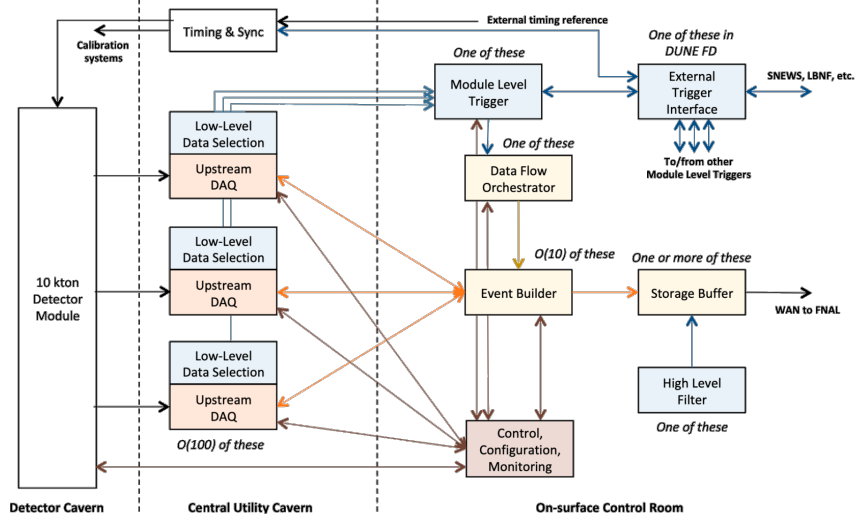


Figure 3.19: Detailed diagram of the DUNE FD DAQ system. Figure taken from Ref. [101].

887 first one is the upstream DAQ, which receives the raw data from the detector, buffers it
 888 and perform some low-level pre-processing. The minimally processed data is then fed
 889 into a hierarchical data selection system, which then performs a module level trigger
 890 decision. In case of a positive decision a trigger command is produced and executed by
 891 the data flow orchestrator, located in the back-end (BE) DAQ subsystem. Subsequently
 892 the DAQ BE retrieves the relevant data from the buffers located in the upstream DAQ,
 893 adds all the data into a cohesive record and saves it to permanent storage. Watching
 894 over all the other subsystems we also have the control, configuration and monitoring
 895 subsystem and the time and synchronization subsystem. Figure 3.19 shows a schematic
 896 diagram of the DAQ system, showing the different subsystems and their relations.

897 A notorious challenge for the DUNE DAQ system comes from its broad physics
 898 goals. We must be prepared to process events spanning a wide range of time windows
 899 (from 5 ms in the case of beam and cosmic neutrinos and nucleon decay to 100 s in the
 900 case of SNBs) and therefore this requires a continuous readout of the detector modules.
 901 Moreover, because of the off-beam measurements we need to ensure the capabilities
 902 of online data processing and self-triggering. Having this into account, together with
 903 the technical constraints, the DUNE FD DAQ faces a series of challenges: it needs to

CHAPTER 3. THE DEEP UNDERGROUND NEUTRINO EXPERIMENT

- 904 be fault tolerant and redundant to reduce downtime, accommodate new components
- 905 while it keeps serving the operational modules, have large upstream buffers to handle
- 906 SNB physics, be able to support a wide range of readout windows and last reduce the
- 907 throughput of data to permanent storage to be at most 30 PB/year.

Matched Filter approach to Trigger

Primitives

911 *It is a capital mistake to theorize before one has data. Insensibly one begins to
912 twist facts to suit theories, instead of theories to suit facts.*

913 – Arthur Conan Doyle, *A scandal in Bohemia*

914 4.1 Motivation

915 The filter implemented in the firmware of the upstream DUNE FD DAQ is a 32nd-order
916 low-pass finite impulse-response (FIR) filter. The output of such filter for a discrete
917 system can be written as:

$$y[i] = \sum_{j=0}^N h[j]x[i-j], \quad (4.1)$$

918 where N is the order of the filter, y is the output sequence, x is the input sequence and h
919 is the set of coefficients of the filter. The current implementation within `dtp-firmware`
920 [102] uses a set of 16 non-zero integer coefficients.

921 Filtering is a vital step in the hit finder chain. It helps to suppress the noise and
922 enhance the signal peaks with respect to the noiseless baseline. A good filtering strategy
923 allows us to use lower thresholds when forming the trigger primitives (TPs) and thus
924 increasing the sensitivity of our detector to low energy physics events. In such events,
925 the hits produced by the ionisation electrons tend to have lower amplitudes than those

CHAPTER 4. MATCHED FILTER APPROACH TO TRIGGER PRIMITIVES

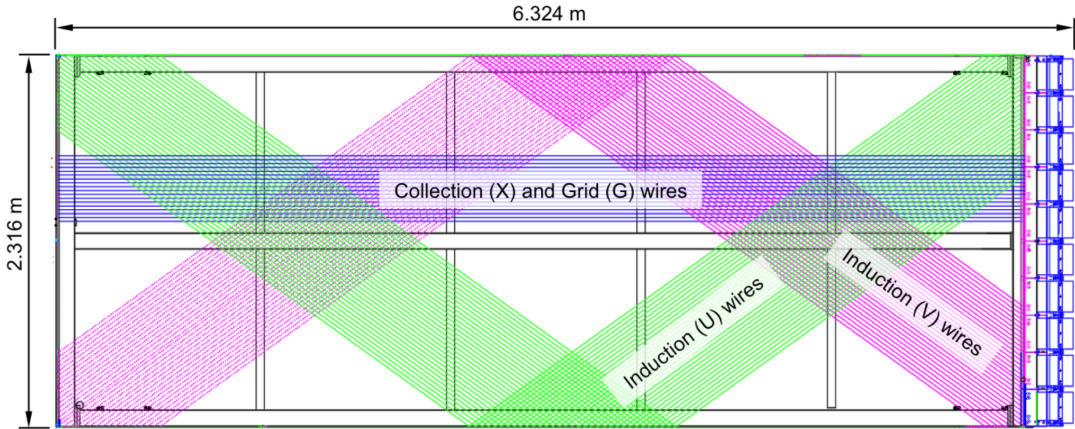


Figure 4.1: Schematic representation of an APA. The black lines represent the APA steel frame. The green and magenta lines correspond to the direction of the U and V induction wires respectively. The blue lines indicate the direction of the X collection wires and the wire shielding G.

of interest to the baseline physics programme of the DUNE experiment.

This is particularly important for the induction planes. In general, signal peaks in the induction wires have smaller amplitude than the ones in the induction plane. This, together with the fact that the pulse shapes are bipolar, reduces our capacity to detect the hits on these channels. The inefficiency of detecting TPs in the induction planes (denoted as U and V planes) lead trigger algorithms to focus mainly on the TPs from the collection plane (so-called X plane). As a result, the possibility of making trigger decisions based on the coincidence of TPs across the three wire planes remains nowadays unexploited in DUNE. Fig. 4.1 shows a schematic view of an anode plane assembly (APA), with the different wire plane orientations highlighted.

A possible improvement of the current hit finder chain could require optimising the existing or choosing a new filter implementation. A filter strategy which improves the induction signals may be able to enhance the detection efficiency of TPs from the induction planes and ideally make it comparable to that of the collection plane.

The goal is to implement a better finite-impulse response filter design and to evaluate its performance relative to the current filter. To do so, we need to take into account the limitations of the firmware: the FIR filter shall have maximum 32 coefficients (so-called

4.2. SIGNAL-TO-NOISE RATIO DEFINITION

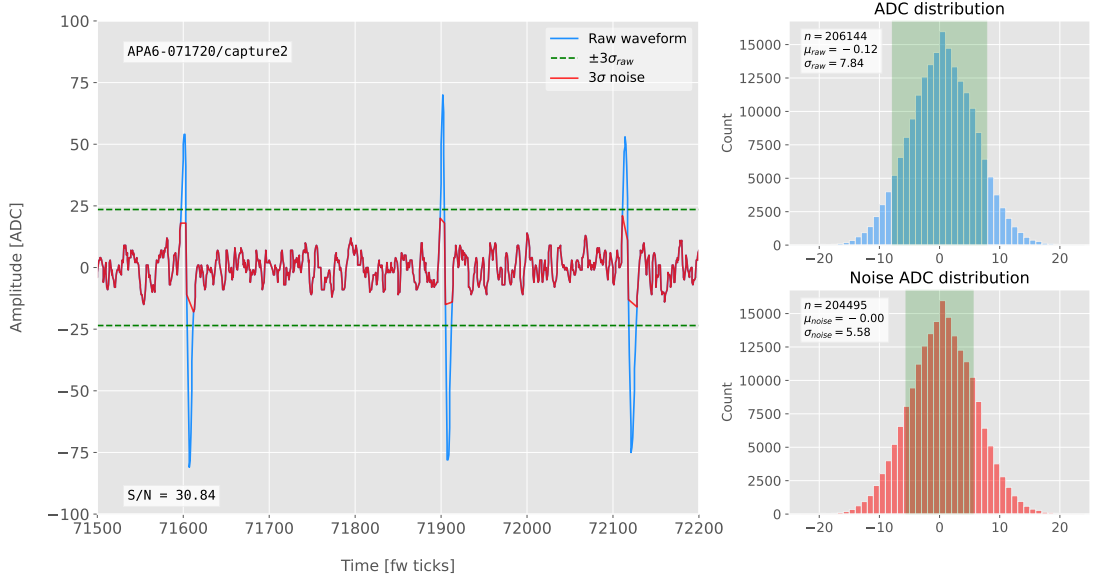


Figure 4.2: Left panel: Zoomed unfiltered waveform corresponding to channel 7840 from the ProtoDUNE-SP raw data capture `felix-2020-07-17-21:31:44` (blue line). The green dashed lines mark the region $\pm 3\sigma_{\text{raw}}$. The resulting noise waveform is also shown (red line). Top right panel: ADC distribution for channel 7840, where the green shaded region represents $\pm \sigma_{\text{raw}}$. Bottom right panel: noise ADC distribution for channel 7840, where the green shaded region represents $\pm \sigma_{\text{noise}}$.

943 taps) whose values are 12-bit unsigned integers. Although it is technically possible to
 944 include non-integer coefficients, it would be a technical challenge as we have 40 FIR
 945 instances per APA, as there are 4 FIR per optical link and 10 optical links per APA.
 946 With these restrictions, the task is to provide a set of 32 coefficients which yield an
 947 optimal filter performance for the induction wires.

948 4.2 Signal-to-noise ratio definition

949 I introduce the signal to noise ratio (S/N) as a measure of the FIR filter performance
 950 and demonstrate how to extract its value for a set of ProtoDUNE-SP data. The S/N
 951 metrics allow us to compare different filter implementations and serve as a basis for more
 952 detailed studies presented later in this document. Specifically, I use the ADC capture
 953 `felix-2020-07-17-21:31:44` (data capture taken for firmware validation purposes). I
 954 defined S/N as the height of the signal peaks relative to the size of the noise peaks.

CHAPTER 4. MATCHED FILTER APPROACH TO TRIGGER PRIMITIVES

955 To quantify this quantity channel by channel one first need to estimate the standard
 956 deviation of the ADC data for each channel, σ_{ADC} . Then, I define the corresponding
 957 noise waveform to be the ADC values in the range $\pm 3\sigma_{ADC}$. From this new noise data
 958 one can estimate again the mean and standard deviation, μ_{noise} and σ_{noise} , so I can
 959 write the S/N for any given channel as:

$$S/N = \frac{\max [ADC] - \mu_{noise}}{\sigma_{noise}}, \quad (4.2)$$

960 where $\max [ADC]$ is simply the maximum ADC value found in the corresponding channel.

961 One can apply this definition of the S/N with a waveform from one of the channels
 962 of the data capture¹. Fig. 4.2 shows a zoomed region of the waveform corresponding to
 963 channel 7840 (blue line), where one can clearly see three signal peaks and continuous
 964 additive noise (we actually see 6 peaks, 3 positive and 3 negative, but, because by design
 965 for induction channels the expected signal pulse shapes are bipolar, I treat them as a
 966 collection of 3 individual signal peaks). I estimated the standard deviation of this raw
 967 waveform to be $\sigma_{raw} = 7.84$ ADC, so I am able to define the noise waveform (red line)
 968 as the ADC values in the range ± 23.52 ADC. This way one obtains $\mu_{noise} = 0$ and
 969 $\sigma_{noise} = 5.58$ ADC, which gives $S/N = 30.84$.

970 We can repeat this calculation now for the corresponding filtered waveform (using the
 971 current firmware FIR filter). In Fig. 4.3 I plotted the same time window for the filtered
 972 waveform from channel 7840 (blue line). In this case, the standard deviation of the
 973 waveform is larger than before, giving $\sigma_{raw} = 10.99$ ADC. The resulting noise waveform
 974 (red line) results from selection the ADC values in the range ± 32.91 ADC, giving now
 975 $\mu_{noise} = -0.47$ ADC and $\sigma_{noise} = 7.03$ ADC. Finally, one obtains $S/N = 24.68$. Notice
 976 that the value of S/N decreases after the filtering. Clearly, one can see that the noise
 977 baseline has increased by a factor of 1.35 when we applied the FIR filter and at the same

¹All the original work was done within the `dtp-simulation` package [103], which offers a variety of tools to read raw data and emulate the TPG block (pedestal subtraction, filtering and hit finder). However, the results shown in this report were re-worked later using the C++ based `dtpemulator` package [104]. Its main purpose is the emulation of the TPG block and, in the same way as its predecessor, it has been cross-checked against the current firmware implementation.

4.3. LOW-PASS FIR FILTER DESIGN

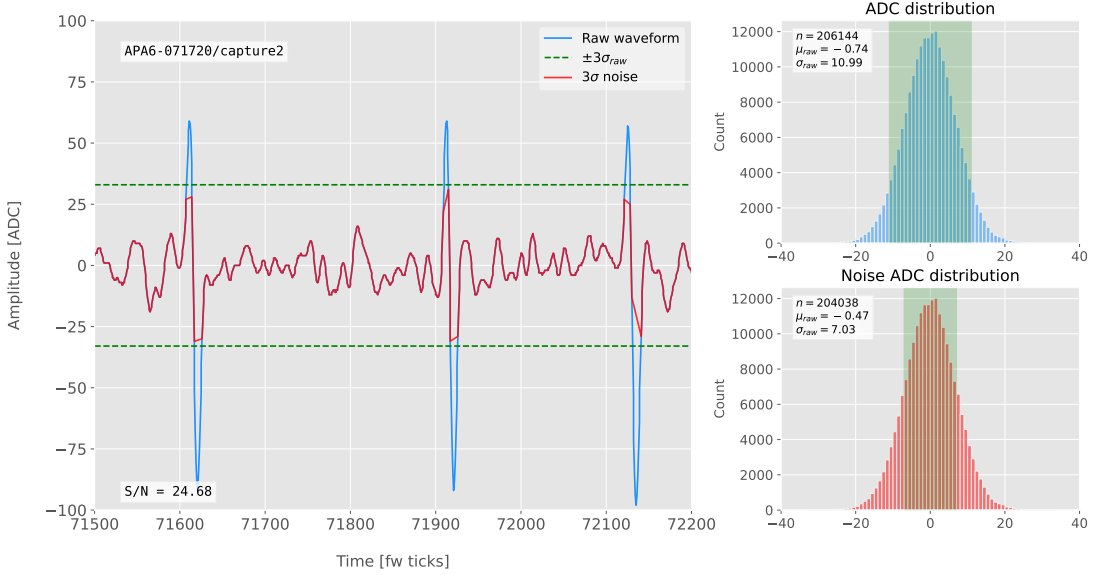


Figure 4.3: Left panel: Zoomed filtered waveform corresponding to channel 7840 from the ProtoDUNE-SP raw data capture `felix-2020-07-17-21:31:44` (blue line). The filter used was the current implementation of the low-pass FIR filter in `dtp-firmware`. The green dashed lines mark the region $\pm 3\sigma_{\text{raw}}$. The resulting noise waveform is also shown (red line). Top right panel: ADC distribution for channel 7840 after filtering, where the green shaded region represents $\pm \sigma_{\text{raw}}$. Bottom right panel: noise ADC distribution for channel 7840 after filtering, where the green shaded region represents $\pm \sigma_{\text{noise}}$

time the amplitude of the signal peaks has remained almost unchanged, leading to this poorer S/N value.

4.3 Low-pass FIR filter design

In general, when one uses a method to optimize the frequency response of a digital filter, such as the Parks-McClellan algorithm, one finds a set of N real coefficients that give the best response for the specified pass-band and order of the filter [105].

In our case, as the sampling frequency is defined as 1 ticks^{-1} , the Nyquist frequency will simply be $1/2 \text{ ticks}^{-1}$. The current implementation of the filter seems to have as pass-band the range $[0, 0.1] \text{ ticks}^{-1}$. This can be seen in Fig. 4.4, where I show the power spectrum, in decibels, of such filter implementation (blue solid line). For instance, the Park-McClellan algorithm finds the optimal Chebyshev FIR filter taking as input

CHAPTER 4. MATCHED FILTER APPROACH TO TRIGGER PRIMITIVES

989 the boundaries of the target pass-band and stop-band, which can be written in the form:

$$\left\{ \begin{array}{l} [0, f_c] \\ [f_c + \delta f, f_N] \end{array} \right. , \quad (4.3)$$

990 where f_c is the cut-off frequency, δf is the transition width and f_N is the aforementioned
 991 Nyquist frequency. A similar behaviour to the one in the current filter can be obtained
 992 by setting $f_c = 0$ and $\delta f = 0.1 \text{ ticks}^{-1}$. The response of the resulting filter is also shown
 993 in Fig. 4.4 (blue solid line). Notice that the suppression of the stop-band is enhanced for
 994 this optimal filter. For comparison I included the power response of the filter obtained
 995 by taking the integer part of the coefficients resulting from the Parks-McClellan method
 996 (red dashed line). One can see that it does not suppress that much the stop-band, in a
 997 similar way to the current implementation of the filter.

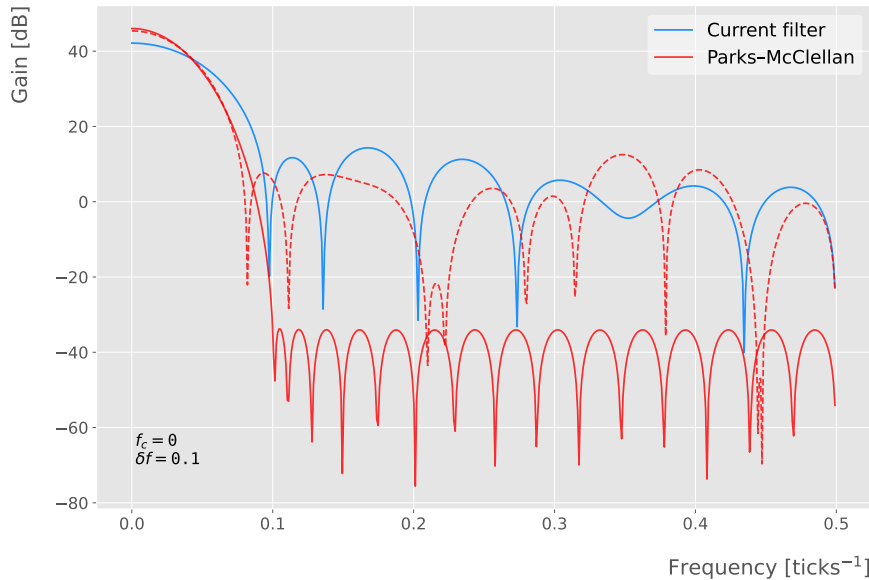


Figure 4.4: Power spectrum in decibels for the current implementation of the low-pass FIR filter in *dtp-firmware* (blue line), compared to the response of an optimal filter obtained using the Parks-McClellan algorithm for the same pass-band (red line). Also for comparison I include the spectrum of the optimal filter when taking only the integer part of the coefficients (red dashed line).

998 At this point, I tried to improve the performance of the FIR filter using the Park-
 999 McClellan method, i.e. maximize the overall S/N, using the available data captures. I
 1000 did so by varying the values of the two quantities that parametrize the pass-band and

4.3. LOW-PASS FIR FILTER DESIGN

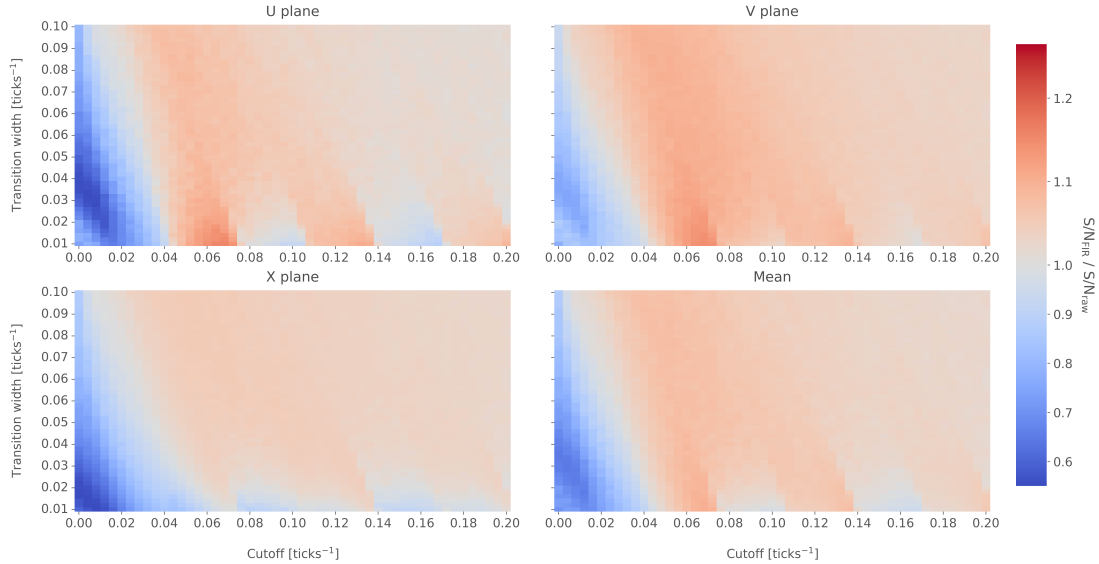


Figure 4.5: Relative change in the S/N for the ProtoDUNE-SP raw data capture `felix-2020-07-17-21:31:44`, using different values of the cutoff frequency f_c and the transition width δf . The optimal Chebyshev filters were applied using just the integer part of the coefficients given by the Parks-McClellan algorithm.

1001 stop-band, the cut-off frequency f_c and the transition width δf .

1002 Fig. 4.5 shows the average relative change in the S/N (i.e. the ratio between the
 1003 value of the S/N after and before the filtering) for capture `felix-2020-07-17-21:31:44`,
 1004 when using filters designed with the Parks-McClellan algorithm for the specified values
 1005 of the cut-off frequency f_c and the transition width δf , restricted to integer values for
 1006 the filter coefficients. One can clearly distinguish different regions where we get an
 1007 improvement of up to a factor of 1.35 for the U plane. For large values of $f_c + \delta f$ the
 1008 ratio tends to 1, as expected (in that limit the width of the stop-band goes to 0, meaning
 1009 that no frequencies are filtered out and thus the waveform remains the same).

1010 Using the configuration which gives the best mean performance for the three
 1011 planes (see bottom right panel of Fig. 4.5), i.e. $f_c = 0.068 \text{ ticks}^{-1}$ and $\delta f =$
 1012 0.010 ticks^{-1} , we can see how such filter affects the different channels. Fig. 4.6 shows the
 1013 distribution of the S/N improvement values for all the channels in the raw ADC capture
 1014 `felix-2020-07-17-21:31:44`, separated by wire plane, after the optimal Chebyshev
 1015 filter was applied. One can see that there is a clear improvement for both U and V

CHAPTER 4. MATCHED FILTER APPROACH TO TRIGGER PRIMITIVES

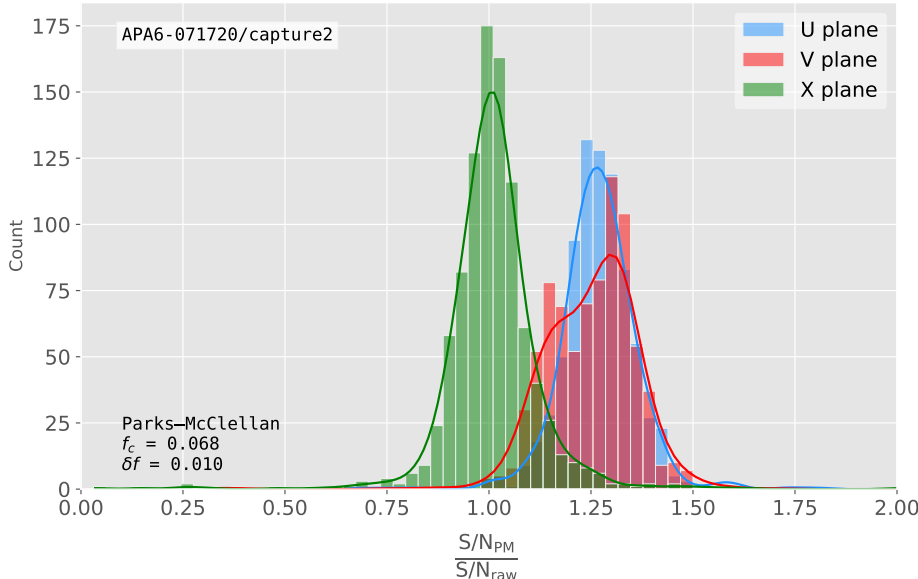


Figure 4.6: Distribution of the relative change of the S/N on the different wire planes from the ProtoDUNE-SP raw data capture *felix-2020-07-17-21:31:44* after the optimal Chebyshev filter was applied. The filter was computed with the Parks-McClellan algorithm using a cutoff of $f_c = 0.068 \text{ ticks}^{-1}$ and a transition width $\delta f = 0.010 \text{ ticks}^{-1}$.

1016 induction wire planes, obtaining a mean change of 1.25 and 1.30 for them respectively.
 1017 However, in the case of the collection plane X the mean of this distribution is roughly 1,
 1018 meaning that a good fraction of channels in that plane get a slightly worse S/N after the
 1019 filter is applied. In any case, this is not a big issue as the S/N for collection channels is
 1020 usually much higher than the one for induction channels.

1021 The results I obtained optimising the low pass filter with the Parks-McClellan method
 1022 are promising. Nonetheless, the improvement found is rather marginal so I wondered
 1023 if there could be an alternative approach to the filtering problem which yields better
 1024 outputs. At this point, I found a possible alternative in matched filters. By construction,
 1025 this kind of filters offer the best improvement on the S/N.

1026 4.4 Matched filters

1027 In the context of signal processing, a matched filter is the optimal linear filter for
 1028 maximising the signal-to-noise ratio (S/N) in the presence of additive noise, obtained

4.4. MATCHED FILTERS

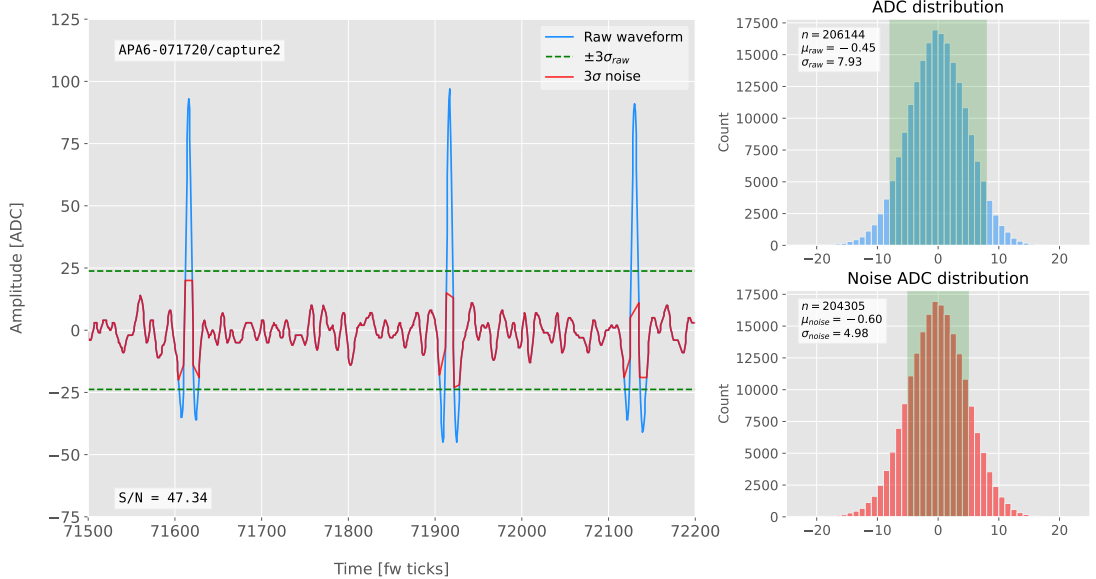


Figure 4.7: Left panel: Zoomed match filtered waveform corresponding to channel 7840 from the ProtoDUNE-SP raw data capture felix-2020-07-17-21:31:44 (blue line). The filter used was directly extracted from the data, being the 32 values around the first peak in the original waveform. The green dashed lines mark the region $\pm 3\sigma_{\text{raw}}$. The resulting noise waveform is also shown (red line). Top right panel: ADC distribution for channel 7840 after match filtering, where the green shaded region represents $\pm \sigma_{\text{raw}}$. Bottom right panel: noise ADC distribution for channel 7840 after match filtering, where the green shaded region represents $\pm \sigma_{\text{noise}}$

1029 by convolving a conjugated time-reversed known template with an unknown signal to
1030 detect the presence of the template in the signal [106].

1031 Given a known signal sequence $s(t)$ and another (a priori unknown) noise sequence
1032 $n(t)$, the input signal can be written as:

$$x(t) = s(t) + n(t). \quad (4.4)$$

1033 Now, considering a linear time-invariant filter, whose impulse-response function I
1034 will refer to as $h(t)$, one can write the output signal as:

$$\begin{aligned} y(t) &= x(t) * h(t) \\ &= (s(t) + n(t)) * h(t) \\ &= y_s(t) + y_n(t), \end{aligned} \quad (4.5)$$

CHAPTER 4. MATCHED FILTER APPROACH TO TRIGGER PRIMITIVES

1035 where $y_s(t)$ and $y_n(t)$ are simply the outputs of the filter due to the signal and the noise
 1036 components respectively.

1037 The goal of the matched filter is to detect the presence of the signal $s(t)$ in the input
 1038 sample $x(t)$ at a certain time t_0 , which effectively means we need to maximise the S/N.
 1039 This way, what one wants is to have a filter which gives a much bigger output when the
 1040 known signal is present than when it is not. Putting it in other words, the instantaneous
 1041 power of the signal output $y_s(t)$ should be much larger than the average power of the
 1042 noise output $y_n(t)$ at some time t_0 .

1043 For the case of the filtered signal, one can easily re-write it as an inverse Fourier
 1044 transform:

$$y_s(t) = \frac{1}{2\pi} \int_{-\infty}^{\infty} d\omega H(\omega)S(\omega)e^{i\omega t}, \quad (4.6)$$

1045 where $H(\omega)$ and $S(\omega)$ are the Fourier transforms of the impulse-response function (i.e.
 1046 the transfer function of the filter) and of the input signal, respectively.

1047 Now focusing on the noise, we can use the Wiener-Khinchin theorem [107] to write
 1048 the mean power of the noise after filtering as:

$$E|y_n(t)|^2 = \frac{1}{2\pi} \int_{-\infty}^{\infty} d\omega |H(\omega)|^2 S_n(\omega), \quad (4.7)$$

1049 where $S_n(\omega)$ is the power spectral density of the noise.

1050 Having these, one can write the instantaneous S/N at time t_0 as:

$$\begin{aligned} \left(\frac{S}{N} \right)_{t_0} &= \frac{|y_s|^2}{E|y_n(t)|^2} \\ &= \frac{1}{2\pi} \frac{\left| \int_{-\infty}^{\infty} d\omega H(\omega)S(\omega)e^{i\omega t_0} \right|^2}{\int_{-\infty}^{\infty} d\omega |H(\omega)|^2 S_n(\omega)}. \end{aligned} \quad (4.8)$$

1051 Once we have this expression, we need to find the upper limit of it to determine what
 1052 would be the optimal choice for the transfer function. One can use the Cauchy-Schwarz

4.4. MATCHED FILTERS

1053 inequality, which in the present case takes the form:

$$\left| \int_{-\infty}^{\infty} dx f(x)g(x) \right|^2 \leq \int_{-\infty}^{\infty} dx |f(x)|^2 + \int_{-\infty}^{\infty} dx |g(x)|^2, \quad (4.9)$$

1054 for any two analytical functions $f(x)$ and $g(x)$. One can prove that making the choice:

$$\begin{aligned} f(x) &= H(\omega) \sqrt{S_n(\omega)} e^{i\omega t_0}, \\ g(x) &= \frac{S(\omega)}{\sqrt{S_n(\omega)}}, \end{aligned} \quad (4.10)$$

1055 leads to the following upper bound for the S/N:

$$\left(\frac{S}{N} \right)_{t_0} \leq \frac{1}{2\pi} \int_{-\infty}^{\infty} d\omega \frac{|S(\omega)|^2}{S_n(\omega)}. \quad (4.11)$$

1056 From Eqs. (4.8), (4.9) and (4.10) one can also derive the form of the transfer function
1057 such that the upper bound is exactly reached [108]:

$$H(\omega) \propto \frac{S^*(\omega) e^{-i\omega t_0}}{S_n(\omega)}. \quad (4.12)$$

1058 From this last expression we can clearly see the way the matched filter acts. As the
1059 transfer function is proportional to the Fourier transform of the signal it will try to only
1060 pick the frequencies present in the signal [109].

1061 The matched filter transfer function can be greatly simplified if the input noise is
1062 Gaussian. In that case, the power spectral density of the noise is a constant, so it can be
1063 re-absorbed in the overall normalisation of the transfer function. Moreover, considering
1064 that the input signal is a real function, one can simply set $S^*(\omega) = S(-\omega)$, which gives:

$$H(\omega) \propto S(-\omega) e^{-i\omega t_0}. \quad (4.13)$$

1065 For a discrete signal, one can think of the input and impulse-response sequences as
1066 vectors of \mathbb{R}^N . Then, the matched filter tries to maximise the inner product of the signal
1067 and the filter while minimising the output due to the noise by choosing a filter vector

CHAPTER 4. MATCHED FILTER APPROACH TO TRIGGER PRIMITIVES

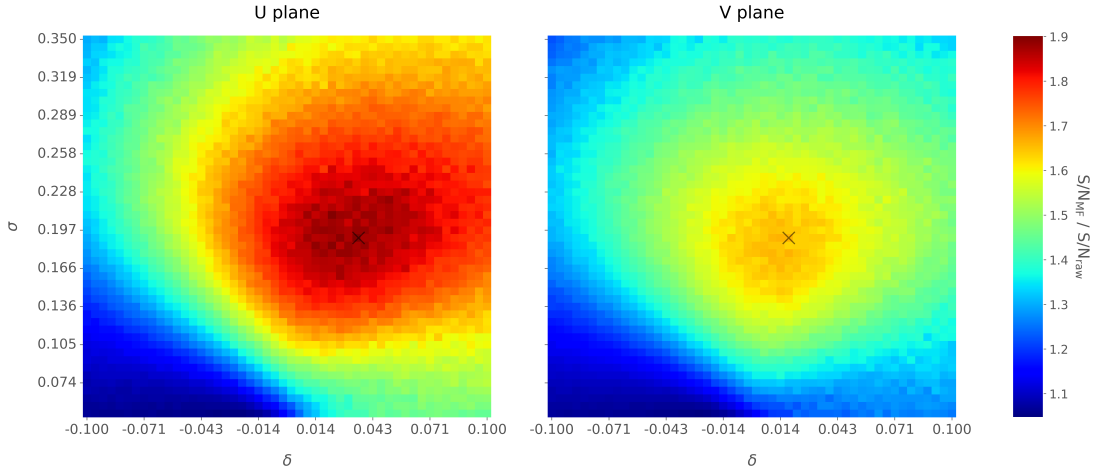


Figure 4.8: Relative improvement in the S/N for the raw data capture *felix-2020-07-17-21:31:44*, using the matched filter following the parametrisation in Eq. (4.17). The black crosses in both panels denote the location of the maximum ratio value.

1068 orthogonal to the later. In the case of additive noise, that leads to the impulse-response
 1069 vector:

$$h = \frac{1}{\sqrt{s^\dagger R_n^{-1} s}} R_n^{-1} s, \quad (4.14)$$

1070 where s is a reversed signal template sequence of length N equal to the order of the filter
 1071 and R_n is the covariance matrix associated with the noise sequence n . For the Gaussian
 1072 noise case, the covariance matrix is simply the unit matrix, so the above expression
 1073 simplifies again to:

$$h = \frac{s}{|s|}. \quad (4.15)$$

1074 For this first stage of the study, I use a definition of the S/N per channel given by:

$$S/N = \frac{\max [ADC] - \mu_{noise}}{\sigma_{noise}}, \quad (4.16)$$

1075 where the subscript *noise* refers to a subset of the data obtained by only taking into
 1076 account waveform values within a $\pm 3\sigma$ range around the mean of the data and $\max [ADC]$
 1077 is the maximum of the original waveform. This definition is further discussed in App.
 1078 4.2, where I also show examples of its application to raw data and to a waveform filtered

4.4. MATCHED FILTERS

1079 with the current low-pass FIR filter.

1080 To test whether this choice of filter is appropriate one needs to choose a signal
1081 template. As an example of how a matched filter would affect our signal, I simply took
1082 the filter coefficients to be the 32 ADC values around a signal peak present in the data.
1083 In Fig. 4.7 (left panel) I plotted a zoomed region for channel 7840 in the raw data capture
1084 `felix-2020-07-17-21:31:44`, after applying the matched filter described before (blue
1085 line). When compared to the raw and FIR filtered case (see App. 4.2), after applying
1086 the match filter the standard deviation of the noise waveform (red line) decreases and at
1087 the same time the signal peaks are enhanced. This leads to an improvement of the S/N
1088 by a factor of 1.92 when compared to the raw waveform.

1089 In order to obtain the matched filter that is more suitable for our data, I explored
1090 different configurations of signal templates. In order to perform this exploration, I
1091 parametrised the signal using the bipolar function:

$$f(x) = -A(x + \delta) e^{-x^2/\sigma^2}, \quad (4.17)$$

1092 where the parameter δ controls the asymmetry between the positive and negative peaks
1093 and σ controls their width. The amplitude parameter A is set such that it keeps the
1094 height of the biggest peak to be less than 200 ADC in absolute value.

1095 As this parametrisation is only adequate for bipolar signals I will focus exclusively
1096 on the induction channels. Also, the optimal configurations I found for the U and V
1097 plane will be kept separate, i.e. I will have two sets of coefficients that will be applied to
1098 either the U and V planes of wires. I do so as I found this was the choice giving the
1099 best performance. Even so, as I will discuss, the differences are not very pronounced. In
1100 case it is not technically possible to separate channels in the firmware according to the
1101 wire plane they come from and use different sets of filter coefficients for them, we can
1102 just find a common unique set of coefficients. In such case, I do not expect our results
1103 to change dramatically.

1104 In Fig. 4.8 I present the results of our parameter scan, for channels in the induction

CHAPTER 4. MATCHED FILTER APPROACH TO TRIGGER PRIMITIVES

planes U (left panel) and V (right panel). For each configuration of σ and δ the resulting matched filter was applied to all channels in the corresponding plane within the data capture `felix-2020-07-17-21:31:44`, the S/N improvement was computed with respect to the raw waveforms and then the S/N mean value was kept as a score for such filter. One can see that the improvement obtained for the U plane is in general higher than the one for the V plane. In any case, I got substantially higher ratios than the ones obtained for the low-pass FIR filters. For the optimal configurations I attained improvements up to a factor of 1.85 for the U plane and 1.65 for the V plane.

The sets of optimal matched filter coefficients were obtained for the parameters $\delta = 0.035$, $\sigma = 0.191$ for the U plane and $\delta = 0.018$, $\sigma = 0.191$ for the V plane. I show these two sets of coefficients in Fig. 4.9 (left panel). Also in Fig. 4.9 (right panel) I plot the distribution of the S/N improvement after the optimal match filters for the U and V were applied to the corresponding channels in the raw data capture `felix-2020-07-17-21:31:44`. As mentioned before, the mean improvement achieved for the U plane channels is slightly bigger than the one for the V channels. Note, however, that the spread of the distribution for the V plane is also smaller than the one for the U plane.

I also performed a similar scan for the case of a low-pass FIR filter using the Parks-McClellan algorithm. In that case, the parameters to check were the cutoff frequency and the transition width of the filter. A summary of the results is given in App. 4.3.

Overall, one can see that the improvements on the S/N are much more significant in the case of the matched filter than it is for the low-pass FIR filters. The analysis of this and other raw data captures from ProtoDUNE-SP suggest that matched filters increase the S/N of induction channels by a factor of 1.5 more than the optimal low-pass FIR filters.

Although these results are by themselves great points in favour of the matched filter, more studies are needed to completely assess the robustness of this approach. I proceeded then to test the matched filter with simulated data samples.

4.5. USING SIMULATED SAMPLES

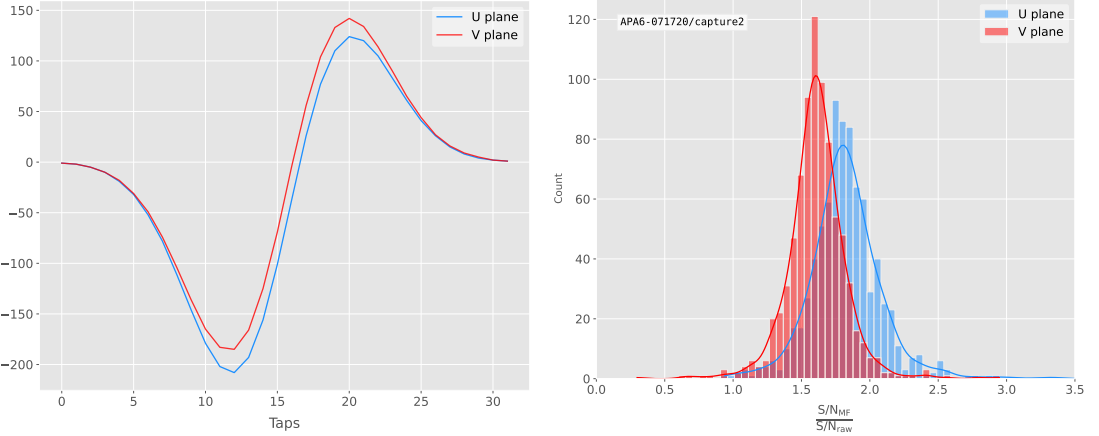


Figure 4.9: Left panel: Optimal matched filter coefficients for the U (blue line) and V (red line) planes. The filters were computed with our parametrisation in Eq. (4.17) for the parameter values $\delta = 0.035$, $\sigma = 0.191$ and $\delta = 0.018$, $\sigma = 0.191$ respectively. Right panel: Distribution of the relative change of the S/N on the two induction wire planes from the ProtoDUNE-SP raw data capture *felix-2020-07-17-21:31:44* after their respective optimal matched filters were applied.

1133 4.5 Using simulated samples

1134 In order to further test the matched filter, the next step was to generate and process
 1135 data samples using *LArSoft* [110]. In this way, one can control the particle content of
 1136 the samples, the orientation of the tracks and their energy, and therefore see how the
 1137 matched filter behaves in various situations.

1138 To begin with, I prepared different monoenergetic and isotropic samples containing
 1139 a single particle per event. Each sample contains a different particle species, namely
 1140 electrons, muons, protons and neutral pions all with a kinetic energy of $E_k = 100$ MeV.
 1141 I chose these because of the fairly different topologies they generate in the liquid argon,
 1142 ranging from shower-like to track-like. The procedure I followed to generate the samples
 1143 and process them is discussed in detail in App. ??.

1144 These were generated with the single particle gun and the Geant4 stage of the
 1145 *LArSoft* simulation [110] was performed with the standard configuration for the DUNE
 1146 FD 10kt module.

1147 For simplicity, I restricted the particles to start drifting in a single TPC volume

CHAPTER 4. MATCHED FILTER APPROACH TO TRIGGER PRIMITIVES

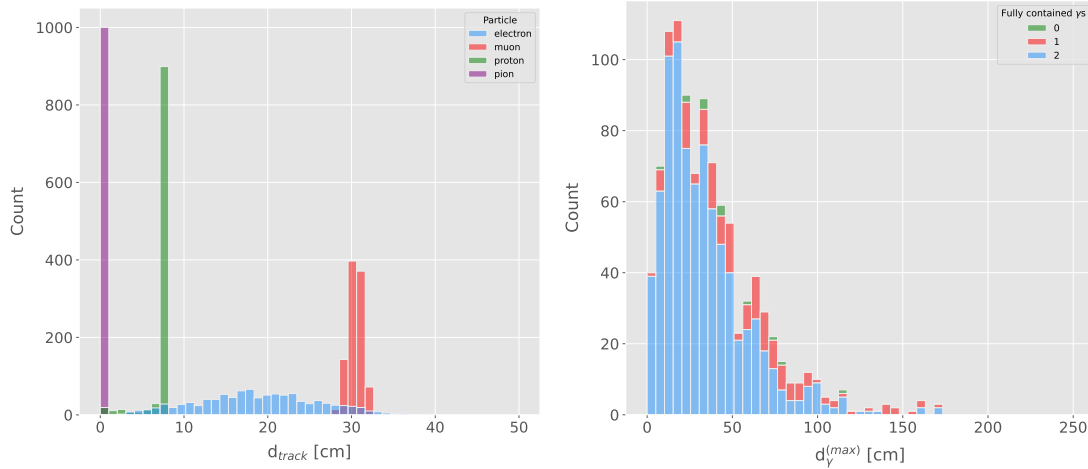


Figure 4.10: Left panel: distributions of the particles track length in the liquid argon for the generated $E_k = 100$ MeV monoenergetic samples, electrons (blue), muons (red), protons (green) and neutral pions (purple). Right panel: distribution of the length of the longest photon in the neutral pion sample after the decay process $\pi^0 \rightarrow \gamma\gamma$.

1148 (in this case TPC 0), so I can focus exclusively on the signals coming from one APA.
 1149 The chosen kinetic energy for all the particles in my first trial is $E_k = 100$ MeV, so a
 1150 necessary check is to see if all our tracks will be typically contained in one TPC volume.
 1151 Fig. 4.10 (left panel) shows the distributions of the track lengths in the liquid argon
 1152 of all generated particles with $E_k = 100$ MeV. One can see that, in the case of the
 1153 track-like particles (i.e. muons and protons), their length distributions are quite sharp
 1154 and centered at relatively low distances (30 and 8 cm, respectively). For electrons, the
 1155 distribution is quite broad but it does not extend past ~ 30 cm. The case of neutral
 1156 pions can be misleading, as they decay promptly the track length associated with the
 1157 true Monte Carlo particle is always < 1 cm. In Fig. 4.10 (right panel) I show the
 1158 effective length distribution of the longest photon after the pion decays as $\pi^0 \rightarrow \gamma\gamma$,
 1159 highlighting the number of fully contained photons in the TPC volume per event (either
 1160 zero, one or both). One can see that the vast majority of events has both photons
 1161 contained and that just a negligible number of them has none of them contained in the
 1162 TPC volume. In any case, for the sake of caution, I will only keep the pion events with
 1163 both photons contained.

1164 Once I have prepared a sample at the Geant4 level, I need to process it through the

4.5. USING SIMULATED SAMPLES

1165 detector simulation. In order to make adequate estimations of the noise levels and run
1166 the filtering and hit finder as I did with the ProtoDUNE data, one needs to turn off
1167 the default zero-suppression of the waveforms produced by the simulation. At this first
1168 stage I am only concerned with the waveforms with the noise added, so I keep the noise
1169 addition option as true in the configuration. However, for studies related to the hit finder
1170 performance one will also need to store the noiseless waveforms in order to retrieve the
1171 truth information of the hits. I will discuss this approach next.

1172 After the detector simulation stage, one needs to extract the no zero-suppressed noisy
1173 waveforms, along with their offline channel numbers, and store them in a certain format
1174 to be analysed later. To reduce the amount of data that will go for processing, I used the
1175 information from the Geant4 step of the simulation to select only the active channels,
1176 i.e. the channels where some ionisation electrons arrive. Moreover, as said previously, I
1177 only extract the waveforms from APA 0 and exclusively the ones coming from induction
1178 channels. The resulting ROOT file contains a tree with two branches, one containing
1179 the waveforms for each event and channel and the other with the corresponding offline
1180 channel numbers.

1181 Finally, to extract the truth values for the orientation of the tracks and the energies
1182 of the particles I used a modified analysis module. This gives a ROOT file with a single
1183 tree, containing several branches with different information such as the components of
1184 the initial momentum of the particles, initial and final *xyz* location, track length, etc.

1185 For the analysis of the resulting waveforms and truth values I used a custom set of
1186 Python libraries (available at [???]). Among other functionalities, these enable the user
1187 to read the ROOT files, export the raw data as pandas objects, apply the filters and
1188 compute the S/N of both the raw and filtered signals. So far, the default configuration
1189 for the filtering uses the set of optimal matched filter coefficients that I found using the
1190 ProtoDUNE data samples.

1191 Additionally, for the analysis of the samples it was necessary to use two different
1192 reference frames, to study separately the signals coming from the U and V induction wire
1193 planes. As I am focussing on a single APA, the U and V wires have a different orientation

CHAPTER 4. MATCHED FILTER APPROACH TO TRIGGER PRIMITIVES

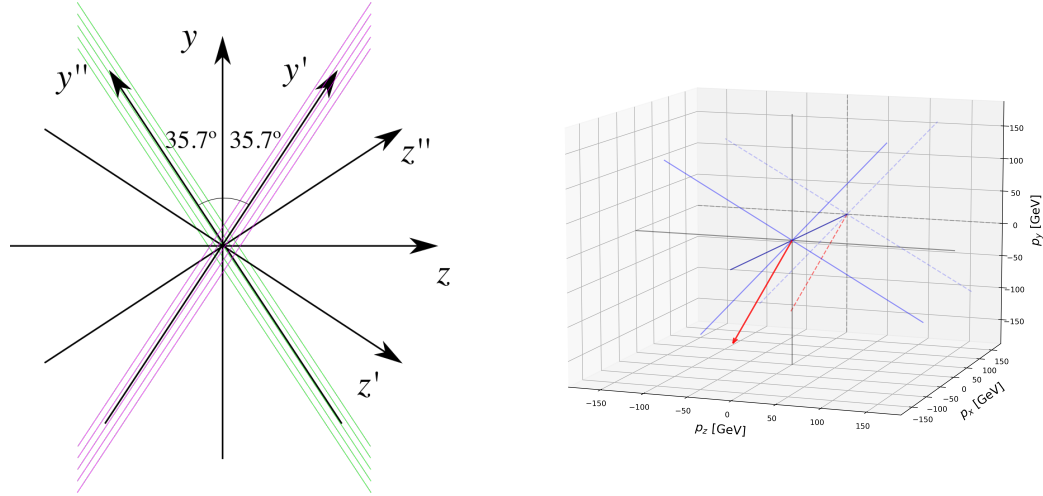


Figure 4.11: Left panel: schematic representation of the two new rotated reference frames used in this analysis (denoted as prime and double prime), viewed from the yz plane. The magenta stack of lines represent the wires in the U plane, whereas the green lines correspond to the wires in the V plane. Right panel: 3D representation of the momentum of one of the generated monoenergetic muons (red arrow) in the original reference frame (black lines), along with the new reference frame used for the U plane waveforms (blue lines). In the yz plane I added the projection of these three.

in the yz plane. In the case of U wires, these are tilted 35.7° clockwise from the vertical (y direction), whereas the V wires are at the same angle but in the counter clockwise direction. Because of this, the best option is to deal with two new coordinate systems rotated by $\pm 35.7^\circ$ along the x axis, so the new y' and y'' directions are aligned with the U and V induction wires. Fig. 4.11 (left panel) shows a schematic representation of the original reference frame together with the two rotated ones (denoted by primed and double primed). This way, one can easily understand how parallel was a track to the wires in the two induction planes. Fig. 4.11 (right panel) shows a 3D representation of the momentum of a track (red arrow) in the original reference frame (black lines), along with the new reference frame for U wires (blue lines). I added the projection in the yz plane of this three, to show the usefulness of the new reference frame to tell whether a track is parallel or normal to the wires in the induction plane.

Fig. 4.12 shows the distribution of the average S/N improvement per event when one applies the optimal matched filters. I produced separate distributions for the channels

4.5. USING SIMULATED SAMPLES

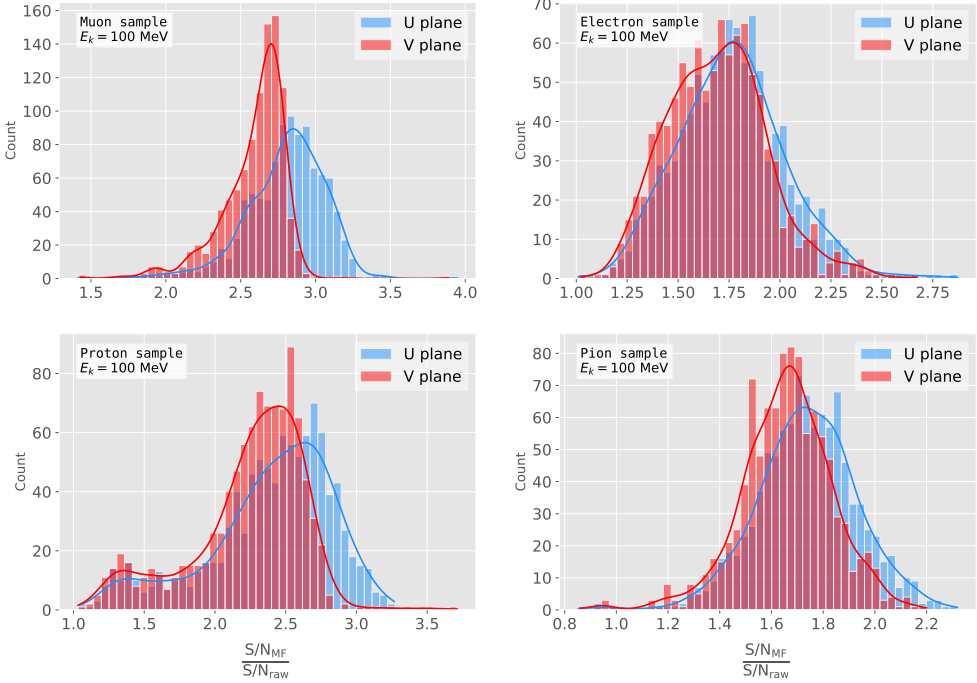


Figure 4.12: Distributions of the mean S/N improvement per event for the corresponding sample after applying the matched filters. Here I separated the change in the U plane (blue) and the V plane (red) channels. From top left to the right: muon, electron, proton and neutral pion. All the events have a fixed kinetic energy of $E_k = 100 \text{ MeV}$.

in the U (red) and V (blue) induction wire planes. Notice that the S/N distributions for the track-like particles, i.e. muons (top left panel) and protons (bottom left panel), have significantly larger mean values than the distributions of the shower like particles, i.e. electrons (top right panel) and neutral pions (bottom right panel). An important difference between these results and the ones seen before for ProtoDUNE data is that, overall, the improvements that I get for simulated data are bigger. This could be due either to the default noise model used in the *LArSoft* simulation or to the simulated hits having higher energy than the ones in the recorded data. Nonetheless, the concluding message is that the previously optimised matched filters give an overall significant improvement of the S/N for the different samples.

About the convention I followed for the plots and results, in the case of the raw and filtered S/N of each event in the sample I simply took the average of the quantities over all the active channels in the event. That is, if a certain event has N_{chan} active channels

CHAPTER 4. MATCHED FILTER APPROACH TO TRIGGER PRIMITIVES

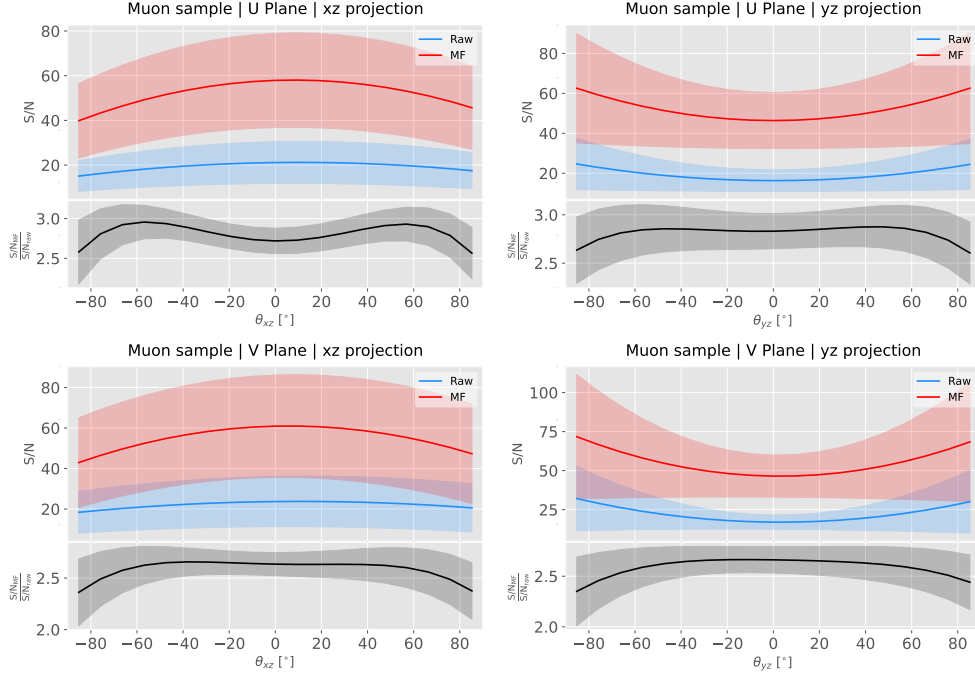


Figure 4.13: Angular dependence of the mean S/N and the S/N improvement, for the different monoenergetic samples considered (from top to bottom: electrons, muons, protons and neutral pions). The two columns on the left represent the values for the U plane waveforms. The top subplots show the mean S/N for raw (green) and filtered (red) waveforms whereas the bottom subplots depict the averaged S/N improvement (black).

1221 these two quantities are computed as:

$$(S/N_{\text{fir}})_{\text{event}} = \frac{\sum_{i=0}^{N_{\text{chan}}} (S/N_{\text{fir}})_i}{N_{\text{chan}}}, \quad (4.18)$$

$$(S/N_{\text{raw}})_{\text{event}} = \frac{\sum_{i=0}^{N_{\text{chan}}} (S/N_{\text{raw}})_i}{N_{\text{chan}}}.$$

1222 However, for the ratio of the raw and filtered S/N (what I called the S/N improvement)
1223 per event I am not just taking the ratio of the previous two quantities but computing
1224 the average of the individual ratios per channel in the event:

$$\left(\frac{S/N_{\text{fir}}}{S/N_{\text{raw}}} \right)_{\text{event}} = \frac{\sum_{i=0}^{N_{\text{chan}}} \left(\frac{S/N_{\text{fir}}}{S/N_{\text{raw}}} \right)_i}{N_{\text{chan}}}, \quad (4.19)$$

1225 and so:

$$\left(\frac{S/N_{\text{fir}}}{S/N_{\text{raw}}} \right)_{\text{event}} \neq \frac{(S/N_{\text{fir}})_{\text{event}}}{(S/N_{\text{raw}})_{\text{event}}}. \quad (4.20)$$

4.5. USING SIMULATED SAMPLES

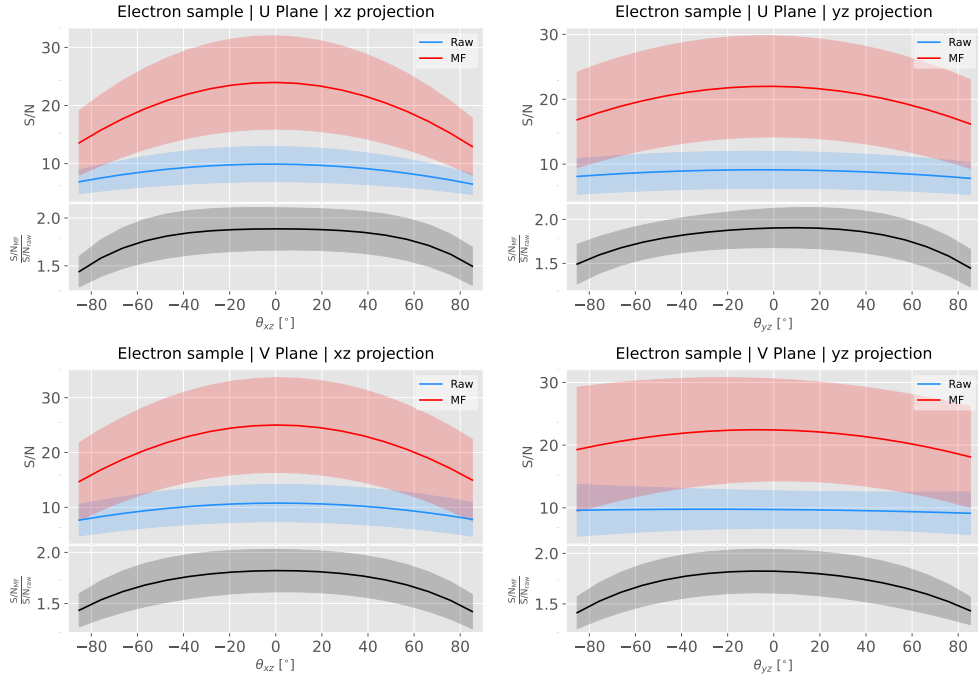


Figure 4.14: Angular dependence of the mean S/N and the S/N improvement, for the different monoenergetic samples considered (from top to bottom: electrons, muons, protons and neutral pions). The two columns on the left represent the values for the U plane waveforms. The top subplots show the mean S/N for raw (green) and filtered (red) waveforms whereas the bottom subplots depict the averaged S/N improvement (black).

1226 4.5.1 Angular dependence

1227 Having these monoenergetic samples, one can also study the angular dependence of the
 1228 performance of the matched filter. This is an important point, as it is a well established
 1229 fact that for certain configurations (an extreme case configuration being signals normal
 1230 to the wire plane and perpendicular to the induction wires at the same time) the S/N is
 1231 much lower than average as the corresponding waveforms are severely distorted. In this
 1232 sense, I am interested to see how the matched filter behaves for these cases and how the
 1233 S/N improvement on those compare to the average.

1234 Fig. 4.13 shows the angular dependence of the S/N for the monoenergetic $E_k =$
 1235 100 MeV isotropic muons, for the different induction wire planes and projections. The
 1236 angles for each event are given by the components of the initial value of the momentum
 1237 of the particles, taking the angles of the projections on the xz and yz planes with respect

CHAPTER 4. MATCHED FILTER APPROACH TO TRIGGER PRIMITIVES

to the z axis (more accurately, one needs to compute these angles twice for each event, a pair for the $xy'z'$ coordinate system and the other for the $xy''z''$). The top row shows the dependence on the angles corresponding to the U plane, i.e. $\theta_{xz'}$ and $\theta_{y'z'}$, whereas the bottom row shows the angular dependence viewed from the V plane, $\theta_{xz''}$ and $\theta_{y''z''}$. In each plot, the top subplot represents the mean values of the S/N for the raw (blue) and matched filtered (red) signals, and the bottom subplot the averaged S/N improvement (black). The solid lines represent the mean value obtained for the corresponding angular value, whereas the semitransparent bands represent one standard deviation around the mean at each point.

As expected, the S/N is in general higher when tracks are parallel to the APA (i.e. $\theta_{xz} \sim 0$) and lower when it is normal to the plane ($\theta_{xz} \sim \pm 90^\circ$). In the same way, tracks parallel to the wires ($\theta_{yz} \sim \pm 90^\circ$) tend to have higher S/N than those perpendicular to these ($\theta_{yz} \sim \pm 0$).

Fig. 4.14 shows the corresponding angular dependence information for the $E_k = 100$ MeV electrons sample. Notice that, in this case, the S/N behaviour discussed above does not hold. A possible explanation can be that, because most hits in these events are produced by the secondary particles generated in the EM shower, the signal peaks whose S/N ratios were computed do not correspond to the directional information of the primary electron.

4.5.2 Distortion and peak asymmetry

As a little case of study, I selected two of the simulated $E_k = 100$ MeV monoenergetic muon events. With respect to the U induction plane, one is parallel to the APA (low $\theta_{xz'}$) and to the wires (high $\theta_{y'z'}$) and the other is normal to the APA plane (high $\theta_{xz'}$) and perpendicular to the wires (low $\theta_{y'z'}$). As expected from the results on the angular dependence discussed above, the former has a higher S/N (before and after the filtering) when compared to the latter. An interesting thing to notice about these two samples is that, even though one has a much bigger S/N than the other, it is the one with the smallest S/N the one that got the biggest averaged S/N improvement. In Table 4.1

4.5. USING SIMULATED SAMPLES

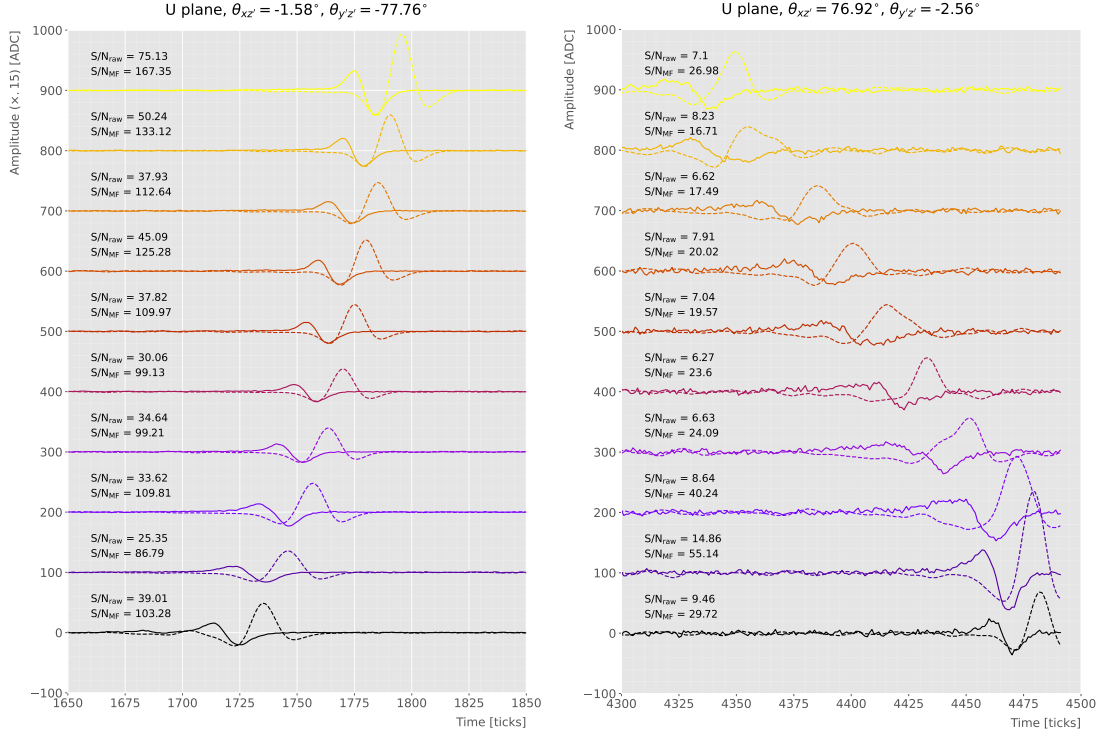


Figure 4.15: Selected consecutive waveforms corresponding to two monoenergetic $E_k = 100$ MeV muon events, one is parallel to the APA and to the wires in the U plane (left panel) and the other is normal to the APA plane and perpendicular to the U plane wires (right panel). The solid lines represent the raw waveforms whereas the dashed lines correspond to the waveforms after the matched filter was applied. The waveforms on the left panel have been scaled by a factor of 0.15 to have similar amplitude to the ones on the right panel.

I included all the relevant parameters of these two $E_k = 100$ MeV muon events I am considering, namely, the angles with respect to the $xy'z'$ reference frame, the values of the S/N, the S/N improvement and also the so-called peak asymmetry Δ_{peak} that I will discuss next.

Table 4.1: Characteristic parameters of the two monoenergetic muon events selected, relative to the U plane: projected angles in the xz' and $y'z'$ planes, S/N values for the raw and filtered waveforms, mean improvement of the S/N and peak asymmetry.

	$\theta_{xz'}$ (°)	$\theta_{y'z'}$ (°)	S/N _{raw}	S/N _{MF}	$\frac{S/N_{MF}}{S/N_{raw}}$	Δ_{peak} (ADC)
High ("parallel")	-1.58	-77.76	41.65	112.44	2.83	-35.73
Low ("normal")	76.92	-2.56	8.07	25.46	3.12	-10.38

One can try to understand better what is going on with these two events by looking

CHAPTER 4. MATCHED FILTER APPROACH TO TRIGGER PRIMITIVES

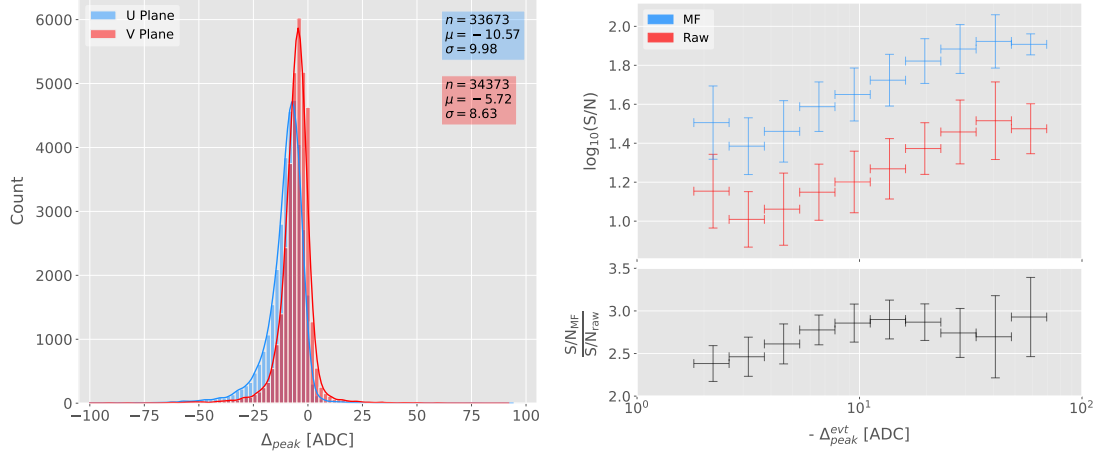


Figure 4.16: Left panel: peak asymmetry distribution for the case of the monoenergetic $E_k = 100$ MeV muon sample. Each value corresponds to a single bipolar signal peak from a channel in any event. The blue distribution represents the peaks on U plane channels, whereas the red corresponds to signal peaks in V wires. Right panel: relation between the mean peak asymmetry per event with the S/N for U channel waveforms from the $E_k = 100$ MeV muon sample. The top subplot shows the decimal logarithm of the mean S/N for the raw (red) and the matched filtered (blue) waveforms. The bottom subplot contains the mean S/N improvement ratio after the matched filter was applied.

at the raw and filtered data from some of their active channels. Fig. 4.15 shows a selection of consecutive raw and filtered U plane waveforms from the event with high S/N (left panel) and the one with low S/N (right panel). Notice that to show both collections of waveforms at a similar scale I had to apply a factor of 0.15 to the waveforms with high S/N. Additionally, next to each waveform I included the values of the raw and matched filtered S/N for the corresponding channel. The first thing to notice in this plot is that the amplitude of the signal peaks from the normal track have a much smaller amplitude, and also appear quite distorted when compared to the others. On the other hand, although the matched filtered S/N is still smaller, the relative improvement is bigger than in the parallel case.

A way I found to quantify the difference between the shapes within these two events is their different peak asymmetry. One can define the peak asymmetry as the (signed) difference between the positive and the negative peaks of the bipolar shape, i.e.:

$$\Delta_{peak} \equiv h_+ - h_-, \quad (4.21)$$

4.5. USING SIMULATED SAMPLES

where both heights h_+ and h_- are positive defined. Fig. 4.16 (left panel) shows the distribution of this peak asymmetry for all the waveforms corresponding to channels in the U (blue) and V (red) planes for the monoenergetic muon sample. One can see that these distributions are clearly shifted to negative values (with mean values $\mu_{\Delta}^U = -10.57$ ADC and $\mu_{\Delta}^V = -5.72$ ADC respectively). It is interesting to notice that the peak asymmetry value of the sample with high S/N sits at the left tail of the distribution whereas the corresponding value of the sample with low S/N lies around the mean.

Now, one can try to correlate the peak asymmetry with the S/N and the S/N change per event. Fig. 4.16 (right panel) shows the result of comparing (minus) the mean peak asymmetry per event to the averaged raw (red) and matched filtered (blue) S/N per event (top subplot). The horizontal lines sit at the mean value obtained in the fit and represent the width of the $-\Delta_{peak}$ bins used, while the vertical lines indicate one standard deviation around that mean value. Notice that, when taking decimal logarithm on both, there is an approximate linear relation between these quantities, except for peak asymmetry values bigger than -5 ADC where the S/N remains constant.

Also, in the bottom subplot of Fig. 4.16 (right panel) I show the relation between the peak asymmetry and the mean S/N improvement. In this case, one see that there is a maximum at $\Delta_{peak} \sim -10$ ADC. As mentioned previously, this is also the value of the mean of the peak asymmetry distribution. In fact, it is expected that our filter favours the signal peaks with the most common values of the peak asymmetry, as this was one of the features I target in our filter coefficient optimisation through the parameter δ .

These results suggest that events with poorer values of the mean S/N, usually associated to non-favourable track orientations, tend to have smaller values of the mean peak asymmetry (in absolute value). Nonetheless, because our matched filters have been optimised to account for these asymmetries, the improvement on the S/N for these events is sizeable if not better than the one for events which already had a high S/N.

CHAPTER 4. MATCHED FILTER APPROACH TO TRIGGER PRIMITIVES

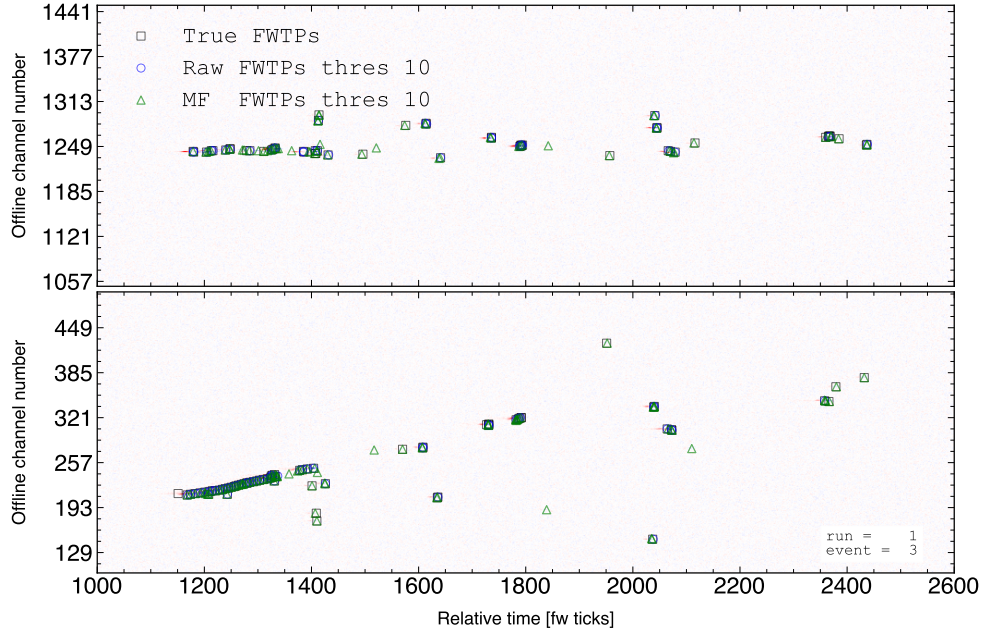


Figure 4.17: Raw data display in the plane time (in firmware ticks) vs. offline channel number for an $E_k = 100$ MeV electron event. The produced true hits are superimposed (black boxes) as well as the hits coming from the standard hit finder chain (blue circles) and the hit finder using the matched filter (green triangles).

4.5.3 Hit sensitivity

One of the advantages of the matched filter, directly related to increasing the S/N, is the capability of picking hits that before fell below the threshold. For instance, Fig. 4.17 shows the raw ADC data from an example event (electron, $E_k = 100$ MeV) with the produced true hits superimposed (black boxes), together with the hits produced by the standard hit finder chain (blue circles), i.e. using the current FIR filter, and the hits obtained using the matched filters (green triangles). Both the standard and the matched filter hit finders were run with a threshold of 10 ADC. Notice that the standard hits match well the true ones at the initial part of the event (where we have a track-like object), but they miss most of the hits produced by the EM shower at later times. On the other hand, the hits produced with the matched filter have a better agreement with the true hits even for the more diffuse shower activity.

Notwithstanding that now I get more hits with this combination of matched filter

4.5. USING SIMULATED SAMPLES

1324 and low threshold as a results of the enhancement of the signal peaks relative to the
1325 noise level, it is also true that I pick some spurious hits not related to any real activity
1326 if one lowers the thresholds too much. Therefore, some optimisation of the threshold is
1327 needed. Basically one will need to make a trade-off between precision and sensitivity.

1328 Having this in mind, I tried to compare the produced hits one gets from the standard
1329 hit finder and the ones resulting from applying the matched filter with the true hits.
1330 By running the hit finders on our samples with different values of the threshold one
1331 can understand, for instance, how low one can set the threshold without getting mostly
1332 spurious hits and then evaluate the gains obtained from this.

1333 Because now I am also interested in seeing how the hit sensitivity changes with the
1334 energy, I prepared new isotropic samples with the same types of particles as before
1335 (muons, electrons, protons and neutral pions) but with a flat kinetic energy distribution
1336 ranging from 5 to 100 MeV.

1337 In order to estimate the hit sensitivity, given a certain sample, one needs to recover
1338 the set of true hits to be able to compare these with the ones produced. To do so,
1339 a modification in the procedure I was using to extract the raw waveforms is needed.
1340 For this kind of study I run the detector simulation in two steps, first I produce the
1341 waveforms without noise and extract them in the same format I used for the raw data,
1342 then the noise is added and the noisy waveforms are then written to a file as well.

1343 To have a better comparison between the true hits and the ones produced from
1344 the raw waveforms after applying the two filters, I applied also the FIR filter and the
1345 matched filters to the noiseless waveforms and then I run the hit finder with a minimal
1346 threshold (in this case I used 1 ADC) on these noiseless filtered waveforms. In this way
1347 I generated two sets of true hits, I will refer to them as standard true hits (with the
1348 current/default FIR filter) and matched filter true hits respectively. This allows a more
1349 precise matching between the different groups of hits produced, as it will account for
1350 any delays and distortions introduced by the FIR and the matched filters.

1351 In the case of the raw waveforms (with noise), I run the hit finder on them, with
1352 different values of the threshold, after applying either the FIR or the matched filters. I

CHAPTER 4. MATCHED FILTER APPROACH TO TRIGGER PRIMITIVES

1353 will name them simply standard hits and matched filter hits respectively. Then, I match
 1354 the generated hits to the true hits (the standard hits with the standard true hits and
 1355 the matched filter hits with the matched filter true hits). The matching is performed by
 1356 comparing the channel number and the timestamp of the hits. To count as a match,
 1357 I require that all hits with the same channel number and timestamp have overlapping
 1358 hit windows, i.e. the time windows between their hit end and hit start times need to
 1359 overlap. If more than one hit in one of the groups have hit overlap with the same hit in
 1360 the other group I only count the hit with closer hit peak time value.

1361 The generation of the samples, the procedure to produce the standard hits (with the
 1362 default FIR filter) and matched filter hits and the matching of these with the true hits
 1363 is described in detail in App. ??.

1364 To quantify the performance of the two hit finder approaches, I use a classical method
 1365 from statistical classification known as confusion matrix [111]. This is basically a way of
 1366 sorting the outputs of a binary classifier, considering the true values of the classification
 1367 and the predicted values. It divides the outputs in four categories: true positive (TP,
 1368 both true and predicted values are 1), false negative (FN, true value is 1 but predicted
 1369 is 0), false positive (FP, true value is 0 but predicted is 1) and true negative (TN, both
 1370 true and predicted values are 0)).

1371 The contents of the confusion matrix allow us to compute other derived scores to
 1372 judge the performance of our classifiers. In this study, I will make use of three of these
 1373 metrics, namely the precision or positive predictive value:

$$\text{PPV} = \frac{\text{TP}}{\text{TP} + \text{FP}}, \quad (4.22)$$

1374 the sensitivity or true positive rate:

$$\text{TPR} = \frac{\text{TP}}{\text{TP} + \text{FN}}, \quad (4.23)$$

4.5. USING SIMULATED SAMPLES

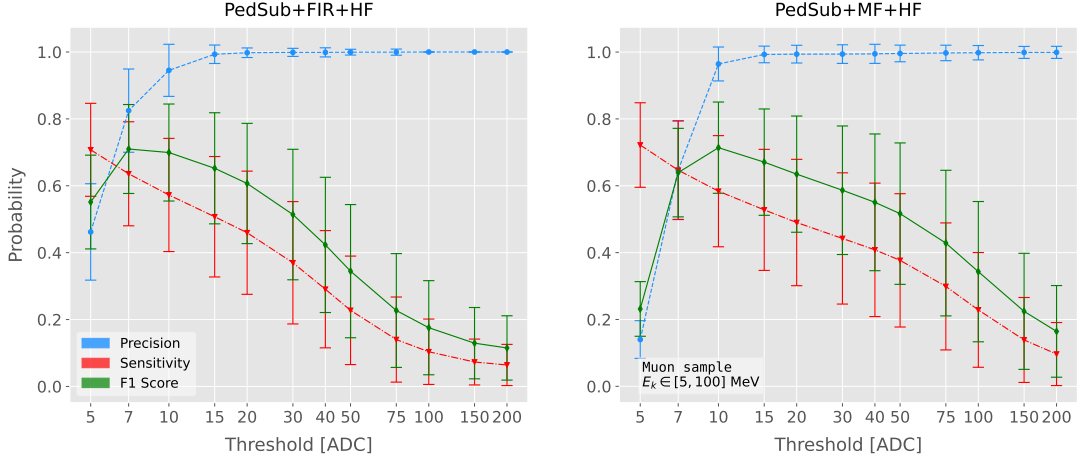


Figure 4.18: Dependence of the precision (blue), sensitivity (red) and F_1 (green) scores on the threshold values used in the hit finder, for the FIR (left panel) and matched filter (right panel) cases. The results were obtained after matching the hits to the true hits in the case of the isotropic muon sample with kinetic energy in the range 5 to 100 MeV, taking only into account the induction plane channels. The points represent the mean value while the error bars indicate one standard deviation around that mean value.

1375 and the F_1 score [112]:

$$F_1 = \frac{2\text{TP}}{2\text{TP} + \text{FP} + \text{FN}}, \quad (4.24)$$

1376 which is the harmonic mean of the precision and the sensitivity.

1377 In our specific case I am not going to make use of the true negative value, as its
1378 definition in this context can be ambiguous because one does not have clear instances in
1379 the classification process. This way, I will only count the number of true positives as the
1380 total amount of hits I can match between true and raw populations, the number of false
1381 negatives will be the number of missing true hits and the false positive the number of
1382 hits which do not match any true hit.

1383 In Fig. 4.18 I show the precision (blue), sensitivity (red) and F_1 (green) scores I
1384 obtained for different values of the threshold used in the hit finder for the case of the
1385 muon sample. Because the matched filters are only applied to induction channels, I only
1386 consider here hits coming from the U and V planes. The panel on the left corresponds
1387 to the scores I got when I ran the hit finder on the FIR filtered waveforms, whereas the
1388 right panel contains the scores for the matched filter case. The points are centered at

CHAPTER 4. MATCHED FILTER APPROACH TO TRIGGER PRIMITIVES

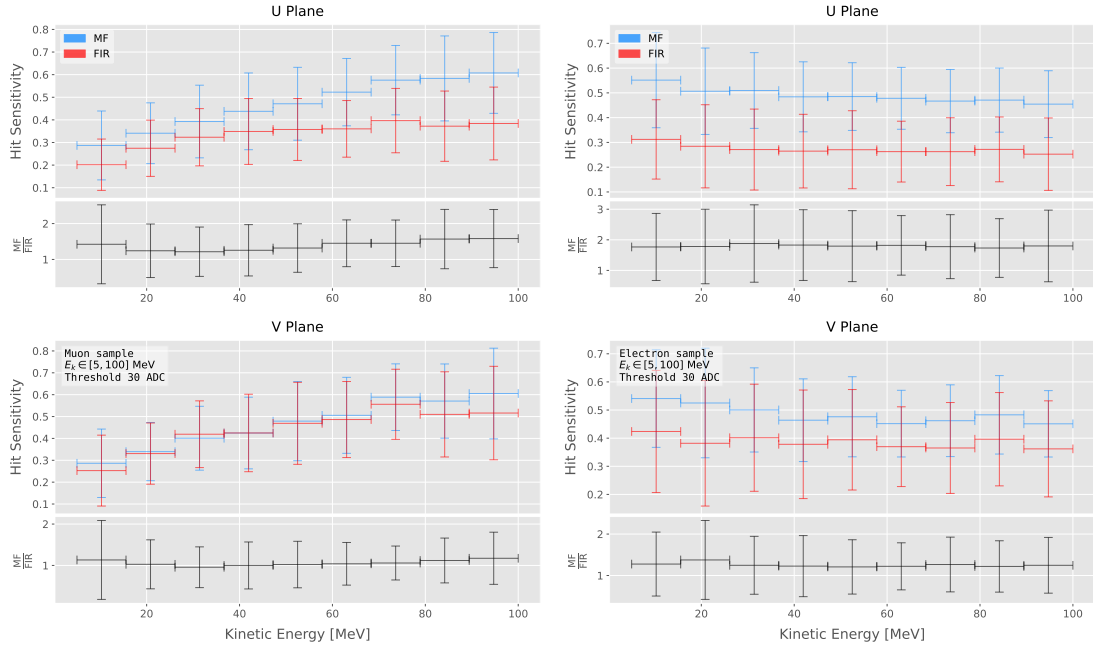


Figure 4.19: Dependence of the averaged hit sensitivity on the kinetic energy of the events for the matched filter (blue) and standard (red) hits, for the case of the muon (left panel) and electron (right panel) samples, separated between U (top plots) and V (bottom plots) induction wire planes. The top subplots contain the hit sensitivities for the two hit finder alternatives, while the bottom subplots show the ratio between the two. The horizontal lines sit at the mean value and represent the size of the energy bins, while the vertical error bars indicate one standard deviation around that mean value.

1389 the threshold value used and represent the mean value obtained for each score using all
 1390 the generated events, while the error bars indicate one standard deviation around the
 1391 mean value.

1392 One can see that the precision for the matched filter case is lower when the thresholds
 1393 are very low, as the noise baseline is slightly amplified, but then rises to high values
 1394 quicker than for the FIR case. The other difference one can spot is that the sensitivity
 1395 in the FIR case starts dropping faster at around the same threshold values where the
 1396 precision stabilizes around 1, while in contrast for the matched filter this rapid decrease
 1397 starts at higher threshold values. A similar scan for the same thresholds was performed
 1398 for the electron sample in the same energy range, yielding similar results.

1399 In Fig. 4.19 I show the averaged hit sensitivity versus the kinetic energy of the
 1400 events, both for the matched filter hits (blue) and the standard hits (red). The left

4.5. USING SIMULATED SAMPLES

1401 panel corresponds to the muon sample, whereas the one on the right corresponds to the
1402 electron sample, both with kinetic energies between 5 and 100 MeV. In each panel the
1403 top plot corresponds to hits in the U plane, while the bottom plot contains the same
1404 information for the V plane. Each plot contains two subplots, the one on the top shows
1405 the hit sensitivity values for the matched filter and standard hits separate, while the
1406 bottom subplot depicts the ratio between the matched filter and standard sensitivities.
1407 The horizontal lines are placed at the mean value obtained in the fit and represent the
1408 width of the E_k bins used, while the vertical error bars indicate one standard deviation
1409 around that mean value. In both cases the threshold used was 30 ADC, as I required
1410 the precision to be higher than 0.99 for both matched filter and standard cases.

1411 One can see that, in general, the improvements are better for the U than for the V
1412 plane. While for the U channels I achieved a mean improvement of 50% and 80% for
1413 muons and electrons respectively, the improvement in the V plane is stalled at 10% and
1414 25%. Nevertheless, if I look at the sensitivities for the matched filter hits in both planes
1415 one can see these have similar mean values for each energy bin, while on the contrary
1416 for the standard hits the sensitivity remains relatively high for the V plane. This way, it
1417 looks there was a less significant gain because the hit sensitivity was already high.

1418 Another interesting observation is the different behaviors for muons and electrons.
1419 While hit sensitivity for muons grows significantly with energy, in the case of electrons
1420 this slightly decreases the higher the kinetic energy of the event is. In any case, when it
1421 comes to the improvement on the sensitivities, this remains almost constant in all cases.

1422 Furthermore, we can look at how the concurrence of hits between the different wire
1423 planes has changed. For any given event, I expect to have a similar number of hits in the
1424 three planes. As the ionisation electrons need to cross the U and V planes prior to reach
1425 the collection plane X they will induce current in those wire planes. A way to check the
1426 concurrence of hits across planes is looking at the relation between the hit sensitivities
1427 for each individual event. One cannot expect the sensitivities to be exactly equal across
1428 planes, but ideally they should be normally distributed around the diagonal.

1429 Fig. 4.20 shows the hit sensitivity in the U (top panels) and V (bottom panels)

CHAPTER 4. MATCHED FILTER APPROACH TO TRIGGER PRIMITIVES

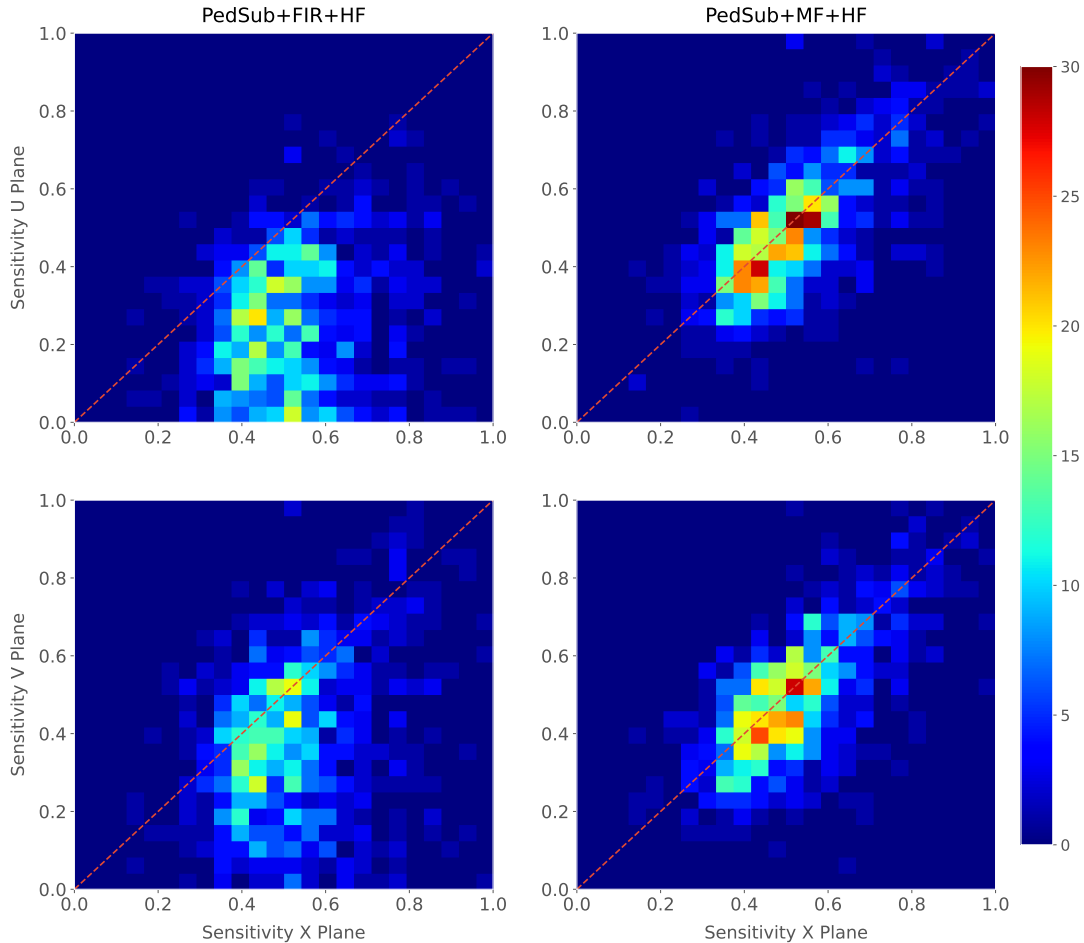


Figure 4.20: Distributions of the hit sensitivity in the U (top panels) and V (bottom panels) planes versus the hit sensitivity in the X plane, both for the standard hits (left panels) and the matched filter hits (right panels), in the case of the electron sample and a threshold of 30 ADC.

planes versus the hit sensitivity in the X plane, for the case of the standard hits (left panels) and the matched filter hits (right panels). All plots were generated for the electron sample and a threshold of 30 ADC. From these one can see a clear trend, when I use the standard hit finder chain the sensitivities in the induction planes are systematically lower than the hit sensitivity in the X plane, i.e. most of the points sit below the diagonal (red dashed line). In contrast, when the matched filters are applied, the majority of the events are distributed around the diagonal. This points out that the concurrence of hits across planes has improved.

To exemplify the improvement I obtained, one can consider the residuals of the hit

4.5. USING SIMULATED SAMPLES

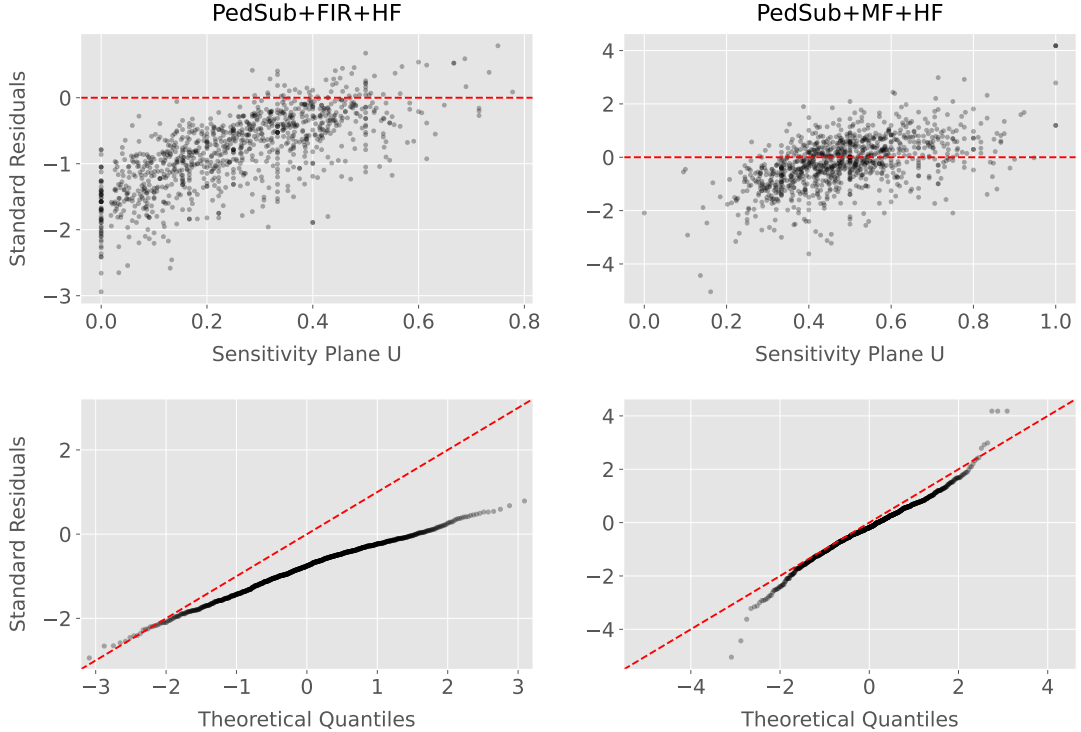


Figure 4.21: Top panels: standard residual plots of the hit sensitivities between the X and U planes. Bottom panels: quantile-quantile plots of the hit sensitivity standard residuals between the X and U planes. In all cases, the left panel corresponds to the standard hits while the right panel represents the matched filter case, all from the electron sample with a 30 ADC threshold.

sensitivities for the X and U planes. Assuming the diagonal hypothesis, i.e. given a dataset of the form (x, y) for any x I take the predicted y value to be equal to the value of x , I can compute the standard residuals for the hit sensitivities in U given the ones for X . In Fig. 4.21 (top panels) I show these standard residuals against the corresponding values of the hit sensitivity in the U plane, for our electron sample with kinetic energy between 5 and 100 MeV. If I compare the scatter points in the case of the standard hits (left panel) and the matched filter hits (right panel), I see that the residuals of the standard hit finder case follow a certain pattern and their mean deviates from 0.

To see clearly if the residuals are normally distributed, in Fig. 4.21 (bottom panels) I plot the corresponding quantile-quantile plot for both the standard (left panel) and matched filter (right panel) standard residuals. One can clearly see that the points for the standard case follow a strongly non-linear pattern, suggesting that the residuals

CHAPTER 4. MATCHED FILTER APPROACH TO TRIGGER PRIMITIVES

1451 do not follow a normal distribution. In contrast, for the matched filter hits the points
1452 conform to a roughly linear path, implying that in this case the normality condition is
1453 fulfilled.

1454 All these results hint at the fact that the concurrence of hits across the wire planes
1455 can be strengthened by applying the matched filters.

1457 DM searches with neutrinos from the Sun

1458 The idea of detecting neutrino signals coming from the Sun’s core to probe DM is not
1459 new. The main focus of these searches has usually been high-energy neutrinos originated
1460 from DM annihilations into heavy particles [113–116], although recent studies have
1461 proposed to look at the low-energy neutrino flux arising from the decay of light mesons
1462 at rest in the Sun [117–120] previously thought undetectable.

1463 In this Chapter I try to demonstrate the capability of DUNE to constrain different
1464 DM scenarios. I used the neutrino fluxes arising from DM annihilations in the core
1465 of the Sun to compute the projected limits that DUNE would be able to set on the
1466 annihilation rates in the Sun and the DM scattering cross sections.

1467 5.1 Gravitational capture of DM by the Sun

1468 The Sun and the centre of the Earth are possible sources of DM annihilations, specially
1469 interesting because of their proximity. Their gravitational attraction ensured the capture
1470 of DM from the local halo through repeated scatterings of DM particles crossing them.
1471 Only neutrinos produced from DM annihilations can escape the dense interior of these
1472 objects. Therefore, neutrino telescopes are the most useful experimental layouts to
1473 pursue DM searches from their cores.

1474 The neutrino flux from DM annihilations inside the Sun depends on the DM capture
1475 rate, which is proportional to the DM scattering cross section, and the annihilation rate,
1476 which is proportional to the velocity-averaged DM annihilation cross-section. The total

CHAPTER 5. DM SEARCHES WITH NEUTRINOS FROM THE SUN

1477 number of DM particles inside the Sun follows the Boltzmann equation [117]:

$$\frac{dN_{DM}}{dt} = C_{\odot} - A_{\odot} N_{DM}^2, \quad (5.1)$$

1478 where C_{\odot} and A_{\odot} are the total Sun DM capture and annihilation rates respectively.
1479 In this expression I neglected the evaporation term, proportional to N_{DM} , which only
1480 contribute for $m_{DM} \lesssim 4$ GeV [121]. As the current threshold of neutrino telescopes
1481 is a few GeV, this region falls below the probed range but can be important in future
1482 low-energy projects.

1483 This equation has an equilibrium solution:

$$N_{DM}^{eq} = \sqrt{\frac{C_{\odot}}{A_{\odot}}}, \quad (5.2)$$

1484 which represents the amount of DM inside the Sun if the capture and annihilation have
1485 reached equilibrium. As the Sun is approximately 4.6 Gyr old, it is usually assumed that
1486 equilibrium has been achieved. Therefore, the anomalous neutrino flux from the Sun
1487 would only depend on the DM scattering cross section, enabling us to set limits on this
1488 quantity. If one does not assume equilibrium, some assumptions on the DM annihilation
1489 cross section are necessary to extract predictions from neutrino signals.

1490 Here, I am going to consider three possible scenarios for the DM interactions: DM
1491 scattering off electrons, spin-dependent (SD) and spin-independent interactions off nuclei.
1492 For the case of these last two, the cross sections will be given in terms of the SD and
1493 SI elastic scattering DM cross section off protons (assuming that DM interactions off
1494 protons and neutrons are identical), σ_p^{SD} and σ_p^{SI} , as [2, 117]:

$$\sigma_i^{\text{SD}} = \left(\frac{\tilde{\mu}_{A_i}}{\tilde{\mu}_p} \right)^2 \frac{4(J_i + 1)}{3J_i} |\langle S_{p,i} \rangle + \langle S_{n,i} \rangle|^2 \sigma_p^{\text{SD}}, \quad (5.3)$$

$$\sigma_i^{\text{SI}} = \left(\frac{\tilde{\mu}_{A_i}}{\tilde{\mu}_p} \right)^2 A_i^2 \sigma_p^{\text{SI}}, \quad (5.4)$$

1495 where $\tilde{\mu}_{A_i}$ is the reduced mass of the DM-nucleus i system, $\tilde{\mu}_p$ is the reduced mass of

5.1. GRAVITATIONAL CAPTURE OF DM BY THE SUN

1496 the DM-proton system, A_i and J_i the mass number and total angular momentum of
 1497 nucleus i and $\langle S_{p,i} \rangle$ and $\langle S_{n,i} \rangle$ the expectation value of the spins of protons and neutrons
 1498 averaged over all nucleons, respectively (see Ref. [122] for a review on spin expectation
 1499 values).

1500 Since the Sun is mainly composed of Hydrogen, the capture of DM from the halo
 1501 is expected to occur mainly through spin-dependent scattering. However, since the
 1502 spin-independent cross section is proportional to the square of the atomic mass, heavy
 1503 elements can contribute to the capture rate (even though they constitute less than 2%
 1504 of the mass of the Sun). Heavy elements can also contribute to the spin-dependent cross
 1505 section if the DM has also momentum-dependent interactions.

1506 DM particles can get captured by the Sun if after repeated scatterings off solar
 1507 targets their final velocity is lower than the escape velocity of the Sun. In the limit of
 1508 weak cross sections, this capture rate can be approximately written as [2]:

$$C_{\odot}^{\text{weak}} = \sum_i \int_0^{R_{\odot}} dr \ 4\pi r^2 \int_0^{\infty} du_{\chi} \frac{\rho_{\chi}}{m_{\chi}} \frac{f_{v_{\odot}}(u_{\chi})}{u_{\chi}} \omega(r) \int_0^{v_e(r)} dv \ R_i^-(\omega \rightarrow v) |F_i(q)|^2, \quad (5.5)$$

1509 where the summation extends over all possible nuclear targets. In this expression, R_{\odot}
 1510 is the radius of the Sun, ρ_{χ} is the local DM density, m_{χ} the mass of the DM particle,
 1511 $f_{v_{\odot}}(u_{\chi})$ the DM velocity distribution seen from the Sun's reference frame, $R_i^-(\omega \rightarrow v)$
 1512 is the differential rate at which a DM particle with velocity v scatters a solar target of
 1513 mass m_i to end up with a velocity ω and $|F_i(q)|$ is the nuclear form factor of target i .

1514 The differential scattering rate takes a rather simple form when considering velocity-
 1515 independent and isotropic cross sections. In that case, this quantity is given by [2, 123]:

$$R_i^-(\omega \rightarrow v) = \frac{2}{\sqrt{\pi}} \frac{\mu_{i,+}^2}{\mu_i} \frac{v}{\omega} n_i(r) \sigma_i \left[\chi(-\alpha_-, \alpha_+) + \chi(-\beta_-, \beta_+) e^{\mu_i(\omega^2 - v^2)/u_i^2(r)} \right], \quad (5.6)$$

1516 where μ_i is the ratio between the DM mass and the mass of target i , $\mu_{i,\pm}$ is defined as:

$$\mu_{i,\pm} \equiv \frac{\mu_i \pm 1}{2}, \quad (5.7)$$

CHAPTER 5. DM SEARCHES WITH NEUTRINOS FROM THE SUN

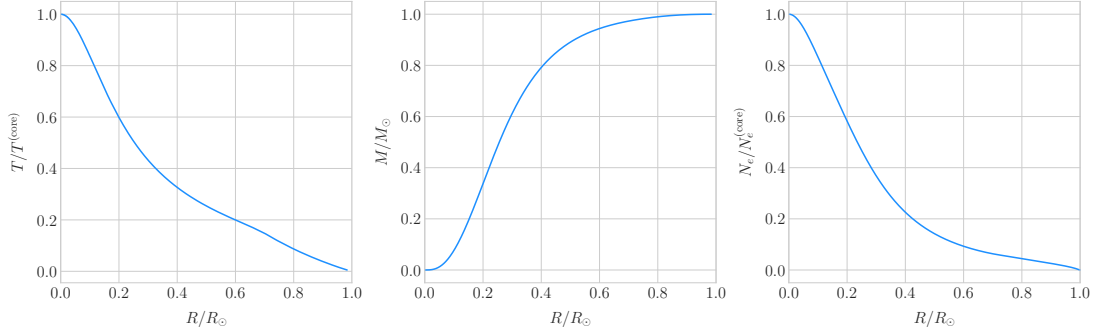


Figure 5.1: Input solar parameters used in our capture rate computation as functions of the Sun’s radius, from left to right: temperature (with respect to the temperature at the core), mass (in solar masses) and electron number density (with respect to the electron density at the core). All quantities shown correspond to the standard solar model BS2005-OP [1].

1517 $n_i(r)$ is the density profile of target i in the solar medium, $u_i(r)$ is the most probable
1518 velocity of target i given by:

$$u_i(r) = \sqrt{\frac{2T_\odot(r)}{m_i}}, \quad (5.8)$$

1519 where $T_\odot(r)$ is the temperature of the Sun, the quantities α_\pm and β_\pm are defined as:

$$\alpha_\pm \equiv \frac{\mu_{i,+}v \pm \mu_{i,-}\omega}{u_i(r)}, \quad (5.9)$$

$$\beta_\pm \equiv \frac{\mu_{i,-}v \pm \mu_{i,+}\omega}{u_i(r)}, \quad (5.10)$$

1520 and the function $\chi(a, b)$ is a Gaussian integral of the form:

$$\chi(a, b) \equiv \int_a^b dx e^{-x^2}. \quad (5.11)$$

1521 Finally, if one assumes the DM halo velocity distribution in the galactic rest frame
1522 to be a Maxwell-Boltzmann distribution, one can write the halo velocity distribution for
1523 an observer moving at the speed of the Sun with respect to the DM rest frame as:

$$f_{v_\odot}(u_\chi) = \sqrt{\frac{3}{2\pi}} \frac{u_\chi}{v_\odot v_d} \left(e^{-\frac{3(u_\chi - v_\odot)^2}{2v_d^2}} - e^{-\frac{3(u_\chi + v_\odot)^2}{2v_d^2}} \right), \quad (5.12)$$

5.1. GRAVITATIONAL CAPTURE OF DM BY THE SUN

1524 where:

$$\omega^2 = u_\chi + v_e(r)^2, \quad (5.13)$$

1525 is the DM velocity squared, v_\odot the relative velocity of the Sun from the DM rest frame
 1526 and $v_d \simeq \sqrt{3/2}v_\odot$ the velocity dispersion.

1527 For the case of strong scattering cross section, Eq. (5.5) ceases to be valid, as it
 1528 escalates indefinitely with the cross section. In that limit, the capture rate saturates to
 1529 the case where the probability of interaction is equal to one, which can be written as:

$$C_\odot^{\text{geom}} = \pi R_\odot^2 \left(\frac{\rho_\chi}{m_\chi} \right) \langle v \rangle \left(1 + \frac{3}{2} \frac{v_e^2(R_\odot)}{v_d^2} \right) \xi(v_\odot, v_d), \quad (5.14)$$

1530 where $v_d = \sqrt{8/3\pi}v_d$ is the mean velocity in the DM rest frame and the factor $\xi(v_\odot, v_d)$
 1531 accounts for the suppression due to the motion of the Sun:

$$\xi(v_\odot, v_d) = \frac{v_d^2 e^{-\frac{3v_\odot^2}{2v_d^2}} + \sqrt{\frac{\pi}{6}} \frac{v_d}{v_\odot} (v_d^2 + 3v_e^2(R_\odot) + 3v_\odot^2) \operatorname{Erf} \left(\sqrt{\frac{3}{2}} \frac{v_\odot}{v_d} \right)}{2v_d^2 + 3v_e^2(R_\odot)}. \quad (5.15)$$

1532 Having these into account, one can write the total capture rate as a combination of
 1533 both contributions, allowing a smooth transition between the two, as:

$$C_\odot = C_\odot^{\text{weak}} \left(1 - e^{C_\odot^{\text{geom}} / C_\odot^{\text{weak}}} \right). \quad (5.16)$$

1534 I computed the capture rate from Eq. (5.16) in the case of interactions with
 1535 electrons. To do so, I used the standard solar model BS2005-OP [1]. Fig. 5.1 shows the
 1536 three parameters from the solar model that are needed for the computation, the solar
 1537 temperature (left panel), mass (central panel) and electron density (right panel) profiles.

1538 For the case of the interactions off nuclei, the computations are more convoluted
 1539 as one needs to add up the contributions of the different most abundant nuclei in
 1540 the Sun. Also, in contrast to the electron scenario where the form factor is trivially
 1541 $|F_e(q)|^2 = 1$, for any nucleus i one would need to consider some appropriate nuclear
 1542 density distribution (either a Gaussian approximation, a Woods-Saxon distribution, etc)

CHAPTER 5. DM SEARCHES WITH NEUTRINOS FROM THE SUN

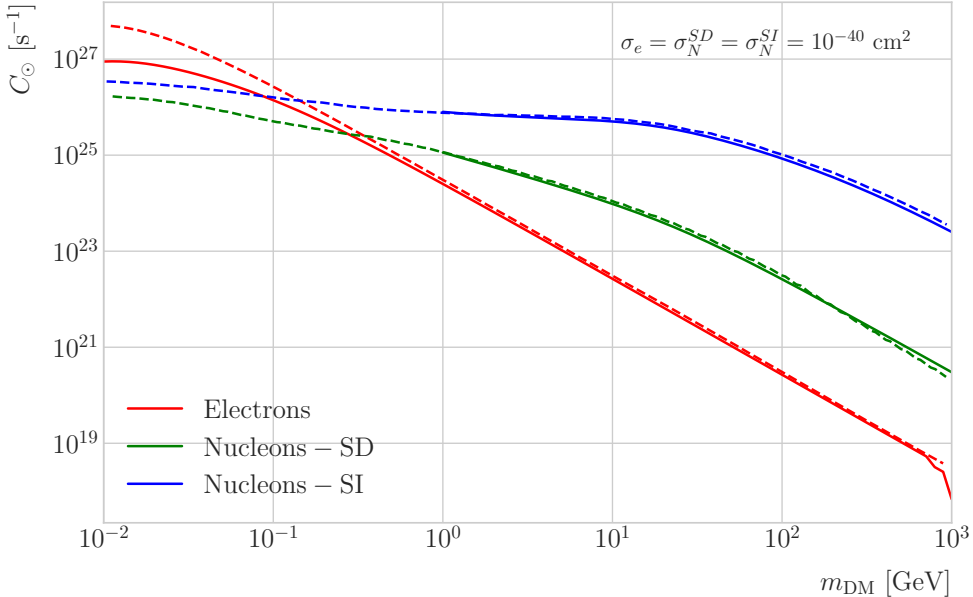


Figure 5.2: Capture rates as a function of the DM mass for the DM-electron interactions (red lines), SD DM-nucleons interactions (green lines) and SI DM-nucleons interactions (blue lines). Solid lines represent the values computed in this work while the dashed lines are the one given in Ref. [2]. All the rates are shown for a choice of scattering cross section of $\sigma_i = 10^{-40} \text{ cm}^2$.

1543 which would complicate the calculations even further.

1544 That is the reason why, at this stage of our study, I decided to take an alternative
 1545 approach to the computation of the DM-nucleus capture rates. I used the **DarkSUSY**
 1546 software, that allows us to compute these quantities performing a full numerical
 1547 integration over the momentum transfer of the form factors. The default standard
 1548 solar model used by **DarkSUSY** is BP2000¹ [124].

1549 In Fig. 5.2 I show the results I obtained for the capture rates, for the case of
 1550 interactions off electrons (red solid line), SD (green solid line) and SI (blue solid line)
 1551 interactions of nucleons. In all cases I used a value of the scattering cross sections of
 1552 $\sigma_i = 10^{-40} \text{ cm}^2$. Note here one of the limitations of the **DarkSUSY** approach, one can
 1553 not extend the computation below $m_{\text{DM}} = 1 \text{ GeV}$. Nevertheless, this is not something
 1554 to worry about in this case, as I will discuss next. As a comparison, I added also the

¹This is what they say in their manual, but I fear it is somewhat outdated. It appears to me this model is relatively old and do not see why they are not using others like [1]. Maybe one can double-check in the code to make sure.

5.1. GRAVITATIONAL CAPTURE OF DM BY THE SUN

values computed in Ref. [2] (same color scheme, dashed lines). One can see there is good agreement between these and the **DarkSUSY** computation of the SD and SI interactions for $m_{\text{DM}} \geq 1$ GeV. In this regime their computations also matches quite well our result for the electron capture rate. However, these start to differ significantly below $m_{\text{DM}} = 1$ GeV, being their estimate up to a factor of 5 bigger than ours for low masses.

Let us comment briefly about the assumption I made before about not including an evaporation term in the Boltzmann equation. If I include this term in the equation (which will be proportional to the number of DM particles) the equilibrium solution takes the form:

$$N_{\text{DM}}^{\text{eq}} = \sqrt{\frac{C_{\odot}}{A_{\odot}}} \frac{1}{\kappa + \frac{1}{2} E_{\odot} \tau_{\text{eq}}}, \quad (5.17)$$

where E_{\odot} is the total evaporation rate, τ_{eq} is the equilibrium time in the absence of evaporation:

$$\tau_{\text{eq}} = \frac{1}{\sqrt{C_{\odot} A_{\odot}}}, \quad (5.18)$$

and κ is defined as:

$$\kappa \equiv \sqrt{1 + \left(\frac{E_{\odot} \tau_{\text{eq}}}{2} \right)^2}. \quad (5.19)$$

Now, it is easy to proof that in case evaporation dominates $\kappa \gg 1$ and therefore:

$$N_{\text{DM}}^{\text{eq}} \simeq \frac{C_{\odot}}{E_{\odot}}. \quad (5.20)$$

In contrast, if evaporation is irrelevant $\kappa \simeq 1$ and one recovers Eq. (5.2).

In this way, one can define the evaporation mass as the mass for which the number of DM particles in equilibrium approaches Eq. (5.20) at 10% level:

$$\left| N_{\text{DM}}^{\text{eq}}(m_{\text{evap}}) - \frac{C_{\odot}(m_{\text{evap}})}{E_{\odot}(m_{\text{evap}})} \right| = 0.1 N_{\text{DM}}^{\text{eq}}(m_{\text{evap}}). \quad (5.21)$$

This can be regarded as the minimum testable mass one can reach using the annihilation products of the DM in the Sun.

It was reported in Ref. [2] that, in the case of both SD and SI DM interactions

CHAPTER 5. DM SEARCHES WITH NEUTRINOS FROM THE SUN

off nuclei, this value ranges from 2 to 4 GeV depending on the specific scattering cross section value, compatible with the usual assumptions in the literature. What is interesting is the case of the electron capture. It was found that, when one applies a cutoff in the velocity distribution of the DM trapped in the Sun slightly below the escape velocity, the evaporation mass for the DM-electron interaction decreases remarkably. For a moderate choice of $v_c(r) = 0.9v_e(r)$ one gets an evaporation mass of around 200 to 600 MeV. This possibility opens a region of the parameter space that could be tested with neutrino detectors.

5.2 Neutrino flux from DM annihilations

When WIMPs annihilate inside the Sun a flux of high-energy neutrinos is expected from heavy quarks, gauge bosons and $\tau^+\tau^-$ final states, which decay before losing energy in the dense solar medium, as they will produce a continuum spectra up to $E_\nu \sim m_\chi$ (in the case of direct annihilation to neutrinos one would have a line at $E_\nu = m_\chi$) [118]. This kind of signal has been extensively studied in the literature, allowing to put strong limits on the SD WIMP-proton cross section for large m_χ . However, the number of high-energy neutrinos per WIMP annihilation is small and the spectrum depends on the unknown final state. Moreover, background rejection is easier for large m_χ but neutrinos with $E_\nu \gtrsim 100$ GeV are significantly attenuated by interactions in the Sun.

Nevertheless, most WIMP annihilation final states eventually produce a low-energy neutrino spectrum. In this case one does not just consider the more massive final states but also annihilations into e^+e^- , $\mu^+\mu^-$ and light quarks [117]. In particular, light mesons would be produced and stopped in the dense medium, thus decaying at rest and producing a monoenergetic neutrino signal. The decay-at-rest of kaons will produce a $E_\nu = 236$ MeV ν_μ while in the case of pions one would have a $E_\nu = 29.8$ MeV ν_μ . In practice only K^+ and π^+ contribute to these signals, as K^- and π^- are usually Coulomb-captured in an atomic orbit and get absorbed by the nucleus. There is also a low-energy neutrino signal coming from muon decays, which are produced in kaon or

5.3. COMPUTING LIMITS FROM SOLAR NEUTRINO FLUXES

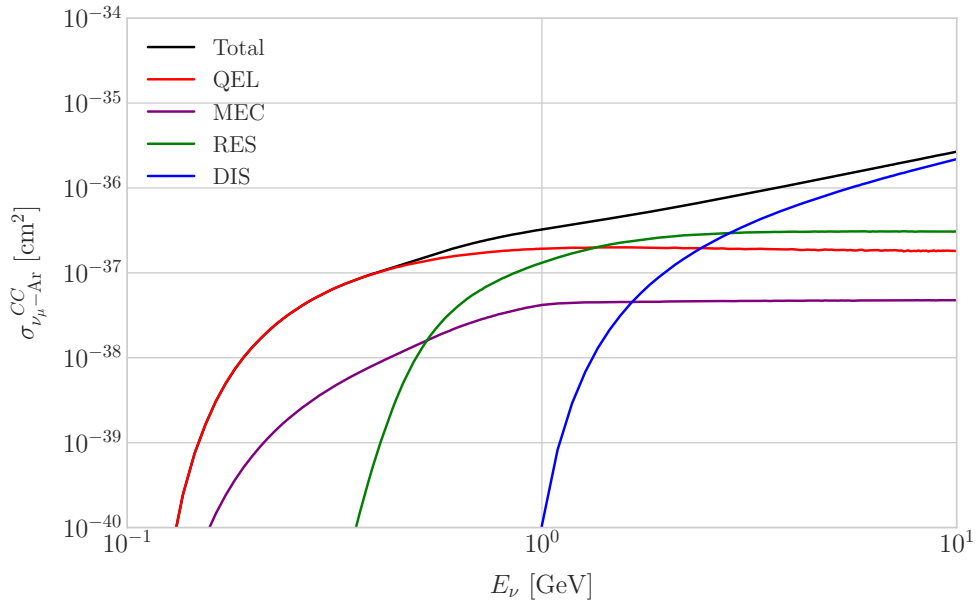


Figure 5.3: *NuWro* computed $\nu_\mu - {}^{40}\text{Ar}$ charged-current scattering cross section as a function of the neutrino energy E_μ . The black line shows to the total cross section, whereas the others correspond to the different contributions (in red quasi-elastic scattering, in green resonant pion exchange, in blue deep inelastic scattering and in purple meson exchange current).

1601 pion decays, leptonic decays of other hadrons and heavy leptons or even directly from
 1602 WIMP annihilations, which can decay at rest and contribute to the previous low-energy
 1603 neutrino flux with a well known spectrum below 52.8 MeV.

1604 These monoenergetic MeV neutrinos were previously considered undetectable but,
 1605 due to the large yield, the known spectra and the modern advances in the detector
 1606 technology, these low-energy neutrino flux can be a good probe of the SD WIMP-proton
 1607 cross-section in standard solar WIMP capture scenario, as it is sensitive to low WIMP
 1608 masses and insensitive to the particular final state. A good place to look for these signals
 1609 are next-generation neutrino experiments such as DUNE.

1610 5.3 Computing limits from solar neutrino fluxes

1611 In order to use the neutrino fluxes from DM annihilations in the Sun, the first thing I
 1612 need to do is to determine the expected number of atmospheric background events, for

CHAPTER 5. DM SEARCHES WITH NEUTRINOS FROM THE SUN

1613 a given exposure, after directionality selection has been applied. I can write this number

1614 as:

$$N_B = \eta_B \int d\Omega \int_{E_{min}}^{E_{max}} dE_\nu \frac{d^2\Phi_{atm}^\mu}{dE_\nu d\Omega} \times \left(A_{eff}^{(\mu)}(E_\nu) T \right), \quad (5.22)$$

1615 where η_B is the background efficiency, E_{min} and E_{max} the minimum and maximum

1616 energies to integrate over, $d^2\Phi_{atm}^\mu/dE_\nu d\Omega$ the differential flux of atmospheric muon

1617 neutrinos, $A_{eff}^{(\mu)}$ is the effective area of DUNE to muon neutrinos and T is the exposure

1618 time. The effective area can be expressed as the product of the neutrino-nucleus scattering

1619 cross section and the number of nuclei in the fiducial volume of the detector. This way

1620 for DUNE I can write:

$$A_{eff}^{(\mu)}(E_\nu) = (6.0 \times 10^{-10} \text{ m}^2) \left(\frac{\sigma_{\nu-\text{Ar}}^{(\mu)}(E_\nu)}{10^{-38} \text{ cm}^2} \right) \left(\frac{M_{target}}{40 \text{ kT}} \right), \quad (5.23)$$

1621 where $\sigma_{\nu-\text{Ar}}^{(\mu)}$ is the $\nu_\mu - {}^{40}\text{Ar}$ charged-current scattering cross section. In Fig. 5.3 I

1622 show the computed value of this cross section as a function of the neutrino energy E_ν ,

1623 in the range of interest both for the atmospheric background and signal events. It was

1624 computed using the NuWro Monte Carlo neutrino event generator [125], including the

1625 charged-current contributions of the quasi-elastic scattering (red line), resonant pion

1626 exchange (green line), deep inelastic scattering (blue line) and meson exchange current

1627 (purple line).

1628 The background rejection will depend on the resolution of the detector and the

1629 selection one applies on the events. A geometry argument can be used to estimate

1630 the maximum background rejection one can achieve in this case, considering one can

1631 efficiently discriminate all events coming from a direction different from that of the

1632 Sun. In that case, the optimal background efficiency will simply be the relative angular

1633 coverage of the Sun. Taking the angular diameter of the Sun as seen from the Earth to

1634 be 0.5° , I have:

$$\eta_B^{(opt)} \approx \frac{\pi \left(\frac{0.5}{2} \right)^2}{360 \times 180} \simeq 3.03 \times 10^{-6}. \quad (5.24)$$

1635 This value will give a very optimistic estimate of the number of background events.

5.3. COMPUTING LIMITS FROM SOLAR NEUTRINO FLUXES

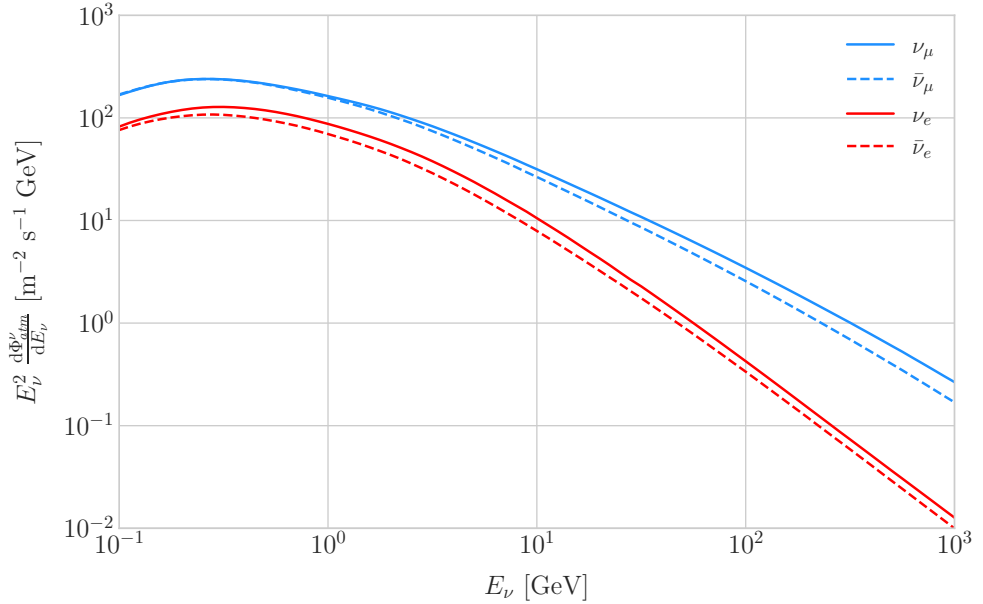


Figure 5.4: Expected atmospheric neutrino flux as a function of the neutrino energy E_ν at Homestake at solar minimum, taken from Ref. [3]. The blue solid (dashed) line correspond to muon neutrinos (antineutrinos) and the red solid (dashed) line correspond to electron neutrinos (antineutrinos).

1636 However, it can be regarded as an lower limit, as it represents the best case scenario.

1637 In Fig. 5.4 I show the fluxes of atmospheric neutrinos at the Homestake mine during
 1638 solar minimum, taken from Ref. [3]. The values are averaged over the two angular
 1639 directions. In blue I have the flux of muon neutrinos while in red I indicate the flux
 1640 of electron neutrinos. Additionally, the dashed lines correspond to both antineutrino
 1641 species.

1642 Using these values for the muon neutrino and the corresponding total CC cross
 1643 section, one can compute the number of expected background events by integrating over
 1644 the given energy range (as in this case the angular integral is trivial). As for the energy
 1645 range to integrate over, I choose the range for DUNE specified in [85], $E_{min} = 10^{-1}$ GeV
 1646 and $E_{max} = 10$ GeV. Taking all these into account, I found the number of background
 1647 events to be:

$$N_B \simeq \eta_B \times (3.827 \times 10^4) \times \left(\frac{\text{exposure}}{400 \text{ kT yr}} \right). \quad (5.25)$$

1648 In order to estimate the sensitivity of DUNE to this kind signal, one can consider a

CHAPTER 5. DM SEARCHES WITH NEUTRINOS FROM THE SUN

1649 hypothetical data set where the number of observed neutrinos is taken to be the expected
 1650 number of background events rounded to the nearest integer, $N_{obs} = \text{round}(N_B)$ [126].
 1651 Now, if I assume that the number of signal and background events seen by DUNE are
 1652 given by Poisson distributions with means equal to the expected number of signal and
 1653 background events, N_S and N_B , one can denote by N_S^{90} to the number of expected
 1654 signal events such that the probability of having an experimental run with a number of
 1655 events greater than N_{obs} is 90%. This number can be obtained as the numerical solution
 1656 to the equation:

$$1 - \frac{\Gamma(N_{obs} + 1, N_S^{90} + N_B)}{N_{obs}!} = 0.9, \quad (5.26)$$

1657 where $\Gamma(x, y)$ is the upper incomplete gamma function.

1658 The number of signal events is related to the neutrino flux from DM annihilations in
 1659 a similar way as the background events to the atmospheric neutrino flux. In this case I
 1660 have:

$$N_S = \eta_S \Gamma_A^{eq} \int_{z_{min}}^{z_{max}} dz \frac{dN_\nu}{dAdN_A dz} \times \left(A_{eff}^\mu(z) T \right), \quad (5.27)$$

1661 where η_S is the signal efficiency, Γ_A^{eq} is the total annihilation rate of DM particles at
 1662 equilibrium, $\Gamma_A^{eq} = A_\odot (N_{DM}^{eq})^2$, z_{min} and z_{max} the minimum and maximum relative
 1663 energies to integrate over (in such a way that $z_{min,max} \leq E_{min,max}/m_{DM}$ for each m_{DM})
 1664 and $dN_\nu/dAdN_A dz$ the muon neutrino flux per DM annihilation in the Sun.

1665 Knowing N_S^{90} one can use the relation in Eq. (5.27) to obtain $\Gamma_A^{eq,90}$ for different
 1666 values of the DM mass. From there I can directly translate those values into the
 1667 upper limits for DUNE on the DM scattering cross sections, for a given exposure. The
 1668 relation between the annihilation rate and the DM-nucleon cross section comes from the
 1669 equilibrium condition through the solar DM capture rate. The details of the evolution
 1670 of the number of DM particles inside the Sun and the computation of the capture rates
 1671 are discussed in App. 5.1.

5.4. EXAMPLE: KALUZA-KLEIN DARK MATTER

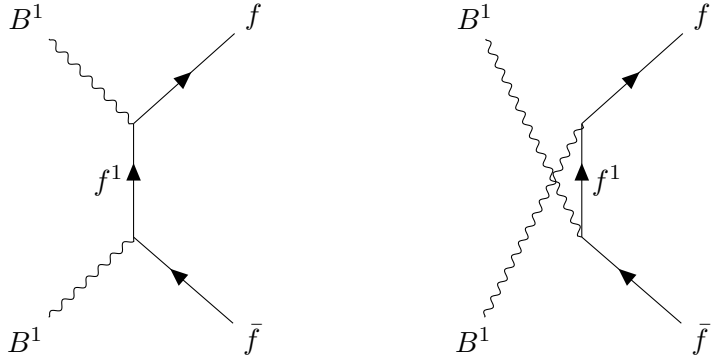


Figure 5.5: Feynman diagrams for $B^1 B^1$ annihilation into SM fermions.

1672 5.4 Example: Kaluza-Klein Dark Matter

1673 Even though there are plenty of BSM theories which provide viable dark matter
1674 candidates, Kaluza-Klein type of models [127, 128] within the universal extra dimensions
1675 (UED) paradigm naturally predict the existence of a massive, stable particle that can
1676 play the role of the dark matter. In the UED scenario all the SM fields can propagate
1677 in one or more compact extra dimensions [129], as opposed to the idea of brane worlds
1678 [130, 131], where just gravity can propagate in the bulk while SM particles live at fixed
1679 points.

1680 Furthermore, in UED there is no violation of the translational invariance along the
1681 extra dimensions, thus leading to degenerate KK modes masses and also the conservation
1682 of the KK number in the effective four dimensional theory. At loop level, radiative
1683 corrections and boundary terms shift the masses of the KK modes and break KK
1684 number conservation into a KK parity. As a result, this theory only contains interactions
1685 between an even number of odd KK modes and therefore the lightest among the first KK
1686 excitations will be stable. This particle is usually denoted as the lightest Kaluza-Klein
1687 particle (LKP) and its mass is proportional to $1/R$, being R the size of the extra
1688 dimension.

1689 A viable DM candidate needs to be electrically neutral and non-baryonic, therefore
1690 good candidates among the first Kaluza-Klein excitations would be the KK neutral

CHAPTER 5. DM SEARCHES WITH NEUTRINOS FROM THE SUN

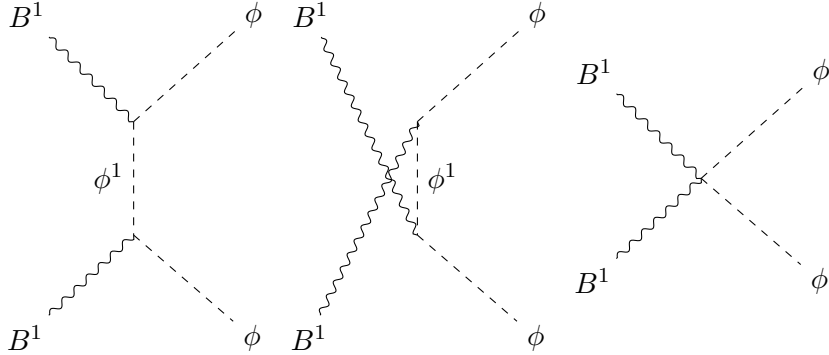


Figure 5.6: Feynman diagrams for B^1B^1 annihilation into a Higgs boson pair.

1691 gauge bosons and the KK neutrinos [132]. Another possible candidate is the first KK
 1692 excitation of the graviton, which receives negligible radiative contributions and therefore
 1693 has a mass almost equal to $1/R$, but it has been shown that the lightest eigenstate from
 1694 the mixing of the gauge mass states (B^1, W_3^1) would be lighter, as B^1 and W_3^1 receive
 1695 negative radiative corrections [133]. It is also understood that, when these corrections
 1696 become sizeable, the eigenstates become approximately pure B^1 and W_3^1 states as the
 1697 Weinberg mixing angle grows small with the KK number [133]. In that case, the LKP
 1698 can be well-approximated as being entirely B^1 .

1699 I need to compute the neutrino flux produced by the annihilations of the LKP in
 1700 the core of the Sun, taking into account their propagation in the solar medium, as
 1701 well as neutrino oscillations. To this end I used `WimpSim` [134, 135] to generate one
 1702 million annihilation events in the Sun over a time span of four years and propagate
 1703 them to the DUNE FD location ($44^\circ 20' \text{ N}, 103^\circ 45' \text{ W}$), for different values of M_{LKP} .
 1704 In Fig. 5.7 I show the obtained muon neutrino spectra arriving to the detector from
 1705 LKP annihilations in the Sun, per unit area and per annihilation, plotted in relative
 1706 energy units for different values of the mass. As one could expect the spectra get
 1707 steeper the higher is the mass, due to the absorption of high-energy neutrinos in the
 1708 solar medium. Also, one can see the peak at $z = 1$ due to the direct annihilation into
 1709 neutrinos $\chi\chi \rightarrow \nu\bar{\nu}$.

1710 Now, one can estimate the sensitivity of DUNE to this particular model by using

5.4. EXAMPLE: KALUZA-KLEIN DARK MATTER

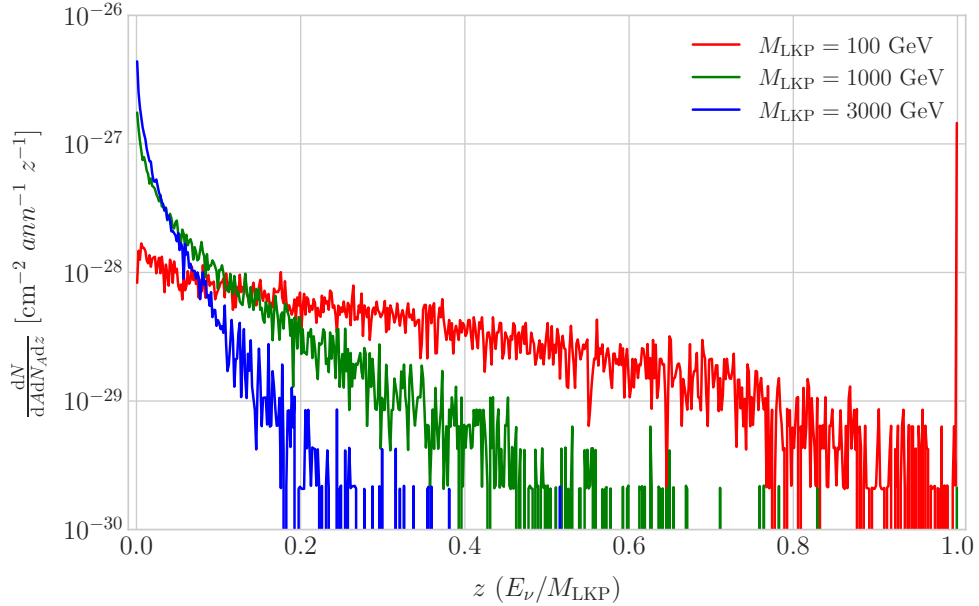


Figure 5.7: Computed spectra of muon neutrinos at the DUNE FD site from B^1 annihilations in the Sun for three different values of M_{LKP} , plotted in relative energy units for legibility.

the methods I previously discussed. To begin with, I will use the optimistic estimation of the background efficiency in Eq. (5.24) to get our upper bound. Using it, one can directly compute the number of expected background events to be $N_B = 0.1101$ for an exposure of 400 kT yr. Then, Eq. (5.26) give us a value of $N_S^{90} = 2.20$ for the 90% exclusion number of expected signal events. By using the NuWro generated cross sections and the computed neutrino fluxes from B^1 annihilations in the Sun I can estimate the limits on the SD and SI DM-nucleus cross section using the relation in Eq. (5.2) and the capture rates I computed with DarkSUSY.

In Fig. 5.8 I show the projected sensitive for DUNE on the spin-dependent B^1 -proton scattering cross section versus the mass of the DM particle, for a exposure of 400 kT yr (green dots). I also include the previous results from IceCube [4] (blue line) and Antares [5] (red line). The shaded area represents the disfavoured region from combined searches for UED by ATLAS and CMS [6].

From the experimental point of view, this estimation lacked a detailed simulation of the detector response and thus this must be consider as a mere optimistic sensitivity

CHAPTER 5. DM SEARCHES WITH NEUTRINOS FROM THE SUN

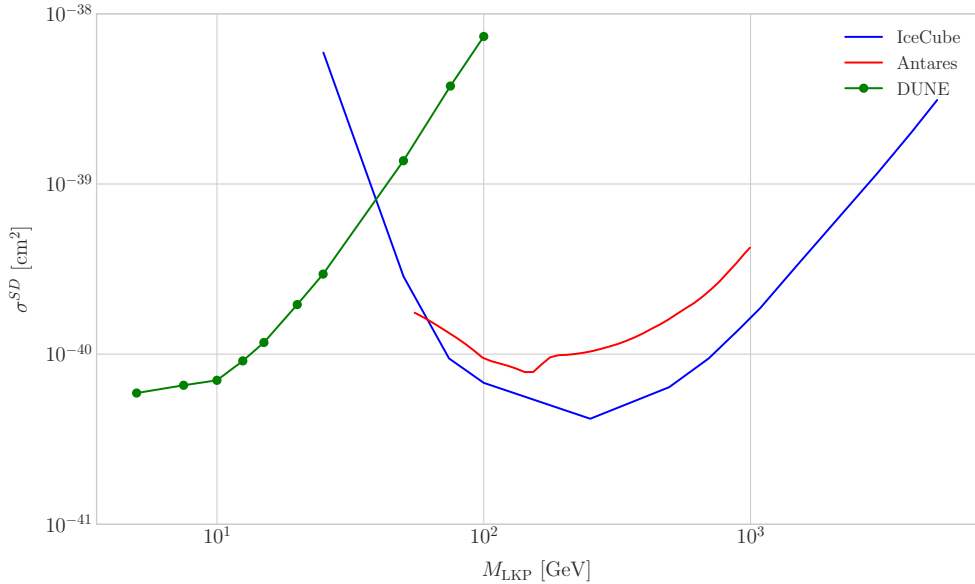


Figure 5.8: Projected 90% confidence level upper limit for DUNE (400 kT yr) on the spin-dependent B^1 -proton scattering cross section as a function of M_{LKP} (green dots). I also show the previous limits from IceCube [4] (blue line) and Antares [5] (red line) on the LKP cross section. The shaded area represents the disfavoured region (at 95% confidence level) on the mass of the LKP from LHC data [6].

computation. However, it shows the potential of DUNE to constrain this kind of exotic scenarios, showing the region where it will be in a position to compete with other neutrino telescopes. A more detailed analysis is needed if I am to make a realistic estimation. Even though the region of the parameter space where DUNE would be sensitive to this particular model is quite constrained by collider searches [6] and other rare decay measurements [136, 137], it still constitutes an alternative indirect probe.

5.5 High energy DM neutrino signals

To have better estimates on the capability of the DUNE FD to constrain the parameter space of DM using solar neutrino fluxes, I need to start accounting for the detector resolution effects and the topologies of the different signatures. As a starting point, I will focus on specific annihilation channels. For the case of DUNE, the relevant ones are mainly the hard channels $\tau^+\tau^-$ and $\nu\bar{\nu}$ and the soft channel $b\bar{b}$. These are the open annihilation channels for relatively low mass WIMPs that will actually give neutrino

5.5. HIGH ENERGY DM NEUTRINO SIGNALS

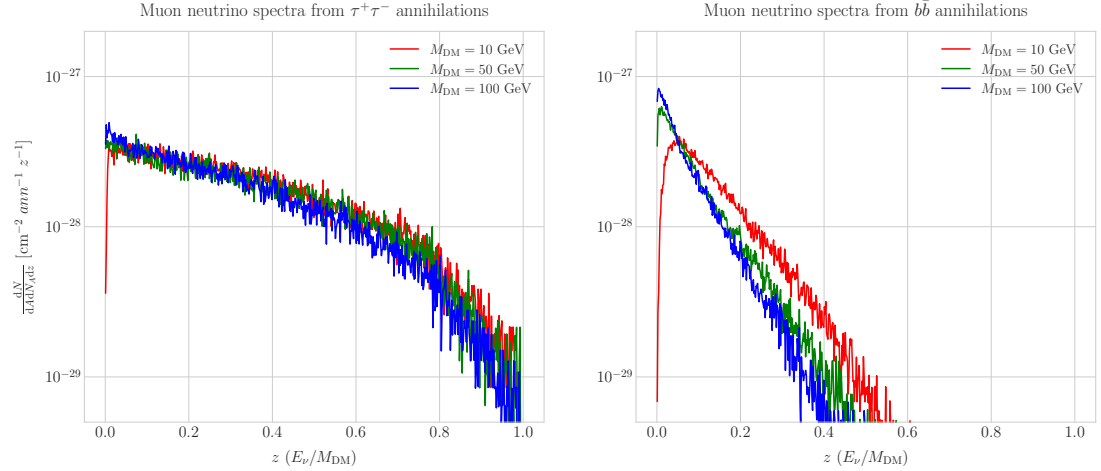


Figure 5.9: Computed spectra of muon neutrinos at the DUNE FD site from $\tau^+\tau^-$ (left panel) and $b\bar{b}$ (right panel) annihilations in the Sun for the DM masses $m_{\text{DM}} = 10 \text{ GeV}$ (red line), 50 GeV (green line) and 100 GeV (blue line), plotted in relative energy units.

1739 fluxes. Other channels, like W^+W^- and ZZ , are open for more massive WIMPs, but
 1740 those will produce usually a higher energy neutrino flux that will be out of reach for
 1741 DUNE (usually the maximum neutrino energy is taken to be $E_{\max} = 10 \text{ GeV}$).

1742 In Fig. 5.9 I show the `WimpSim` [134, 135] generated muon neutrino spectra at the
 1743 DUNE FD location ($44^\circ 20' \text{ N}, 103^\circ 45' \text{ W}$) from $\tau^+\tau^-$ (left panel) and $b\bar{b}$ (right panel)
 1744 annihilations in the core of the Sun, for different DM masses. Here, one can clearly see
 1745 the meaning of the previous distinction between hard and soft channels. For the same
 1746 DM mass value, the muon neutrino spectrum from the $\tau^+\tau^-$ channel is more flat and
 1747 reaches higher energies than the one from the $b\bar{b}$ channel, which drops faster.

1748 In this case, I prepared two sets of files, one for $\tau^+\tau^-$ and the other for $b\bar{b}$, for DM
 1749 masses in the range from 5 to 100 GeV (actually for $b\bar{b}$ the first mass point I took is
 1750 7.5 GeV , as a WIMP with $m_{\text{DM}} = 5 \text{ GeV}$ can not kinematically self annihilate into $b\bar{b}$).
 1751 Then, I prepared the `WimpSim` output fluxes in a specific way to use them as inputs to
 1752 `NuWro`, which simulates the neutrino interaction with the argon.

1753 Because `WimpSim` outputs an event list together with the fluxes, I can use the former
 1754 to generate the events. The direction of these is given in terms of the azimuth and
 1755 altitude angles viewed from the specified location, so first I need to convert these into the

CHAPTER 5. DM SEARCHES WITH NEUTRINOS FROM THE SUN

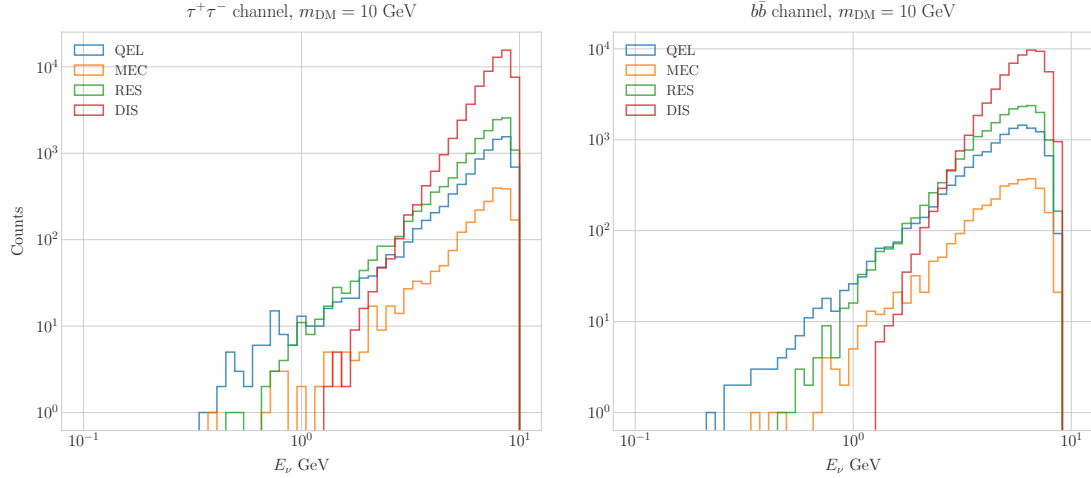


Figure 5.10: Distribution of the muon neutrino energies from the $\tau^+\tau^-$ (left panel) and $b\bar{b}$ (right panel) annihilation channels, for $m_{DM} = 10$ GeV, separated by CC interaction type: QEL (blue), MEC (orange), RES (green) and DIS (red).

1756 DUNE FD coordinates. Once I have done it, each event can be processed with `NuWro`.
 1757 To increase the number of samples and optimise the computation time, I generate 100
 1758 interactions (i.e. `NuWro` events) for each `WimpSim` event². I restrict the event generation
 1759 to charged current interactions, but I allow all the different contributions to the CC
 1760 cross section, i.e. quasielastic scattering (QEL), meson exchange current process (MEC),
 1761 resonant pion production (RES) and deep inelastic scattering (DIS). I just take into
 1762 account the CC contribution because I am only interested in final states with charged
 1763 leptons, as we have better chances of reconstructing the kinematics of CC events.

1764 For the atmospheric fluxes I follow a similar procedure, only that this time I do not
 1765 have a set of events but the fluxes binned in azimuth and altitude angles. This way, I
 1766 transform these to DUNE coordinates and process the fluxes for each bin separated with
 1767 `NuWro`.

1768 At this point, I have two sets of events with different energies and final states.
 1769 In Fig. 5.10 one can see the distribution of the muon neutrino energies for the case
 1770 $m_{DM} = 10$ GeV, both for the $\tau^+\tau^-$ (left panel) and $b\bar{b}$ (right panel) channels, separated

²This also solves a problem related with the generation of the neutrino interactions in `NuWro`, as if you only produce one event each time you launch `NuWro` it will always produce an interaction of the dominant interaction type for that particular energy.

5.5. HIGH ENERGY DM NEUTRINO SIGNALS

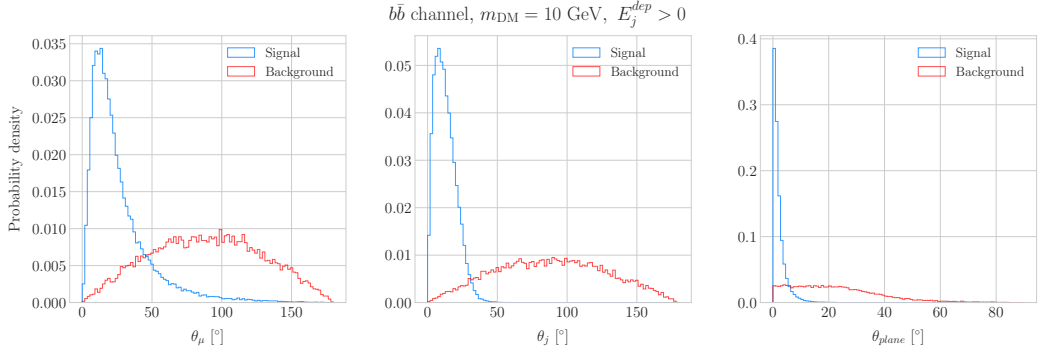


Figure 5.11: Distributions of θ_μ (left panel), θ_j (central panel) and θ_{plane} (right panel) for the $b\bar{b}$ sample with $m_{\text{DM}} = 10$ GeV (blue) and the atmospheric background (red).

by interaction. One can clearly see that there are different energy regimes where the primary interaction type is different. This leads to a plurality of event topologies, therefore making it difficult to implement a general approach to the selection of events in detriment of the background. As a way to proceed, I decided to split our samples, based on the different interaction modes and contents of the final state, into a CC DIS sample and a single proton CC QEL sample.

5.5.1 DIS events

To begin with, I consider the high energy part of the spectrum. In this region DIS events dominate, i.e. interactions of the form $\nu_\mu + q_d(\bar{q}_u) \rightarrow \mu^- + q_u(\bar{q}_d)$. Therefore, our final estates will contain a muon and a hadronic jet from the fragmentation of the outgoing quark. As all these events have $E_\nu \gtrsim 1$ GeV the momentum transfer to the remnant nucleus is negligible, for this reason the neutrino energy can be effectively reconstructed just taking into account the momenta of the muon and the jet. This technique was successfully used in Ref. [138] to select monoenergetic DM solar neutrino events from $\nu\bar{\nu}$ annihilation channels.

Using momentum conservation one sees that the plane generated by the momenta of the muon and the jet needs to also contain the momentum of the neutrino. As we are interested in neutrinos coming from the Sun, the momentum of the neutrino can be regarded as known beforehand. This will allow us to define the angle of the outgoing

CHAPTER 5. DM SEARCHES WITH NEUTRINOS FROM THE SUN

1790 muon and jet with respect to the incoming neutrino. Moreover, one can also use that
 1791 information to reject poorly reconstructed jets, checking for deviations of these from the
 1792 momentum conservation plane.

1793 To account for the limited angular resolution of the detector, I smeared the momenta
 1794 of the muons and hadrons. In a liquid argon TPC muons are expected to be tracked with
 1795 high precision, therefore I take the associated angular resolution to be 1° . In the case of
 1796 jets, it is expected that for the hadrons dominating the cascade a detector like DUNE
 1797 has an angular resolution between 1° to 5° [85], so I take the latter, more conservative,
 1798 estimate.

1799 As a first selection step, I will just take into account particles with kinetic energies
 1800 above the detection threshold of DUNE. For muons and photons the specified threshold
 1801 energy is 30 MeV, for charged pions 100 MeV and for other hadrons 50 MeV [85]. This
 1802 way, if the outgoing muon in a certain event has an energy lower than the required
 1803 threshold I will drop such event. For the case of hadrons and photons, I will only require
 1804 to have at least one particle above the energy threshold, so then one can compute the
 1805 jet momentum using the (smeared) momenta of the N particles above threshold as:

$$\vec{p}_j = \sum_{i=1}^N \vec{p}_i. \quad (5.28)$$

1806 Additionally, I will also define an estimation of the deposited hadronic energy as:

$$E_j^{dep} = m_{^{39}\text{Ar}} - m_{^{40}\text{Ar}} + \sum_{i=1}^N \sqrt{|\vec{p}_i|^2 + m_i^2}. \quad (5.29)$$

1807 This quantity is useful to select events with enough hadronic visible energy in the
 1808 detector. For events where most of the hadronic energy is scattered across plenty of
 1809 hadrons with individual energies below the detection threshold, this estimation will
 1810 give $E_j^{dep} \leq 0$. In these cases it could be expected that the jet momentum is poorly
 1811 reconstructed, and therefore I require events to pass the cut $E_j^{dep} > 0$.

1812 For the events I can compute the angles for the muon and jet with respect to the

5.5. HIGH ENERGY DM NEUTRINO SIGNALS

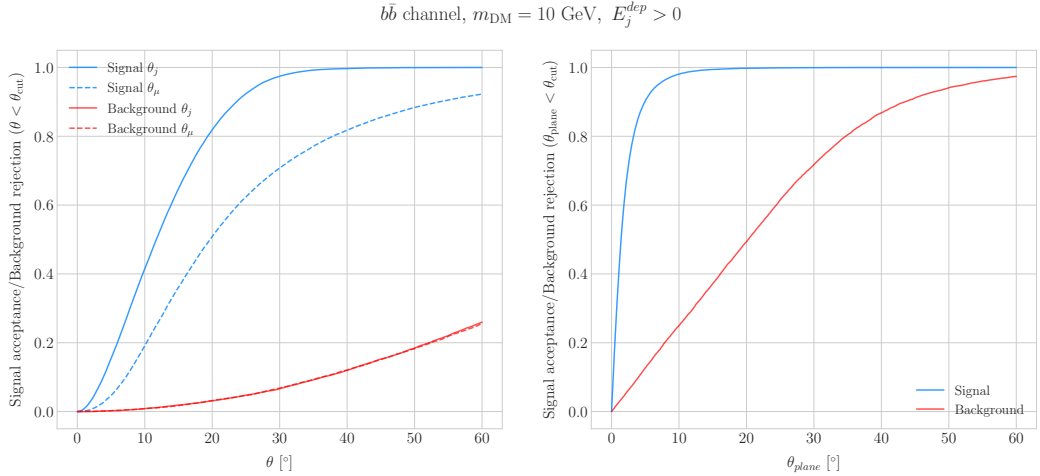


Figure 5.12: Left panel: signal efficiencies (blue lines) and background rejections (red lines) for events passing the cuts $\theta < \theta_{cut}$ for the jet (solid lines) and muon (dashed lines) angles. Right panel: signal efficiency (blue line) and background rejection (red line) for events passing the cut $\theta_{plane} < \theta_{cut}$ for the momentum conservation plane deviation.

1813 incoming neutrino as:

$$\cos \theta_\mu = \hat{p}_\nu \cdot \hat{p}_\mu, \quad (5.30)$$

$$\cos \theta_j = \hat{p}_\nu \cdot \hat{p}_j, \quad (5.31)$$

1814 and the deviation from the momentum conservation plane as:

$$\sin \theta_{plane} = \left| \frac{\hat{p}_\mu \times \hat{p}_\nu}{|\hat{p}_\mu \times \hat{p}_\nu|} \cdot \hat{p}_j \right|. \quad (5.32)$$

1815 In Fig. 5.11 I show some distributions of these quantities for the case of the $b\bar{b}$ sample
 1816 with $m_{DM} = 10$ GeV (blue histograms) and for the atmospheric backgrounds (red).
 1817 In order to select the atmospheric events I followed the same criteria as for the signal
 1818 events. However, because in the signal case I used the true direction of the neutrino
 1819 as input, as it should be that of the Sun at that time and therefore known, in the
 1820 atmospheric case I used a set of solar positions as our ansatz for the neutrino direction.
 1821 From the distributions, one can see that the muon and the jet for the signal events are
 1822 predominantly forward and also that the deviations from the momentum conservation

CHAPTER 5. DM SEARCHES WITH NEUTRINOS FROM THE SUN

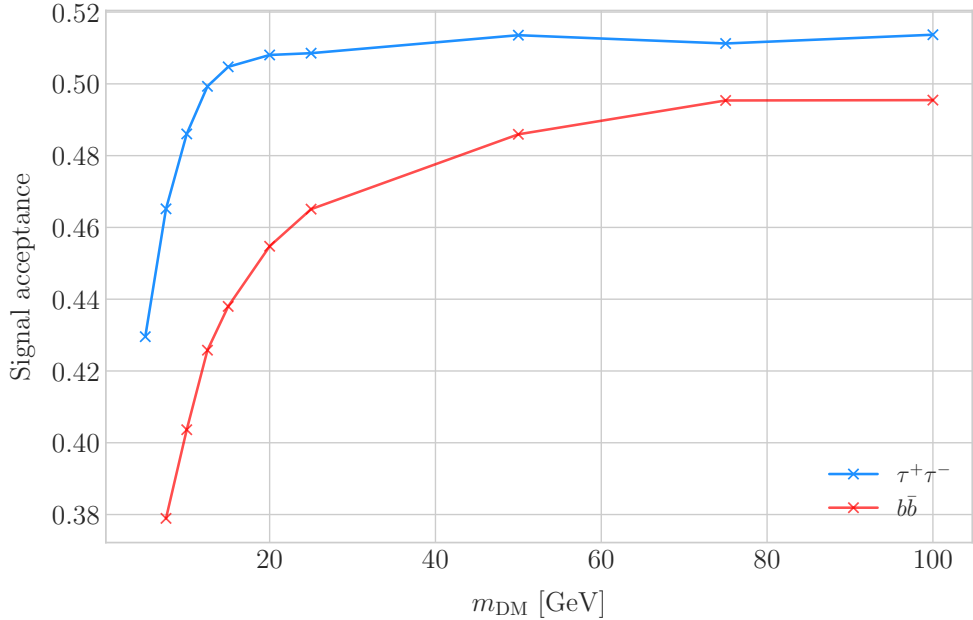


Figure 5.13: Signal efficiencies for the $\tau^+\tau^-$ (blue line) and $b\bar{b}$ (red line) DIS samples as functions of the DM mass, m_{DM} , obtained by applying the optimal angular cuts $\theta_\mu < 27^\circ$, $4^\circ < \theta_j < 26^\circ$ and $\theta_{\text{plane}} < 3.5^\circ$.

1823 plane are peaked at zero, as one should expect.

1824 Now, I can start applying cuts to maximise our signal selection efficiency while at
 1825 the same time I try to minimise the amount of atmospheric background events passing
 1826 the selection. To this end, I will need to find some lower and upper cuts for θ_j and
 1827 θ_μ and an upper bound for θ_{plane} . In Fig. 5.12 I show how upper bound cuts in the
 1828 different angular variables affect the signal efficiency (blue lines) and the background
 1829 rejection (red lines). Notice that the signal efficiency behaves in a quite different way
 1830 when I apply cuts in the jet and the muon angles. On the contrary, the cuts on both
 1831 variables have a similar effect on the background rejection.

1832 In order to obtain the optimal set of cuts, I perform a multidimensional scan. I
 1833 do this separately for the $\tau^+\tau^-$ and the $b\bar{b}$ samples. For each case, I scan the possible
 1834 cuts for each mass point and then I take the mean value of the signal efficiency for
 1835 each configuration, to get the mean efficiency for each set of cuts. I do a similar scan
 1836 for the atmospheric sample independently. Then, I take the sets of cuts such that
 1837 the background rejection achieved is greater than 99.8% and search for the one which

5.5. HIGH ENERGY DM NEUTRINO SIGNALS

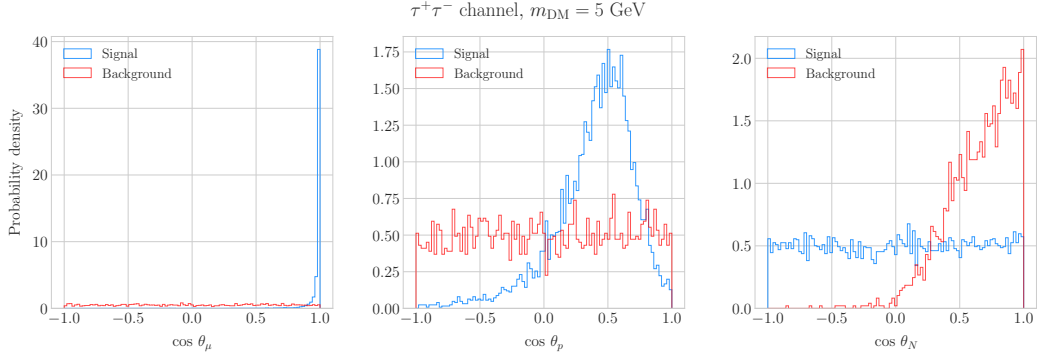


Figure 5.14: Distributions of $\cos \theta_\mu$ (left panel), $\cos \theta_p$ (central panel) and $\cos \theta_N$ (right panel) for the $\tau^+\tau^-$ QEL sample with $m_{\text{DM}} = 5 \text{ GeV}$ (blue) and the atmospheric background (red).

maximises the $\tau^+\tau^-$ and $b\bar{b}$ sample mean efficiencies. I found that with the cuts $\theta_\mu < 27^\circ$, $4^\circ < \theta_j < 26^\circ$ and $\theta_{\text{plane}} < 3.5^\circ$ I get a background rejection of 99.80% while achieving a 49.40% and 44.92% mean signal efficiencies for the $\tau^+\tau^-$ and $b\bar{b}$ signals respectively.

In Fig. 5.13 I show the signal efficiencies as a function of the DM mass for the $\tau^+\tau^-$ (blue line) and the $b\bar{b}$ (red line) DIS events, after applying the cuts discussed above, as well as the energy threshold and hadronic visible energy selections. One can see that the efficiency grows with the mass, as annihilations of more massive DM particles will produce a neutrino spectrum centered at higher energies, where DIS events dominate. Notice also that the efficiency is higher for the $\tau^+\tau^-$ case at every mass point, as in general this channel produces neutrinos at higher energies than the corresponding $b\bar{b}$ channel.

5.5.2 Single proton QEL events

Now, one can try to explore the low energy tail of the neutrino energy distributions. This regime is dominated by the QEL interactions, i.e. events of the type $\nu_\mu + n \rightarrow \mu^- + p$. In this case, as the typical energies are $E_\nu \lesssim 1 \text{ GeV}$, the momentum transfer to the remnant nucleus is sizeable. Therefore, I can not make the approximation I did before and assume that the momentum of the muon and the proton will give an adequate estimation of the reconstructed neutrino energy.

CHAPTER 5. DM SEARCHES WITH NEUTRINOS FROM THE SUN

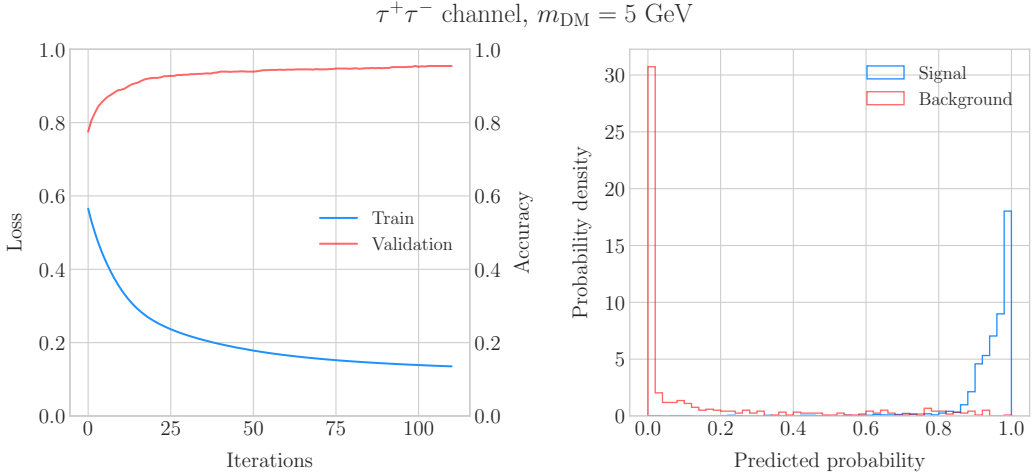


Figure 5.15: Left panel: value of the loss function for the training sample (blue line) and accuracy for the validation sample (red line) versus the number of iterations for the MLP classifier training. Right panel: distributions of the predicted probabilities assigned by the MLP classifier to the test sample for the $\tau^+\tau^-$ QEL signal with $m_{\text{DM}} = 5 \text{ GeV}$ (blue) and the atmospheric background (red).

1856 In any case, as before, I can take the direction of the incoming neutrino as known.

1857 That way, one can estimate the energy of the neutrino as:

$$E_\nu^{reco} = E_\mu + E_p + m_{39\text{Ar}} - m_{40\text{Ar}}, \quad (5.33)$$

1858 and using momentum conservation I can write the momentum of the remnant nucleus

1859 as:

$$\vec{p}_N = \hat{p}_\nu (E_\mu + E_p + m_{39\text{Ar}} - m_{40\text{Ar}}) - \vec{p}_\mu - \vec{p}_p. \quad (5.34)$$

1860 As in the previous case, I need to drop the events where the muon or the proton fall

1861 below the kinetic energy detection threshold [85]. Also, I again apply a smearing to the

1862 momenta of the particles, a 1% for muons and 5% for protons.

1863 Having done that, one can compute the following angular variables for our selected

1864 events:

$$\cos \theta_\mu = \hat{p}_\nu \cdot \hat{p}_\mu, \quad (5.35)$$

$$\cos \theta_p = \hat{p}_\nu \cdot \hat{p}_p, \quad (5.36)$$

5.5. HIGH ENERGY DM NEUTRINO SIGNALS

$$\cos \theta_N = \hat{p}_\nu \cdot \hat{p}_N. \quad (5.37)$$

1865 Fig. 5.14 shows the distributions of these angular variables for the $\tau^+\tau^-$ QEL
 1866 sample with $m_{\text{DM}} = 5$ GeV (blue) and the atmospheric background (red). Again, for
 1867 the atmospheric events I used a random solar position as the ansatz for the incoming
 1868 neutrino direction. Notice that now, opposed to the DIS case where the signal had very
 1869 sharp distributions for the variables considered, the shapes of the angular distributions
 1870 for signal and background are not that much different.

1871 This effectively means that the usual approach of applying simple angular cuts would
 1872 not work as well as in the previous situation. Therefore, as a possible solution, I tried to
 1873 use a multilayer perceptron (MLP) classifier to separate between signal and background
 1874 events. Thus, the power of the hypothesis test will serve as an estimate of the signal
 1875 efficiency, and in the same way one can take the size of the test to be our background
 1876 rejection.

1877 For each DM mass value and channel, as well as for the background sample, I divide
 1878 our events into training, validation and test samples. The input variables for the classifier
 1879 were the reconstructed neutrino energy from Eq. (5.33) and the angular variables defined
 1880 in Eqs. (5.35 - 5.37). I used the MLP classifier implemented in **scikit-learn** [139], with
 1881 a total of five hidden layers, the rectified linear unit activation function and adaptive
 1882 learning rate. In order to account for fluctuations due to artifacts in the training process I
 1883 repeated the training a thousand times for each sample, redefining each time the training,
 1884 validation and test subsets, so one can take as our signal efficiency and background
 1885 rejection the mean values of the powers and sizes of the tests.

1886 The results of one of these training processes for the $\tau^+\tau^-$ QEL signal with $m_{\text{DM}} =$
 1887 5 GeV is shown in Fig. 5.15. On the left panel I show the loss function values (blue) and
 1888 accuracy (red) at each iteration for the training and the validation samples respectively.
 1889 The training stops either when the maximum number of iterations is reached (1000 in
 1890 this case) or when the accuracy for the validation sample reaches a certain tolerance
 1891 (I chose 10^{-4} as our tolerance). On the right panel I have the distributions for the

CHAPTER 5. DM SEARCHES WITH NEUTRINOS FROM THE SUN

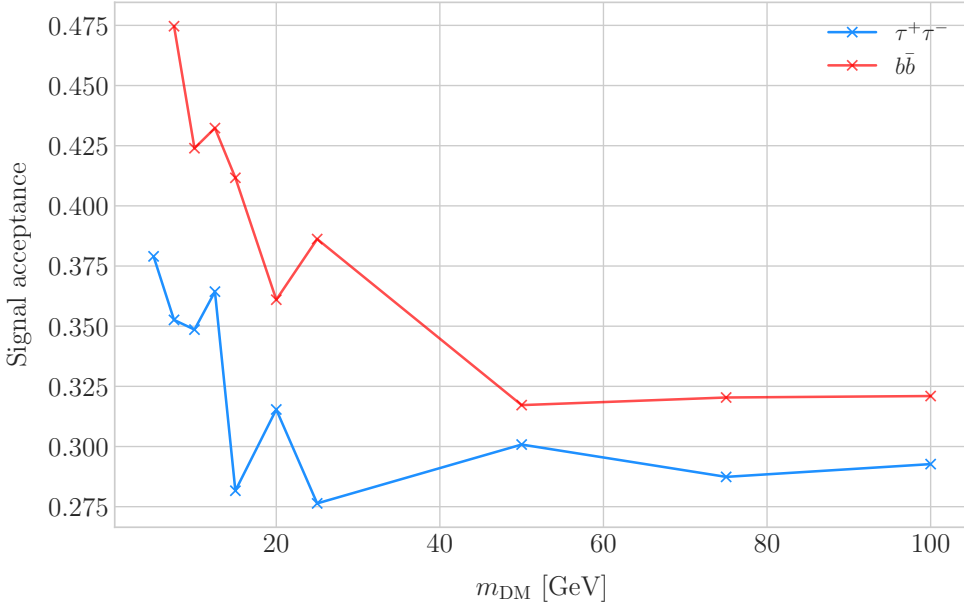


Figure 5.16: Signal efficiencies for the $\tau^+\tau^-$ (blue line) and $b\bar{b}$ (red line) single proton QEL samples as functions of the DM mass, m_{DM} , obtained by requiring a minimum predicted probability from the MLP classifier of 0.97 in order to achieve a background rejection greater than 99.8%.

1892 predicted probability by the model, separated in true signal (blue) and background
 1893 (red) events, for the test sample. One can see that both populations are well separated,
 1894 obtaining a power of 44.97% and a size of 0.17% when I require a predicted probability
 1895 greater than 0.97.

1896 Applying this criteria for each sample, I obtain the mean signal efficiencies shown in
 1897 Fig. 5.16. Notice that the efficiencies for the channel $\tau^+\tau^-$ (blue line) are consistently
 1898 lower than the ones for the $b\bar{b}$ channel (red line). This can be due to the fact that, for
 1899 each DM mass point, the neutrino spectrum coming from the $b\bar{b}$ annihilation channel is
 1900 centered at lower energies when compared to the $\tau^+\tau^-$ spectrum. This directly translates
 1901 into more low energy neutrinos undergoing QEL interactions, which give signals that
 1902 can be easily separated from the atmospheric background. This explanation also help us
 1903 understand why in both cases the signal acceptance drops when the DM mass increases.
 1904 In all cases, the background rejection took values between 99.8% to 99.9%. I will assume
 1905 a 99.8% background rejection value in all cases to keep our estimation conservative.

5.5. HIGH ENERGY DM NEUTRINO SIGNALS

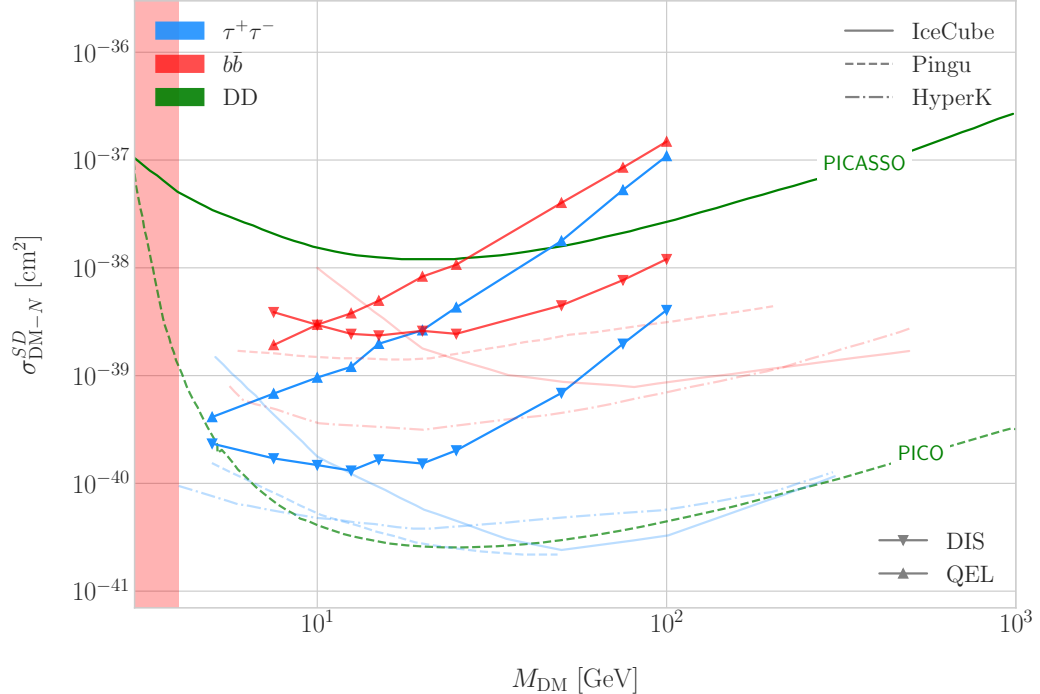


Figure 5.17: Projected 90% confidence level upper limit for DUNE (400 kT yr) on the spin-dependent DM-nucleon scattering cross section as a function of m_{DM} , for the annihilation channels $\tau^+\tau^-$ (blue) and $b\bar{b}$ (red) separated by interaction type (up triangles denote DIS interactions whereas down triangles represent QEL interactions). I also show the previous limits from IceCube [7] (solid lines) and the projected sensitivities for Pingu [8] (dashed lines) and Hyper-Kamiokande [9] (dash-dotted lines), as well as the direct detection limits from PICASSO [10] (solid green line) and PICO-60 C₃F₈ [11] (dashed green line).

1906 5.5.3 Results

1907 In order to estimate the DM-nucleon cross section sensitivities in the present case I need
 1908 again to compute the expected number of background events. As I am now separating
 1909 events by interaction type Eq. (5.25) does not hold anymore, as in that case I integrated
 1910 over the total neutrino-argon cross section. In this instance, the expected background
 1911 events for DIS events is approximately given by:

$$N_B^{DIS} \simeq \eta_B^{DIS} \times (4.655 \times 10^3) \times \left(\frac{\text{exposure}}{400 \text{ kT yr}} \right), \quad (5.38)$$

CHAPTER 5. DM SEARCHES WITH NEUTRINOS FROM THE SUN

1912 whereas for QEL events we have:

$$N_B^{QEL} \simeq \eta_B^{QEL} \times (2.248 \times 10^4) \times \left(\frac{\text{exposure}}{400 \text{ kT yr}} \right). \quad (5.39)$$

1913 Now, using these together with Eqs. (5.26) and (5.27) one can obtain the 90% C.L.
1914 upper limit on the total annihilation rate at equilibrium for both kind of events. Then,
1915 applying the computed DM-nucleons capture rates I can translate these into limits on
1916 the DM-nucleon cross section by means of Eqs. (5.2), (5.5) and (5.6).

1917 Fig. 5.17 shows the obtained limits on the SD DM-nucleon cross section for DUNE,
1918 using the DIS (up triangles) and QEL (down triangles) events both for the $\tau^+\tau^-$ (blue)
1919 and the $b\bar{b}$ (red) samples, for an exposure of 400 kT yr. I also include the corresponding
1920 current limits from IceCube [7] (solid lines), as well as the projected sensitivities of
1921 Pingu [8] (dashed lines) and Hyper-Kamiokande [9] (dash-dotted lines). For comparison,
1922 I also show the reported direct detection limits from PICASSO [10] (solid green line)
1923 and PICO-60 C_3F_8 [11] (dashed green line).

1924 Notice that, for most of the mass range, the limits one can set by using the DIS
1925 events are stronger than those of the QEL interactions, except for the low mass part
1926 of both the $\tau^+\tau^-$ and the $b\bar{b}$ curves where the QEL events dominate. In general, the
1927 expected sensitivity of DUNE for DM masses $\lesssim 25$ GeV surpasses the stronger current
1928 indirect limits. However, experiments like Hyper-Kamiokande are foreseen to have an
1929 overall better sensitivity in this kind of searches, as they have a bigger active volume
1930 and accept a broader energy range.

1931 A pending question is what happens when we add the RES and MEC charged-current
1932 interaction contributions. In that case it would probably be more convenient to split
1933 the samples by final state interaction topologies. Also, another necessary improvement
1934 would be adding a full detector simulation and reconstructions. This will also require
1935 considering the effect of poorly reconstructed events or final states containing neutral
1936 particles such that they mimic the desired topology at the reconstruction level.

5.6. EXAMPLE: LEPTOPHILIC DARK MATTER

1937 5.6 Example: Leptophilic Dark Matter

1938 In general, the capture rate of DM particles by the Sun via interactions with electrons is
1939 several orders of magnitude smaller than the capture via DM-nucleus scattering. Thus,
1940 it would be sub-leading even when nucleon capture is loop suppressed. As I showed in
1941 Fig. 5.2, the capture rate via scattering off electrons only surpasses the capture rates
1942 via DM-nucleons interactions for DM masses $\lesssim 100 - 500$ MeV.

1943 However, if one considers a model where DM-nucleon interactions are forbidden even
1944 at loop level, then electron interactions will be the sole contributor to DM capture in
1945 the Sun. One can describe such scenario where the DM particles couple to leptons but
1946 not to the quark sector using effective operators.

1947 In general, assuming that the DM particle is a Dirac fermion, the dimension six
1948 operators describing the interaction between two DM particles and two leptons can be
1949 written as:

$$\mathcal{L}_{eff} = G \sum_i (\bar{\chi} \Gamma^i \chi) (\bar{\ell} \Gamma^i \ell), \quad (5.40)$$

1950 where $G = 1/\Lambda^2$ is the effective coupling strength, Λ the cut-off of the effective field
1951 theory and ℓ denotes any lepton. In principle, one should consider all the possible
1952 Lorentz structures Γ_f^i in order to have a complete set of effective operators.

1953 However, some combinations will induce interactions with nucleons at loop level.
1954 As we are specifically interested in interactions which forbid any communication with
1955 the quark sector, I will not consider those [140]. In addition, some of the effective
1956 operators give rise to velocity-suppressed scattering cross sections between DM particles
1957 and leptons. I will also neglect those, as the suppression goes with the square of the DM
1958 halo velocity which in units of the speed of light is $\sim 10^{-6}$.

1959 This way, the only Lorentz tensor structure that do not induce interactions with
1960 quarks at loop level and gives a contribution to the scattering cross section that is not
1961 velocity suppress is the axial-axial interaction. The effective Lagrangian is then given

CHAPTER 5. DM SEARCHES WITH NEUTRINOS FROM THE SUN

1962 by:

$$\mathcal{L}_{eff} = \frac{c_A^\chi c_A^\ell}{\Lambda^2} (\bar{\chi} \gamma^\mu \gamma^5 \chi) (\bar{\ell} \gamma_\mu \gamma^5 \ell), \quad (5.41)$$

1963 where c_A^χ and c_A^ℓ are the couplings for the different species. As the DM coupling appears
1964 as a common factor for any lepton choice, I will redefine the corresponding coupling c_A^ℓ
1965 to absorb c_A^χ . Also, for simplicity, I will assume that the couplings between the DM
1966 particles and the leptons are flavour independent, i.e. I have just two couplings, c_A^e for
1967 charged leptons and c_A^v for neutrinos.

1968 In the case of a scalar DM particle, the lowest order effective interaction with
1969 leptons happens through a dimension five operator, generating scalar and pseudoscalar
1970 interactions. However, the former induces interactions with quarks at two loop level
1971 whereas the latter gives a velocity suppressed scattering cross section.

1972 From the effective Lagrangian in Eq. (5.41) it can be shown that the axial-axial
1973 contribution to the scattering cross section for the fermionic DM and a charged lepton
1974 is given by:

$$\sigma_{DM-e}^{AA} = 3 (c_A^e)^2 \frac{m_e^2}{\pi \Lambda^4}. \quad (5.42)$$

1975 If the DM interacts exclusively with fermions, then the only annihilation channels
1976 that will give us a measurable neutrino flux coming out of the Sun are $\tau^+ \tau^-$ and $\nu \bar{\nu}$. The
1977 former channel, already explored previously in the more mainstream scenario of the DM
1978 capture via scattering off nucleons, is open only for $m_{DM} > m_\tau \simeq 1776.86 \pm 0.12$ MeV
1979 [141], a mass region where the solar DM capture by electrons is at least one order of
1980 magnitude smaller than the capture via interactions with nucleons. On the contrary, the
1981 latter allows us to explore a region where the capture rate via scattering off electrons
1982 dominates over the rest.

1983 One downside of focusing in such low mass range is that it falls below the usual
1984 limit of $m_{evap} \sim 4$ GeV usually explored in the literature. The pretext to explore this
1985 region is the result discussed previously reported in Ref. [2], where DM evaporation in
1986 the Sun for the case of capture via electron scattering could be negligible for masses
1987 as low as $m_{evap} \sim 200$ MeV. This result is quite sensitive to the high velocity tail of

5.6. EXAMPLE: LEPTOPHILIC DARK MATTER

1988 the DM velocity distribution in equilibrium inside the Sun, and therefore full numerical
 1989 simulations would be needed to asses the impact of this effect. However, this falls out of
 1990 the scope of our work.

1991 In this case, as I have an specific realisation of the interaction between the DM
 1992 and leptons, one can estimate the relic density of our DM for different values of the
 1993 couplings and the effective field theory scale Λ . The first step to do so is compute the
 1994 self-annihilation cross section. Because I consider cold relics, at the freeze-out time our
 1995 DM particles were non-relativistic and so one can expand the annihilation cross section
 1996 in terms of the relative velocity v between two annihilating DM particles as [142]:

$$\sigma_{ann}^{AA}|v| \approx \frac{1}{2\pi\Lambda^4} \sum_{\ell} \left(c_A^{\ell}\right)^2 m_{\chi}^2 \sqrt{1 - \frac{m_{\ell}^2}{m_{\chi}^2} \left[\frac{m_{\ell}^2}{m_{\chi}^2} + \frac{1}{12} \left(2 - \frac{m_{\ell}^2}{m_{\chi}^2}\right) v^2 \right]}, \quad (5.43)$$

1997 where the sum includes all the possible lepton final states with mass m_{ℓ} .

1998 Solving the Boltzmann equation for the evolution of the DM density gives as a
 1999 solution a relic density of:

$$\Omega_{\chi} h^2 \approx \frac{(1.04 \times 10^9) x_F}{M_{Pl} \sqrt{g_*} (a + 3b/x_F)}, \quad (5.44)$$

2000 where $x_F = m_{\chi}/T_F$ being T_F the freeze-out temperature, g_* the number of relativistic
 2001 degrees of freedom at freeze-out and a and b the terms in the annihilation cross section
 2002 expansion $\sigma_{ann}|v| \approx a + bv^2 + \mathcal{O}(v^4)$. Using the current best fit for the relic DM density
 2003 $\Omega_{\chi} h^2 = 0.1198 \pm 0.0012$ [143] one can use these relations to compute the required
 2004 effective theory scale Λ at which the correct density is achieved for any combinations of
 2005 m_{χ} and c_A^{ℓ} .

2006 As discussed before, in the low DM mass region QEL interactions dominate. Moreover,
 2007 if I focus on direct annihilation to neutrinos, the energy of the muon neutrino flux is
 2008 known as it must be equal to the mass of the DM particle, $E_{\nu} = m_{\chi}$. That way, now
 2009 I do not need to use Eq. (5.33) in order to estimate the momentum transfer to the

CHAPTER 5. DM SEARCHES WITH NEUTRINOS FROM THE SUN

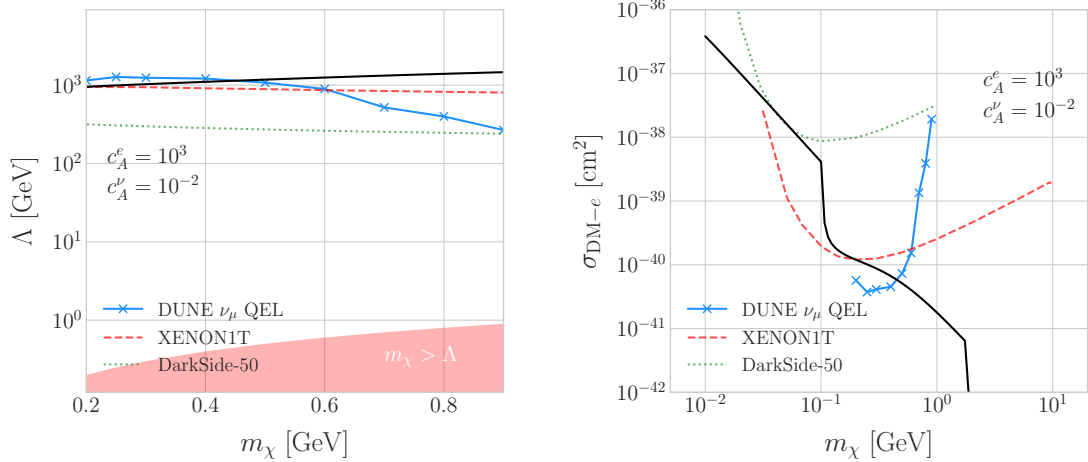


Figure 5.18: Left panel: Projected 90% confidence level sensitivity of DUNE (400 kT yr) to the scale Λ of an EFT containing only leptophilic DM axial-axial interactions (blue line). Right panel: . In both cases the corresponding limits from DarkSide-50 [12] (dotted green line) and XENON1T [13] (dashed red line) are also shown, together with the configurations for which the correct relic density is achieved (black line), all for the coupling values $c_A^e = 10^3$ and $c_A^\nu = 10^{-2}$.

2010 remnant nucleus, I can simply take:

$$\vec{p}_N = \hat{p}_\nu m_\chi - \vec{p}_\mu - \vec{p}_p. \quad (5.45)$$

2011 To estimate the signal efficiency and background rejection for this case I used again
 2012 the MLP classifier from `scikit-learn`, using the same specifications as before. The
 2013 only difference now is that I add also the reconstructed neutrino energy as one of the
 2014 features to train the classifier with, because the characteristic monoenergetic flux for
 2015 each m_χ value will help to distinguish between signal and background events.

2016 In this case, for masses below ~ 500 MeV I obtain a signal efficiency close to unity
 2017 while keeping a background rejection of 99.9%. For bigger values of the mass, the signal
 2018 efficiency drops significantly if I require to keep the background acceptance under 0.01%.
 2019 However, because this kind of search is dominated by the background, sacrificing the
 2020 signal acceptance to keep the background rejection to a minimum enhances the reach
 2021 of the analysis. This way, for DM masses of the order of $m_\chi \sim 1$ GeV I end up with
 2022 efficiencies as low as 1%.

5.7. SYSTEMATIC UNCERTAINTIES

Now, estimating the number of background events using Eq. (5.39) one can go on and apply Eqs. (5.26) and (5.27) together with Eq. (5.42) to derive the sensitivity of DUNE to this kind of model. Fig. 5.18 (left panel) shows the potential reach of DUNE to constrain the EFT scale Λ this model containing only leptophilic DM axial-axial interactions (blue line), for a choice of couplings $c_A^e = 10^3$ and $c_A^\nu = 10^{-2}$. I also included the current limits on the DM-electron scattering cross section from DarkSide-50 [12] (dotted green line) and XENON1T [13] (dashed red line), reworked with Eq. (5.42) to show their implications for the EFT scale. The values of Λ for which the correct DM relic density value is achieved for each mass are also shown (black line). This tells us that, for that specific choice of couplings, DUNE would be sensitive to DM configurations allowed by the relic density constraint up to a mass of $m_\chi \sim 400$ MeV.

In Fig. 5.18 (right panel) I show the same upper limits but for the DM-electron scattering cross section. From this view one can see that DUNE would be able to offer complementary information to the low energy DM-electron interaction searches performed by direct detection experiments, in a slightly higher mass range.

With the present example, although it focuses on a very specific realisation of the DM interactions, I show the potential of DUNE to constrain exotic DM scenarios. Thanks to its low backgrounds and superb angular resolution DUNE will be able to help with the systematic searches for dark sectors physics.

5.7 Systematic uncertainties

The estimation of the DM cross sections using neutrinos from WIMP annihilations inside the Sun is affected by systematic uncertainties from different sources. Surely, the atmospheric background estimation is also affected by systematic uncertainties. There are uncertainties common to both types of events, as well as others specific to each. In this section, I try to provide a comprehensive summary of the main sources of uncertainty for this analysis, which should be taken into account in any future extensions of the same.

CHAPTER 5. DM SEARCHES WITH NEUTRINOS FROM THE SUN

Table 5.1: Systematic uncertainties for the solar WIMP signal events. Table adapted from Ref. [144].

Systematic	Value
Form factor	Does not apply to SD [145]
Solar model	3% [145]
Local DM density	Not relevant for relative interpretations [145, 146]
Dynamics of solar system	Negligible [147]
Velocity distributions	20% at 20 GeV [145, 146]
Oscillation parameters	8% for $\tau^+\tau^-$, 5% for $b\bar{b}$ [148]
Neutrino interactions in the Sun	10%
Matter effects in the Earth	10%

2050 5.7.1 Systematic uncertainties in the solar WIMP signal

2051 The systematic uncertainties affecting the solar WIMP neutrino signal can be divided in
 2052 two categories. On the one hand, we have those affecting the solar WIMP annihilation
 2053 rate. On the other hand, there are the ones which modify the neutrino flux resulting
 2054 from the annihilations reaching our detector.

2055 • **Uncertainties on the annihilation rate.** These include the astrophysical effects
 2056 that affect the normalisation of the solar DM neutrino flux. The main contributions
 2057 are the solar model choice, the form factor uncertainties (only for SI searches), the
 2058 gravitational effect of other planets, the local DM density (not relevant for relative
 2059 comparisons, as it affects direct detection experiments in the same way), and the
 2060 DM halo and dispersion velocities.

2061 • **Uncertainties on the neutrino flux.** These are related to the oscillation effects,
 2062 as well as the absorption and regeneration of neutrinos in the Sun. Matter effects
 2063 inside the Earth also affect the neutrino flux the measured at the detectors.

2064 Table 5.1 summarises the contributions of the different sources of uncertainty for the
 2065 signal events. These are the signal systematic uncertainties that have been taken into
 2066 account in previous solar DM searches with neutrinos [144, 146, 148].

5.7. SYSTEMATIC UNCERTAINTIES

Table 5.2: Systematic uncertainties for the solar WIMP atmospheric background events. Table adapted from Ref. [51].

Systematic	Value
Flux normalisation	25 – 7% for $0.1 < E_\nu \leq 1$ GeV (linear in $\log E_\nu$) 7% up to 10 GeV
$(\nu_\mu + \bar{\nu}_\mu)/(\nu_e + \bar{\nu}_e)$	2% for $E_\nu \leq 1$ GeV 3% for $1 < E_\nu \leq 10$ GeV
$\bar{\nu}_\mu/\nu_\mu$	2% for $E_\nu \leq 1$ GeV 6% for $1 < E_\nu \leq 10$ GeV
K/ π ratio	5% $E_\nu \leq 100$ GeV

2067 5.7.2 Systematic uncertainties in the atmospheric background

2068 For the atmospheric background events, one needs to take into account the systematic
2069 uncertainties affecting the atmospheric ν_μ flux. These have been extensively studied
2070 in the context of atmospheric neutrino oscillation measurements. Among these, the
2071 energy-dependent flux normalisation uncertainty is the in the low energy regime. Other
2072 important contributions to the uncertainty come from the ratios between the muon to
2073 electron neutrino and the muon to anti-muon neutrino components of the flux. Additional
2074 uncertainty is introduced by the errors in the pion and kaon production rates calculated
2075 for the hadronic interactions of cosmic rays in the atmosphere [149].

2076 Table 5.2 shows a summary of the leading contributions to the uncertainty on the
2077 atmospheric muon neutrino flux, in the energy range relevant for this analysis.

2078 5.7.3 Common systematic uncertainties

2079 Finally, there are sources of uncertainty common to both signal and backgrounds. These
2080 have two different origins:

- 2081** • **Uncertainties on the neutrino cross section.** These are introduced by the
2082 modelling of the neutrino-nucleus interactions. In the context of the solar WIMP
2083 analysis, these have been estimated to be 10% for DM masses around 10 GeV
2084 [148].

CHAPTER 5. DM SEARCHES WITH NEUTRINOS FROM THE SUN

- 2085 • **Uncertainties related to the detector.** They affect the measurement of the
2086 neutrino interaction and the final state particles produced. The main detector
2087 uncertainties relevant to this analysis are those of the energy and angular resolutions
2088 of the DUNE FD. Other effects, like the timing and triggering efficiencies, will
2089 also contribute to the uncertainties. The particular values these will take for this
2090 analysis need to be worked out in the context of DUNE.

2091

2092

Particle ID in ND-GAr

2093 ND-GAr is a magnetised, high-pressure gaseous argon TPC (HPgTPC), surrounded by
2094 an electromagnetic calorimeter (ECal) and a muon detector (commonly refer to as μ ID).
2095 A detailed discussion on the requirements, design, performance and physics of ND-GAr
2096 can be found in the DUNE ND CDR [91] and the ND-GAr whitepaper (cite).

2097 In DUNE Phase II ND-GAr will fulfill the role of TMS, measuring the momentum
2098 and sign of the charged particles exiting ND-LAr. Additionally, it will be able to measure
2099 neutrino interactions inside the HPgTPC, achieving lower energy thresholds than those
2100 of the ND and FD LArTPCs. By doing so ND-GAr will allow to constrain the relevant
2101 systematic uncertainties for the LBL analysis even further.

2102 The goal of the present chapter is to review the requirements that the physics program
2103 of DUNE impose on ND-GAr, present the current status of its design and describe the
2104 GArSoft package, its simulation and reconstruction software.

2105 As decided during the DUNE Phase II workshop in June 2023 [reference], we want
2106 to build ND-GAr physics case by showing:

- 2107 • That ND-GAr can constrain systematic uncertainties that ND-LAr might miss.
- 2108 • The impact on the neutrino oscillation results if such systematic uncertainties are
2109 missed.
- 2110 • That ND-GAr is necessary to reach DUNE's main physics goals.

2111 This way, the design of ND-GAr will be physics driven.

CHAPTER 6. PARTICLE ID IN ND-GAr

2112 In order to study the effects of final state interactions (FSI) in CC interactions,
2113 ND-GAr should be able to measure the spectrum of protons and charged pions at low
2114 energies. ND-GAr also needs to be able to measure the pion multiplicity, specially for
2115 energies above 100 MeV as at these energies the pions shower in the LAr, to inform the
2116 pion mass correction in the ND and FD LArTPCs.

2117 In order to correctly identify electrons, muons, pions, kaons and protons ND-GAr
2118 can use a combination of: dE/dx measurements in the HPgTPC, E_{ECAL}/p using the
2119 ECAL total energy and the momentum obtained from magnetic spectroscopy in the
2120 HPgTPC and penetration information through the ECAL and muon tagger.

2121 6.1 GArSoft

2122 GArSoft is a software package developed for the simulation and reconstruction of events
2123 in ND-GAr. It is inspired by the LArSoft toolkit used for the simulation of LArTPC
2124 experiments, like the DUNE FD modules. It is based on `art`, the framework for event
2125 processing in particle physics experiments [150]. Other of its main dependencies are
2126 `ROOT`, `NuTools`, `GENIE` and `Geant4`. It allows the user to run all the steps of a generation-
2127 simulation-reconstruction workflow using FHiCL configuration files.

2128 6.1.1 Event generation

2129 The standard generator FHiCLs in GArSoft run the event generation and particle
2130 propagation simulation (i.e. Geant4) in the same job by default. However, it is possible
2131 to split them up if needed. The current version of GArSoft provides five different event
2132 generators, each of them producing `simb::MCTruth` products defined in `NuTools`. The
2133 available modules are:

- 2134 • **SingleGen**: particle gun generator. It produces the specified particles with a given
2135 distribution of momenta, initial positions and angles.
- 2136 • **TextGen**: text file generator. The input file must follow the `hepevt` format¹, the

¹In brief, each event contains at least two lines. The first line contains two entries, the event number

6.1. GARSOFT

2137 module simply copies this to `simb::MCTruth` data products.

2138 • **GENIEGen**: GENIE neutrino event generator. The module runs the neutrino-nucleus
2139 interaction generator using the options specified in the driver FHiCL file (flux file,
2140 flavour composition, number of interactions per event, t_0 distribution, ...). Current
2141 default version is v3_04_00.

2142 • **RadioGen**: radiological generator. It produces a set list of particles to model
2143 radiological decays. Not tested.

2144 • **CRYGen**: cosmic ray generator. The module runs the CRY event generator with a
2145 configuration specified in the FHiCL file (latitude and altitude of detector, energy
2146 threshold, ...). Not tested.

2147 The module **GArG4** searches for all the generated `simb::MCTruth` data products, using
2148 them as inputs to the Geant4 simulation with the specified detector geometry. A constant
2149 0.5 T magnetic field along the drift coordinate is assumed. The main outputs of this step
2150 are `simb::MCParticle` objects for the generated Geant4 particles, `gar::EnergyDeposit`
2151 data products for the energy deposits in the HPgTPC and `gar::CaloDeposit` data
2152 products for the energy deposits in the ECal and muon system.

2153 6.1.2 Detector simulation

2154 The standard detector simulation step in GArSoft is all run with a single FHiCL, but
2155 the different modules can be run independently as well. First the `IonizationReadout`
2156 module simulates the charge readout of the HPgTPC, and later the `SiPMReadout` module
2157 runs twice, once for the ECal and then for the muon system, with different configurations.

2158 The `IonizationAndScintillation` module collects all the `gar::EnergyDeposit`
2159 data products, to compute the equivalent number of ionization electrons for each energy

and the number of particles in the event. Each following line contains 15 entries to describe each particle. The entries are: status code, pdg code for the particle, entry of the first mother for this particle, entry of the second mother for this particle, entry of the first daughter for this particle, entry of the second daughter for this particle, x component of the particle momentum, y component of the particle momentum, z component of the particle momentum, energy of the particle, mass of the particle, x component of the particle initial position, y component of the particle initial position, z component of the particle initial position and time of the particle production.

CHAPTER 6. PARTICLE ID IN ND-GAr

deposit. The `ElectronDriftAlg` module simulates the electron diffusion numerically both in the longitudinal and transverse directions and applies an electron lifetime correction factor. The induced charge on the nearest and neighbouring readout pads is modeled using the provided pad response functions. The digitisation of the data is then simulated with the `TPCReadoutSimAlg` module. By default, the ADC sampling rate used is 50.505 MHz. The resulting raw waveforms for each channel are stored with zero-suppression, in order to save memory and CPU time. The algorithms keep blocks of ADC values above a certain threshold, plus some adjustable additional early and late tick counts. The results of these three steps are `gar::raw::RawDigit` data products.

For the ECal and the muon system the `SiPMReadout` module calls either the `ECALReadoutSimStandardAlg` or `MuIDReadoutSimStandardAlg` modules. These take all the `gar::CaloDeposit` data products in the corresponding detector and do the digitisation depending on whether the hit was in a tile or strip layer. They include single photon statistics, electronic noise, SiPM saturation and time smearing. The resulting objects are `gar::raw::CaloRawDigit` data products.

6.1.3 Reconstruction

The reconstruction in GArSoft is also run as a single job by default. It first runs the hit finding, clustering, track fitting and vertex identification in the HPgTPC, followed by the hit finding and clustering in the ECal and muon system. After those it produces the associations between the associations between the tracks and the ECal clusters.

Focusing first on the HPgTPC reconstruction, the `CompressedHitFinder` module takes the zero-suppressed ADCs from the `gar::raw::RawDigit` data products. The reconstructed hits largely correspond to the above threshold blocks, however the hit finder identifies waveforms with more than one maximum, diving them in multiple hits if they dip below a certain threshold. The data products produced are of the form `gar::rec::Hit`. These are the inputs to the clustering of hits in the `TPCHitCluster` module. Hits close in space and time are merged, and the resulting centroids are found. This module outputs `gar::rec::TPCClusters` objects and associations to the input

6.1. GARSOFT

2188 hits.

2189 The following step prior to the track fitting is pattern recognition. The module
2190 called `tpcvechitfinder2` uses the `gar::rec::TPCClusters` data products to find track
2191 segments, typically called vector hits. They are identified by performing linear 2D fits
2192 to the positions of the clusters in a 10 cm radius, one fit for each coordinate pair. A
2193 3D fit defines the line segment of the vector hit, using as independent variable the one
2194 whose sum of (absolute value) slopes in the 2D fits is the smallest. The clusters are
2195 merged to a given vector hit if they are less than 2 cm away from the line segment. The
2196 outputs are `gar::rec::VecHit` data products, as well as associations to the clusters. The
2197 `tpcpatrec2` module takes the `gar::rec::VecHit` objects to form the track candidates.
2198 The vector hits are merged together if their direction matches, their centers are within
2199 60 cm and their direction vectors point roughly to their respective centers. Once
2200 the clusters of vector hits are formed they are used to make a first estimation of the
2201 track parameters, simply taking three clusters along the track. The module produces
2202 `gar::rec::Track` data products and associations between these tracks and the clusters
2203 and vector hits.

2204 The track is fitted by means of a Kalman filter in the `tpctrackfit2` module, using
2205 the position along the drift direction as the independent variable. Two different fits are
2206 performed per track, a forward and a backwards fit, each starting from one of the track
2207 ends. The Kalman filter state vector ($y, z, R, \phi, \tan\lambda$) is estimated at each point along
2208 the track using a Bayesian update. The track parameters reported in the forward and
2209 backwards fits are the ones computed at the opposite end where the fit started. The
2210 main outputs of the track fit are the `gar::rec::Track` objects. Additionally, the module
2211 stores the fitted 3D positions along the track in the `gar::rec::TrackTrajectory` data
2212 products and the total charge and step sizes for each point also get stored in the form of
2213 `gar::rec::TrackIonization` objects.

2214 After the tracking step, the `vertexfinder1` module looks at the reconstructed
2215 `gar::rec::Track` products, creating vertex candidates with the track ends that are
2216 within 12 cm of each other. The vertices are then fitted using linear extrapolations from

CHAPTER 6. PARTICLE ID IN ND-GAr

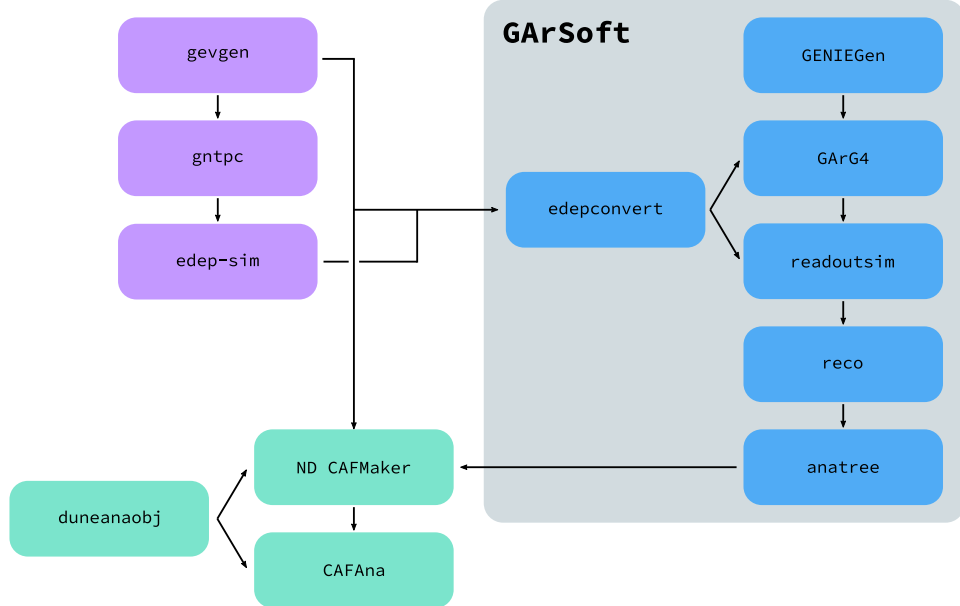


Figure 6.1: Schematic diagram showing the different modules involved in the ND-GAr production.

the different track ends associated. The results are `gar::rec::Vertex` data products, and associations to the tracks and corresponding track ends.

For the ECal and muon tagger, the `SiPMHitFinder` module runs twice with different configurations, adapted to the particular capabilities of both. The module simply takes the `gar::raw::CaloRawDigit` products, applies a calibration factor to convert the ADC counts to MeV and for the strip layer hits it calculates the position along the strip using the times recorded of both SiPMs. This module produces `gar::rec::CaloHit` data products. Next, these objects are used as inputs to the `CaloClustering` module. It merges the hits based on a simple nearest neighbours (NN) algorithm. For the resulting clusters it also computes the total energy and position of the centroid. The results are stored as `gar::rec::Cluster` data products, with associations to the hits.

The last step in the reconstruction is associating the reconstructed tracks in the HPgTPC to the clusters formed in the ECal and muon system. The `TPCECALAssociation` module checks first the position of the track end points, considering only the points that are at least 215 cm away from the cathode or have a radial distance to the center

6.2. dE/dx MEASUREMENT IN THE TPC

greater than 230 cm. The candidates are propagated up to the radial position, in the case of clusters in the barrel, or the drift coordinate position, for the end cap cluster, of the different clusters in the collection using the track parameters computed at the end point. The end point is associated to the cluster if certain proximity criteria are met. This module creates associations between the tracks, the end points and the clusters. The criteria for the associations are slightly different for the ECal and the muon tagger.

6.2 dE/dx measurement in the TPC

Among the parameters extracted from the track fitting, ionisation is particularly useful for particle identification, as it is a function of the particle velocity. Although for the case of relativistic particles this dependence is not very strong, measuring the track on a large number of points may allow us to estimate the amount of ionisation accurately. This, paired with a measurement of the momentum, may allow us to identify the particle type.

The first calculation of the energy loss per unit length of relativistic particles using a quantum-mechanical treatment is due to Bethe [151]. Using this approach, the mean ionisation rate of a charged particle traveling through a material medium is (using natural units $G = \hbar = c = 1$):

$$\left\langle \frac{dE}{dx} \right\rangle = \frac{4\pi Ne^4}{m_e \beta^2} z^2 \left(\log \frac{2m_e \beta^2 \gamma^2}{I} - \beta^2 \right), \quad (6.1)$$

where N is the number density of electrons in the medium, e the elementary charge, m_e is the electron mass, z the charge of the particle in units of e , β is the velocity of the particle, $\gamma = (1 - \beta^2)^{-1}$ and I denotes the effective ionisation potential averaged over all electrons. This relation is known as the Bethe-Bloch formula.

From Eq. (6.1) one can see that the ionisation loss does not depend explicitly on the mass of the charged particle, that for non-relativistic velocities it falls as β^{-2} , then goes through a minimum and increases as the logarithm of γ . This behaviour at high velocities is commonly known as the relativistic rise. The physical origin of this effect

CHAPTER 6. PARTICLE ID IN ND-GAr

2257 is partly due to the fact that the transverse electromagnetic field of the particle is
2258 proportional to γ , therefore as it increases so does the cross section.

2259 It was later understood that the relativistic rise could not grow indefinitely with γ .
2260 A way to add this feature in the Bethe-Bloch formula is by introducing the so-called
2261 density effect term. It accounts for the polarisation effect of the atoms in the medium,
2262 which effectively shield the electromagnetic field of the charged particle halting any
2263 further increase of the energy loss [152]. Denoting the correction as $\delta(\beta)$, one can rewrite
2264 Eq. (6.1) as:

$$\left\langle \frac{dE}{dx} \right\rangle = \frac{4\pi Ne^4}{m_e \beta^2} z^2 \left(\log \frac{2m_e \beta^2 \gamma^2}{I} - \beta^2 - \frac{\delta(\beta)}{2} \right). \quad (6.2)$$

2265 In general, the form of $\delta(\beta)$ depends on the medium and its state of aggregation,
2266 involving the usage of tabulated parameters and implicit relations [153].

2267 Another standard method to compute the amount of ionisation a charged particle
2268 produces is the so-called photo-absorption ionisation (PAI) model proposed by Allison
2269 and Cobb [154]. Within their approach, the mean ionisation is evaluated using a
2270 semiclassical calculation in which one characterises the continuum material medium by
2271 means of a complex dielectric constant $\epsilon(k, \omega)$. However, in order to model the dielectric
2272 constant they rely on the quantum-mechanical picture of photon absorption and collision.
2273 Therefore, in the PAI model the computation of the ionisation loss involves a numerical
2274 integration of the measured photo-absorption cross-section for the relevant material.

2275 In a particle physics experiment, the typical way of determining the energy loss
2276 per unit length as a function of the particle velocity is studying identified particles
2277 over a range of momenta. Once we have established this relation we can use it for
2278 other, unknown particles. In this sense, it makes sense to have a regular mathematical
2279 expression for this relation that one can use.

2280 It happens that neither the Bethe-Bloch theory nor the PAI model from Allison and
2281 Cobb offer a close mathematical form for the ionisation curve. This is the reason why a
2282 full parametrisation of the ionisation curves can be useful. A parametrisation originally
2283 proposed for the ALEPH TPC [155] and later used by the ALICE TPC [156] group that

6.2. dE/dx MEASUREMENT IN THE TPC

2284 manages to capture the features of the ionisation energy loss is:

$$f(\beta\gamma) = \frac{P_1}{\beta^{P_4}} \left(P_2 - \beta^{P_4} - \log \left[P_3 + \frac{1}{(\beta\gamma)^{P_5}} \right] \right), \quad (6.3)$$

2285 where P_i are five free parameters. Hereafter, we will refer to Eq. (6.3) as the ALEPH

2286 dE/dx parametrisation.

2287 6.2.1 Energy calibration

2288 In order to obtain the amount of energy loss by a charged particle due to ionisation
2289 in our TPC we need to determine the conversion between the charge deposited in our
2290 readout planes and the actual energy depositions. This procedure is known as energy
2291 calibration.

2292 In a general, the first step of the calibration involves a non-uniformity correction,
2293 to make sure that the detector response is uniform throughout the TPC. These are
2294 typically divided into three categories, non-uniformities in the transverse YZ plane,
2295 non-uniformities along the drift direction X and variations of the detector response
2296 over time (would not apply to us as the detector is not built yet). These would correct
2297 for effects such as electron diffusion and attenuation, space charge effects or channel
2298 misconfiguration. However, because at the moment I am only interested in making sure
2299 we recover a sensible result from our simulation, I will not apply uniformity corrections
2300 to our charge deposits.

2301 Other effects, like electron-ion recombination or ADC saturation, lead to a non-linear
2302 relation between the observed charge and the deposited energy in the detector, with the
2303 observed readout charge saturating at high ionisation energies. In this case, because we
2304 are dealing with gaseous argon and therefore recombination is not as important as in
2305 liquid, we do not simulate recombination effects in the TPC. Even so, the simulation of
2306 the electronic response will still introduce charge saturation, and one needs to correct
2307 for it in order to obtain the exact amount of energy loss due to ionisation.

2308 By default, the track fitting algorithm in GArSoft provides a `TrackIonization`

CHAPTER 6. PARTICLE ID IN ND-GAr

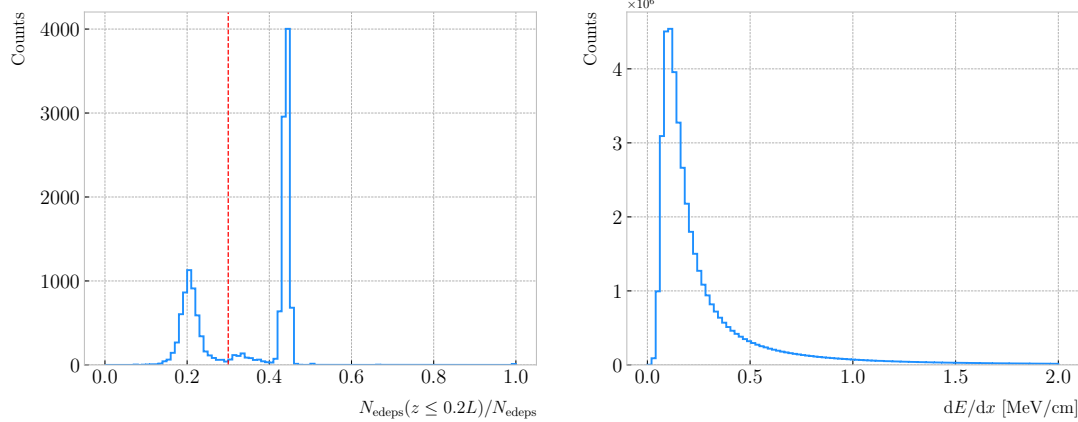


Figure 6.2: Left panel: distribution of the fraction of Geant4-level energy deposits per track with residual range less than 20% of the total track length, for the isotropic proton sample. Right panel: distribution of the ionisation per unit length of the energy deposits in the proton sample after removing the tracks with less than 30% of their energy deposits in the last 20% of the track.

object associated to each reconstructed track. It contains two collections of charge deposits, one for each fitting direction, consisting on pairs of charge values (dQ , in ADC) and step sizes (dx , in cm).

In order to estimate the ionisation loss in the ND-GAr TPC, I have used an MC sample consisting of single, isotropic protons propagating in the TPC. The starting points of the protons were sampled inside a $50 \times 50 \times 25$ cm box centered at $(100, -150, 1250)$, and their momenta are uniformly distributed in the range $0.25 - 1.75$ GeV. I ran the simulated sample through GArSoft's default detector simulation and reconstruction, and then a custom analyser module that extracts the ionisation data together with other reconstructed track information from the Kalman fit.

For studying the energy loss of the protons I select the reconstructed tracks that range out (i.e. slow down to rest) inside the TPC. A characteristic feature of the energy loss profile of any stopping ionising particle is the so-called Bragg peak, a pronounced peak that occurs immediately before the particle comes to rest. From Eq. (6.1) we can see that this behaviour is expected, as the energy loss for non-relativistic particles is inversely proportional to β^2 . In data, a way of identifying the Bragg peak, and thus select the stopping particles, is checking the number of energy deposits towards the

6.2. dE/dx MEASUREMENT IN THE TPC

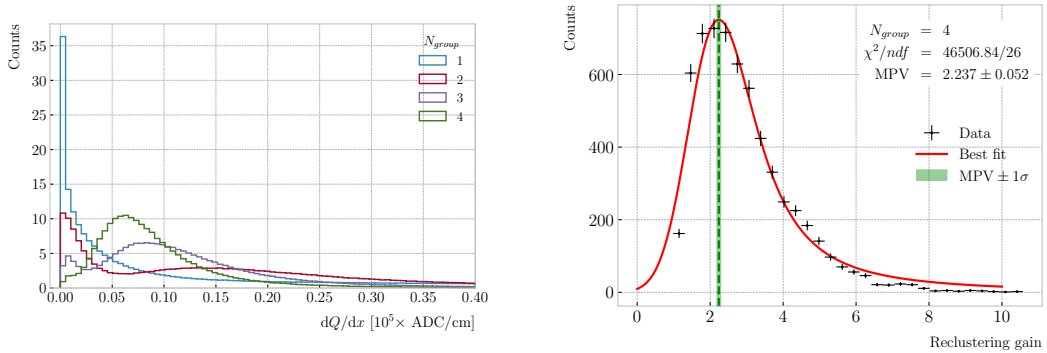


Figure 6.3: Left panel: distribution of the reconstructed ionisation charge per unit length for our MC stopping proton sample. The different colors indicate how many consecutive dQ/dx pairs were grouped together. Right panel: distribution of the median change in dQ/dx per track after $N_{group} = 4$ clusters were reclustered together.

end of the track. In this case, I count the fraction of the Geant4 simulated energy deposits with a residual range value (the distance from a given energy deposit to the last deposit in the track trajectory) less than a 20% of the corresponding track length². The distribution of this fraction of energy deposits for our proton sample is shown in Fig. 6.2 (left panel). We can clearly see two well separated peaks in this distribution, one centered at 0.2 and another, narrower, one centered at a higher value. The first one corresponds to non-stopping protons, as in that case the number of energy deposits towards the end of the track is uniformly distributed due to the absence of the Bragg peak. In that way, I apply a cut in this distribution, requiring that at least 30% of the simulated energy deposits sit in the last 20% of the tracks, to ensure that the Bragg peak is present.

Figure 6.2 (right panel) shows the distribution of the energy loss per unit length for the Geant4 simulated energy deposits of the selected stopping protons. We can see that it follows the expected shape of a Landau distribution, which describes the fluctuations of the ionisation energy losses [157]. This distribution has a characteristic asymmetric PDF, with a long right tail that translates into a high probability for high-energy ionisation losses. The origin of these fluctuations is mainly the possibility of transferring a high

²As we are applying this selection at the Geant4 level we could have simply selected the stopping protons using the `EndProcess` labels from the simulation. However, the Bragg peak identification method displayed here could serve as a starting point for a selection of stopping protons in real data.

CHAPTER 6. PARTICLE ID IN ND-GAr

2343 enough energy to an electron, so it becomes a ionising particle itself.

2344 Now, from the point of view of the reconstruction, the objects that we have available
 2345 to extract the ionisation information for the different reconstructed tracks are the
 2346 collections of dQ and dx pairs, as stated before. The dQ values come from adding up
 2347 the amplitude of all the reconstructed hits in a cluster, which is the input object to the
 2348 Kalman fit.

2349 Figure 6.3 (left panel) shows the distribution of the ionisation charge deposits
 2350 per unit length for the track in the stopping proton sample (blue line). As one can
 2351 notice, this distribution does not resemble the expected shape of the Landau PDF. This
 2352 distribution peaks sharply at 0 and has a heavy tailed behaviour. Notice, however, how
 2353 the distribution changes its shape as we group together N_{group} consecutive charge deposit
 2354 pairs (red, purple and green lines). The distribution in the $N_{group} = 4$ case already has
 2355 a shape which resembles that of the Geant4-level ionisation per unit length, so I will
 2356 proceed using this amount of reclustering for the reconstruction-level depositions.

2357 An extra factor I need to account for, when reclustering is applied, is how the overall
 2358 dQ/dx per track changes. To do so, we can look at the ratio between the median dQ/dx
 2359 after and before the reclustering. Figure 6.3 (right panel) shows the median enhancement
 2360 in dQ/dx per track for the stopping proton sample in the case $N_{group} = 4$. Fitting a
 2361 Landau distribution convolved with a Gaussian³, I estimate the most probable value of
 2362 this ratio to be $G_{group} = 2.24 \pm 0.05$.

2363 At this point, I am left with determining the conversion between the charge deposits
 2364 per unit length dQ/dx and the energy deposits per unit length dE/dx . To this end, we
 2365 need a way of comparing the two. I can use the residual range z to get a prediction of
 2366 the most probable dE/dx by using the following empirical parametrisation [158]:

$$\frac{dE}{dx}(z) = \frac{z^{\frac{1}{p}-1}}{p\Lambda^{\frac{1}{p}}}, \quad (6.4)$$

2367 which is quoted in the literature as the Bragg-Kleeman formula. In order to obtain the

³In the literature, this distribution is often referred to as Landau+Gaussian or langau. In the following, I will use LanGauss to refer to such PDF.

6.2. dE/dx MEASUREMENT IN THE TPC

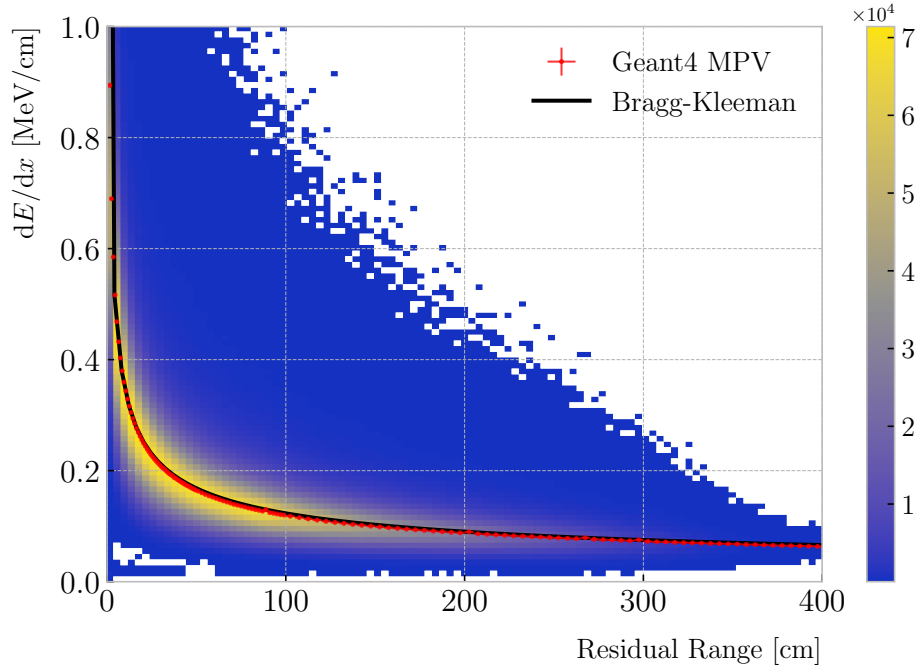


Figure 6.4: Distribution of the Geant4-simulated energy losses per unit length versus residual range for the stopping proton sample. The overlaid points represent the fitted most probable value of the dE/dx distribution in each residual range bin, whereas the curve is their best fit to the Bragg-Kleeman formula from Eq. (6.4).

2368 p and Λ parameters I perform a fit using the energy losses and the residual ranges given
 2369 by the Geant4 stage of our proton sample.

2370 Within our simulation, the residual range is sampled with a maximum size of
 2371 5 mm. Therefore, to perform the fit to the Bragg-Kleeman formula, we can use a
 2372 fine-grained residual range binning. For each of the residual range bins I extract the
 2373 dE/dx distribution and fit it to a LanGauss distribution, to obtain the value of the
 2374 most probable dE/dx in the bin together with a statistical uncertainty. I then fit Eq.
 2375 (6.4) to these most probable values and the centres of the residual range bins. This
 2376 procedure is depicted in Fig. 6.4, where I show the distribution of the energy loss per
 2377 unit length versus the residual range, together with the most probable dE/dx values
 2378 and their uncertainty in each bin (red points) and the curve with the best fit of the
 2379 Bragg-Kleeman relation to those values (black line). The best fit is obtained for the

CHAPTER 6. PARTICLE ID IN ND-GAr

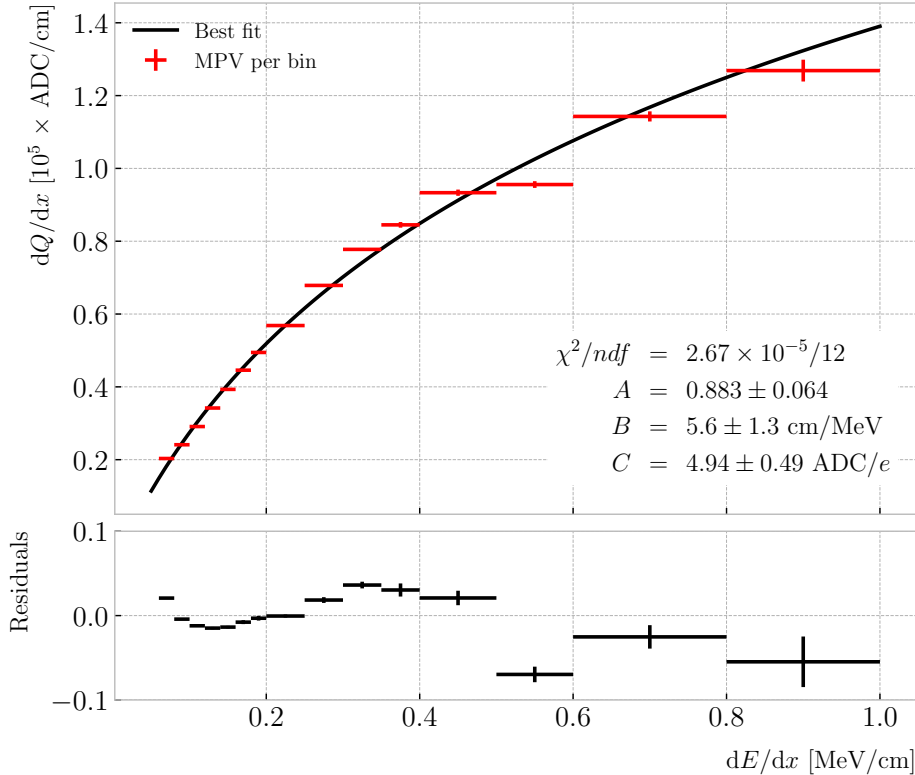


Figure 6.5: Fitted most probable dQ/dx values for each dE/dx bin (red points), obtained from the stopping proton sample. The overlaid curve (black line) represents the best fit to the logarithmic calibration function from Eq. (6.5).

2380 parameter values $p = 1.8192 \pm 0.0005$ and $\Lambda = 0.3497 \pm 0.0008 \text{ cm/MeV}^{p4}$.

2381 Having an analytical expression that relates the residual range to dE/dx , I can take
2382 our reconstruction-level residual ranges from the stopping proton sample and compute
2383 the most probable energy loss associated.

2384 In order to parametrise the charge saturation, we can use the following logarithmic
2385 function inspired by the modified box model for recombination:

$$\frac{dE}{dx} = \frac{e^{\frac{dQ}{dx} B \frac{W_{ion}}{G_{group} C}} - A}{B}, \quad (6.5)$$

2386 where A and B are the calibration parameters we need to determine, W_{ion} is the average
2387 energy to produce an electron-ion pair, G_{group} is the gain from the reclustering discussed

⁴These strange units for Λ come from dimensional analysis, just to keep the Bragg-Kleeman formula (6.4) consistent.

6.2. dE/dx MEASUREMENT IN THE TPC

Table 6.1: Calibration parameters obtained from the fit of the ND-GAr simulated stopping proton sample to the calibration function from Eq. (6.5). The fits were performed for the 10, 12, and 16-bit ADC limits.

	χ^2/ndf	Best fit $\pm 1\sigma$		
		A	B (cm/MeV)	C (ADC/e)
10-bit	$1.83 \times 10^{-6}/12$	-9.3 ± 3.9	270 ± 69	27.1 ± 5.4
12-bit	$2.67 \times 10^{-5}/12$	0.883 ± 0.064	5.6 ± 1.3	4.94 ± 0.49
16-bit	$1.44 \times 10^{-5}/12$	0.949 ± 0.024	3.53 ± 0.58	4.52 ± 0.29

above and C is the calibration constant to convert number of electrons to ADC counts, commonly refer to as gain (also to be obtained in the fit). In this case, I use a value for the electron-ion production energy of $W_{ion} = 26.4$ eV [159]. This value, used in our simulation as well, was measured for gaseous argon in normal conditions, and therefore should be checked in the future to describe correctly the high-pressure argon-CH₄ mixture of ND-GAr.

For the calibration fit I follow a procedure similar to the previous one for Eq. (6.4). Binning the dE/dx range, I fit a LanGauss distribution to the corresponding dQ/dx distribution to obtain the most probable value. The resulting data points (red bars) are shown in Fig. 6.5 (top panel), the horizontal error bars depict the width of the dE/dx bin whereas the vertical bars represent the error associated to the most probable value estimation. A fit to the logarithmic function in Eq. (6.5) is also shown (black line). For this I weighted the data points using the inverse of their relative error, obtaining a reduced chi-square value of $\chi^2/ndf = 2.22 \times 10^{-6}$. The best fit parameters I found from this fit are $A = 0.883 \pm 0.064$, $B = 5.6 \pm 1.3$ cm/MeV and $C = 4.94 \pm 0.49$ ADC/e. Figure 6.5 (bottom panel) shows the residuals between the data points and the fit.

The value for the gain I obtained from the fit is in reasonable agreement with our expectation. This value is set in GArSoft to 5 ADC/e by default.

One interesting thing to check is what induces this non-linear relation between charge and energy. The only effects that modify the amount of electrons reaching the readout planes in the simulation are the transverse diffusion and the finite electron lifetime. Once the electrons reach the readout chambers, the pad response functions are applied,

CHAPTER 6. PARTICLE ID IN ND-GAr

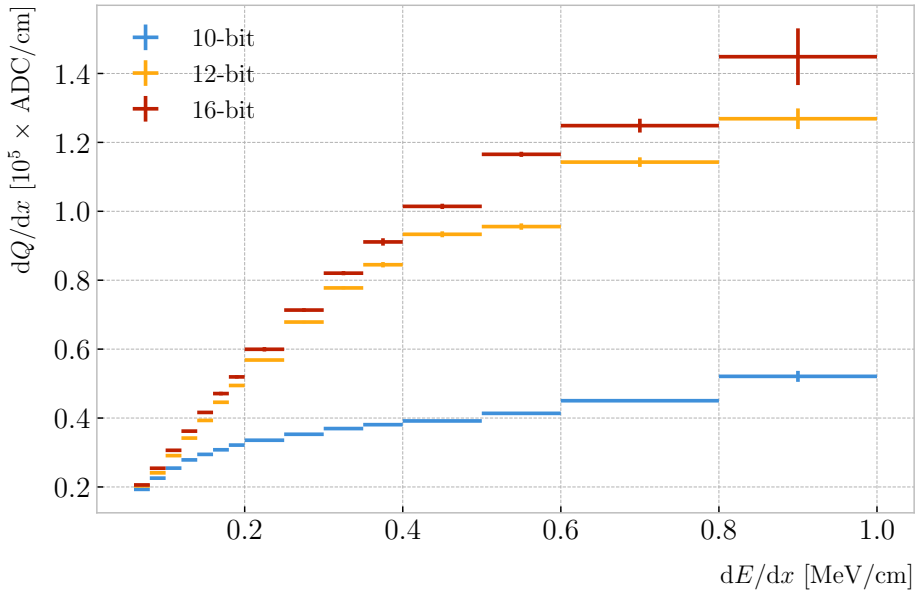


Figure 6.6: Fitted most probable dQ/dx values for each dE/dx bin for three different ADC bit limits, 10 (blue points), 12 (default, yellow points) and 16-bit (red points).

2410 together with an electrons-to-ADC conversion and the ADC saturation limit.

2411 By default, GArSot applies a 12-bit ADC limit, which can be changed in the
 2412 simulation configuration. However, it can only be increased up to 16-bit, as we represent
 2413 the ADC collection as a `std::vector<short>`. This way, I tried to change the saturation
 2414 parameter to see how it affects the relation between reconstructed charge and energy.
 2415 Figure 6.6 shows a comparison between the most probable dQ/dx for 10, 12 and 16-
 2416 bit ADC limits. As expected, the lower the limit is the sooner the charge saturates.
 2417 For higher ADC limits the relation between energy and charge remains linear up to
 2418 higher dE/dx values, but even for the 16-bit limit the saturation is noticeable for values
 2419 $\gtrsim 0.5$ MeV/cm.

2420 Table 6.1 shows the results of fitting the samples with 10 and 16-bits ADC limits to
 2421 the calibration function from Eq. (6.5), using the weights based on their relative error
 2422 as described previously. One interesting feature to notice is how different the best fit
 2423 points look for the 10-bit ADC saturation when compared to the other two, which are
 2424 consistent with each other.

2425 At this point we can compare the dE/dx distribution one gets from Geant4, i.e. the

6.2. dE/dx MEASUREMENT IN THE TPC

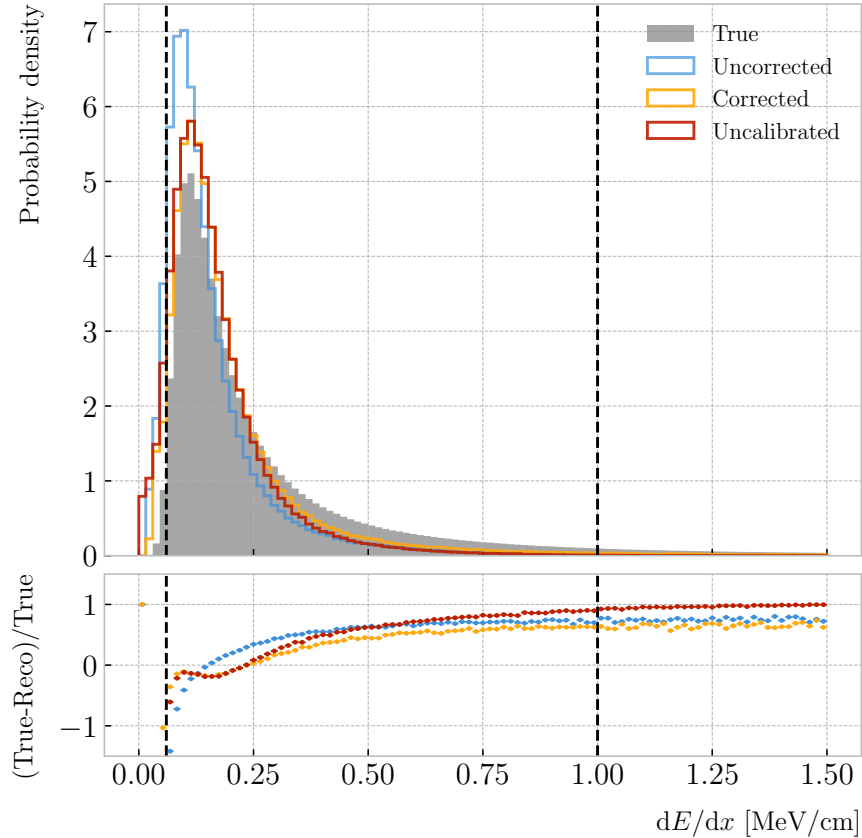


Figure 6.7: Top panel: area normalised dE/dx distributions for the true (solid grey) and the reconstructed energy deposits in the stopping proton sample, both after applying the calibration (blue) and the calibration and the normalisation correction (yellow). Also shown is the distribution obtained by applying a correction factor to the dQ/dx values but not the calibration (red). Bottom panel: fractional residuals for the uncorrected (blue), corrected (yellow) and uncalibrated (red) samples.

2426 true energy loss distribution, and the distribution I found by applying the calibration
 2427 function to our collection of reconstructed dQ/dx values. Figure 6.7 (top panel) shows
 2428 the true (solid grey) and reconstructed (blue, labeled as uncorrected) distributions
 2429 together. The dashed vertical lines indicate the region of validity of the calibration fit, i.e.
 2430 the left and right edges of the first and last dE/dx bin respectively. Notice that these
 2431 histograms are area-normalised, as the total number of true energy deposits is much
 2432 higher than the number of reconstructed charge deposits. This is due to a combination
 2433 of effects, like the finite spatial resolution of the detector, the hit clustering used in the
 2434 track fitting and the reclustering we have applied here.

CHAPTER 6. PARTICLE ID IN ND-GAr

2435 The two distributions are significantly different. That can be seen clearly when
2436 looking at the fractional residuals, shown in Fig. 6.7 (bottom panel). In particular,
2437 the position of the peak is off, which could bias the mean energy loss predictions. It
2438 seems like the difference between these may be due to an overall scaling factor. One
2439 possibility is to scale the most probable value of the reconstructed distribution to
2440 the most probable value predicted by Geant4. I do this by fitting both distributions
2441 using a LanGauss function, obtaining $dE/dx_{MPV, true} = 0.1145 \pm 0.0005$ MeV/cm and
2442 $dE/dx_{MPV, reco} = 0.0928 \pm 0.0005$ MeV/cm for the true and reconstructed most probable
2443 values respectively. These can be translated into an scaling factor $S = 0.579 \pm 0.006$.

2444 The result of applying the scaling correction can be seen in Fig. 6.7 (top panel).
2445 The corrected dE/dx distribution (yellow, labeled as corrected) peaks around the same
2446 value the true distribution does, as expected. Moreover, the high energy region is also
2447 slightly better described. For low ionisations, below the lower limit of the calibration
2448 fit, the differences between true and reconstructed are still significant. This low energy
2449 excess may be migration of some events from the peak region. The overall effect of the
2450 correction can be seen in the fractional residual plot in Fig. 6.7 (bottom panel).

2451 One can also check what happens if instead of applying the logarithmic calibration we
2452 simply scale the dQ/dx distribution (post reclustering) to have the same most probable
2453 value as the true dE/dx distribution. In this case, following an analogous procedure to the
2454 one described earlier, I found the scaling factor $S_{uncalibrated} = 0.414 \pm 0.002$ MeV/ADC⁵.
2455 The resulting distribution (red, labeled as uncalibrated) is also shown in in Fig. 6.7 (top
2456 panel). The behaviour of the new distribution is similar to the corrected case at low
2457 energy losses, around the peak of the true distribution, but it is worse at describing the
2458 high energy tail. This is expected, it is in the high ionisation regime where saturation
2459 effects apply and therefore calibration is needed.

6.2. dE/dx MEASUREMENT IN THE TPC

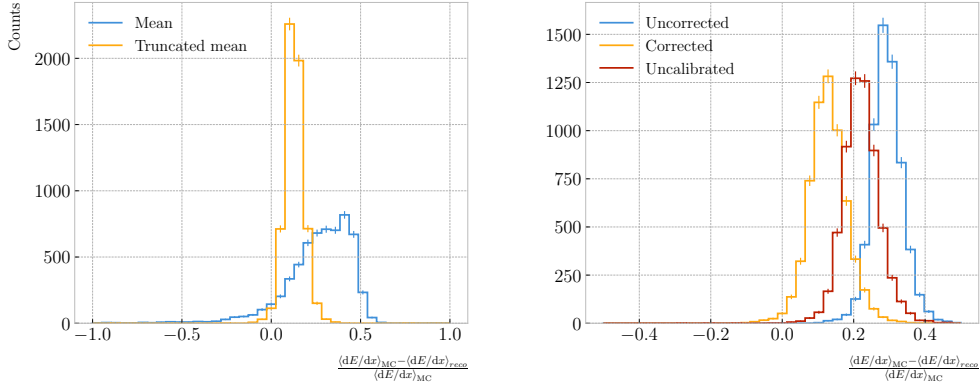


Figure 6.8: Left panel: fractional residuals between the true and the corrected dE/dx means (blue) and the 60% truncated means (yellow), for each event in the stopping proton sample. Right panel: fractional residuals between the true and the uncorrected (blue), corrected (yellow) and uncalibrated (red) dE/dx 60% truncated means, for each event in the stopping proton sample.

2460 6.2.2 Truncated dE/dx mean

2461 Once we have a collection of dE/dx values for each reconstructed track, we can compute
 2462 the corresponding most probable ionisation loss per unit length of the particle. This
 2463 is the value predicted by the Bethe-Bloch or the PAI models, and together with a
 2464 measurement of the momentum it allows for particle identification.

2465 However, estimating the most probable dE/dx value for each reconstructed track
 2466 is not a trivial task. As mentioned before, the dE/dx distributions follow Landau-like
 2467 distributions. Therefore, one should perform e.g. a LanGauss fit to correctly estimate
 2468 the most probable values. Automating this kind of fits is often problematic, as they
 2469 usually incur in convergence problems. Moreover, the reconstructed dE/dx distributions
 2470 we obtain tend to have relatively small statistics, which may also produce poor fits. In
 2471 practice, doing these unsupervised fits may degrade our performance, and a more robust
 2472 method is preferred.

2473 A possibility could be taking the mean of the reconstructed dE/dx distribution for
 2474 each particle. The problem with this approach is that the high energy Landau tail,
 2475 combined with our limited statistics, can induce large fluctuations in the computation

⁵Notice that now the scaling factor is not dimensionless, as it acts more like a conversion factor here.

CHAPTER 6. PARTICLE ID IN ND-GAr

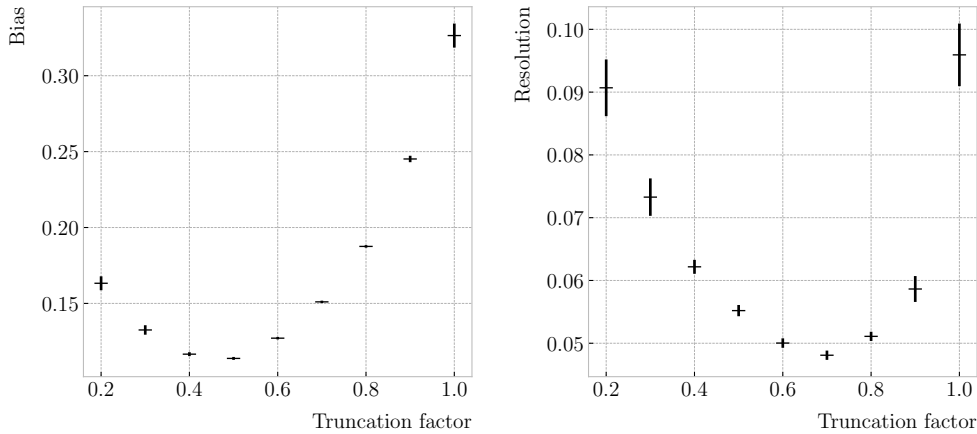


Figure 6.9: Estimated values of the mean dE/dx bias (left panel) and resolution (right panel) obtained using the corrected data from the stopping proton sample, for different values of the truncation factor.

of the mean. Imagine you have two protons with the same kinetic energy, but due to reconstruction problems in one case you did not get as many charge deposits reconstructed in its high ionisation loss region. If you do not remove the tails the computed dE/dx means will be significantly different.

In order to avoid those fluctuations, one can compute the mean of a truncated dE/dx distribution instead. By keeping only a given fraction of the lowest energy deposits we obtain an estimate of the mean energy loss that is more resilient to reconstruction inefficiencies and statistical effects. Figure 6.8 (left panel) shows a comparison between the $\langle dE/dx \rangle$ computed by taking the mean of the full distribution (blue line) and the 60% lowest energy clusters (yellow line), for the stopping proton sample. The fractional residuals are computed for each proton, taking the corresponding means using their collections of true and reconstructed energy deposits. One can see that using the simple mean translates into a high bias and uncertainty in the $\langle dE/dx \rangle$ estimation, whereas applying the truncation reduces both significantly.

Additionally, I performed a comparison between the 60% truncated mean dE/dx obtained using the different calibration methods discussed earlier, namely the uncorrected (blue), corrected (yellow) and uncalibrated (red) distributions. The results are shown in Fig. 6.8 (right panel). While the widths of these distributions are similar, the bias

6.2. dE/dx MEASUREMENT IN THE TPC

2494 obtained for the corrected sample, i.e. calibration function and correction factor applied,
 2495 is a factor of ~ 2 lower than in the uncalibrated case and almost three times smaller
 2496 than for the uncorrected sample.

2497 The next step is to optimise the level of truncation we are going to apply to our
 2498 data. To do so, I used different truncation factors, i.e. the percentage of energy-ordered
 2499 reconstructed energy deposits we keep to compute the mean, on the corrected dE/dx
 2500 sample of the stopping protons. Then, following the same procedure of computing the
 2501 fractional residuals as before, I fitted the resulting histograms using a double Gaussian
 2502 function. This is simply the sum of two Gaussian functions of the type:

$$g(x; \mu, \sigma, A) = A e^{-\frac{(x-\mu)^2}{2\sigma^2}}. \quad (6.6)$$

2503 I do not add the classical normalisation factor of the Gaussian, $1/\sqrt{2\pi}\sigma$, therefore
 2504 the amplitude A simply represents the maximum of the function. One of the two
 2505 Gaussian functions describes the core part of the distribution, while the other captures
 2506 the behaviour of the tails.

2507 For each truncation factor, I look at the bias and the resolution I obtain. I define
 2508 these as the weighted means of the corresponding parameters in the fits:

$$\bar{x} = \frac{A_{core} x_{core} + A_{tail} x_{tail}}{A_{core} + A_{tail}}, \quad (6.7)$$

2509 where A_{core} and A_{tail} are the amplitudes of the core and tail distributions respectively
 2510 and x is either the mean μ or the width σ of said distributions.

2511 Figure 6.9 shows the bias (left panel) and the resolution (right panel) I obtained
 2512 for the stopping proton sample, using different values of the truncation. From these, it
 2513 can be seen that a truncation factor of 50% minimises the bias in the estimation, while
 2514 70% gives the best resolution. That way, I settled on the intermediate value of 60%
 2515 truncation, which yields a $\langle dE/dx \rangle$ resolution of 5.00 ± 0.08 % for stopping protons.

CHAPTER 6. PARTICLE ID IN ND-GAr

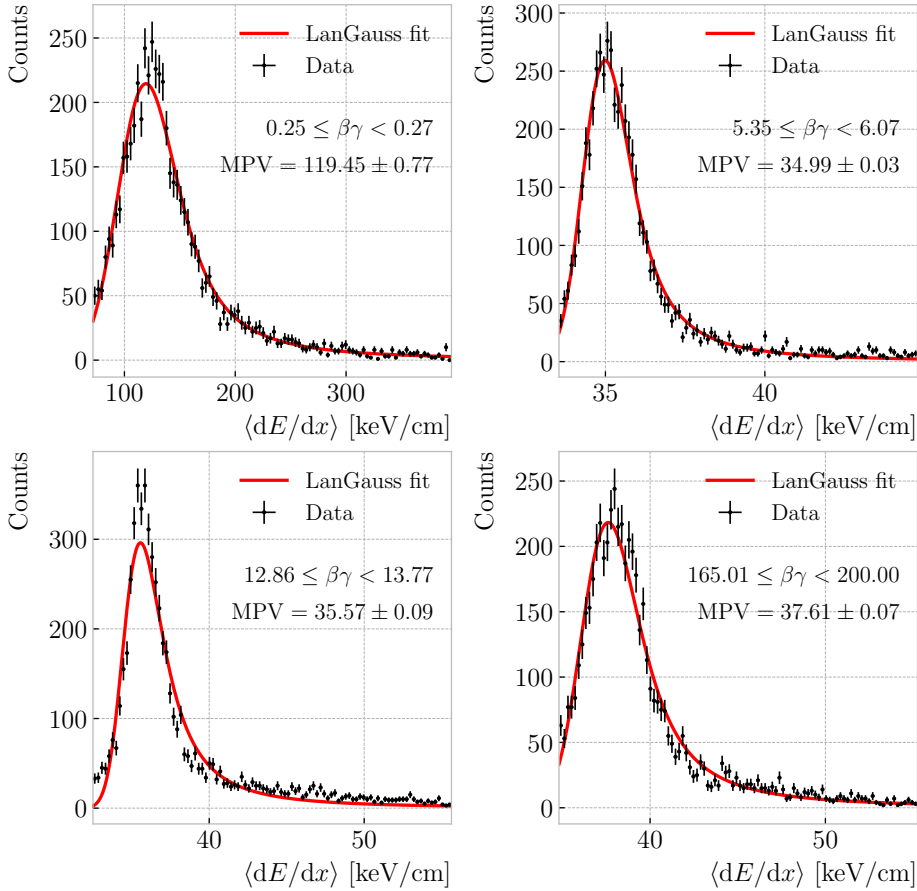


Figure 6.10: Examples of the truncated mean dE/dx LanGauss fits for various $\beta\gamma$ bins, from a simulated FHC neutrino sample.

2516 6.2.3 Mean dE/dx parametrisation

2517 Now that we have a way to estimate the mean energy loss of a particle in the HPgTPC,
 2518 we can determine the value of the free parameters in the ALEPH formula, Eq. (6.3).
 2519 For this, I used a sample of 10^5 reconstructed FHC neutrino events inside ND-GAr. In
 2520 this case I cannot use the stopping proton sample, as we need to cover the full kinematic
 2521 range of interest for the neutrino interactions in our detector.

2522 The original data does not contain an estimation of the velocity of the tracks, instead
 2523 the tracks have a value for the reconstructed momentum and the associated PDG code
 2524 of the Geant4-level particle that created the track. Therefore, one can select some of the
 2525 particles in the data, in this case I selected electrons, muons, pions and protons, and

6.2. dE/dx MEASUREMENT IN THE TPC

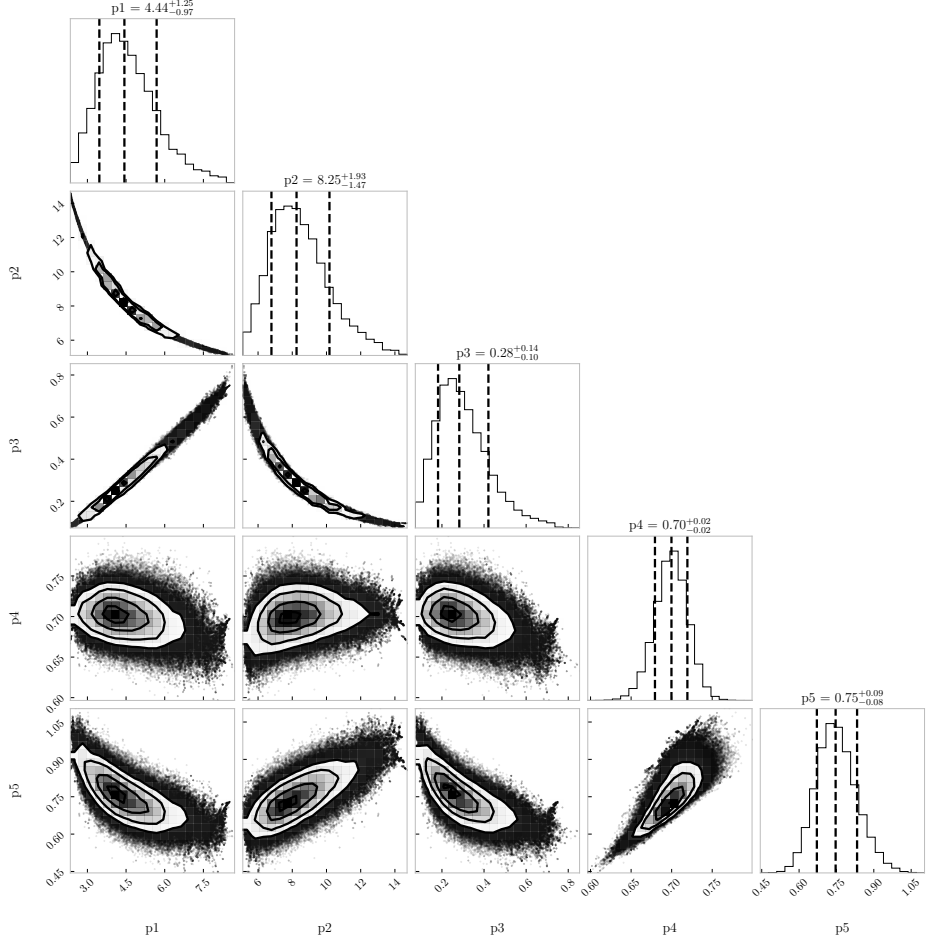


Figure 6.11: Resulting one and two dimensional projections of the posterior probability distributions of the ALEPH $\langle dE/dx \rangle$ parameters obtained by fitting the 60% truncated mean dE/dx values from a FHC neutrino sample in ND-GAr. The vertical dashed lines in the 1D distributions represent the 16th, 50th and 84th percentiles.

2526 compute β and γ using the reconstructed momentum and their mass. In terms of $\beta\gamma$
 2527 the mean dE/dx does not depend on the particle species, so one can consider all the
 2528 dataset as a whole. For this fit, I will express β in terms of the $\beta\gamma$ product as:

$$\beta = \frac{\beta\gamma}{\sqrt{1 + (\beta\gamma)^2}}, \quad (6.8)$$

2529 which can be easily proven from the definition of γ .

2530 Next, I bin the data in $\beta\gamma$. I chose a fine binning so as to capture the different
 2531 features of the ionisation curve. Instead of fixing the bin width, I select them so each one

CHAPTER 6. PARTICLE ID IN ND-GAr

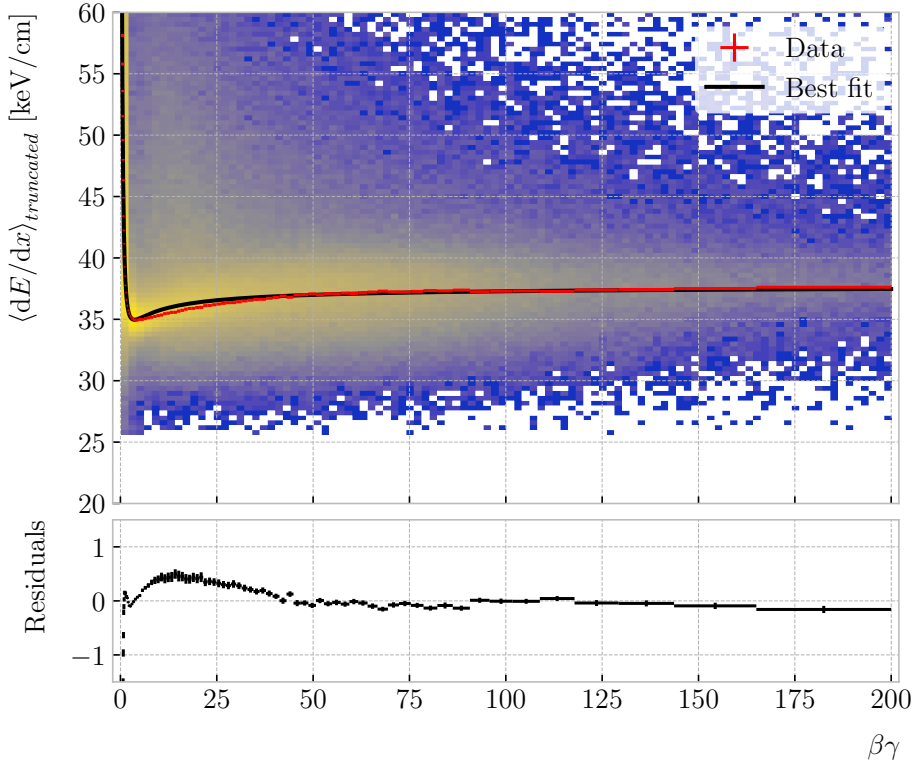


Figure 6.12: Truncated mean dE/dx obtained for the FHC neutrino sample as a function of the $\beta\gamma$ product (upper panel). Also shown are the fitted most probable values for each $\beta\gamma$ bin (red points) and the best fit obtained using the ALEPH parametrisation (black line). The residuals resulting from the fit are shown in the lower panel.

2532 has approximately the same statistics. Then, for each $\beta\gamma$ slice, I compute the median
 2533 and the interquartile range (IQR) of the $\langle dE/dx \rangle$ distribution. Using these, I make a
 2534 histogram in the range [median – IQR, median + 5 IQR], which I fit to a LanGauss
 2535 function in order to extract the MPV. Using this range accounts for the asymmetric
 2536 nature of the distributions, while also helps avoiding a second, lower maximum present
 2537 at low $\beta\gamma$, probably a result of reconstruction failures.

2538 A few examples of these fits are shown in Fig. 6.10. The chosen values of $\beta\gamma$ sit in
 2539 very distinct points along the $\langle dE/dx \rangle$ curve, going from the high ionisation region at
 2540 low velocities (top left panel), to the minimum point (top right panel), the beginning of
 2541 the relativistic rise (bottom left panel), and the plateau produced by the density effect
 2542 (bottom right panel).

6.2. dE/dx MEASUREMENT IN THE TPC

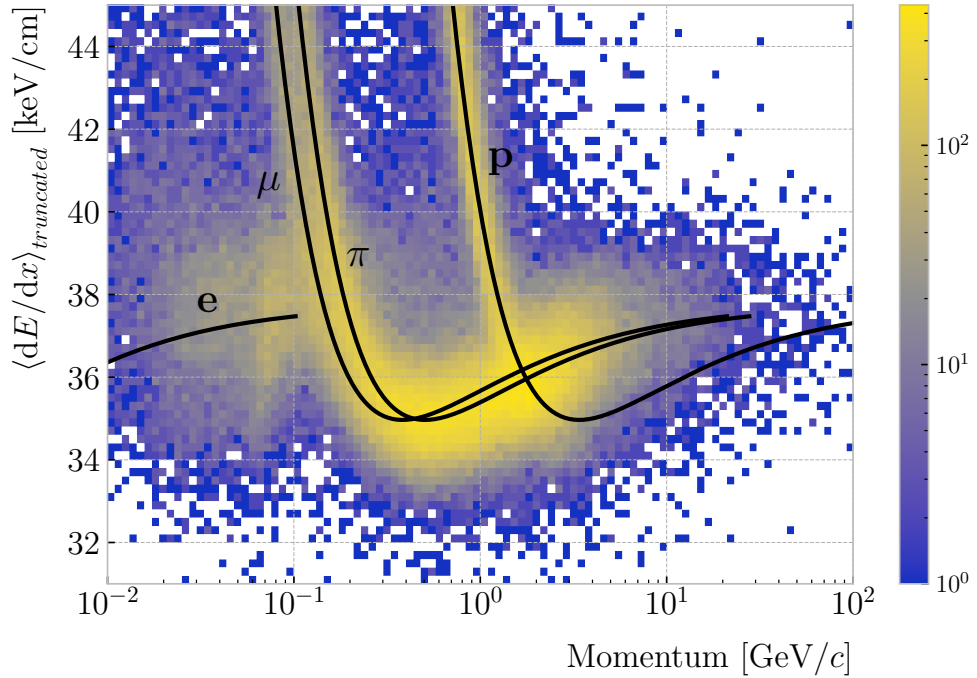


Figure 6.13: Distribution of the 60% truncated mean dE/dx versus reconstructed momentum for the FHC neutrino sample. The black lines indicate the predictions of the ALEPH parametrisation for electrons, muons, charged pions and protons.

2543 I used the resulting most probable $\langle dE/dx \rangle$ values and the centres of the $\beta\gamma$ bins as
 2544 the points to fit to the ALEPH formula. For this particular fit I used the least-squares
 2545 method to get a first estimation of the ALEPH parameters. Applying some uniform
 2546 priors, I then used these values as the starting point of a 100000 steps MCMC. Figure 6.11
 2547 shows the posterior probability distributions I obtain for each parameter. The reported
 2548 best fit points are based on the 16th, 50th, and 84th percentiles in the marginalised
 2549 distributions.

2550 The resulting fit (black line), compared to the data points (red points) and the
 2551 underlying distribution is shown in Fig. 6.12 (top panel). The overall fit is good, with a
 2552 reduced chi-squared of $\chi^2/ndf = 1.02$. However, there are some regions where the fit
 2553 does not describe the data correctly, like the very low $\beta\gamma$ regime, where the fit severely
 2554 underestimates for energy losses $\gtrsim 50$ keV/cm, and the start of the relativistic raise,
 2555 where we have a slight overestimation. This is a result of those points having a larger
 2556 uncertainty when compared to the ones around the dip or the plateau areas. These

CHAPTER 6. PARTICLE ID IN ND-GAr

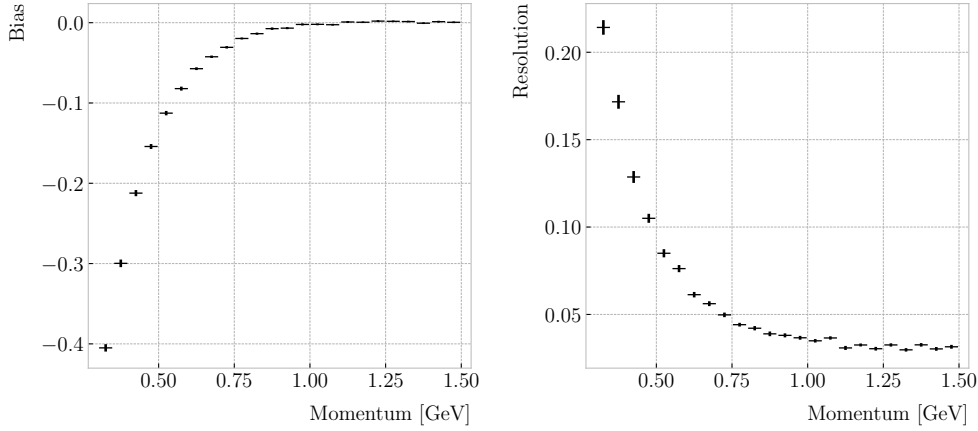


Figure 6.14: Estimated values of the mean dE/dx bias (left panel) and resolution (right panel) obtained for the true protons in a FHC neutrino sample.

2557 differences can be better seen in the residual plot, Fig. 6.12 (bottom panel).

2558 6.2.4 Particle identification

2559 6.3 Muon and pion separation in the ECal and MuID

2560 As it could be seen from Fig. 6.13, it is not possible to separate muons and charged pions
 2561 in the HPgTPC using dE/dx for momenta $\gtrsim 300 \text{ MeV}/c$. In ND-GAr, approximately
 2562 70% of the interactions in FHC mode will be ν_μ CC (compared to the 47% of $\bar{\nu}_\mu$ CC
 2563 interactions when operating in RHC mode), while 24% are neutral currents. Out of
 2564 these, around 53% and 47% of them will produce at least one charged pion in the final
 2565 state, respectively. Figure 6.15 shows a comparison between the spectra of the primary
 2566 muons and the charged pions for ν_μ CC interactions in ND-GAr producing one or more
 2567 charged pions. From this, one can see that (i) the majority of muons and charged pions
 2568 are not going to be distinguishable with a $\langle dE/dx \rangle$ measurement, and that (ii) particle
 2569 identification is necessary both to classify correctly the ν_μ CC events and identify the
 2570 primary muon within them.

2571 ND-GAr features two other subdetectors which can provide additional information
 2572 for this task, namely the ECal and MuID. The current ECal design, described in (ref
 2573 section), consists of 42 layers, made of 5 mm of Pb, 7 mm of plastic scintillator and a

6.3. MUON AND PION SEPARATION IN THE ECAL AND MUID

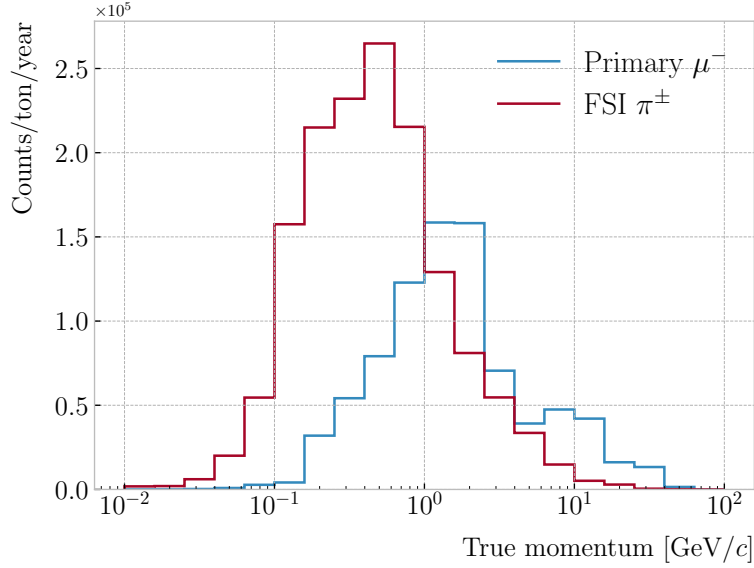


Figure 6.15: True momentum distribution for the primary muon in ν_μ CC $N\pi^\pm$ interactions inside the fiducial volume of ND-GAr (blue line), compared to the post FSI charged pion spectrum (red line).

2574 1 mm PCB board. The total thickness of this calorimeter is 1.66 nuclear interaction
 2575 lengths or 1.39 pion interaction lengths. The Muid design is in a more conceptual
 2576 stage, however it is envisioned to feature layers with 10 cm of Fe and 2 cm of plastic
 2577 scintillator⁶. With its three layers, it will have a thickness of 1.87 or 1.53 nuclear or pion
 2578 interaction lengths, respectively.

2579 Because pion showers are dominated by inelastic nuclear interactions, the signatures
 2580 of these particles in the calorimeter will look significantly different from those of muons.
 2581 Although our ECal is not thick enough to fully contain the hadronic showers of the
 2582 charged pions at their typical energies in FHC neutrino interactions, they can still be
 2583 used to understand whether the original particle was more hadron-like or MIP-like. In
 2584 Fig. 6.16 I show two examples of energy distributions created by a muon (left panel)
 2585 and a charged pion (right panel) of similar momenta interacting in the ECal. These
 2586 figures represent the transverse development of the interactions. For each of them, I
 2587 computed the principal component and centre of mass of the interaction, projecting

⁶It is not mentioned anywhere, but I assume that there should also be another layer of PCB board of 1 mm. However, in this case its contribution to the total thickness of the sampling calorimeter would be negligible.

CHAPTER 6. PARTICLE ID IN ND-GAr

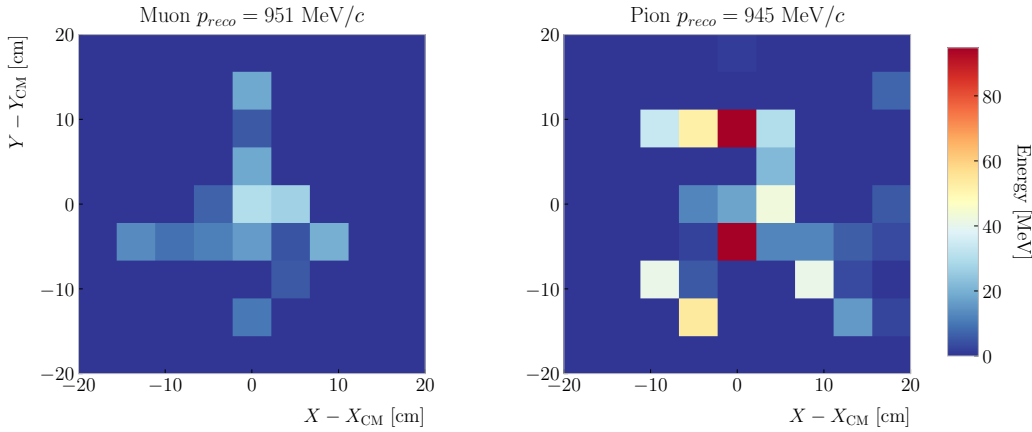


Figure 6.16: Distributions of energy deposits in the ECal for a muon (left panel) and a charged pion (right panel) with similar momenta. The energy is projected onto the plane perpendicular to the principal component of the hits, and the positions are relative to the center of the interaction.

2588 the position of the hits onto the plane perpendicular to that direction, and taking the
 2589 distances relative to the centre. It can be seen that the muon follows an almost MIP-like
 2590 behaviour, being the central bin in the histogram the one with the highest deposited
 2591 energy. On the other hand, the pion not only deposits more energy overall, but also this
 2592 energy is more spread-out among the different hits. It is this kind of information that
 2593 would allow us to tell apart muons from pions.

2594 This way, I identify three main action points that need to be addressed if one wants
 2595 to use these detectors to distinguish between muons and charged pions. These are:

- 2596 1. the way we make the associations between tracks in the HPgTPC to the activities
 2597 (what in GArSoft we call clusters) in the ECal and the MuID,
- 2598 2. what variables or features one can extract from the calorimeters that encapsulate
 2599 the information we are interested about,
- 2600 3. and how to carry out the classification problem.

6.3. MUON AND PION SEPARATION IN THE ECAL AND MUID

2601 6.3.1 Track-ECal matching

2602 One of the main players in the muon and pion separation is the way we associate clusters
2603 in the ECal to reconstructed tracks in the TPC. Missing some associations or making
2604 wrong ones can bias the ECal quantities that we can use for classifying particles. The
2605 current algorithm in GArSoft provides precise associations, i.e. most of the associations
2606 that it produces are correct, but it appears to miss an important number of associations
2607 (at least when using the default configuration).

2608 The current TPC track-ECal cluster association algorithm is divided in four parts.
2609 It first checks whether the track end point fulfils certain conditions to be extrapolated.
2610 There are two cut values in this step, one for the drift direction and other radial.

2611 If the point can be extrapolated, the code computes the coordinates of the centre
2612 of curvature using the Kalman fit estimates at the track end (y , z , $1/R$, ϕ , $\tan\lambda$). It
2613 then compares the distance between this and the cluster in the (z, y) plane with R . This
2614 introduces another cut in the perpendicular direction.

2615 The next step is different for clusters in the barrel or in one of the end caps. If it
2616 is a barrel cluster the algorithm extrapolates the track up to the radial distance of the
2617 cluster. There are three possible outcomes, the extrapolated helix can cut the cylinder
2618 of radius r_{clus} two, one or zero times. I get the cut point that is closer to the cluster and
2619 check that it is either in the barrel or the end caps. Computing the difference between
2620 the x coordinates of the cluster and the extrapolated point, the module checks that this
2621 is not greater than a certain cut. If the cluster is in an end cap, I propagate the track
2622 up to the x position of the cluster. Then, the algorithm computes the angle in the (z, y)
2623 plane between the centre of curvature and the cluster, α , and the centre of curvature
2624 and the propagated point, α' . A cut is applied to the quantity $(\alpha - \alpha')R$.

2625 If the cluster contains more than a certain number N of hits, I apply an extra cut to
2626 the dot product of the direction of the track at the propagated x value and the cluster
2627 direction.

2628 The code makes sure to only associate one end of the track (if any) to a cluster.

CHAPTER 6. PARTICLE ID IN ND-GAr

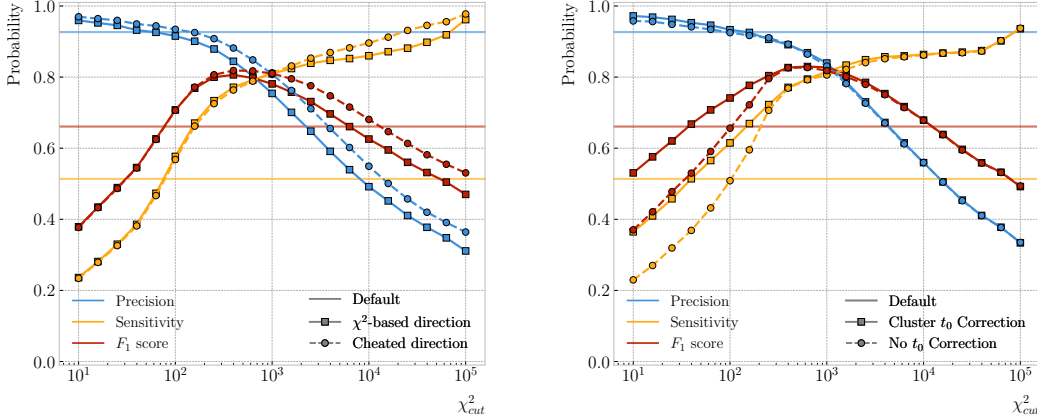


Figure 6.17: Left panel: comparison between the precision (blue), sensitivity (yellow) and F_1 score (red) obtained for the default (horizontal lines) and new algorithms, both with the χ^2 -based direction estimator (squares) and cheating the directions (circles), for different values of the chi^2 cut. Right panel: comparison of the performance of the new algorithm when applying the cluster t_0 correction (squares) and when (circles).

2629 However, it can associate more than one track to the same cluster. This makes sense,
2630 as different particles can contribute to the same cluster in the ECal, but it makes it
2631 difficult to quantify the relative contributions of the tracks to a certain cluster.

2632 As a way of comparing the performance of this algorithm, a new, simpler association
2633 module was written. The goal was to have a simple and robust algorithm, which depends
2634 on as few parameters as possible and that can produce a one-to-one matching between
2635 tracks and ECal clusters.

2636 For each reconstructed track, the new algorithms applies the same procedure to the
2637 forward and the backward fits irrespective of their end point positions. It first gets the
2638 Kalman fit parameters at the corresponding end point together with the X position, x_0 ,
2639 (y_0 , z_0 , $1/R$, ϕ_0 , $\tan\lambda$).

2640 For each ECal cluster, I compute the radial distance to the centre of the TPC and
2641 find the ϕ value in the range $[\phi_0, \phi_0 + \text{sign}(R)\phi_{max}]$ that makes the propagated helix
2642 intersect with the circle defined with such radius. The (x, y, z) position of the helix for
2643 the ϕ value found (if any) is then computed. In case there are two intersections, I keep
2644 the one that minimises the distance between (y, z) and (y_c, z_c) .

2645 I then calculate χ^2 value based on the Euclidean distance between the propagated

6.3. MUON AND PION SEPARATION IN THE ECAL AND MUID

2646 point and the cluster:

$$\chi^2/ndf = \frac{\sum_{n=0}^2 (x^{(n)} - x_c^{(n)})^2}{3}. \quad (6.9)$$

2647 If there was no intersection I store a -1 instead. In the end, for each reconstructed track
2648 in the event one ends up with two collections of χ^2 values, one for each ECal cluster
2649 and fit directions.

2650 The current code only supports having ECal clusters associated to one end of each
2651 track. We have two options to decide what track end to keep. The first one tries to
2652 cheat the selection, looking at the distance between the two track ends and the true
2653 start position of the associated MC particle. The second one keeps the track end with
2654 more χ^2 entries below the cut.

2655 This feature of only considering one track end limits the algorithm, making it not
2656 suitable for reconstructing events with particles originating outside the TPC. However,
2657 as for the moment the main concern of the group is the study of neutrino interactions
2658 off the gaseous argon, this is an acceptable assumption.

2659 In order to associate a cluster to a track, I take all clusters with a χ^2 value in the
2660 range $[0, \chi_{cut}^2]$. If a cluster has been assigned to more than one track we leave it with
2661 the one with the lowest χ^2 .

2662 This default behaviour of the algorithm can be modified to associate more than one
2663 track to each cluster. Not only that, but the χ^2 values can be used to assign relative
2664 weights to the different contributions.

2665 To evaluate the performance of the association method, I use a binary classification
2666 approach. In this case, I check the leading MC Track IDs associated to the reconstructed
2667 tracks and ECal clusters. I count an association as true positive (TP) if both Track
2668 IDs coincide. An association is considered false positive (FP) when the Track IDs are
2669 different. If a cluster has not been associated to any track but it shares the Track ID
2670 with a reconstructed track it is counted as a false negative (FN).

2671 For the testing, I used a sample of 10000 FHC neutrino events inside the HPgTPC.
2672 Figure 6.17 (left panel) shows the precision (blue line), sensitivity (yellow line), and F_1

CHAPTER 6. PARTICLE ID IN ND-GAr

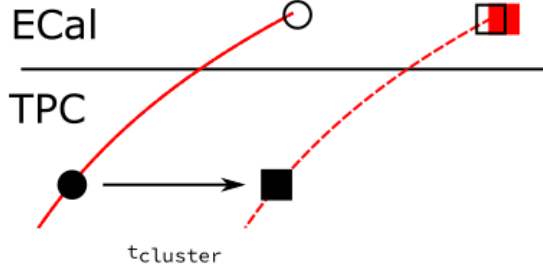


Figure 6.18: Schematics of a possible option to deal with track-ECal associations in non-zero t_0 neutrino interaction events, trying to correct for the drift direction uncertainty in a cluster-by-cluster basis using the cluster time, $t_{cluster}$.

2673 score (red line) I obtained for different values of χ^2_{cut} . For comparison, the same metrics
 2674 computed for the default algorithm with the current configuration are also shown (dashed
 2675 lines). In the case of the new algorithm, I used both the χ^2 -based method to estimate
 2676 the track direction described earlier (square markers) and the cheated direction from the
 2677 Geant-level information (circle markers). For either of these we achieve similar values of
 2678 the precision compared to the old code, while having a considerably higher sensitivity.
 2679 It can be seen that cheating the direction of the tracks only makes a difference at high
 2680 χ^2_{cut} , past the optimal value of the cut around the F_1 score maximum. Therefore, I set
 2681 the χ^2 method as the default.

2682 One of the possible weak points of this approach is that it relies on the position along
 2683 the drift direction to make the decisions. Within the current ND-GAr design implemented
 2684 in GArSoft, the timing information is provided by the ECal. That effectively means
 2685 that prior to make the track-ECal associations the reconstructed x positions of the track
 2686 trajectories differ from the simulated ones by an amount:

$$x_{reco}^{(n)} - x_{sim}^{(n)} = v_{drift} t_0, \quad (6.10)$$

2687 where v_{drift} is the mean drift velocity in our medium and the initial time is in the range
 2688 $t_0 \in [0, t_{spill}]$ where t_{spill} is the spill length. For a $10 \mu\text{s}$ spill this translates into a
 2689 maximum 30 cm uncertainty on the drift direction position.

2690 The current default in GArSoft sets $t_0 = 0$, but the functionality to randomly sample

6.3. MUON AND PION SEPARATION IN THE ECAL AND MUID

2691 this within the spill time is in place. Therefore, we need to understand what is the impact
2692 of a non-zero t_0 on the associations algorithm and foresee possible ways of minimising a
2693 loss in performance.

2694 Figure 6.18 represents a possible option to tackle the association problem when
2695 having events with a non-zero initial time t_0 . The black and white circles represent the
2696 original points, whereas the squares indicate the corrected positions. The end points of
2697 the track and the propagated points up to the cluster radius are indicated using filled
2698 and unfilled markers respectively. The red square represents the position of the cluster.

2699 Here I try to correct for the drift coordinate position using the time associated to the
2700 cluster. Assuming that the drift time is much larger than the propagation time, $t_{cluster}$
2701 could be used as a good estimation of the t_0 . An alternative can be using the earliest
2702 time associated to a hit in said cluster. Doing this for each cluster before computing
2703 the χ^2 value could be used as an alternative to knowing the specific value of the t_0 , as
2704 when the association is correct this will provide the right correction but its impact is
2705 small enough to not change the position significantly in the case the cluster does not
2706 correspond to a given track.

2707 I tested the effect of this correction again using a sample of 10000 FHC neutrino
2708 events. Figure 6.17 (right panel) shows the precision (blue line), sensitivity (yellow line),
2709 and F_1 score (red line) for the case the cluster t_0 correction is applied (square markers)
2710 and for the no correction case (circle markers), as a function of χ^2_{cut} . In this case, the
2711 differences are particularly notorious at low values of the cut. It makes sense, as the t_0
2712 effect becomes subdominant when the distance we consider grows large. Overall, the
2713 correction increases the sensitivity while keeping the precision almost unchanged. As a
2714 result, I apply the t_0 correction to the generated samples as the default.

2715 6.3.2 Classification strategy

2716 The problem of the muon and charged pion separation has to be viewed in the broader
2717 context of the particle identification in our detector. Focusing on the beam neutrino
2718 interactions, it is clear that we are going to have muons and pions spanning a broad

CHAPTER 6. PARTICLE ID IN ND-GAr

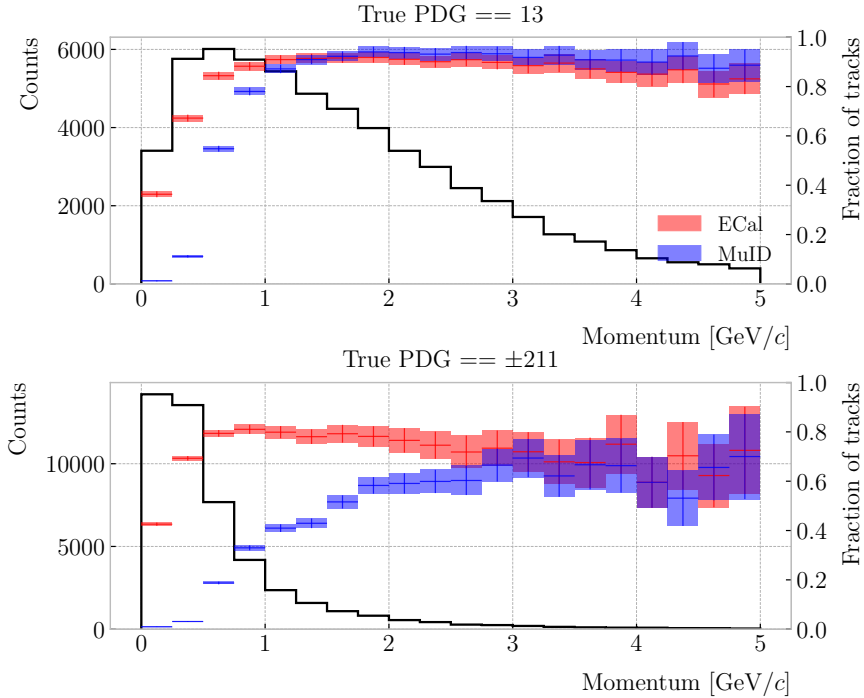


Figure 6.19: Momentum distribution for the reconstructed muons (top panel) and charged pions (bottom panel) in a FHC neutrino sample, together with the fraction of them reaching the ECal (red) and MuID (blue). Each entry corresponds to a reconstructed track, backtracked to a true muon or pion which has not produced any other reconstructed track.

2719 momentum range. Not only that, but we will also have other particles with similar
 2720 characteristics that will make the classification even more challenging. Therefore, we are
 2721 presented with a task that will depend heavily on the kinematic range we are looking at
 2722 each time, as both the available information and the possible impurities of other particle
 2723 species vary.

2724 For instance, distinguishing muons from pions could be difficult at low momenta, as
 2725 a great number of them do not reach the ECal. Therefore, we could think of tailoring a
 2726 version of the classification for that particular case, which could be complemented with
 2727 a dE/dx measurement. Likewise, for momenta $\gtrsim 1$ GeV muons and pions reach the
 2728 calorimeters efficiently, but so do protons. Because of this, one can try to train another
 2729 classifier for this energy range, and rely on other methods to remove as many of the
 2730 protons as possible.

6.3. MUON AND PION SEPARATION IN THE ECAL AND MUID

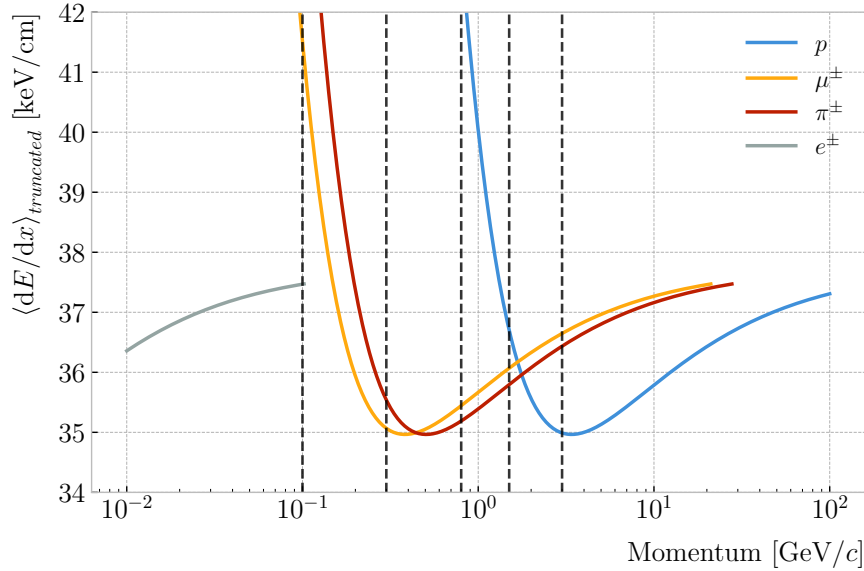


Figure 6.20: Predicted truncated mean dE/dx versus momentum, for electrons, muons, charged pions and protons, obtained using the ALEPH parametrisation. The vertical dashed lines represent the boundaries of the six regions used for the muon and pion classification training.

2731 Figure 6.19 shows the momentum distribution of the reconstructed muons (top) and
 2732 pions (bottom) in a FHC sample. It also contains the fraction of particles reaching the
 2733 ECal (red) and MuID (blue), for the different momentum bins. In Fig. 6.20 I show the
 2734 mean dE/dx of different particles as a function of the momentum, computed using the
 2735 ALEPH parametrisation with the best fit parameters found in Subsec. 6.2.2.

2736 Using these two figures as references, I decided to approach the classification by
 2737 dividing the problem into six different momentum regions. A summary of these can be
 2738 found in Tab. 6.2. The basic idea is to exploit all the information that is available in
 2739 each region and . For the problem at hand, I prepared separated samples of isotropic
 2740 single muons and pions, with momenta uniformly distributed along the corresponding
 2741 momentum range. Each sample contains 50000 events of the corresponding particle
 2742 species. I did not generate samples for the first region, as it is assumed that the separation
 2743 can be achieved using dE/dx only. For the last region, I generated particles up to a
 2744 momentum of 10 GeV/c , as that is well above the typical energies of muons and pions
 2745 from FHC neutrino interactions in ND-GAr.

CHAPTER 6. PARTICLE ID IN ND-GAr

Table 6.2: Momentum ranges and description of the PID approach assumed for the muon and pion classification task.

Momentum range	Description
$< 0.1 \text{ GeV}/c$	All tracks can be separated with dE/dx
$[0.1, 0.3) \text{ GeV}/c$	Use ECal for reaching muons and pions, dE/dx for the rest
$[0.3, 0.8) \text{ GeV}/c$	Use ECal for muons and pions, dE/dx for protons
$[0.8, 1.5) \text{ GeV}/c$	Use ECal and MuID for muons and pions, dE/dx for protons
$[1.5, 3.0) \text{ GeV}/c$	Use ECal and MuID for muons and pions, ToF for protons
$\geq 3.0 \text{ GeV}/c$	Use ECal and MuID for muons and pions, dE/dx and ToF for protons

2746 Additionally, I prepared another sample of 100000 FHC neutrino events. For each
 2747 interaction, I select the reconstructed particles which were backtracked to true muons or
 2748 charged pions. I use this dataset to perform validation checks, to see how the models
 2749 trained with the single particle data generalise to a more realistic scenario.

2750 To tackle this classification problem, I make use of Boosted Decision Trees (BDT). A
 2751 decision tree uses a flowchart-like structure to make decisions based on some input data.
 2752 It starts from a root node, which represents the complete dataset, and then it splits
 2753 this based on the variable or feature which gives the best separation between classes,
 2754 creating two new nodes. The process repeats for each node until it reaches a certain
 2755 limit, like a maximum number of splits or some tolerance criteria. The last set of nodes
 2756 are often called leave nodes, and represent the final prediction of the classifier.

2757 Boosting refers to a family of methods to combine the predictions from multiple
 2758 classifiers, following a sequential approach where each new model learns from the errors
 2759 of the previous one. The process starts with a simple decision tree, which is used to
 2760 make predictions on the training data. Then, the data points misclassified by the first
 2761 model are assigned higher weights, and another decision tree is trained on the data with
 2762 adjusted weights. The predictions of the two trees are then combined, and the cycle
 2763 repeats for a predefined number of iterations. Gradient boosting uses the direction of
 2764 the steepest error descent to guide the learning process and improve the accuracy with
 2765 each iteration.

6.3. MUON AND PION SEPARATION IN THE ECal AND MuID

2766 6.3.3 Feature selection and importance

2767 Using the reconstructed tracks as a starting point, I compute a number of ECal and
2768 MuID variables for each of them. As there can be more than one cluster associated to a
2769 track, what I do is collect all associated clusters and compute these variables from the
2770 complete collection of associated hits. For the MuID, because it only features three layers
2771 and typically there will be less hits, I also allow single hits to be associated with tracks⁷.
2772 I can roughly divide the variables in three types: energy-related, geometry-related and
2773 statistical. In the following, I briefly describe the variables related exclusively to the
2774 ECal:

2775 • Energy-related ECal

- 2776 – ECal total energy (ClusterTotalEnergy): sum of the energy of all the ECal
2777 hits.
- 2778 – Mean ECal hit energy (HitMeanEnergy): mean of the hit energy distribution.
- 2779 – Standard deviation ECal hit energy (HitStdEnergy): standard deviation of
2780 the hit energy distribution.
- 2781 – Maximum ECal hit energy (HitMaxEnergy): maximum of the hit energy
2782 distribution.

2783 • Geometry-related ECal

- 2784 – Mean distance hit-to-cluster (DistHitClusterMean): mean of the distance
2785 distribution between the hits and the corresponding cluster's main axis.
- 2786 – RMS distance hit-to-cluster (DistHitClusterRMS): root mean square of the
2787 distance distribution between the hits and the corresponding cluster's main
2788 axis.

⁷At the reconstruction level what happens is that non-clustered hits are put into single hit clusters, instead of being thrown away. This is necessary to keep the consistency of the track-cluster association code.

CHAPTER 6. PARTICLE ID IN ND-GAr

- 2789 – Maximum distance hit-to-centre (DistHitCenterMax): maximum of the
2790 distance distribution between the hits and the centre of the TPC.
- 2791 – Time-of-Flight velocity (TOFVelocity): slope obtained when fitting a straight
2792 line to the hit time versus hit distance to the centre (i.e. $d = v \times t$).

2793 • Energy and geometry ECal

- 2794 – Radius 90% energy (Radius90E): distance in the hit-to-cluster distribution
2795 for which 90% of the total energy is contained in the hits that are closer to
2796 the axis (i.e. radius that contains 90% of the energy).

2797 • Statistical ECal

- 2798 – Number of hits (NHits): total number of hits associated to the track.
- 2799 – Number of layers with hits (NLayers): not really a count of all layers with
2800 hits but the difference between the last and the first layer with hits.

2801 Figure 6.21 shows the distributions of three different ECal variables, separating true
2802 muons (blue) and charged pions (red), for the five momentum ranges considered. I chose
2803 to show one feature from each category, namely the mean energy per hit (left column),
2804 the mean distance between the hits and the centre of the cluster (middle column), and
2805 the number of ECal layers with hits (right column). These give an idea of the separating
2806 power of the different features, and how it changes considerably with the energy. In
2807 the number of layers with hits distributions, the peak at 6 is due to the fact that the
2808 first six ECal layers sit inside the pressure vessel⁸. Therefore, some of the particles get
2809 stopped crossing it, never making it to the seventh layer.

2810 In the case of the MuID, because at low momenta a significant fraction of the particles
2811 do not make it past the ECal, I only consider the information coming from this detector
2812 for momenta ≥ 0.8 GeV/c, i.e. for the last three momentum regions. The variables I
2813 extract from it are the following:

⁸Note to self: check this. I thought the ECal barrel had 8 layers of tiles, and that all of them were inside the pressure vessel.

6.3. MUON AND PION SEPARATION IN THE ECAL AND MUID

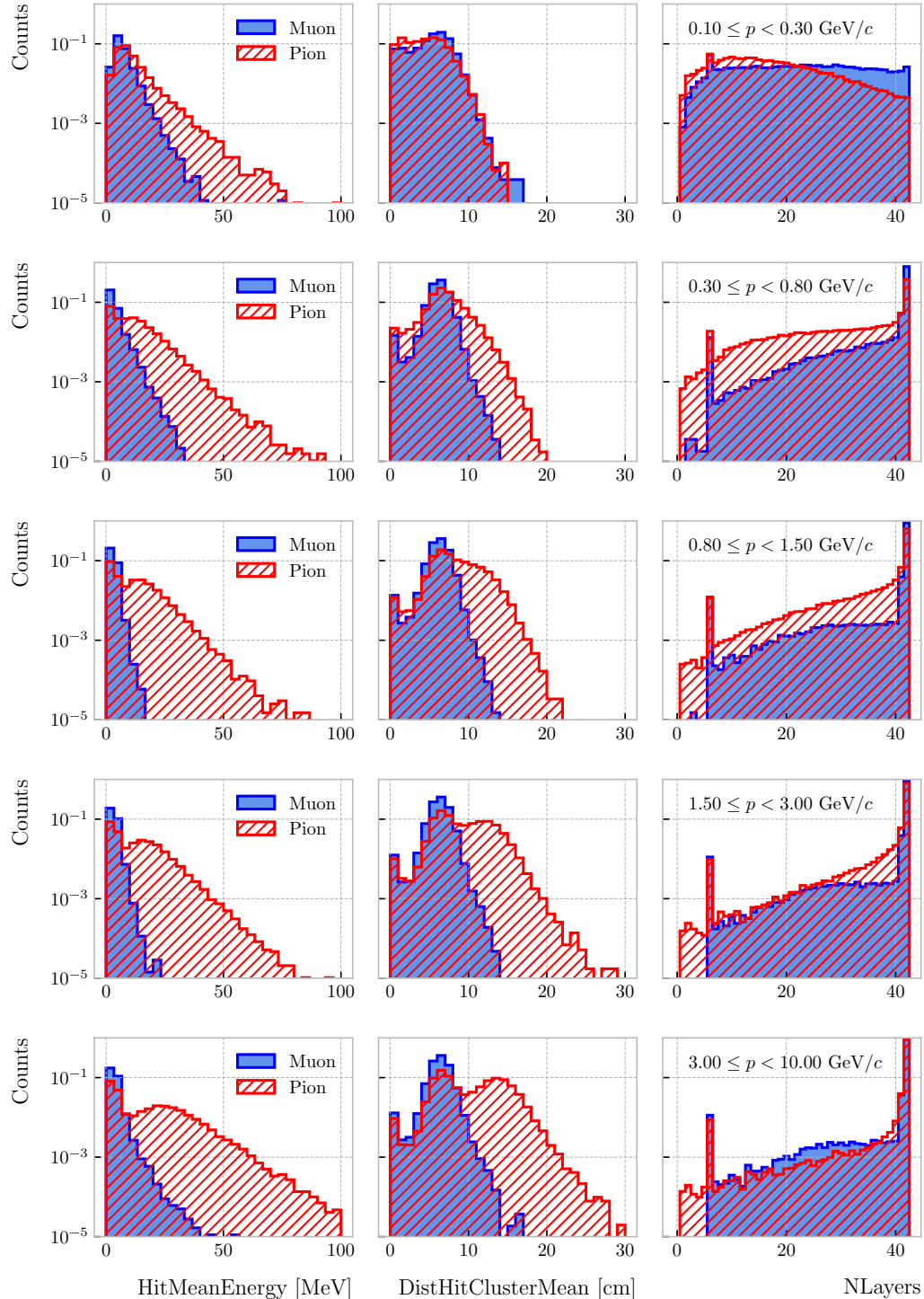


Figure 6.21: Example ECal feature distributions for muons (blue) and charged pions (red) in the five different momentum ranges considered (from top to bottom, in ascending momentum order). From left to right: mean hit energy, mean distance hit-to-cluster, and number of layers with hits.

CHAPTER 6. PARTICLE ID IN ND-GAr

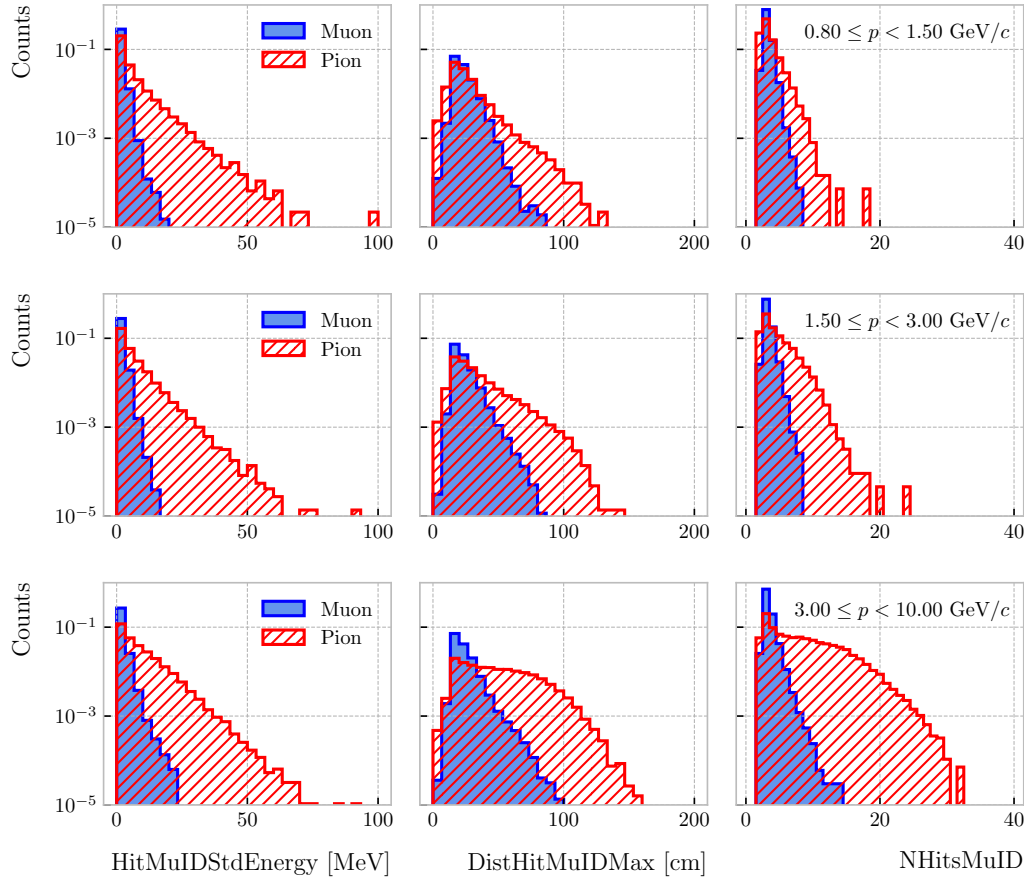


Figure 6.22: Example MuID feature distributions for muons (blue) and charged pions (red) in the three different momentum ranges considered (from top to bottom, in ascending momentum order). From left to right: standard deviation hit energy, maximum distance hit-to-hit, and number of hits.

• Energy-related MuID

- MuID total energy (ClusterMuIDTotalEnergy): sum of the energy of all the MuID hits.
- Mean MuID hit energy (HitMuIDMeanEnergy): mean of the MuID hit energy distribution.
- Standard deviation MuID hit energy (HitMuIDStdEnergy): standard deviation of the MuID hit energy distribution.
- Maximum MuID hit energy (HitMuIDMaxEnergy): maximum of the MuID hit energy distribution.

6.3. MUON AND PION SEPARATION IN THE ECAL AND MUID

• Geometry-related MuID

- Maximum distance MuID hit-to-hit (DistHitMuIDMax): maximum distance between pairs of MuID hits (not sure this is a good variable, distribution looks nuts).
- Maximum distance MuID hit-to-centre (DistHitCenterMuIDMax): maximum of the distance distribution between the MuID hits and the centre of the TPC.

• Statistical MuID

- Number of hits (NHitsMuID): total number of MuID hits associated to the track.
- Number of layers with hits (NLayersMuID): not really a count of all layers with MuID hits but the difference between the last and the first layer with MuIDhits.

Figure 6.22 shows the distributions of three different MuID variables, separating true muons (blue) and charged pions (red), for the three momentum ranges which use the muon tagger information. In this case I decided to standard deviation of the MuID hit energy distribution (left column), the maximum distance between the MuID hit pairs (middle column), and the number of MuID hits (right column). These variables are used together with the ECal features at high momenta, providing additional disambiguation power.

Once our features have been defined, one can do some exploratory analysis to understand how well the variables describe the target class, and avoid the black-box approach by what features are most relevant for the learning process. This way, I performed a feature analysis for each of the momentum ranges I divided this classification problem into. It follows three steps: first a principal component analysis (PCA), followed by a feature importance study using Gini and Shapley values, and finally a feature permutation importance analysis.

CHAPTER 6. PARTICLE ID IN ND-GAr

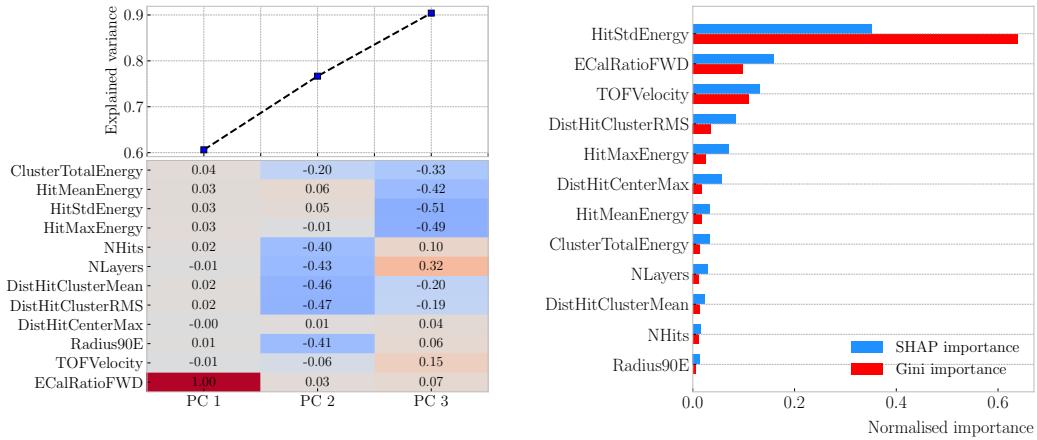


Figure 6.23: Left panel: cumulative explained variance for the first three principal components (top panel) and contribution of the different features to the principal axes in feature space (bottom panel). Right panel: Shapley (blue) and Gini (red) feature importances for the different input features. Both figures correspond to the samples in the momentum range $0.3 \leq p < 0.8$ GeV/c.

2850 The PCA is useful to understand the variance of the feature space. It is an
 2851 unsupervised machine learning technique that allows the user to perform a dimensionality
 2852 reduction. It uses a singular value decomposition of the input features to project them
 2853 into a lower dimensional space. The idea is to find the matrix \mathbf{C}_m , whose columns are
 2854 the first m orthonormal eigenvectors of the input covariance matrix. Consider the $n \times p$
 2855 real matrix of input data \mathbf{X} , where n is the number of samples and p the number of
 2856 features. If \mathbf{X} is centred, i.e. the means of its columns are equal to zero, we can write the
 2857 covariance matrix of \mathbf{X} as $\mathbf{C} = \mathbf{X}^\top \mathbf{X} / (n - 1)$. This matrix can be diagonalised, yielding:

$$\mathbf{C} = \mathbf{V} \mathbf{L} \mathbf{V}^\top, \quad (6.11)$$

2858 where \mathbf{V} is a matrix of eigenvectors and \mathbf{L} a diagonal matrix with eigenvalues λ_i . Then,
 2859 performing SVD on \mathbf{X} gives us:

$$\mathbf{X} = \mathbf{U} \mathbf{S} \mathbf{W}^\top, \quad (6.12)$$

2860 where \mathbf{U} is a unitary matrix, whose columns are called left singular vectors, \mathbf{S} is a
 2861 diagonal matrix of single values s_i , and \mathbf{W} is another unitary matrix, its columns known

6.3. MUON AND PION SEPARATION IN THE ECAL AND MUID

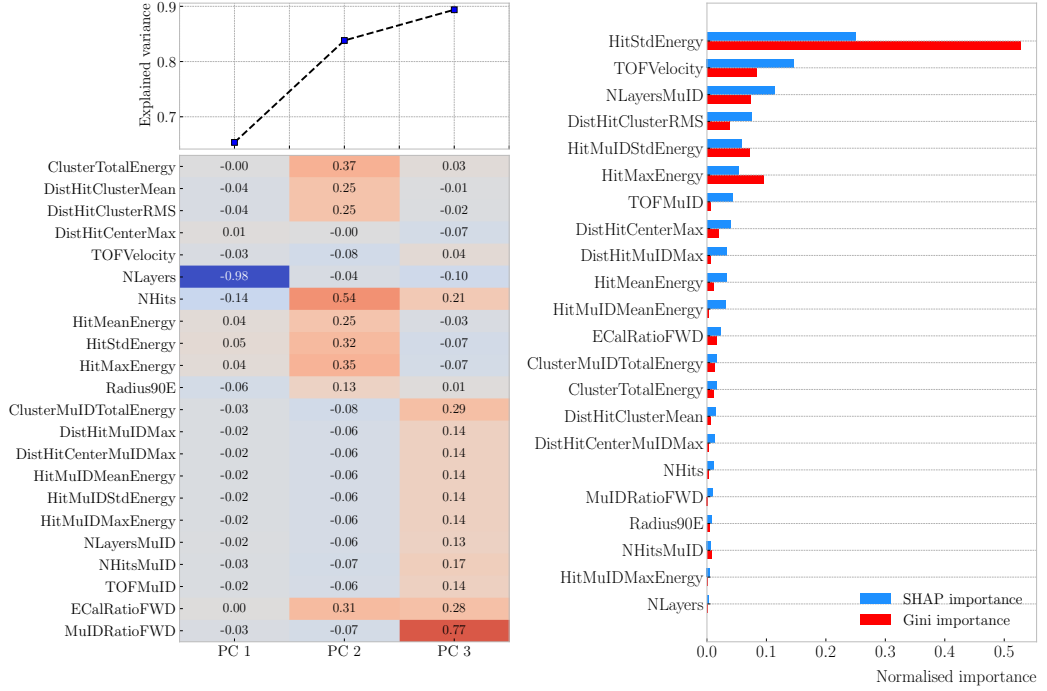


Figure 6.24: Left panel: cumulative explained variance for the first three principal components (top panel) and contribution of the different features to the principal axes in feature space (bottom panel). Right panel: Shapley (blue) and Gini (red) feature importances for the different input features. Both figures correspond to the samples in the momentum range $0.8 \leq p < 1.5$ GeV/c.

as right singular vectors. This way, we can write:

$$\mathbf{C} = \mathbf{W}\mathbf{S}\mathbf{U}^\top\mathbf{U}\mathbf{S}\mathbf{W}^\top/(n-1) = \mathbf{W}\frac{\mathbf{S}^2}{n-1}\mathbf{W}^\top. \quad (6.13)$$

meaning that the right singular vectors are also the eigenvectors of the covariance matrix.

The SVD can be computed numerically following an iterative approach.

This way, taking an input data vector $X \in \mathbb{R}^n$, the resulting feature vector $Y \in \mathbb{R}^m$

is given by:

$$Y = \mathbf{C}_m^\top X. \quad (6.14)$$

The new features capture most of the variance of the original sample, while being lower dimensional, as $m < n$.

Before applying the PCA reduction one needs to centre and scale the input data.

CHAPTER 6. PARTICLE ID IN ND-GAR

2870 Centring is necessary when using SVD to obtain the eigenvectors of the covariance
2871 matrix, as only in that case we can do the identification with the right singular vectors
2872 from the input data. Scaling is needed when variables are on different scales, as some
2873 can then dominate the PCA procedure.

2874 I used the PCA module of `scikit-learn`, together with the `RobustScaler`, which
2875 centres the data and scales it based on the interquartile range. In Fig. 6.23 (left panel)
2876 and Fig. 6.24 (left panel) I show the results I obtained from the PCA for the momentum
2877 ranges $0.3 \leq p < 0.8 \text{ GeV}/c$ and $0.8 \leq p < 1.5 \text{ GeV}/c$, respectively. Notice that in
2878 the second case the number of features increases considerably, as this is the first region
2879 which uses the MuID variables. I found that, in all the cases, adding a fourth PC does
2880 not add additional information. As it can be seen in the top panels of the figures, the
2881 cumulative explained variance is already over 80% with three PCs.

2882 The bottom panels show the contribution of the variables to the principal axes. For
2883 the two first momentum regions, I observe a tendency of the energy-related and the
2884 geometry-related ECal variables to be clustered together. For the other ranges, when
2885 I include the MuID variables, there seems to be a division between ECal and MuID
2886 variables. For these, it seems like the number of ECal layers with hits also plays an
2887 important role.

2888 The next step in the analysis is to quantify the importance of the features based on
2889 two additional metrics, namely the Gini and the Shapley values. The Gini importance,
2890 often called mean decrease impurity, is based on how much a feature contributes to the
2891 purity improvement at the splits in each decision tree. The purity is measured in terms
2892 of the Gini impurity index, defined as:

$$I_G = 1 - \sum_i f_i, \quad (6.15)$$

2893 where f_i is the fractional abundance of the i -th class. Then, for each split one can

6.3. MUON AND PION SEPARATION IN THE ECAL AND MUID

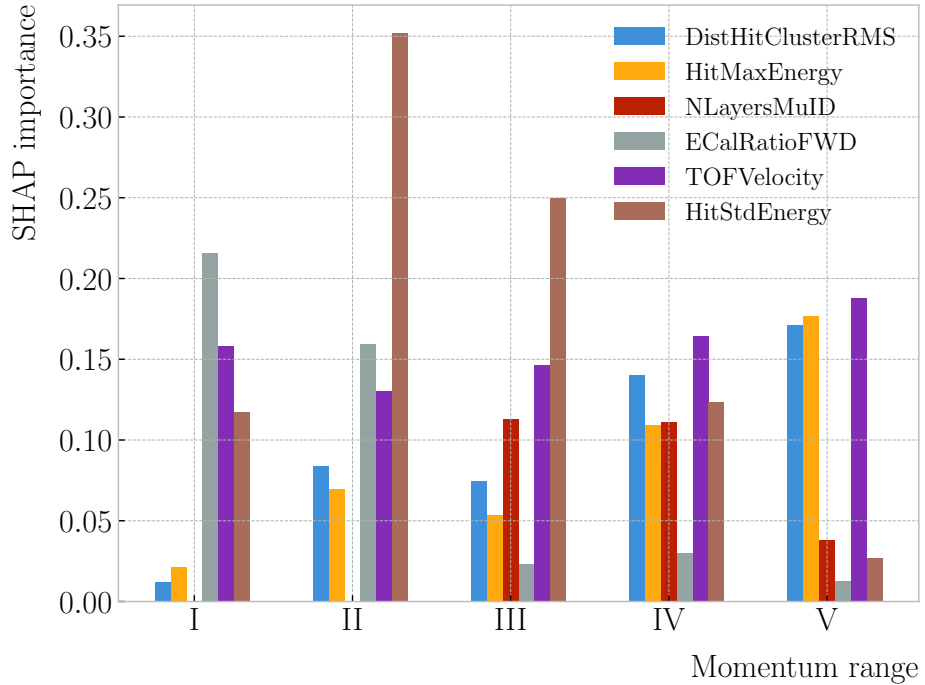


Figure 6.25: Evolution of the SHAP importance for the top six most important features across all five momentum ranges.

2894 compute the weighted decrease in impurity as:

$$\Delta_G = \frac{N_t}{N} \left(I_G - \frac{N_t^R}{N_t} I_G^R - \frac{N_t^L}{N_t} I_G^L \right), \quad (6.16)$$

2895 where N represents the total number of samples, N_t the number of samples at the current
 2896 node, N_t^R and N_t^L the number of samples in the right and left children respectively,
 2897 I_G is the Gini impurity at the current node, and I_G^R and I_G^L the Gini impurities of the
 2898 resulting right and left children.

2899 For each decision tree, one will have a normalised vector with the accumulated
 2900 decrease in Gini impurity for each feature. In the case of a BDT, the feature importances
 2901 are simply the mean for all the estimators in the ensemble⁹.

2902 The concept of Shapley values originated in the context of game theory, and it
 2903 measures the marginal contribution of a feature in enhancing the accuracy of a classifier.

⁹Note to self: this appears not to be the case. If you get the `feature_importance` for each tree in the BDT and take the average, the result is not the same to be one reported in the `feature_importance` attribute of the BDT.

CHAPTER 6. PARTICLE ID IN ND-GAr

2904 Take F to be the set of all features in a problem, and $S \subseteq F$ the subset of features. To
 2905 compute the Shapley value of the i -th feature, one has to train a model with that feature
 2906 present, $f_{S \cup \{i\}}$, and another model trained without it, f_S . This has to be repeated for
 2907 all possible combinations of subsets $S \subset F \setminus \{i\}$, and evaluating the models predictions
 2908 on the appropriate sets of data x_S . This way, the Shapley value results:

$$\varphi_i = \sum_{S \subset F \setminus \{i\}} \frac{|S|! (|F| - |S| - 1)!}{|F|!} [f_{S \cup \{i\}}(x_{S \cup \{i\}}) - f_S(x_S)]. \quad (6.17)$$

2909 I trained the `GradientBoostingClassifier` from `scikit-learn` with the default
 2910 configuration in order to evaluate both the Gini and Shapley importances. The Gini
 2911 scores are automatically computed by `scikit-learn`, using the training data. For the
 2912 Shapley importance, I used the implementation from the `SHAP` package, computing
 2913 it using the test sample. The results can be seen in Fig. 6.23 (right panel) and
 2914 Fig. 6.24 (right panel), again for the momentum ranges $0.3 \leq p < 0.8 \text{ GeV}/c$ and
 2915 $0.8 \leq p < 1.5 \text{ GeV}/c$. The length of the bars denote either the SHAP (blue) or the Gini
 2916 (red) importance of the feature. One interesting thing to notice is that, when looking at
 2917 the Gini importance, there is always one feature that dominates over the rest. This is
 2918 not the case for the SHAP importance, where importances tend to be more balanced.

2919 Across all momentum ranges, I observe that the most important features are. For
 2920 the five momentum ranges considered, only six variables sit in the top five at least once.
 2921 Figure 6.25 shows the evolution of the SHAP importance of these six features. It is
 2922 interesting to see that the time-of-flight variable keeps its importance almost unchanged
 2923 for all momenta. Also, it looks like the ECal energy ratio gets less relevant the higher the
 2924 momentum is, but the RMS of the hit-to-cluster distance distribution and the maximum
 2925 ECal hit energy become more important in the last momentum ranges.

2926 The last step in the feature selection analysis is the feature permutation. This
 2927 technique measures the contribution of each feature to the performance of a model by
 2928 randomly shuffling its values and checking how some scores degrade. For the present
 2929 case, I am interested in the precision or purity, and the sensitivity or efficiency, as these

6.3. MUON AND PION SEPARATION IN THE ECAL AND MUID

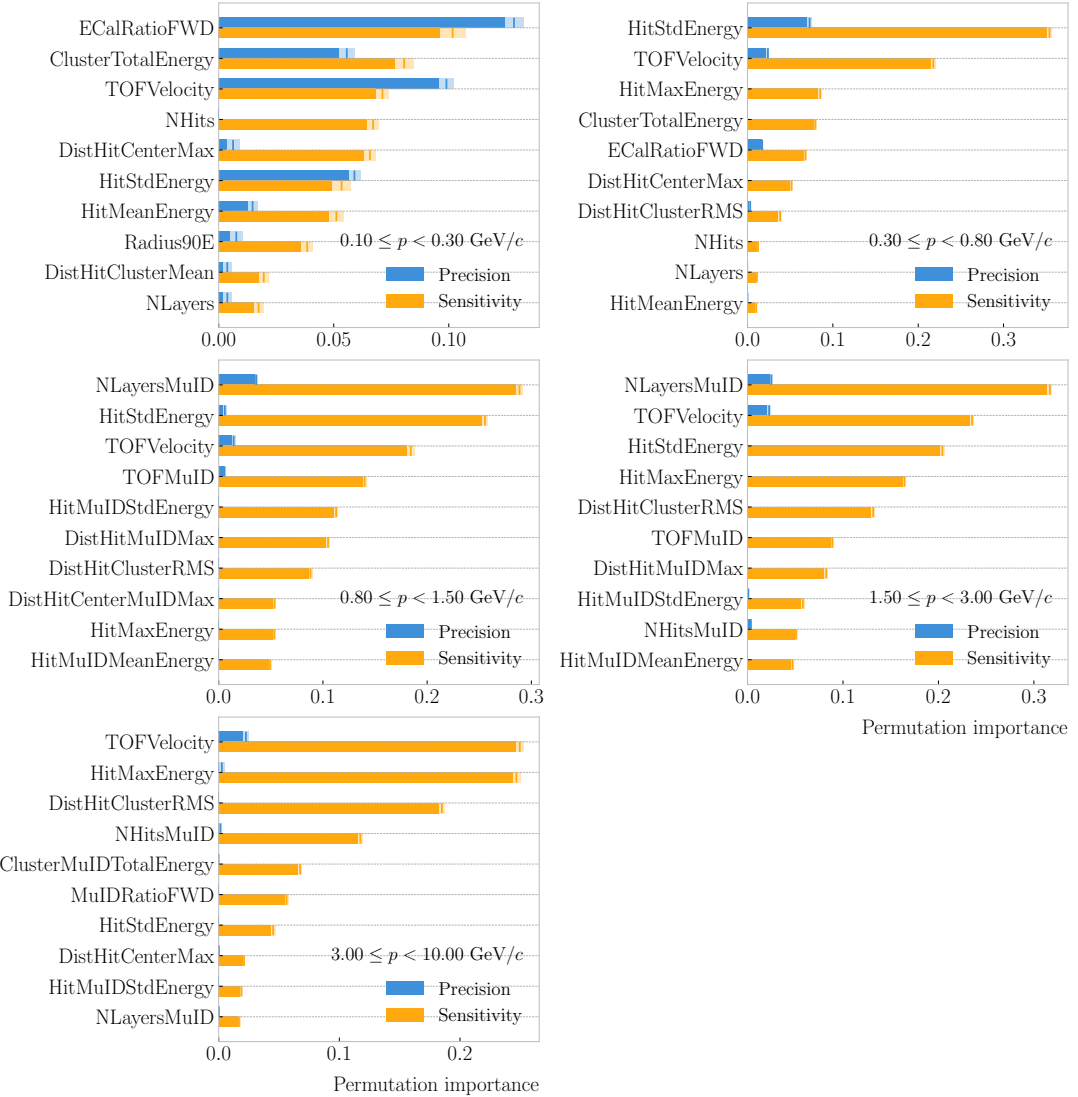


Figure 6.26: Permutation importances for the ten most important features in the different momentum ranges (from left to right, top to bottom, in increasing momentum order). The bars indicate the effect that permutations of each feature have on the purity (blue) and the sensitivity (yellow), the translucent regions representing one standard deviation around the central value.

CHAPTER 6. PARTICLE ID IN ND-GAR

2930 two are the most relevant metrics from a physics point of view. The `scikit-learn`
2931 module provides the user with a method to perform the permutation scans.

2932 The results of these are shown in Fig. 6.26. For the different momentum ranges
2933 I show the permutation importances for the ten most important features. For each
2934 of the variables I report the effect the permutations have on the precision (blue) and
2935 sensitivity (yellow) of the models. The bars indicate the importance value, with the
2936 lighter part representing one standard deviation around the mean (hinted as an additional
2937 vertical line). Something to notice is that, in the first momentum region, the feature
2938 permutations have an effect on both the precision and the sensitivity. However, for the
2939 rest the precision is almost unaffected, while the sensitivity changes are considerably
2940 larger.

2941 It is also interesting to see that most of the variables identified as important here
2942 are the same I found when looking at the Shapley values. The behaviour of these across
2943 the momentum ranges is also similar, with the same patterns of some features being
2944 important at low momenta and then dropping in importance for the high momentum
2945 ranges.

2946 Wit this, I conclude the study of the features. I have prepared the training and
2947 testing datasets and understood what features are likely to have the largest impact on
2948 the performance of the classifiers.

2949 6.3.4 Hyperparameter optimisation

2950 Any BDT requires the user to specify a number of parameters that will dictate its
2951 behaviour. They can be divided into two categories: (i) tree-specific parameters, which
2952 affect each individual tree in the model, and (ii) boosting parameters, which control the
2953 boosting operation in the model. The value of these so-called hyperparameters affect the
2954 performance and predictive power of the models. Therefore, one needs to carefully select
2955 their optimal values in order to extract as much information as possible from the data.

2956 From all the parameters used to define a tree in the `scikit-learn` implementation
2957 of the BDT classifier, I only consider a subset of them. This is due to the fact that some

6.3. MUON AND PION SEPARATION IN THE ECAL AND MUID

2958 are mutually exclusive, but also because I noticed that others have little effect on the
2959 problem at hand. Therefore, the parameters I investigate are the following:

- 2960 • `min_samples_split`: defines the minimum number of samples required in a node
2961 to be considered for splitting. Higher values prevent a model from learning relations
2962 which might be highly specific to the particular sample, but may lead to under-fitting
2963 if the value is too low.
- 2964 • `min_samples_leaf`: defines the minimum samples required in a leaf node. For
2965 imbalanced problems it should take a low value, as there will not be many cases
2966 where the minority class dominates.
- 2967 • `max_depth`: maximum depth of a tree. Useful to prevent over-fitting, as higher
2968 depth will allow a model to learn relations specific to the training sample.

2969 In the case of the boosting parameters, the ones I look at are:

- 2970 • `learning_rate`: determines the impact of each tree on the final outcome. Low
2971 values make the model robust to the specific characteristics of a tree, and thus
2972 allow it to generalise well. However, that usually requires a large number of trees
2973 to model the data properly.
- 2974 • `n_estimators`: number of sequential trees to be trained. In general, BDTs are
2975 fairly robust at higher number of trees but it can still overfit at a point.
- 2976 • `subsample`: fraction of observations to be selected for each tree. Values slightly
2977 less than 1 make the model robust by reducing the variance.

2978 In general, hyperparameters depend on each other. Thus, it is not possible to
2979 optimise them independently. In the literature, we find two main strategies to explore
2980 the hyperparameter space. We could use a grid search, in which one discretises a
2981 portion of the space of hyperparameters and evaluates the model at each point. Another
2982 approach is the randomised search, where a certain number of random configurations of
2983 hyperparameters are explored.

CHAPTER 6. PARTICLE ID IN ND-GAR

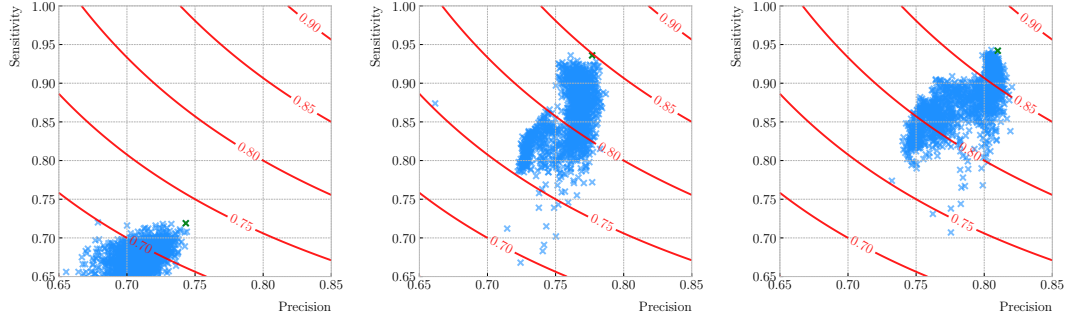


Figure 6.27: Values of the precision and sensitivity obtained for 10000 BDT hyperparameter configurations, for the momentum regions I, III and V. The red contours indicate the curves of equal F_1 -score, while the green crosses are the selected configurations.

2984 In this case, I used the random search to scan the hyperparameter space. Also,
 2985 because it is not guaranteed that a set of hyperparameters can be efficiently applied
 2986 across different datasets, I perform the optimisation for each of the momentum ranges
 2987 considered. Table 6.3 shows the list of hyperparameters considered, and the range within
 2988 which I let them vary. I decided to fix the number of estimators to 400 in all cases, as
 2989 its value is correlated with that of the learning rate.

2990 I evaluate 10000 different hyperparameter configurations for each momentum range.
 2991 For the hyperparameter tuning, I used subsamples containing 10% of the full datasets,
 2992 keeping the original proportions between classes, in order to reduce the computational
 2993 load. The performance of the models was assessed using a stratified 3-fold cross-validation
 2994 with replacement. Cross-validation involves dividing the data in a number of subsets,
 2995 training the model using some of them, and testing it with the rest. In our case, I
 2996 divide the data in 3 equal-sized subsets, maintaining the class proportions of the original
 2997 dataset. Then, for 3 consecutive iterations, I train the models using 2 of the subsets
 2998 while I compute the precision and sensitivity scores with the other. This approach
 2999 provides a more robust estimate of the performance on unseen data.

3000 Figure 6.27 shows the results in the precision versus sensitivity plane, for the
 3001 momentum regions I, III and V (from left to right). The contours represent the curves
 3002 of equal F_1 -score, i.e. the harmonic mean of the precision and the sensitivity. In order

6.3. MUON AND PION SEPARATION IN THE ECAL AND MUID

Table 6.3: Optimal values of the hyperparameters used by the BDT, for each momentum range.

Hyperparameter	Range	Best value				
		I	II	III	IV	V
<code>min_samples_split</code>	[0.001, 1]	0.10	0.06	0.05	0.27	0.06
<code>min_samples_leaf</code>	[0.001, 1]	0.02	0.03	0.01	0.02	0.07
<code>max_depth</code>	{2, 3, ..., 8}	8	2	4	2	7
<code>learning_rate</code>	[0.05, 1]	0.10	0.23	0.07	0.13	0.09
<code>subsample</code>	[0.01, 1]	0.75	0.65	0.79	0.86	0.95

Table 6.4: Performance metrics of the BDTs with optimal hyperparameters, for the different momentum ranges.

Metric	Value $\pm 1\sigma$				
	I	II	III	IV	V
Accuracy	0.779 ± 0.003	0.812 ± 0.003	0.846 ± 0.002	0.861 ± 0.003	0.874 ± 0.002
Precision	0.769 ± 0.003	0.752 ± 0.005	0.788 ± 0.002	0.805 ± 0.003	0.815 ± 0.003
Sensitivity	0.745 ± 0.009	0.921 ± 0.006	0.965 ± 0.002	0.967 ± 0.002	0.976 ± 0.001
F_1 -score	0.757 ± 0.004	0.828 ± 0.003	0.867 ± 0.002	0.879 ± 0.002	0.889 ± 0.002
ROC AUC	0.868 ± 0.003	0.865 ± 0.003	0.899 ± 0.002	0.902 ± 0.002	0.911 ± 0.001

3003 to select the optimal configurations (indicated in the plots with a green cross), I chose
 3004 the point with the highest F_1 -score.

3005 The results for the different momentum ranges are summarised in Tab. 6.3. One
 3006 can see some consistency in hyperparameter choices, with models generally preferring
 3007 small values for the tree-specific parameters, small learning rate, and relatively large
 3008 subsample sizes.

3009 Now that I have obtained the optimal values of the hyperparameters, I can train
 3010 the different BDTs. In this case I use the complete datasets, keeping 20% of the data
 3011 for testing. Table 6.4 shows the values of the different performance metrics obtained
 3012 using the selected hyperparameters and 5-fold cross-validation. The last row indicates
 3013 the value of the area under the receiver operating characteristic (ROC) curve. This
 3014 represents the sensitivity of a model as a function of the false positive rate. I have

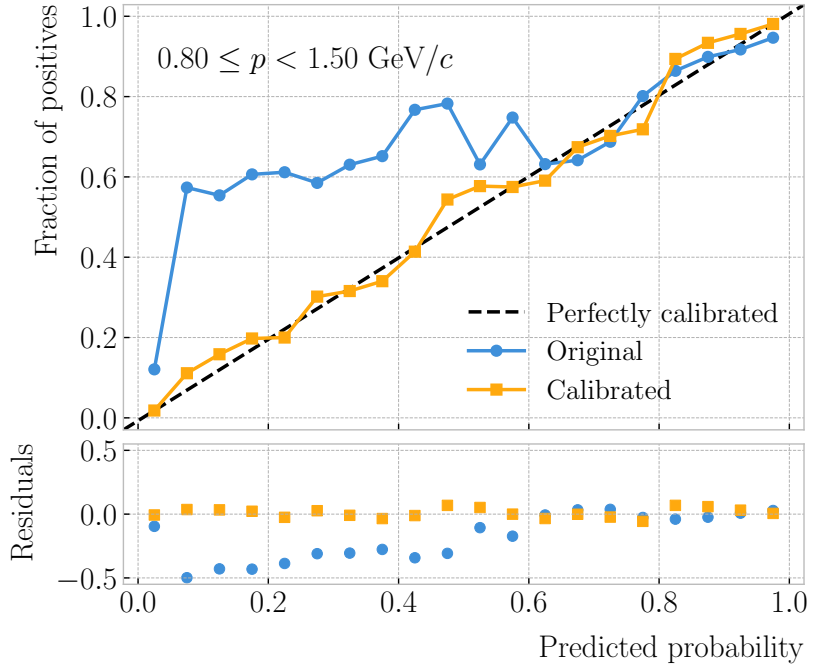


Figure 6.28: Reliability diagrams for the BDT classifier used in the momentum range $0.3 \leq p < 0.8 \text{ GeV}/c$, both for the original (blue circles) and calibrated (yellow squares) responses. For reference, the response of a perfectly calibrated classifier is also shown (black dashed line).

3015 included it here as it is a classic model metric used in the machine learning community.

3016 Overall, there is a clear trend of models performing better at higher momentum.

3017 6.3.5 Probability calibration

3018 So far, the trained BDTs are able to provide predictions of the class labels. Ideally,
 3019 one would like the output of a classifier to give a confidence level about the prediction.
 3020 However, it is not straightforward to interpret the outputs of our BDTs in terms of
 3021 probabilities.

3022 A way to visualise how well the predictions of a classifier are calibrated is using
 3023 reliability diagrams [160]. They represent the probability of the positive label versus the
 3024 probability predicted by the classifier. These can be obtained by binning the predicted
 3025 probabilities, and then compute the conditional probability $P(y_{true} = 1 | y_i \leq y_{pred} <$
 3026 $y_{i+1})$ by checking the fraction of true positive instances in each bin. The reliability

6.3. MUON AND PION SEPARATION IN THE ECAL AND MUID

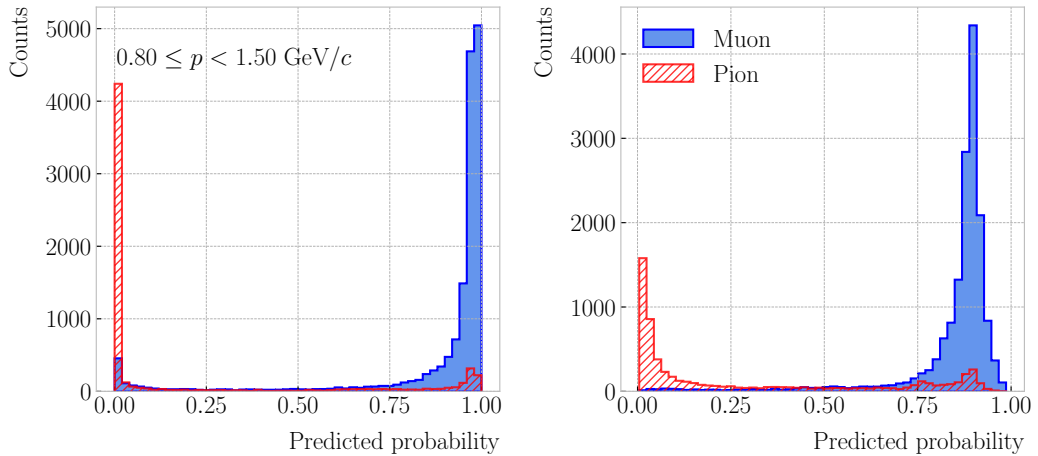


Figure 6.29: Uncalibrated (left panel) and calibrated (right panel) predicted probabilities assigned by the BDT classifiers for true muons (blue) and charged pions (red) in the momentum range $0.3 \leq p < 0.8 \text{ GeV}/c$.

3027 diagram of a perfectly calibrated classifier would be a diagonal line.

3028 In this case, I try to correct the raw response of the classifiers by applying a sigmoid
3029 function:

$$\sigma(x; A, B) = \frac{1}{1 + e^{Ax+B}}, \quad (6.18)$$

3030 where the parameters A and B are real numbers determined using the method of least
3031 squares.

3032 For each classifier, I perform a grid search to obtain the optimal values of A and B .
3033 For any pair, I compute the predicted probabilities as $y_{pred} = \sigma(y_{raw}; A, B)$, where y_{raw}
3034 are the raw predictions of the classifier¹⁰. Then, I calculate the corresponding reliability
3035 curve, and take the sum of the squared residuals between it and the response of the
3036 perfectly calibrated classifier.

3037 Figure 6.28 shows the reliability diagrams for the original (blue) and calibrated
3038 (yellow) probability predictions of the classifier for the III momentum range, $0.3 \leq p <$
3039 $0.8 \text{ GeV}/c$. The original response of the classifier is given by $y_{pred} = \sigma(y_{raw}; -2, 0)$,
3040 which is the transformation applied by `scikit-learn` to produce the probability estimate.
3041 Notice how the calibrated prediction matches the ideal response much better than the

¹⁰In `scikit-learn` these correspond to the outputs of the `decision_function` method.

CHAPTER 6. PARTICLE ID IN ND-GAr

3042 original, across all the probability range.

3043 One can also compare the responses of the uncalibrated and calibrated classifiers
3044 broken down by true particle type, as shown in Fig. 6.29. It can be seen that the
3045 distributions for both muons (blue) and charged pions (red) smoothen after calibration,
3046 but still the separating power of the classifier remains unchanged.

3047 At this point, having the trained classifiers and the probability calibration parameters,
3048 I am able to assess the performance of the classification strategy in a physics-relevant
3049 case.

3050 6.3.6 Performance

3051 6.4 ECal time-of-flight

3052 Looking at Fig. 6.20, it is clear that for momentum values in the range $1.0 - 3.0 \text{ GeV}/c$
3053 it is not possible to separate pions and protons using a $\langle dE/dx \rangle$ measurement in the
3054 HPgTPC. However, in the previous section I assumed that protons at those energies
3055 could be identified by other means, and therefore were not an issue for the muon and
3056 pion discrimination.

3057 Some detectors, like ALICE [161] or the ILD concept [162], complement the PID
3058 capabilities of their gaseous trackers with time-of-flight measurements. The use of
3059 fast timing silicon sensors, with hit time resolutions under 100 ps, would allow for the
3060 identification of charged hadrons via a ToF measurement up to $5.0 \text{ GeV}/c$. In the case
3061 of ND-GAr, one could think of using the inner layers of the ECal, the ones consisting of
3062 high-granularity tiles, to obtain a ToF-based PID, with some inputs from the TPC.

3063 Measuring the momentum and the velocity of a charged particle allows for a
3064 determination of the mass through the relativistic momentum formula:

$$m = \frac{p}{\beta} \sqrt{1 - \beta^2}. \quad (6.19)$$

3065 In our case, the momentum is measured in the TPC, using the curvature and the dip

6.4. ECAL TIME-OF-FLIGHT

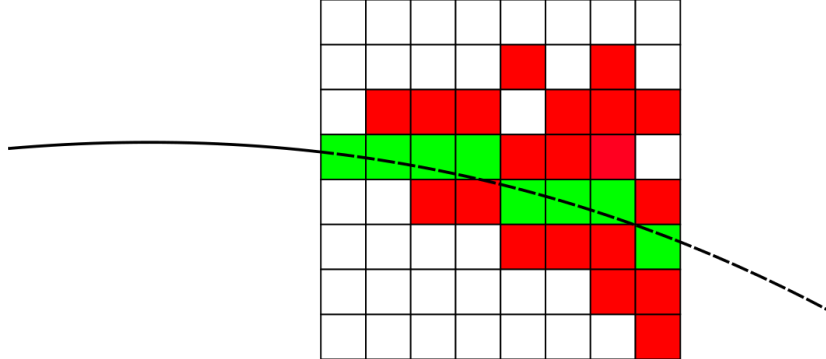


Figure 6.30: Schematic of the hit selection used for the ToF measurement. The grid represents the layers of the inner ECAL, with coloured squares indicating the tiles with hits. Green squares indicate the selected hits.

3066 angle of the helix inside the magnetic field. The velocity of the particle can be written
3067 as:

$$\beta = \frac{\ell_{track}}{c\tau}, \quad (6.20)$$

3068 where ℓ_{track} is the length of the track, and τ the arrival time to the ECAL.

3069 In GArSoft, the track length is computed at the Kalman filter stage. It is simply the
3070 sum of the line segments along the track, either in the forward or backward fit. In this
3071 case, because we are only interested in the particles that make it to the ECAL, I choose
3072 the fit direction based on the results of the track-cluster associations.

3073 Additionally, because the last 30 cm of the TPC radius are uninstrumented¹¹, I need
3074 to correct for the length of the tracks. Using the track fit parameters to propagate the
3075 helix to its entry point in the ECAL, one can write the total track length as:

$$\ell_{track} = \ell + \left| \frac{\phi_{EP} - \phi}{R^{-1}} \right| \sqrt{1 + \tan^2 \lambda}, \quad (6.21)$$

3076 where ϕ_{EP} is the angle of rotation at the entry point to the calorimeter, and ℓ , ϕ , R and
3077 λ are the track length, angle of rotation, radius of curvature and dip angle at the last
3078 point in the fit, respectively.

3079 To test the idea of performing a ToF measurement with the inner ECAL, I generated

¹¹Note to self: check this number.

CHAPTER 6. PARTICLE ID IN ND-GAr

3080 two data samples. Each consists of 10000 single particle events, either charged pions or
3081 protons. Their momenta are uniformly distributed in the range $0.5 - 5.0 \text{ GeV}/c$, and
3082 their directions are isotropic. I process each sample using different values of the time
3083 resolution, from $\Delta\tau = 0$, the perfect time resolution case for comparison, to the current
3084 nominal value of $\Delta\tau = 0.7 \text{ ns}$, and the worse scenario of $\Delta\tau = 1.0 \text{ ns}$.

3085 6.4.1 Arrival time estimations

3086 In the simulation, the limited time resolution of the ECal is taken into account by
3087 applying a Gaussian smearing to the true hit times. Other effects, like the digitisation
3088 of the signals, are not taken into account and fall beyond the scope of this study. After
3089 the track-cluster, one ends up with a collection of ECal hits associated to each particle.
3090 From these, the arrival time of the particle to the ECal can be extracted.

3091 The simplest possibilities are to either take the time of the earliest hit or the hit
3092 closest to the entry point. Because these two coincide, in general, I focused only in
3093 the earliest hit time. However, this needs to be corrected, to account for the distance
3094 travelled from the entry point to the position of the hit:

$$\tau_{earliest} = \tau_{hit} - \frac{d_{EP-hit}}{c}, \quad (6.22)$$

3095 where τ_{hit} is the time of the earliest hit, and d_{EP-hit} is the distance between that hit
3096 and the entry point of the particle to the ECal. This is computed as the arc length
3097 between the entry point and the point of the extrapolated helix up to the layer of the
3098 hit. This way of correcting the time assumes c for the propagation of the particle, which
3099 may lead to biased estimates.

3100 I also tried to estimate the arrival times using information from the rest of the hits.
3101 In order to do this, as a simplifying assumption, I approximate the hadronic shower
3102 considering only its MIP component. For each layer, I keep only the hit in the tile closest
3103 to the point of the extrapolated track up to that layer. Figure 6.30 shows an example of
3104 how this hit selection works. The dashed line represents the extrapolated track, while

6.4. ECAL TIME-OF-FLIGHT

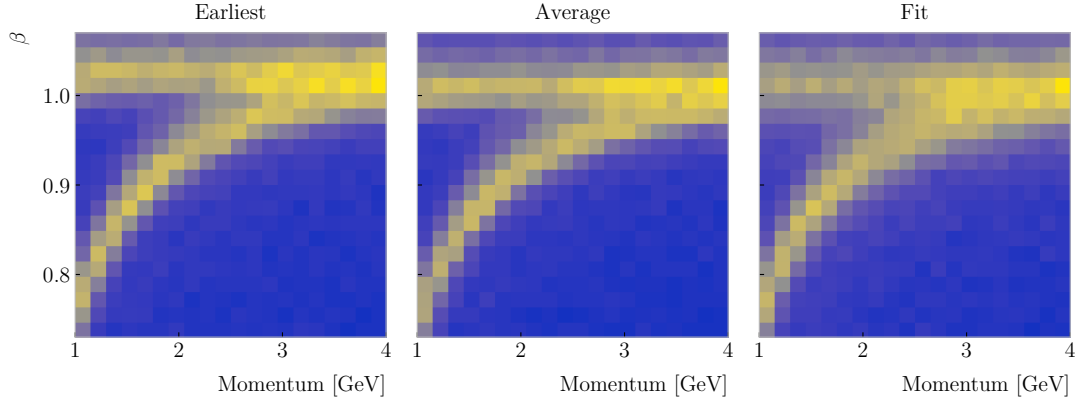


Figure 6.31: Particle velocity versus momentum measured with different ECal arrival time estimations. From left to right: earliest hit time, average hit time, and fitted hit time. In all cases the time resolution is $\Delta\tau = 0.1$ ns.

the coloured squares are the tiles containing hits. Green indicates the tiles closer to the track in each layer (in the sketch they correspond to the grid columns).

Now, I can use these collections of hits to estimate the arrival times. A possibility is to take the average of the times of the selected hits, denoted $\tau_{average}$. For that to work, one needs to correct these times, in a similar way as in Eq. (6.22), before taking the average. However, as before, this correction assumes that the particle travels at the speed of light inside the ECal. Another option is to perform a linear fit to the hit times and the distances to the entry point. In that case, the arrival time would be the fitted value of the intercept, τ_{fit} . This method would not assume a speed of light propagation.

Figure 6.31 shows the velocity estimations as a function of the particle momentum, for the earliest hit time (left panel), average hit time (middle panel), and fitted hit time (right panel). The two bands correspond to the π^\pm and the p particles. $\Delta\tau = 0.1$ ns. Notice how, for the earliest hit time method, the velocities are significantly biased towards larger values. For the multi-hit methods, the τ_{fit} estimate appears to produce a larger variance than when using the $\tau_{average}$ method.

CHAPTER 6. PARTICLE ID IN ND-GAr

3120 6.4.2 Proton and pion separation

3121 Once we have the velocities of the particles, one can estimate their masses through
3122 Eq. (6.19). The resulting mass spectra are shown in Fig. 6.32. I computed the masses
3123 for the three arrival time estimates discussed above, and three different values of the
3124 time resolution: $\Delta\tau = 0.00$ (perfect time resolution), $\Delta\tau = 0.10$ ns, and $\Delta\tau = 0.70$ ns.
3125 Although in all cases we have the same number of events, it appears as if the entries
3126 in the histograms decrease as the time resolution increases. Sometimes, the particles
3127 get unphysical values of $\beta > 1$, and in turn they do not contribute to the mass spectra.
3128 This is more likely to happen for higher values of $\Delta\tau$.

3129 As noted before, the average hit time method produces the most robust estimates
3130 when increasing $\Delta\tau$. Intuitively this makes sense, as by taking the mean one averages
3131 out the effect of the Gaussian smearing. Going forward, I will use this arrival time
3132 estimator, as it appears to be the best performing one.

3133 It is possible to use the velocity estimations to select a sample of protons. In this
3134 case, I do so by dividing the relevant momentum range in bins of $0.1 \text{ GeV}/c$. For each
3135 momentum bin, I compute the expected velocity for the protons via the inverse of Eq.
3136 (6.19), and then take the fractional residuals of the measured velocities. Using that
3137 distribution, I choose the cut that maximises the F_1 -score of the proton selection.

3138 The results can be seen in Fig. 6.33, for the case $\Delta\tau = 0.10$ ns. As expected from
3139 Fig. 6.31, the performance of the selection degrades rapidly with increasing momentum.
3140 However, the purity is still around 75% at $3.0 \text{ GeV}/c$. This is likely to be sufficient, as
3141 we do not expect protons or charged pions with higher energies from the beam neutrino
3142 interactions.

3143 Figure 6.34

3144 6.5 Charged pion decay in flight

3145 As discussed previously, in GArSoft the TPC tracks are formed after a pattern recognition
3146 algorithm and a Kalman filter are applied to the TPC clusters. These two steps can

6.5. CHARGED PION DECAY IN FLIGHT

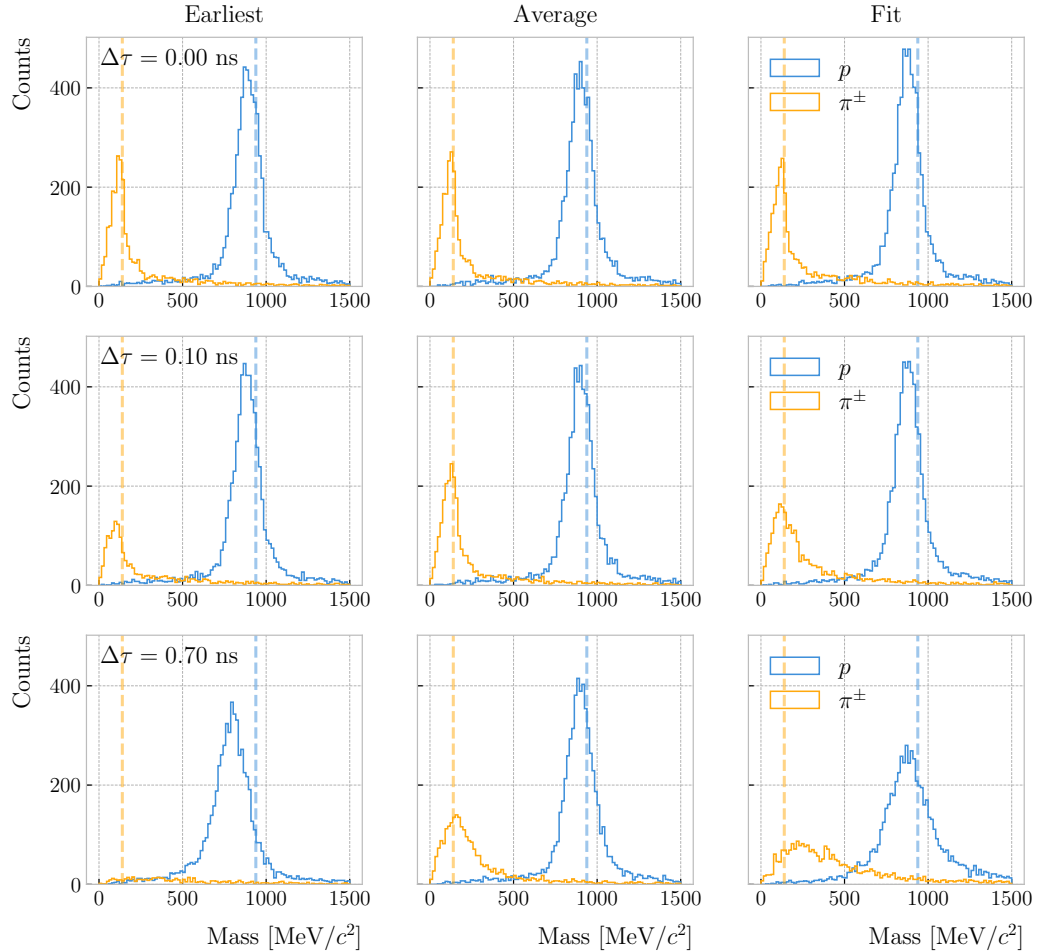


Figure 6.32: Mass spectra for p (blue) and π^\pm (yellow) particles, using different ECal time resolution values (from top to bottom, in ascending order), and arrival time estimates. From left to right: earliest hit time, average hit time, and fitted hit time. The dashed lines indicate the true masses of the particles.

3147 find discontinuities in the track candidates (e.g. due to a particle decay) when these
 3148 so-called breakpoints are large enough. However, for some, more subtle, cases they may
 3149 miss them and form a single reconstructed track. It has been noted in the literature
 3150 that Kalman filters offer, as a by-product, additional information to form test statistics
 3151 to identify these breakpoints [163, 164].

3152 Considering the mean life of the charged pion, $\tau = (2.6033 \pm 0.0005) \times 10^{-8}$ s, one
 3153 can estimate that about 12% of the pions with momentum $p \sim \mathcal{O}(500 \text{ MeV}/c)$ (roughly
 3154 the peak of the pion momentum distribution in ν_μ CC interactions off argon) decay

CHAPTER 6. PARTICLE ID IN ND-GAr

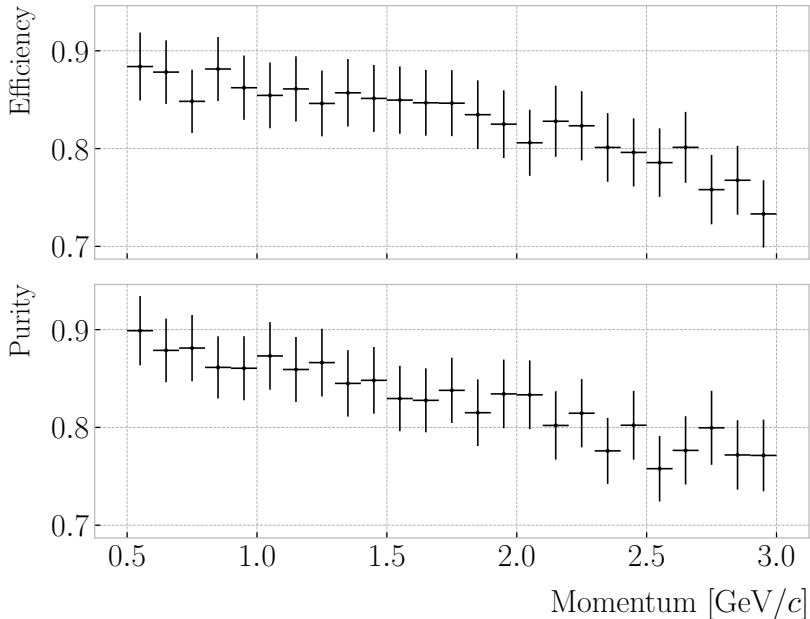


Figure 6.33: Efficiency (top panel) and purity (bottom panel) for the proton selection as a function of the momentum, for $\Delta\tau = 0.10$ ns.

3155 inside the TPC. Figure 6.35 (left panel) shows the amount of charged pions decaying in
 3156 the full TPC and fiducial volumes from an isotropic, monoenergetic sample of 100000
 3157 negatively charged pions with $p = 500$ MeV/ c . We see that about 10% of those decayed,
 3158 with more than half of them decaying inside the TPC fiducial volume.

3159 Figure 6.35 (right panel) shows an example event display of a charged pion (magenta
 3160 line) decays in flight inside the TPC, but because the angle of the muon (blue line) is
 3161 small both were reconstructed as one single track (black line). In this case, the composite
 3162 track reaches the ECal, where it undergoes a muon-like interaction, thus being classified
 3163 as a muon.

3164 A way to understand what decaying pion tracks were totally or partially reconstructed
 3165 together with the daughter muon is looking at the relative energy contributions to the
 3166 reconstructed track. In order to select a sample of such events, I require that a minimum
 3167 50% of the total energy comes from the pion and at least 20% from the muon.

6.5. CHARGED PION DECAY IN FLIGHT

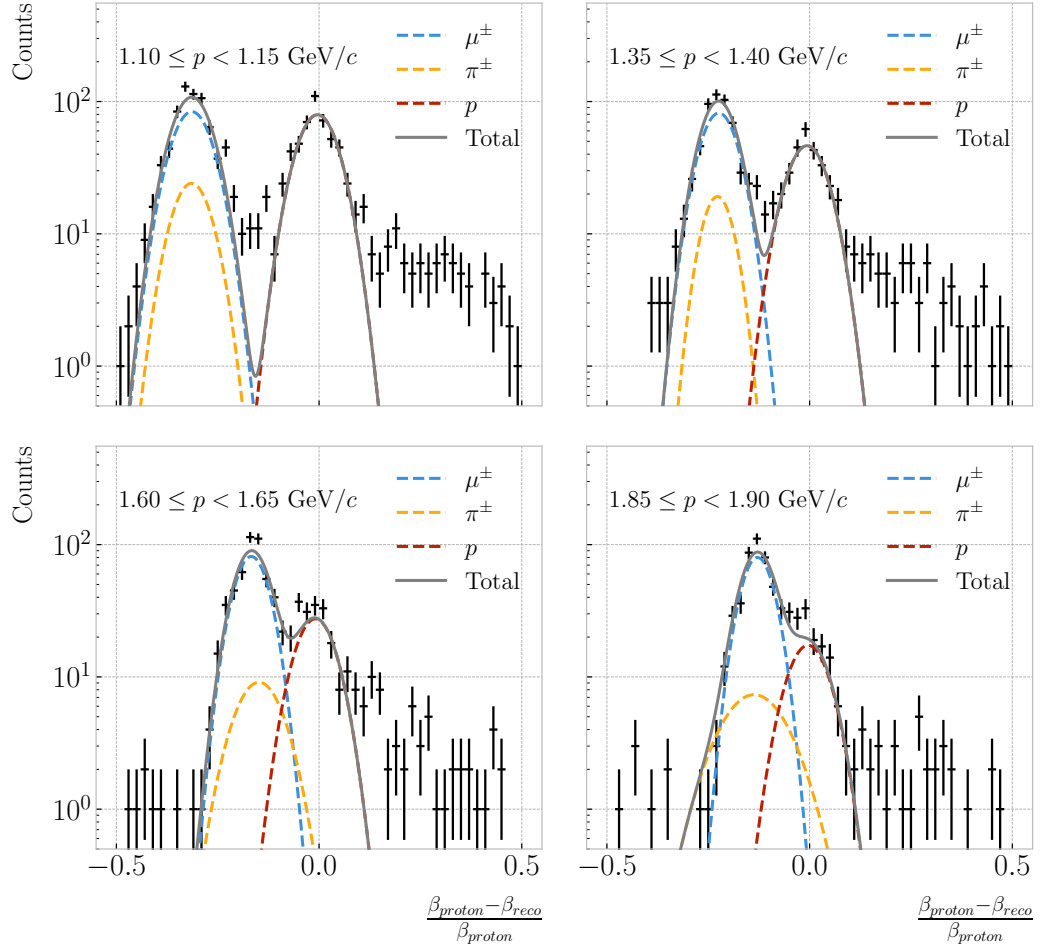


Figure 6.34: Distributions of the velocities measured by ToF with the inner ECal, for different momentum bins, in a FHC neutrino interaction sample. The Gaussian fits are performed around the maxima for each particle species.

3168 6.5.1 Track breakpoints

3169 To identify potential decays we can use the information we obtain from the Kalman
 3170 filter at each step of the fitted track. The simplest test we can think about is computing
 3171 the χ^2 of the mismatch between all the parameters in the forward and the backward fits:

$$\chi_k^{2 (FB)} = (\hat{x}_k^B - \hat{x}_k^F)^T [V^{(\hat{x}_k, B)} + V^{(\hat{x}_k, F)}]^{-1} (\hat{x}_k^B - \hat{x}_k^F), \quad (6.23)$$

3172 where \hat{x}_k^F , \hat{x}_k^B are the Kalman filter state vector estimates at step k in the forward and
 3173 backward fits and $V^{(\hat{x}_k, F)}$, $V^{(\hat{x}_k, B)}$ the covariance matrices of \hat{x}_k^F and \hat{x}_k^B respectively.

CHAPTER 6. PARTICLE ID IN ND-GAr

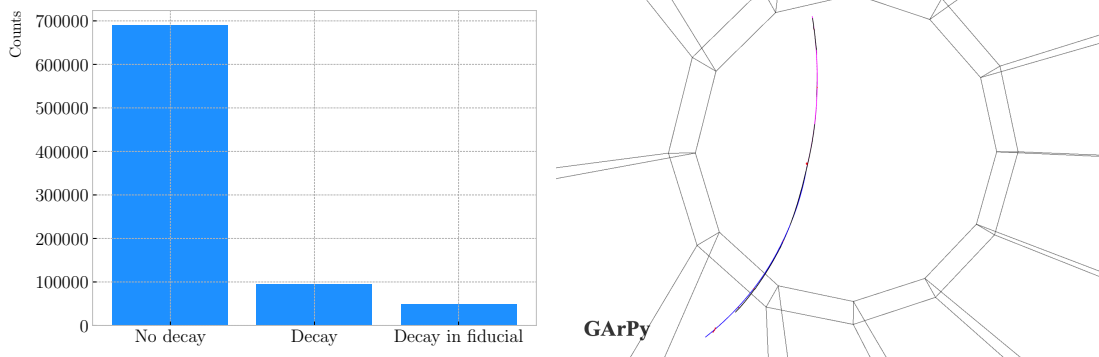


Figure 6.35: Left panel: number of non-decaying, decaying and decaying in the fiducial volume pions for a MC sample of 100000, $p = 500$ MeV/c isotropic positively charged pions inside the TPC. Right panel: event display for a positive pion decaying inside the fiducial volume, with a single reconstructed track for the pion and muon system.

3174 Using the values of the χ^2 at measurement k for the forward and backward fits we can
3175 compute another χ^2 value that characterises the overall track fit:

$$\chi_{track}^2 = \chi_k^{2(F)} + \chi_k^{2(B)} + \chi_k^{2(FB)}, \quad (6.24)$$

3176 which remains approximately constant for all k .

3177 An alternative approach proposed in the context of the NOMAD experiment was
3178 using a fit with a more elaborate breakpoint hypothesis, so we can perform a comparison
3179 of the χ^2 with and without breakpoints. This can be achieved by using some alternative
3180 parametrisation with extra parameters, which allows some of the track parameters to
3181 be discontinuous at certain points. A decay changes the momentum magnitude and
3182 direction, so we can use the new state vector:

$$\alpha = (y, z, 1/R_F, 1/R_B, \phi_F, \phi_B, \tan\lambda_F, \tan\lambda_B)^T. \quad (6.25)$$

3183 As we already have the estimates from the standard Kalman filter and their
3184 covariance matrices at each point, we do not need to repeat the Kalman fit for the new
3185 parametrisation. Instead, I can compute the values of α at each point k that minimise

6.5. CHARGED PION DECAY IN FLIGHT

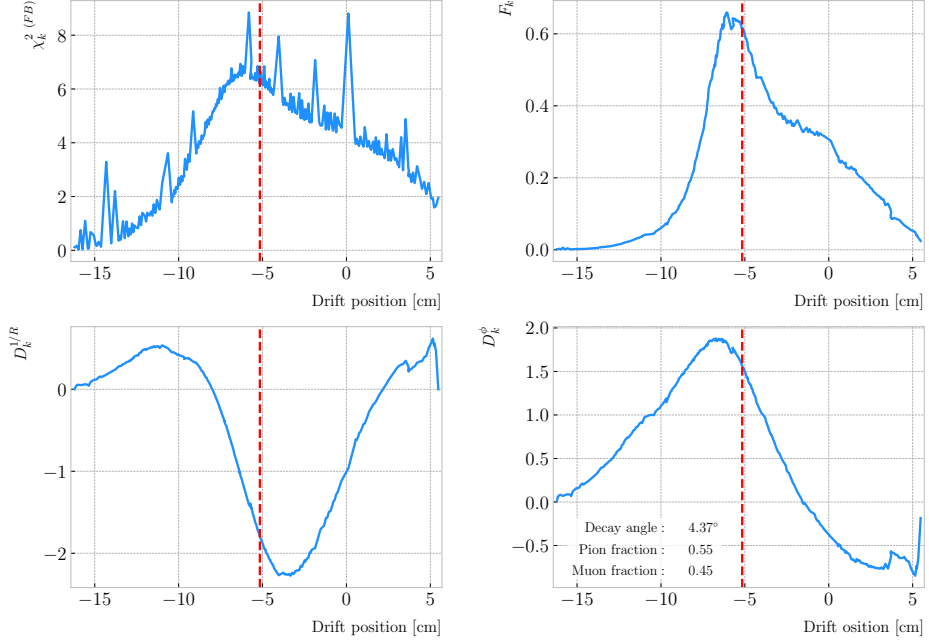


Figure 6.36: Values of $\chi_k^2(FB)$ (top left panel), F_k (top right panel), $D_k^{1/R}$ (bottom left panel) and D_k^ϕ (bottom right panel) versus position along the drift direction for a reconstructed track in a positive pion decay event. The vertical red dashed line indicates the true location of the decay point.

3186 the χ^2 resulting from comparing them to $\{\hat{x}_k^B, \hat{x}_k^F\}$. Introducing the two 5×8 matrices:

$$H^F = \begin{pmatrix} 1 & 0 & 0 & 0 & 0 & 0 & 0 & 0 \\ 0 & 1 & 0 & 0 & 0 & 0 & 0 & 0 \\ 0 & 0 & 1 & 0 & 0 & 0 & 0 & 0 \\ 0 & 0 & 0 & 0 & 1 & 0 & 0 & 0 \\ 0 & 0 & 0 & 0 & 0 & 0 & 1 & 0 \end{pmatrix}, \quad H^B = \begin{pmatrix} 1 & 0 & 0 & 0 & 0 & 0 & 0 & 0 \\ 0 & 1 & 0 & 0 & 0 & 0 & 0 & 0 \\ 0 & 0 & 0 & 1 & 0 & 0 & 0 & 0 \\ 0 & 0 & 0 & 0 & 0 & 1 & 0 & 0 \\ 0 & 0 & 0 & 0 & 0 & 0 & 0 & 1 \end{pmatrix}, \quad (6.26)$$

3187 we can write this as:

$$\begin{aligned} \chi_k^2(FB)(\alpha) &= (\hat{x}_k^F - H^F \alpha)^T \left[V^{(\hat{x}_k, F)} \right]^{-1} (\hat{x}_k^F - H^F \alpha) \\ &\quad + (\hat{x}_k^B - H^B \alpha)^T \left[V^{(\hat{x}_k, B)} \right]^{-1} (\hat{x}_k^B - H^B \alpha). \end{aligned} \quad (6.27)$$

3188 The minimum of $\chi_k^2(FB)(\alpha)$ is found when the measured new state vector takes the

3189 value:

$$\hat{\alpha}_k = V^{(\hat{\alpha}_k)} H^T (V^{(\hat{x}_k)})^{-1} \hat{X}, \quad (6.28)$$

CHAPTER 6. PARTICLE ID IN ND-GAr

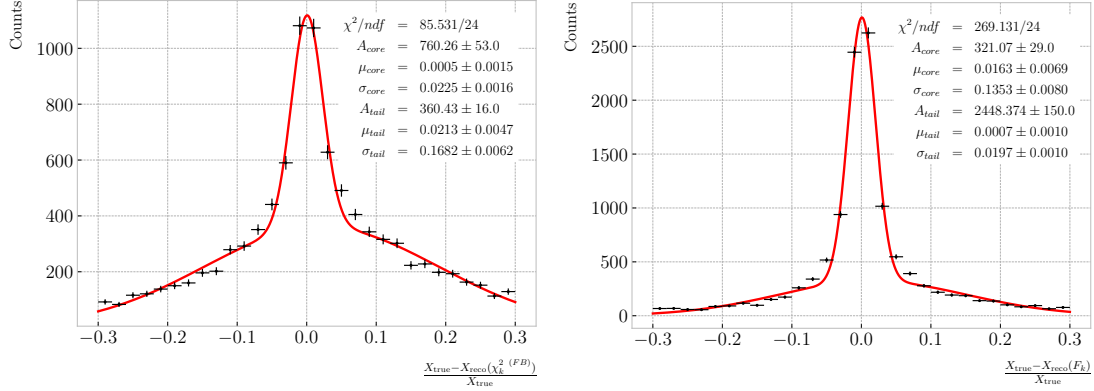


Figure 6.37: Fractional residual distributions of the true and reconstructed decay position along the drift coordinate, using the position of the maximum of $\chi_k^2(FB)$ (left panel) and F_k (right panel) as estimates of the decay position. Also shown are double Gaussian fits to these points (red lines).

where $\hat{\mathbf{X}} = \{\hat{\mathbf{x}}_k^B, \hat{\mathbf{x}}_k^F\}$, $V^{(\hat{\mathbf{x}}_k)}$ is the block diagonal matrix formed by $V^{(\hat{\mathbf{x}}_k, F)}$ and $V^{(\hat{\mathbf{x}}_k, B)}$ and $V^{(\hat{\alpha}_k)}$ is the covariance matrix of $\hat{\alpha}_k$, given by:

$$V^{(\hat{\alpha}_k)} = \left(H^T (V^{(\hat{\mathbf{x}}_k)})^{-1} H \right)^{-1}. \quad (6.29)$$

From these new fit estimates we can compute the F statistic, which tells us whether the model with breakpoint provides a statistically significant better fit:

$$F_k = \left(\frac{\chi_{\text{track},k}^2 - \chi_{\text{full},k}^2}{8 - 5} \right) / \left(\frac{\chi_{\text{full},k}^2}{N - 8} \right). \quad (6.30)$$

One can also compute the signed difference of the duplicated variables divided by their standard deviation at each point. These represent how significant the discontinuity in each variable is. For any variable η we can write it as:

$$D_k^\eta = \frac{\hat{\eta}_k^B - \hat{\eta}_k^F}{\sqrt{\text{Var}[\hat{\eta}_k^F] + \text{Var}[\hat{\eta}_k^B] - 2\text{Cov}[\hat{\eta}_k^F, \hat{\eta}_k^B]}}. \quad (6.31)$$

In our case, the relevant ones to look at are $D_k^{1/R}$ and D_k^ϕ .

Figure 6.36 shows the values of $\chi_k^2(FB)$, F_k , $D_k^{1/R}$ and D_k^ϕ as functions of the position along the drift direction, for an example reconstructed track with 55.5% of the energy

6.5. CHARGED PION DECAY IN FLIGHT

coming from the charged pion and 45.5% from the daughter muon. The true position of the decay is indicated (dashed red lines). Notice how $\chi_k^2(FB)$ and F_k , $D_k^{1/R}$ reach their maxima near the decay point. In the former case this indicates a large forward-backward difference in the track fit. In the later it represents that the extended state vector improves the fit particularly around that point.

I can estimate the decay position finding resolution by computing the difference between the X position of the maxima of $\chi_k^2(FB)$ and F_k and the X position of the true decay. Figure 6.37 represent the the fractional residual distributions for both cases, from the sample of tracks containing pion decays. Fitting a double Gaussian to the distributions (red lines) I find a resolution of $(3.31 \pm 0.15)\%$ and $(6.94 \pm 0.31)\%$ respectively.

In principle, the F -statistic should follow a Fisher distribution with $(8 - 5)$ and $(N - 8)$ degrees of freedom under the null hypothesis. In most of our cases $N \sim \mathcal{O}(100)$, so the probability density functions will look very similar. In this case, it is safe to take the limit $N \rightarrow \infty$ in the Fisher PDF:

$$\begin{aligned} \tilde{f}(x; a - b) &= \lim_{N \rightarrow \infty} f(x; a - b, N - a) \\ &= \frac{2^{-\frac{a-b}{2}}}{\Gamma\left(\frac{a-b}{2}\right)} (a - b)^{\frac{a-b}{2}} x^{\frac{a-b}{2}-1} e^{-\frac{a-b}{2}x}. \end{aligned} \quad (6.32)$$

In our case $a - b = 8 - 5 = 3$, so we would obtain a p-value of 0.05 at $x = 2.60$.

Figure 6.38 contains the distributions of the maxima of $\chi_k^2(FB)$, F_k and D_k^ϕ and the minima of $D_k^{1/R}$ for a sample of non-decaying pion tracks (blue) and another sample of reconstructed tracks containing part of the pion and the daughter muon from a decay inside the fiducial volume (red). Notice that, even though the values of $F_k^{(max)}$ for the decay sample are typically larger than for the non-decaying one, just a small fraction of the events go beyond the aforementioned value of $F = 2.60$. Therefore, from a practical point of view, it is not the most efficient variable to use for selecting the decay events.

However, looking at the $D_k^{1/R \ (min)}$ distribution we can see there is a big difference between non-decaying and decaying events in this variable. One can use a combination

CHAPTER 6. PARTICLE ID IN ND-GAr

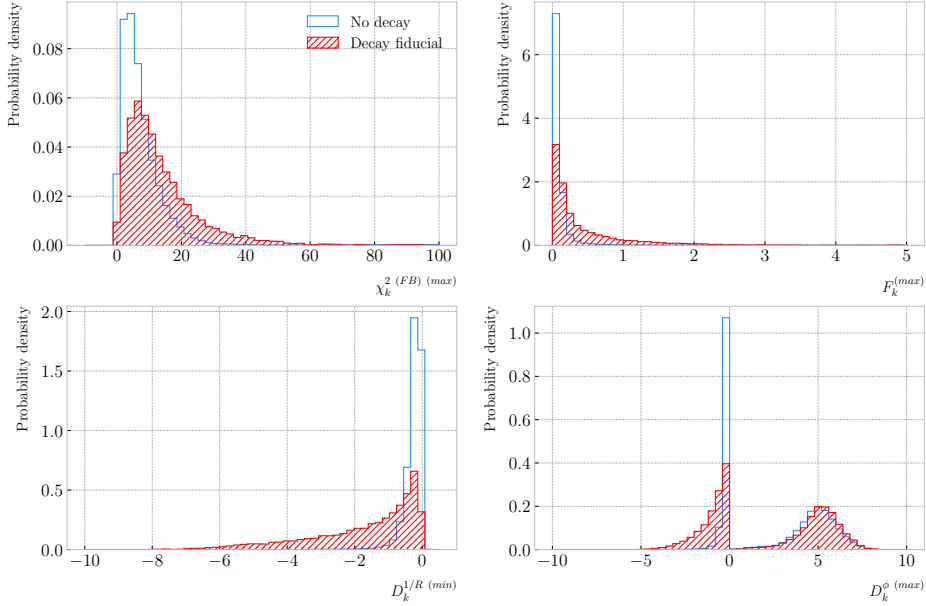


Figure 6.38: Distributions of the extreme values of $\chi_k^2(FB)$ (top left panel), F_k (top right panel), $D_k^{1/R}$ (bottom left panel) and D_k^ϕ (bottom right panel) for non-decaying reconstructed pion tracks (blue) and tracks which include the decay inside the fiducial volume (red).

of these four variables to distinguish between the pion decay events (signal) and the non-decaying pions (background).

An approach to this classification could be using a boosted decision tree (BDT). One of the advantages of BDTs is that they are easy to interpret and identify the relative importance of the different input variables. Training a BDT with 400 estimators and a maximum depth of 4 I can obtain an efficient classification without overtraining. Figure 6.39 (left panel) shows the distribution of probabilities predicted by the BDT for a test sample. The signal efficiency as a function of background acceptance, the so-called ROC curve, is shown in Fig. 6.39 (right panel). With a relative importance of 0.83, the most important variable turned out to be $D_k^{1/R} \text{ (min)}$.

One thing we can check is how the resolution to the decay and the signal efficiency in the classification changes with the true decay angle. Using an equal-frequency binning for the decay angles, we can repeat the previous steps for each bin.

Figure 6.40 (left panel) shows the dependence on the decay angle of the decay finding

6.5. CHARGED PION DECAY IN FLIGHT

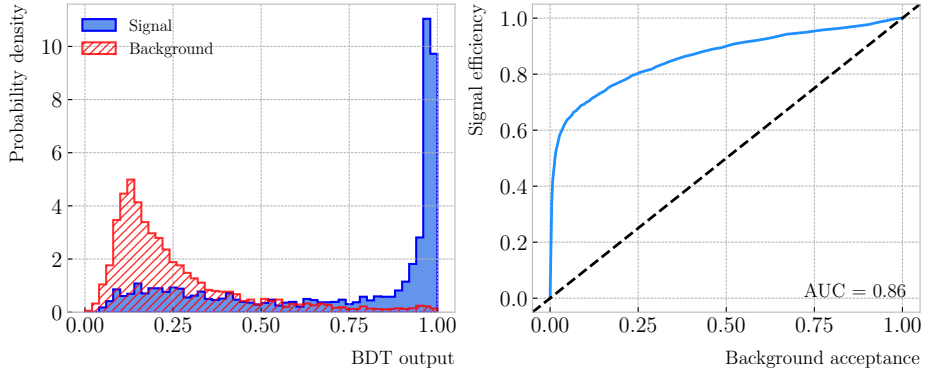


Figure 6.39: Left panel: distributions of the predicted probabilities assigned by the BDT classifier to a test sample of decaying pion+muon tracks (blue) and non-decaying pion tracks (red). Left: signal efficiency versus background acceptance (ROC curve) obtained from the BDT for the test sample.

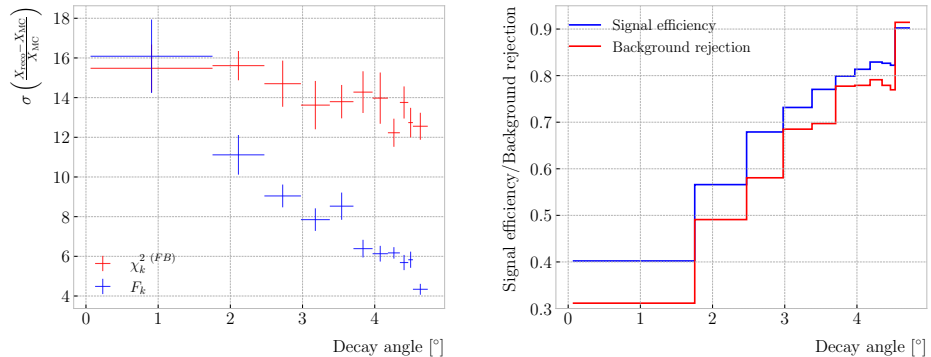


Figure 6.40: Left panel: dependence of the decay position finding resolution on the true value of the decay angle for the $\chi_k^2(FB)$ (red) and F_k (blue) methods. Right panel: signal efficiency (blue line) and background rejection (red line) from the BDT classifier versus true decay angle.

resolution. We can see that for the $\chi_k^2(FB)$ maximum location method the resolution consistently lies between 12 to 16%. However, the $F_k^{(\max)}$ approach gives a significantly better resolution for high angle values, reaching the 4 – 6% range for decay angles $\geq 4^\circ$.

For the classification dependence on the angle, I use the same classifier I trained before but evaluating the test sample for each individual angular bin. I compute the signal efficiency in each bin for a fixed value of the background rejection, in this case 90%. Similarly, for the background rejection estimation I use a fixed signal efficiency value of 90%. Figure 6.40 (right panel) represents the change in signal efficiency (blue)

CHAPTER 6. PARTICLE ID IN ND-GAr

3247 and background rejection (red) with the value of the true decay angles.

3248 6.6 Neutral particle identification

3249 6.6.1 ECal clustering

3250 Another important reconstruction item is the clustering algorithm of ECal hits in
3251 GArSoft. The default module features a NN algorithm that treats all hits in the same
3252 way, independently of the layer each hit comes from. However, the current ECal design
3253 of ND-GAr has two very different types of scintillator layers. The inner layers are made
3254 out of tiles, which provide excellent angular and timing resolutions. On the other hand,
3255 the outer layers are cross scintillator strips. That way, an algorithm that treats hits
3256 from both kinds of layers differently may be able to improve the current performance.

3257 Inspired by the reconstruction of T2K’s ND280 downstream ECal [165], the idea
3258 was to put together a clustering module that first builds clusters for the different ECal
3259 views (tiles, strips segmented in the X direction and strips segmented in Y direction),
3260 and then tries to match them together to form the final clusters.

3261 Working on a module-by-module basis, the algorithm first separates the hits depending
3262 on the layer type they come from. Then, it performs a NN clustering for the 3 sets of
3263 hits separately. For the tile hits it clusters together all the hits which are in nearest-
3264 neighbouring tiles and nearest-neighbouring layers, for strip hits it looks at nearest-
3265 neighbouring strips and next-to-nearest-neighbouring layers (as the layers with strips
3266 along the two directions are alternated). For strip clusters an additional cut in the
3267 direction along the strip length is needed.

3268 After this first clustering I then apply a recursive re-clustering for each collection
3269 of strip clusters based on a PCA method. In each case, we loop over the clusters with
3270 $N_{hits} \geq 2$, computing the centre of mass and three principal components. Propagating
3271 these axes up to the layers of the rest of the clusters, we check if the propagated point
3272 and the centre of mass of the second cluster are within next-to-nearest-neighbouring
3273 strips. An additional cut in the direction along the strip length is also needed. Moreover,

6.6. NEUTRAL PARTICLE IDENTIFICATION

3274 I require that the two closest hits across the two clusters are at most in next-to-nearest-
3275 neighbouring strips. I merge the clusters if these three conditions are satisfied. The
3276 re-clustering is repeated until no more cluster pairs pass the cuts.

3277 The clusters in each strip view are combined if their centres of mass are close enough
3278 and they point in the same direction. An alternative approach for the strip cluster
3279 merging could be to compute the overlap between the ellipsoids defined by the principal
3280 axes of the clusters, and then merge the pair if the overlap exceeds some threshold.
3281 Further study is needed to understand if this change would have an impact in the overall
3282 clustering performance.

3283 To merge the tile clusters to the combined strip clusters I propagate the principal
3284 axis of the strip cluster towards the inner layers, up to the centre of mass layer of the
3285 tile cluster. I merge the clusters if the distance between the propagated point and the
3286 centre of mass is below a certain cut.

3287 The last step is to check if clusters in neighbouring modules should be merged
3288 together, both across two barrel modules, across end cap modules and between barrel
3289 end cap modules. I check the distance between the two closest hits in the pair of clusters
3290 and merge them if it passes this and an additional direction cut.

3291 Figure ?? presents an example of the clustering steps relevant for strip layer hits, from
3292 the input hits (top left panel) to the NN clustering (top right panel) and re-clustering
3293 (bottom left panel) for each strip view and the final merging strip clusters (bottom
3294 right panel). It shows the hits from a single ECal barrel module in a ν_μ CC interaction
3295 event with a neutral pion and a proton in the final state. The two clusters on the left
3296 correspond to the photon pair from the π^0 decay and the one on the upper right corner
3297 is associated to the proton.

3298 This algorithm has a total number of eight free parameters that need to be optimised.
3299 I used a sample of 1000 ν_μ CC interactions in order to obtain the optimal configuration of
3300 clustering parameters. This sample was generated up to the default ECal hit clustering
3301 level, so then I could run the new clustering algorithm each time with a different
3302 configuration of parameters. As the number of parameters is relatively large, I only

CHAPTER 6. PARTICLE ID IN ND-GAr

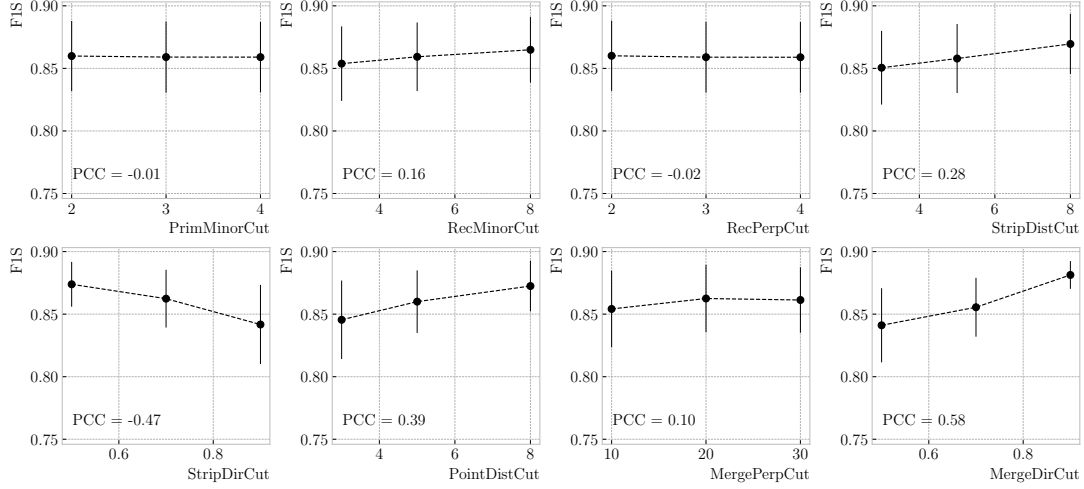


Figure 6.41: Mean values of the F_1 -score marginal distributions for the different free parameters of the new clustering algorithm, with the error bars representing one standard deviation around the mean. The F_1 -score values were computed for the 6561 possible parameter configurations using 1000 ν_μ CC interaction events.

Table 6.5: Summary of parameters and sampled values used in the optimisation of the clustering algorithm.

Name	Units	Sampled values	Description
PrimMinorCut	strips	2, 3, 4	Distance along strip length in NN clustering
RecMinorCut	strips	3, 5, 8	Distance between propagated point and CM along strip length in re-clustering
RecPerpCut	strips	2, 3, 4	Closest hit pair distance in re-clustering
StripDistCut	strips	3, 5, 8	Distance between CMs in strip cluster merging
StripDirCut	cos	0.5, 0.7, 0.9	Main axes direction cut in strip cluster merging
PointDistCut	tiles	3, 5, 8	Distance between propagated point and CM in strip-tile matching
MergePerpCut	cm	10, 20, 30	Closest hit pair distance in module merging
MergeDirCut	cos	0.5, 0.7, 0.9	Main axes direction cut in module merging

3303 performed a coarse-grained scan of the parameter space. Sampling each of the eight
 3304 parameters at three different points each I obtain 6561 different configurations. These
 3305 parameters, together with the used values, are summarised in Tab. 6.5.

3306 In order to measure the performance of the clustering, I use a binary classification
 3307 approach. For each formed cluster, I identify the Geant4 Track ID of the matching MC
 3308 particle and the energy fraction of each hit. Then, I assign to each cluster the Track ID
 3309 with the highest total energy fraction. For each of the different Track IDs associated to

6.6. NEUTRAL PARTICLE IDENTIFICATION

3310 the clusters, I select the cluster with the highest energy (only from the hits with the
3311 same Track ID). I identify such a cluster as the main cluster for that Track ID. I count
3312 as true positives (TPs) the hits with the correct Track ID in each main cluster. False
3313 positives (FPs) are the hits with the incorrect Track ID for the cluster they are in, not
3314 only main clusters. The false negatives (FNs) are the hits with the correct Track ID in
3315 clusters other than the main.

3316 Figure 6.41 shows the computed F_1 -score values for the different cuts. In each case,
3317 the central value represents the mean of the F_1 -score distribution for the specified value
3318 of the corresponding variable and the vertical error bar represents one standard deviation
3319 around the mean. Also shown are the Pearson correlation coefficients of these central
3320 values. We can see that five of the variables have a sizeable effect on the F_1 -score, with
3321 an absolute difference between the last and first values as big as 4%.

3322 The working configuration is obtained as follows. I first select all configurations
3323 with purity $\geq 90\%$. Among those, I choose the combinations that yield the maximum
3324 F_1 -score. If more than one configuration remains I select the one with the highest
3325 sensitivity. Doing so, I end up with a parameter configuration with an efficiency of 88%
3326 and a 90% purity. Compared with the default algorithm, which gives an efficiency of
3327 76% and a purity of 91% for the same sample, I have managed to improve the efficiency
3328 by a factor of 1.16.

3329 6.6.2 π^0 reconstruction

3330 One of the potential applications of the new ECal hit clustering is the reconstruction of
3331 neutral particles, in particular pions. Neutral pions decay promptly after being produced,
3332 through the $\pi^0 \rightarrow \gamma\gamma$ channel ($98.823 \pm 0.034\%$) of the time. The photon pair does
3333 not leave any traces in the HPgTPC (unless one or both of them converts into an
3334 electron-positron pair), but each of them will produce an electromagnetic shower in
3335 the ECal.

3336 To test the potential impact of the new algorithm in π^0 reconstruction, I generated
3337 a MC sample of single, isotropic neutral pions inside the HPgTPC. All pions were

CHAPTER 6. PARTICLE ID IN ND-GAr

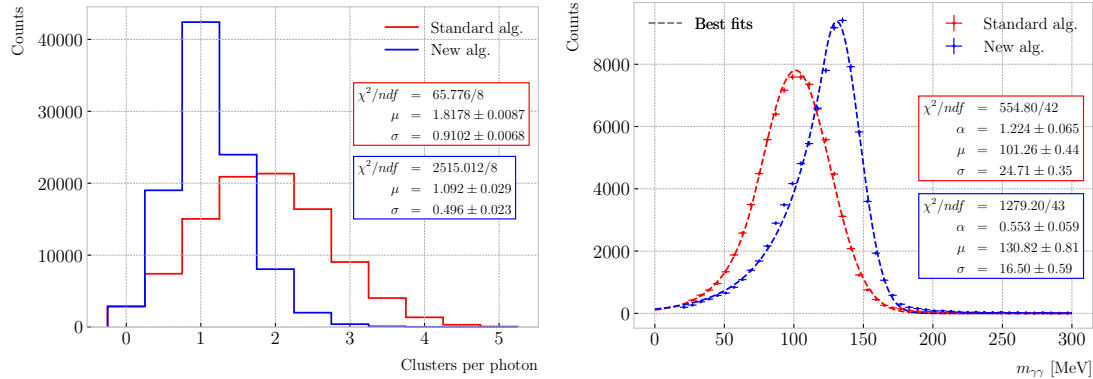


Figure 6.42: Left panel: distributions of the number of ECal clusters per photon from π^0 decays for the standard (red) and new (blue) clustering algorithms. Right panel: reconstructed invariant mass distributions for photon pairs from single π^0 events using the standard (red) and new (blue) ECal clustering algorithms.

generated with a momentum $p = 500$ MeV and their initial positions were uniformly sampled inside a $2 \times 2 \times 2$ m box aligned with the centre of the TPC. I ran both the default and the new clustering algorithms, using for the latter the optimised configuration discussed above.

The first thing to notice is that the number of clusters produced per photon has decreased. Figure 6.42 (left panel) shows these distributions for the default (red) and new (blue) algorithms. Using a simple Gaussian fit, we see that the mean number of ECal clusters per photon went from 1.82 ± 0.01 to 1.09 ± 0.03 . This effectively means that with the new algorithm the ECal activity of one true particle is typically reconstructed as a single object. From the reconstruction point of view this can be an advantage. As now most of the photon energy ends up in a single ECal cluster, I can simply use cluster pairs to identify the π^0 decay.

In general, one calculates the invariant mass of the photon pair as:

$$m_{\gamma\gamma} = \sqrt{2E_1E_2(1 - \cos \theta)}, \quad (6.33)$$

where E_i are the energies of the photons and θ the opening angle between them. In this case I can use the energies deposited in the ECal and their incident directions. This quantity is computed for all possible pairs of clusters, using their position together with

6.7. INTEGRATION IN GArSOFT

3354 the true decay point. In a more realistic scenario, e.g. ν_μ CC interaction, one could use
 3355 the position of the reconstructed primary vertex instead. I also tried to use the principal
 3356 direction of the clusters, but that approach gave considerably worse results. For each
 3357 event I only keep the pair with an invariant mass closer to the true π^0 mass value.

3358 Figure 6.42 (right panel) shows the invariant mass distributions for the photon pairs
 3359 we get using the default (red) and the new (blue) ECal clustering algorithms. For the fit
 3360 I used a modified version of the Crystal Ball function [166], obtained by taking the limit
 3361 where the parameter controlling the power-law tail goes to infinity:

$$f(x; N, \mu, \sigma, \alpha) = N \cdot \begin{cases} e^{\frac{\alpha(2x-2\mu+\alpha\sigma)}{2\sigma}}; & x \leq \mu - \alpha\sigma, \\ e^{-\frac{(x-\mu)^2}{2\sigma^2}}; & x > \mu - \alpha\sigma. \end{cases} \quad (6.34)$$

3362 Comparing the fitted mean and standard deviation values for the Gaussian cores, we
 3363 see that the distribution for the new algorithm is a 67% narrower and also peaks much
 3364 closer to the true m_{π^0} value, going from 101.3 ± 0.4 MeV to 130.8 ± 0.6 MeV.

3365 6.7 Integration in GArSoft

3366 All the additions and improvements to the reconstruction discussed in this Chapter
 3367 had to be integrated in the GArSoft framework. This is necessary both to allow a
 3368 more streamlined path for development, as this makes testing and adding features
 3369 straightforward, as well as make the changes usable in future productions of simulated
 3370 data. In this section, I outline the current status of the integration in GArSoft of the
 3371 reconstruction work presented above.

3372 The new track-cluster association code has been implemented in GArSoft, under
 3373 the name of `TPCECALAssociation2`, and has now become the new default in the
 3374 reconstruction. The structure of the module is similar to the previous implementation,
 3375 and the data products they output are identical in form. Therefore, any existing code
 3376 using the association objects does not need to be modified.

3377 The computation of the truncated mean dE/dx of the tracks, the evaluation of

CHAPTER 6. PARTICLE ID IN ND-GAr

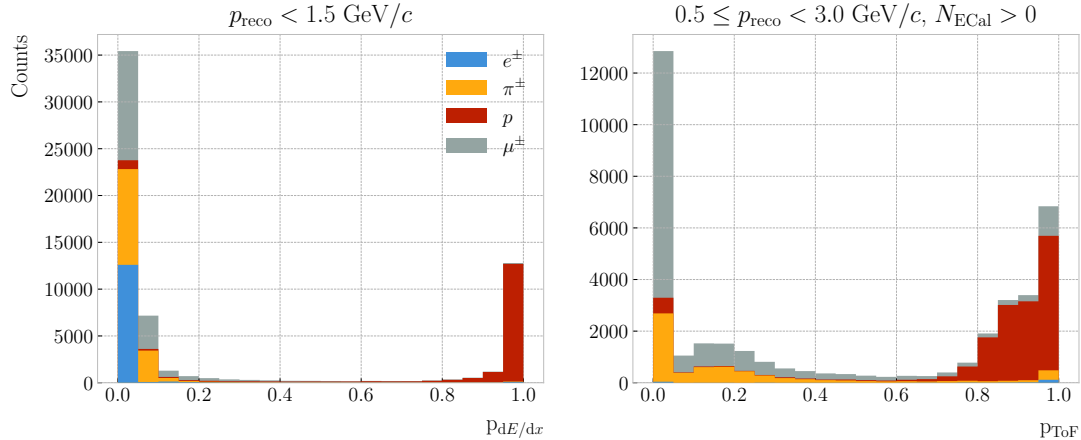


Figure 6.43: Distributions of proton dE/dx (left panel) and ToF (right panel) scores for a sample of 100000 FHC neutrino interactions in the HPgTPC. The distributions are broken down by the true particle type associated to the reconstructed particle.

the muon score for muon and pion separation, and the estimation of the velocity from time-of-flight are all orchestrated by the `CreateRecoParticles` module. Each one of these is implemented as a separate algorithm, which is then called by the parent module. This generates the `gar::rec::RecoParticle` products, a new high-level data object in GArSoft. These combine the information from the HPgTPC, ECal, and μ ID to create an object useful for analysers. At the moment, these data products are only generated for charged particles. However, in the future the module can be extended to incorporate other algorithms used for the identification of neutral particles, like neutral pions and neutrons.

Additionally, analogous to the muon score, the `gar::rec::RecoParticle` objects contain two other scores based on the $\langle dE/dx \rangle$ and ToF estimates which measure the “protoness” of a reconstructed particle. These are obtained in a number of momentum bins, and are a measure of the distance to the point in the corresponding distribution that maximises the F_1 -score for the proton separation. This distance is then transformed applying a sigmoid function, which produces a score in the 0 – 1 range, with coefficients obtained following a procedure similar to the one used to calibrate the response of the muon score. The dE/dx proton score is defined for all particles with momenta $p_{\text{reco}} < 1.5 \text{ GeV}/c$, whereas the ToF proton score is available for the particles with at least

6.7. INTEGRATION IN GArSOFT

3396 one associated hit in the inner ECal and momentum in the range $0.5 \leq p_{\text{reco}} < 3.0 \text{ GeV}/c$.
3397 As an example, Fig. 6.43 shows the distributions of the dE/dx (left panel) and ToF
3398 (right panel) proton scores for the reconstructed particles in a 100000 FHC neutrinos
3399 sample.

3400 The calculation of the track breakpoint variables for pion decay identification is
3401 currently implemented as an analysis module in GArSoft. It would be interesting to add
3402 this information to the `gar::rec::RecoParticle` products, possibly calling the code as
3403 an additional algorithm in the `CreateRecoParticles` module. However, the best way
3404 to propagate the information to the high-level objects is still unclear.

3405 About the new ECal clustering algorithm, it is still in a development phase, and
3406 as such it has not replaced the current clustering module. At the moment, its latest
3407 version is integrated in GArSoft as the `CaloClustering2` module. The algorithm used
3408 is implemented separately, and then invoked in the main code. The module can be
3409 run standalone on the outputs of the reconstruction, creating a second instance of the
3410 `gar::rec::Cluster` collection. In the future it may replace the current algorithm as
3411 the default in the reconstruction chain. However, more work is needed in order to
3412 understand its performance in all the different use cases.

3413

3414

Event selection in ND-GAr

7.1 Data sample

3416 In this section I need to make sure to mention:

3417 • I need to comment on the versions of the software that were used for the production
3418 of the different samples (if we end up having more than one). The version of GENIE
3419 used was

3420 • We use GArG4 instead of `edep-sim` for the particle propagation. Because both
3421 `Geant4` wrappers use different configurations for the simulation, the results obtained
3422 are different. The default `edep-sim` configuration used by the DUNE ND is
3423 appropriate for ND-LAr, where thresholds for particle production are higher. In
3424 the case of ND-GAr, these parameters need to be adjusted accordingly. For the
3425 time being, in these first productions of analysis files, we will use our standalone
3426 `Geant4` implementation. For future iterations these differences will need to be
3427 revisited and understood, so we can use the same simulation workflow as the rest
3428 of the ND.

3429 • I need to comment on the sample size. The first sample produced was simply 10^5
3430 events inside the HPgTPC volume. There is also the question of the other sample
3431 we may want to produce for the $\geq 3\pi^\pm$ selection (ask Naseem).

3432 • So far we have only simulated single interaction events. Ideally, we should move
3433 to simulate full spills. Of course, we need to understand how many interactions

CHAPTER 7. EVENT SELECTION IN ND-GAR

Table 7.1: Event rates in ND-GAr.

Process	Events/ton/year	
	1.1×10^{21} POT/year	1.9×10^{21} POT/year
All ν_μ -CC	1.60×10^6	2.83×10^6
CC 0π	5.28×10^5	9.35×10^5
CC $1\pi^\pm$	3.02×10^5	5.34×10^5
CC $1\pi^0$	1.65×10^5	2.92×10^5
CC 2π	3.18×10^5	5.63×10^5
CC 3π	1.36×10^5	2.41×10^5
CC other	1.52×10^5	2.69×10^5
All $\bar{\nu}_\mu$ -CC	7.54×10^4	1.33×10^5
All NC	5.50×10^5	9.73×10^5
All ν_e -CC	2.70×10^4	4.78×10^4

3434 we expect in ND-GAr per spill. Also, there is the question of having neutrino
3435 interactions happening in the other detector volumes (ECal, magnet, . . .).

3436 • At some point, we should generate a sample of rock muons making it to ND-GAr.

3437 • I think I should comment on the run plan (at least the part that concerns ND-GAr),
3438 and what it means in terms of generating a full production sample. It will be
3439 good to have an understanding of the POT we need on-axis and at each off-axis
3440 positions (for both FHR and RHC).

3441 7.2 ν_μ CC selection

3442 In a ν_μ CC inclusive selection, the signal topology we look for is a neutrino-induced
3443 muon with or without other final state particles. Here, I also require the neutrino vertex
3444 to be located inside the fiducial volume (FV) of ND-GAr.

3445 The FV is defined as a smaller cylinder within the cylindrical volume of the HPgTPC.

3446 The FV has a radius R_{FV} and a half-length L_{FV} . For a particle position to lie within

7.2. ν_μ CC SELECTION

3447 the FV it must satisfy:

$$\vec{x}_i \in \left\{ \vec{x} \in \mathbb{R}^3 \mid |x_0| \leq L_{\text{FV}} \text{ \& } \sqrt{x_1^2 + x_2^2} \leq R_{\text{FV}} \right\}, \quad (7.1)$$

3448 in the reference frame of the HPgTPC. For convenience, I define:

$$\begin{aligned} \Delta R_{\text{FV}} &= R_{\text{HPgTPC}} - R_{\text{FV}}, \\ \Delta L_{\text{FV}} &= L_{\text{HPgTPC}} - L_{\text{FV}}, \end{aligned} \quad (7.2)$$

3449 where R_{HPgTPC} and L_{HPgTPC} refer to the radius and the half-length of the HPgTPC,
3450 respectively. Figure 7.1 shows the HPgTPC volume with the FV inside of it. In that
3451 representation, the FV is defined as $\Delta L_{\text{FV}} = 30.0$ cm and $\Delta R_{\text{FV}} = 30.0$ cm. Also shown
3452 is the HPgTPC reference frame, with x being the drift direction and z aligned along the
3453 beam direction.

3454 In some cases, it is interesting to divide the signal events in different categories
3455 based on their true interaction mode. In this work, I will distinguish between charged-
3456 current quasi-elastic (CCQE), coherent (CCCOH), resonant (CCRES), and deep-inelastic
3457 (CCDIS) interactions. I also use a separate category for the interactions not included in
3458 any of the other categories (CCOther).

3459 Any other events are considered backgrounds. For this selection, I use the following
3460 categorisation of background events:

- 3461 • Out of FV: if the true neutrino vertex lies outside the defined FV.
- 3462 • NC: if the event is a true neutral-current event.
- 3463 • $\bar{\nu}_\mu$ CC: if the true neutrino candidate is of muon antineutrino flavour.
- 3464 • Other: if the event is not signal nor falls in any of the other background categories.

3465 The key to the CC selection is the identification of a primary muon candidate.
3466 Typically, this is the longest track in the event. However, sometimes protons and pions
3467 leave tracks longer than that of the muon. This is particularly important in the GAr

CHAPTER 7. EVENT SELECTION IN ND-GAR

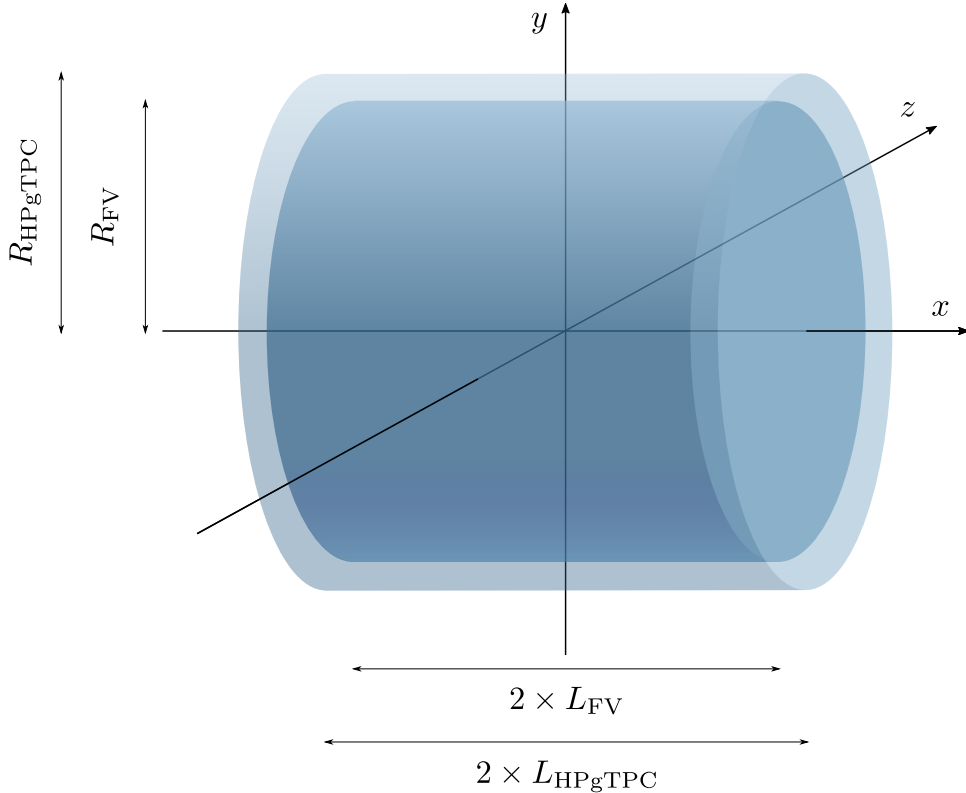


Figure 7.1: Schematic diagram of the HPgTPC including the fiducial volume (FV). In this case the FV is given by $\Delta L_{\text{FV}} = 30.0$ cm and $\Delta R_{\text{FV}} = 30.0$ cm.

3468 medium, considerably less dense than the LAr. For this reason, the muon identification
 3469 in ND-GAr relies heavily on the capabilities of the ECal.

3470 The selection strategy proposed combines the information coming from the three
 3471 main detection systems of ND-GAr: the HPgTPC charge readout, and the ECal and
 3472 μ ID detectors. It consists of five steps:

- 3473 1. Event contains reconstructed particles.
- 3474 2. Select particles with reconstructed negative charge, $q_{\text{reco}} = -1$.
- 3475 3. Select particles passing the muon score cut, $\mu_{\text{score}} \geq \mu_{\text{score}}^{\text{cut}}$.
- 3476 4. Keep reconstructed particle with the highest momentum, $\max [p_{\text{reco}}]$.
- 3477 5. Check that the remaining particle starts within the FV.

7.2. ν_μ CC SELECTION

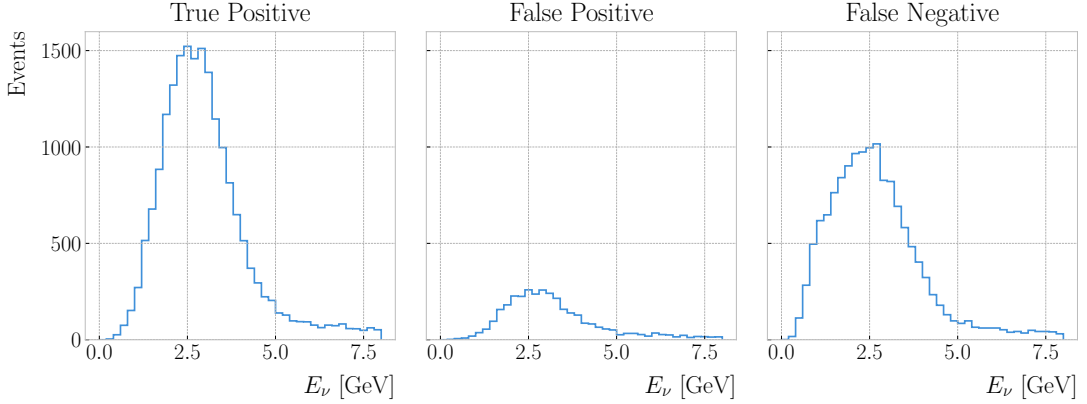


Figure 7.2: True positive (left panel), false positive (middle panel), and false negative (right panel) true neutrino energy distributions for the ν_μ CC selection given by a muon score cut of $\mu_{\text{score}}^{\text{cut}} = 0.75$, and a FV defined as $\Delta L_{\text{FV}} = 30.0$ cm and $\Delta R_{\text{FV}} = 30.0$ cm.

3478 All the events passing these cuts are classified as signal, and the selected particle is
3479 regarded as the primary muon candidate.

3480 **7.2.1 Selection optimisation**

3481 I performed an optimisation of this selection, comparing the performance of a number of
3482 configurations. For the muon selection, I varied the value of $\mu_{\text{score}}^{\text{cut}}$ from 0.05 to 0.95,
3483 using a step size of 0.05. Additionally, to optimise the FV, I systematically explored a
3484 number of different parameter configurations, moving within the 10.0 – 70.0 cm range for
3485 ΔL_{FV} and 25.0 – 75.0 cm for ΔR_{FV} , in increments of 10.0 cm and 5.0 cm respectively.

3486 For each parameter configuration, I extract three different true neutrino energy
3487 distributions. These are built combining the results of the selection described previously,
3488 which we can refer to as the ‘reco’ selection, and a ‘true’ selection. The later identifies
3489 the true ν_μ CC events using the GENIE event records, and checks that the true neutrino
3490 vertices are contained in the FV.

3491 The first distribution consists of the events passing both selections, i.e., these are
3492 the true ν_μ CC events which pass the ‘reco’ selection. The second distribution contains
3493 the events passing the ‘reco’ selection but failing the ‘true’ selection. These are
3494 the background events that the selection misidentifies. Finally, the third distribution

CHAPTER 7. EVENT SELECTION IN ND-GAR

3495 corresponds to the events picked by the “true” selection but not by the “reco” one. In
 3496 other words, these are the true ν_μ CC events that our selection misses. In analogy to
 3497 the machine learning jargon, I refer to these distributions as the true positive (TP),
 3498 false positive (FP), and false negative (FN) spectra, respectively. Figure 7.2 shows an
 3499 example of these three distributions for the case $\mu_{\text{score}}^{\text{cut}} = 0.75$, $\Delta L_{\text{FV}} = 30.0$ cm, and
 3500 $\Delta R_{\text{FV}} = 30.0$ cm.

3501 By making different combinations of these distributions one can compute a series of
 3502 performance metrics. Using the full information from the spectra allows to obtain the
 3503 scores as a function of the true neutrino energy, whereas the totals can be obtained by
 3504 integrating the histograms. This way, the efficiency of the selection is given by:

$$\begin{aligned} \text{Efficiency} &= \frac{\text{Selected true } \nu_\mu \text{ CC events}}{\text{Total true } \nu_\mu \text{ CC events}} \\ &= \frac{\text{TP}}{\text{TP} + \text{FN}}, \end{aligned} \quad (7.3)$$

3505 while the purity can be written as:

$$\begin{aligned} \text{Purity} &= \frac{\text{Selected true } \nu_\mu \text{ CC events}}{\text{Total selected events}} \\ &= \frac{\text{TP}}{\text{TP} + \text{FP}}. \end{aligned} \quad (7.4)$$

3506 Another scoring metric typically used when quantifying the performance of a selection
 3507 is the significance. It is defined as:

$$\text{Significance} = \frac{S}{\sqrt{S + B}} = \frac{\text{TP}}{\sqrt{\text{TP} + \text{FP}}}. \quad (7.5)$$

3508 The significance measures the relative size of the true signal within the selection, $S = \text{TP}$
 3509 with respect to one standard deviation of the counting experiment. Assuming Poisson
 3510 statistics, the variance is equal to the number of observations, and therefore the standard
 3511 deviation equals to $\sqrt{N} = \sqrt{S + B} = \sqrt{\text{TP} + \text{FP}}$. I use this metric to

3512 Figure 7.3 shows the change in efficiency (blue) and purity (red) of the ν_μ CC
 3513 selection as a function of the different cuts. From left to right, I vary $\mu_{\text{score}}^{\text{cut}}$, ΔL_{FV} ,

7.2. ν_μ CC SELECTION

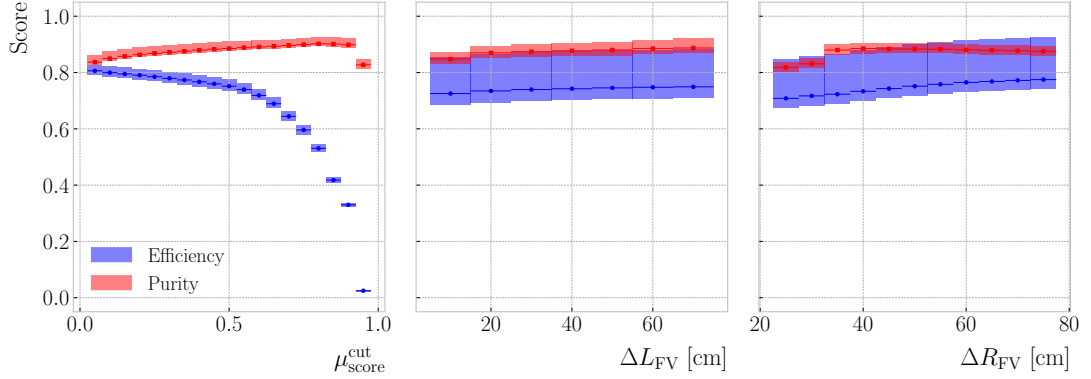


Figure 7.3: Efficiency (blue) and purity (red) for the ν_μ CC selection as a function of the muon score cut (left panel), FV half-length cut (middle panel), and radial cut (right panel). The height of the boxes represents the IQR of the conditional distributions, whereas the horizontal line corresponds to the median.

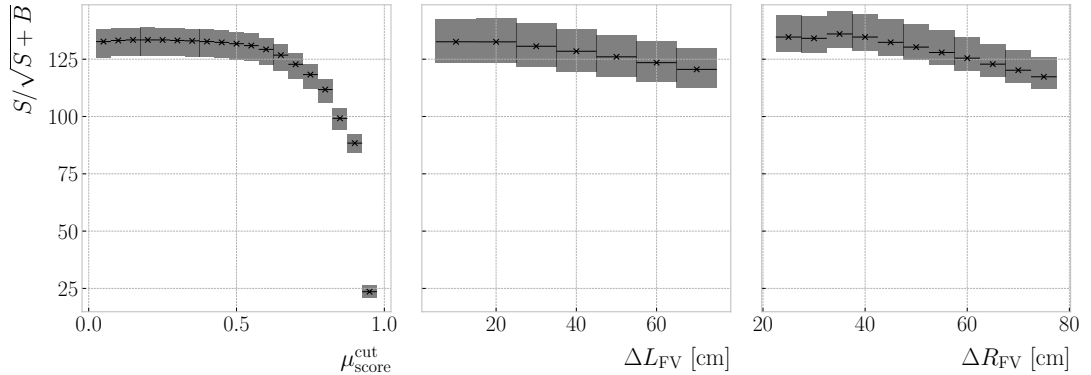


Figure 7.4: Significance for the ν_μ CC selection as a function of the muon score cut (left panel), FV half-length cut (middle panel), and radial cut (right panel). The height of the boxes represents the IQR of the conditional distributions, whereas the horizontal line corresponds to the median.

and ΔR_{FV} . For each value of the cuts, I compute the median and IQR (represented by the horizontal lines and the heights of the boxes, respectively) of the corresponding conditional distributions of efficiency and purity. This representation is useful to get an idea of the general trend the scores follow with the cuts, as well as the spread. It is clear that the muon score cut has the biggest impact on the efficiency, which ranges between 0.05 to 0.80, whereas the purity remains stable with values around 0.85.

A similar depiction of the significance can be found in Fig. 7.4. In this case, one can see that the $S/\sqrt{S+B}$ decreases as the cuts grow tighter. However, there are hints of

CHAPTER 7. EVENT SELECTION IN ND-GAR

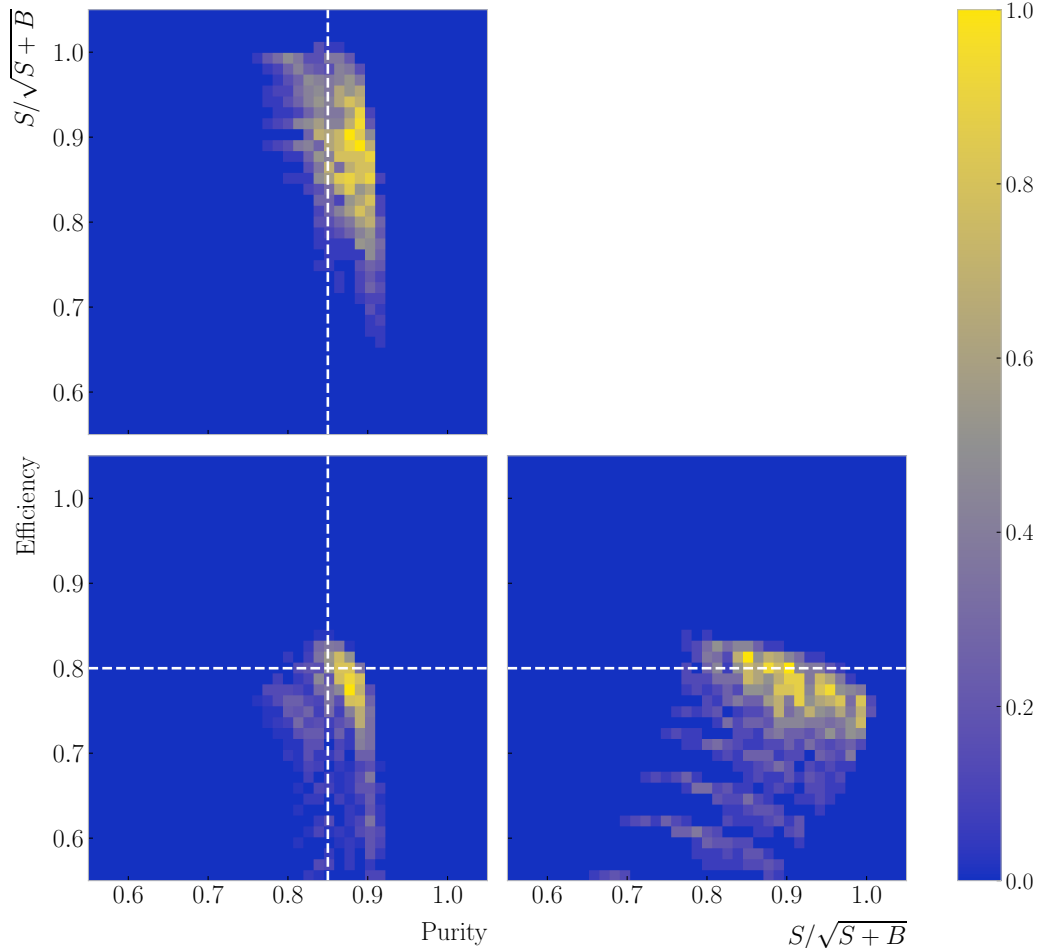


Figure 7.5: Normalised 2D distributions of efficiency, purity and significance for the ν_μ CC selection. The $S/\sqrt{S+B}$ is normalised to the highest value achieved. The vertical dashed line indicates a purity value of 0.85, whereas the horizontal one corresponds to an efficiency of 0.80.

3522 local maxima at intermediate values.

3523 Selecting the cut configuration with the highest significance, 147 ± 11 for the parameter
 3524 values explored here, results in an efficiency and purity of 0.754 ± 0.006 and 0.833 ± 0.007 ,
 3525 respectively. Figure 7.5 shows the 2D distributions resulting when combining pairs of
 3526 efficiency, purity and significance, obtained for the cut configurations explored. The
 3527 significance is normalised to the highest value obtained in the parameter scan. Looking
 3528 at this, it is clear that a selection with highest efficiency and purity can be achieved,
 3529 maintaining a similar significance level.

7.2. ν_μ CC SELECTION

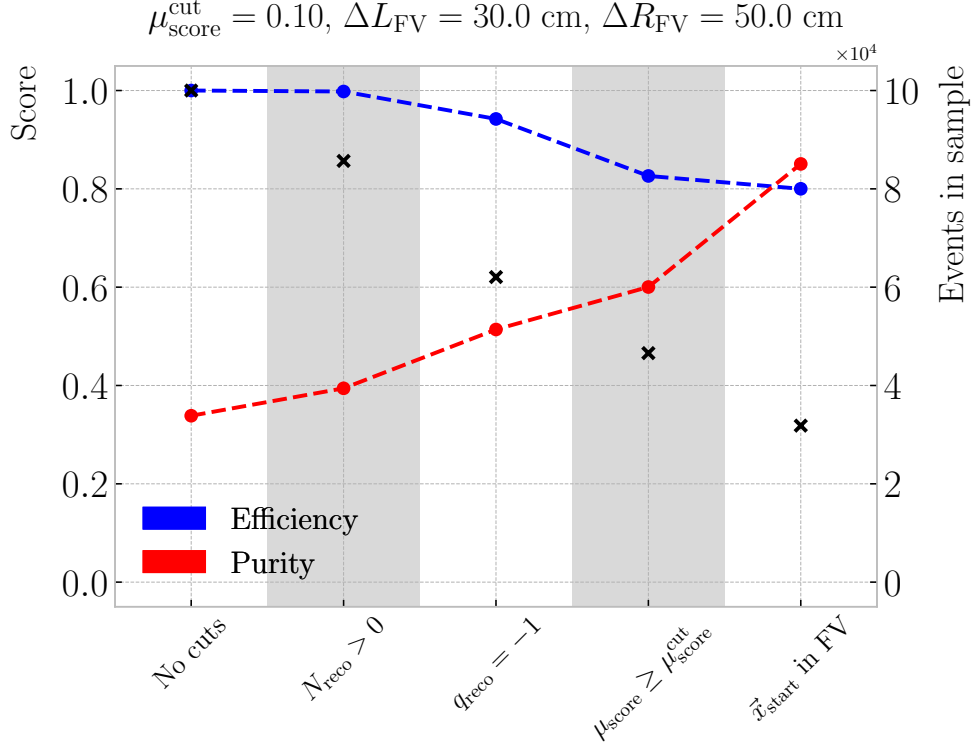


Figure 7.6: Cumulative efficiency (blue) and purity (red) of the ν_μ CC selection. The secondary axis indicates the number of events in the sample after each cut (black crosses).

Table 7.2: Step-by-step ν_μ CC selection cuts and cumulative passing rates. Relative passing rates are indicated in parentheses.

Cut #	Selection cut	Events	Passing rates
0	Total number of events (No cuts)	100000	100.00% (100.00%)
1	At least one reconstructed particle	85680	85.68% (85.68%)
2	Negatively charged particles only	62054	62.05% (72.43%)
3	$\mu_{\text{score}} \geq \mu_{\text{score}}^{\text{cut}}$	46585	46.59% (75.07%)
4	Candidate \vec{x}_{start} in FV	31834	31.83% (68.34%)

3530 Therefore, to get a more refined selection, I first select the configurations with a
 3531 purity and an efficiency higher than 0.85 and 0.80, respectively. After that, I select the
 3532 tuple of cuts yielding the highest significance. The resulting value for the muon score
 3533 cut is $\mu_{\text{score}}^{\text{cut}} = 0.10$, and the FV is given by $\Delta L_{\text{FV}} = 30.0 \text{ cm}$ and $\Delta R_{\text{FV}} = 50.0 \text{ cm}$.
 3534 With these, one obtains a total efficiency of 0.800 ± 0.007 and purity of 0.851 ± 0.008 ,

CHAPTER 7. EVENT SELECTION IN ND-GAR

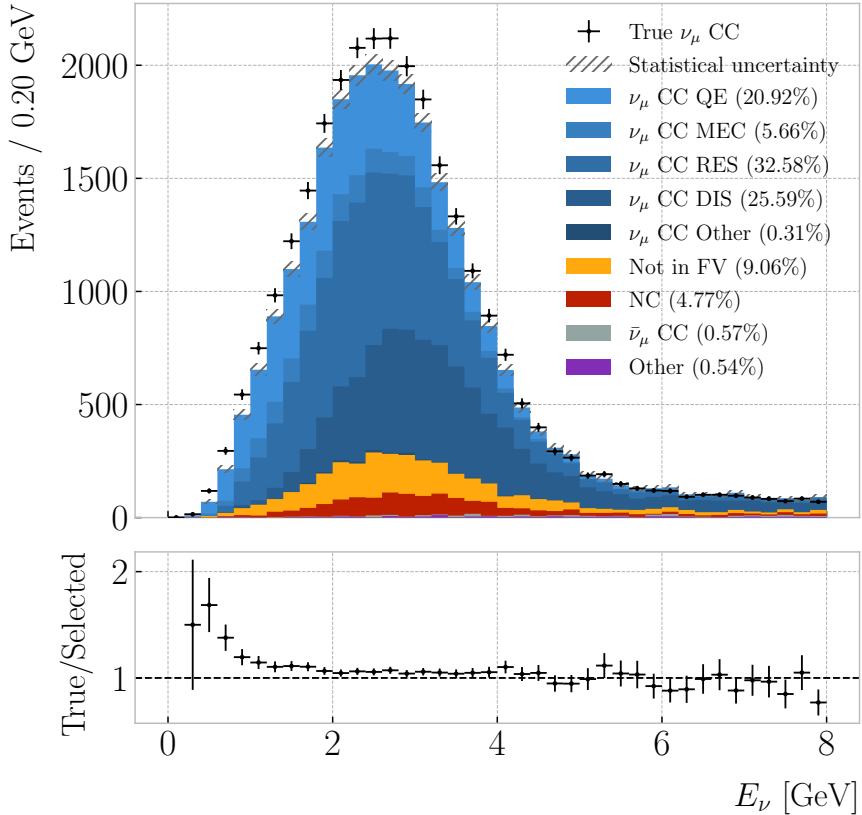


Figure 7.7: True neutrino energy spectra for the ν_μ CC selection. The selected events correspond to the coloured stacked histogram, broken down by signal and background subcategories. The statistical uncertainty is drawn in hatched gray. The true distribution is also shown with the black data points. The bottom panel shows the ratio between the number of true and selected ν_μ CC events per bin.

3535 with a significance of 138 ± 11 . Hereafter, I use this optimised selection cuts, unless
 3536 specified otherwise.

3537 A summary of the selection can be found in Tab. 7.2. It shows the number of
 3538 events in the selected sample after each selection cut, as well as the absolute and relative
 3539 passing rates. Figure 7.6 shows the overall efficiencies (blue) and purities (red) after
 3540 each cut in the event selection is applied. As expected, the efficiency drops while the
 3541 purity increases with the successive cuts.

3542 Notice how, out of the cuts prior to the FV constraint, the sign selection produces
 3543 the highest increase in purity. This is one of the advantages of having a magnetised
 3544 TPC, and can also be used for a $\bar{\nu}_\mu$ CC selection when running in RHC mode.

7.2. ν_μ CC SELECTION

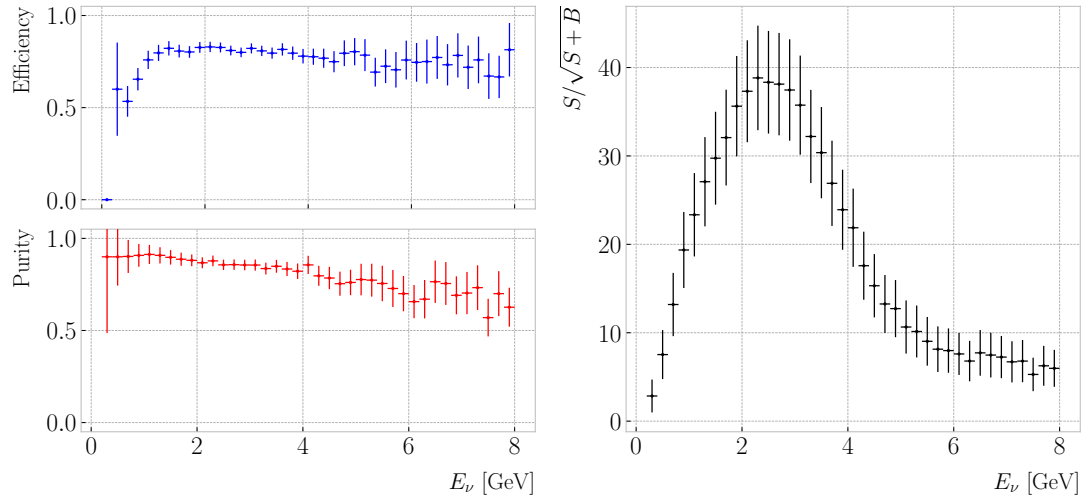


Figure 7.8: Left panel: efficiency (top panel) and purity (bottom panel) for the ν_μ CC selection as a function of the true neutrino energy. Right panel: significance for the ν_μ CC selection as a function of the true neutrino energy

3545 7.2.2 Selection performance

3546 Using the stored spectra discussed above, the true neutrino energy distribution for the
 3547 selected events can be recovered doing TP + FP. Similarly, the combination TP + FN
 3548 gives the true spectrum. Figure 7.7 shows the true (black data points) and selected
 3549 (coloured stacked histogram) E_ν distributions for the optimised ν_μ CC selection. The
 3550 colours in the selected spectrum indicate the different signal categories and backgrounds,
 3551 with the overall statistical uncertainty represented by the gray hatched mess. The ratio
 3552 between the true and selected events is also shown. One can see that it sits around 1 for
 3553 most of the energy range. However, for energies ≤ 1 GeV there is a significant deficit of
 3554 selected events.

3555 These spectra also allow to compute the efficiency and purity of the selection as
 3556 a function of the true neutrino energy, as shown in Fig. 7.8 (left panel). As it could
 3557 be expected from the previous ratio plot, the efficiency is low at low neutrino energies.
 3558 Nonetheless, it raises quickly with the energy, until it stabilises around a value of 0.80.
 3559 Looking at the purity, one may notice that, although it starts at around 0.90, there is a
 3560 significant decrease towards the high end of the spectrum. Figure 7.8 (right panel) also

CHAPTER 7. EVENT SELECTION IN ND-GAR

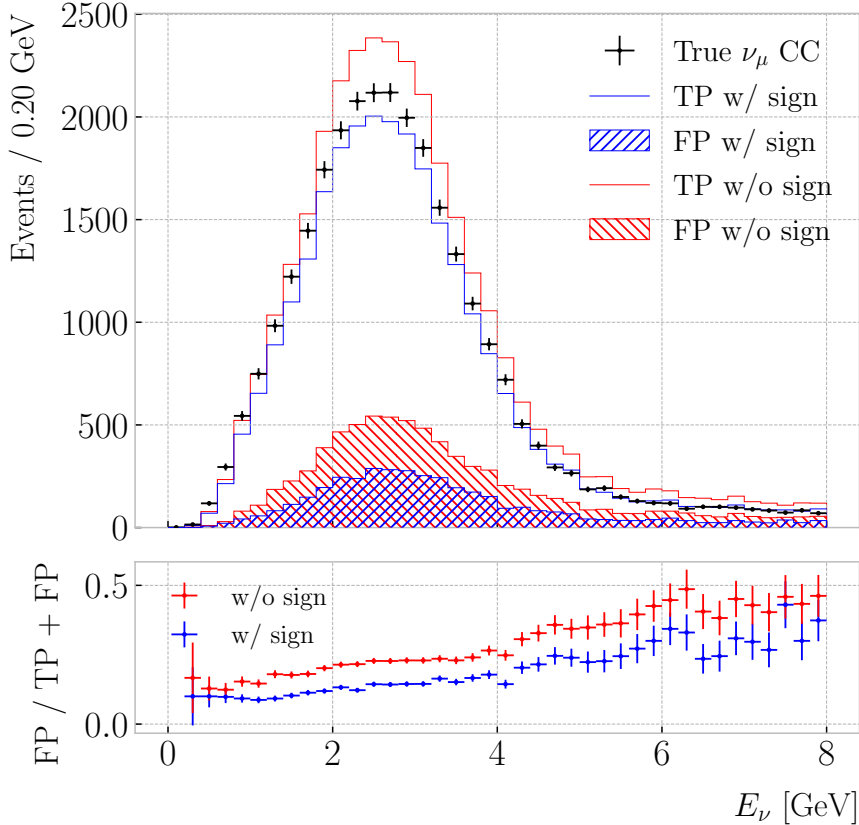


Figure 7.9: True neutrino energy spectra for the ν_μ CC selection with (blue) and without (red) sign selection. The selected events are broken down by true positives (signal) and false positives (background). The true distribution is also shown (black data points). The bottom panel shows the ratios between the number of false positives and total selected events per bin.

3561 shows the significance as a function of the energy. In this case, the highest $S/\sqrt{S+B}$ is
 3562 achieved around the energies where the spectrum peaks.

3563 A variation of the ν_μ CC selection one can try is to apply it without the reconstructed
 3564 charge cut. Figure 7.9 (top panel) shows the E_ν distributions corresponding to the
 3565 selection with (blue stacked histogram) and without (red stacked histogram) the sign
 3566 selection. In the former case, the out of FV contamination amounts to 9.06% of the
 3567 total, while the NC contamination results 4.77% and the wrong-sign contamination
 3568 0.57%. For the later, these backgrounds account for the 10.01%, 10.82%, and 2.18%
 3569 of the selected events, respectively. As expected, removing the positive particles does
 3570 not change the FV-related effects noticeably. However, the sign selection proves its

7.2. ν_μ CC SELECTION

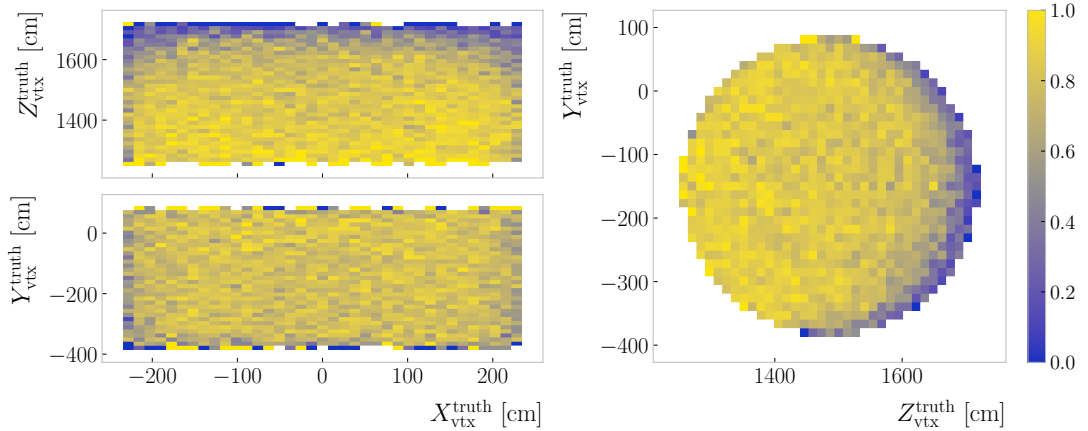


Figure 7.10: Efficiency 2D distributions for the ν_μ CC selection given the true position of the interaction vertex.

worth in the rejection of $\bar{\nu}_\mu$ CC events, which drop almost by one order of magnitude.
 Additionally, the charge selection cuts the NC events in half, as it reduces the chances
 of misidentifying a positively charged hadron for a muon.

As an additional check, I explored how the performance of the ν_μ CC selection
 depends on the position of the neutrino interaction within the HPgTPC. Maps of the
 selection efficiency for the X, Z (top left panel), X, Y (bottom left panel), and Z, Y
 (right panel) true vertex position pairs are given in Fig. 7.10. It can be seen that the
 efficiency remains stable along the drift direction, only slightly degrading close to the
 edges of the FV. Regarding the radial direction, it is clear that an important number of
 events with high $Z_{\text{vtx}}^{\text{truth}}$ are not being selected. Intuitively, the muons arising from these
 interactions will leave short tracks. As their directions are typically aligned with the
 beam direction, they enter the ECal shortly after production. This is likely to affect
 the tracking, and therefore their identification. As a result, the regions with the lowest
 efficiency are the downstream corners of the HPgTPC, i.e. the areas with high $|X_{\text{vtx}}^{\text{truth}}|$
 and $Z_{\text{vtx}}^{\text{truth}}$.

7.2.3 Primary muon kinematics

This ν_μ CC selection relies on the identification of the a primary muon, meaning that
 for each selected event a particle is picked out as the muon candidate. It is because of

CHAPTER 7. EVENT SELECTION IN ND-GAR

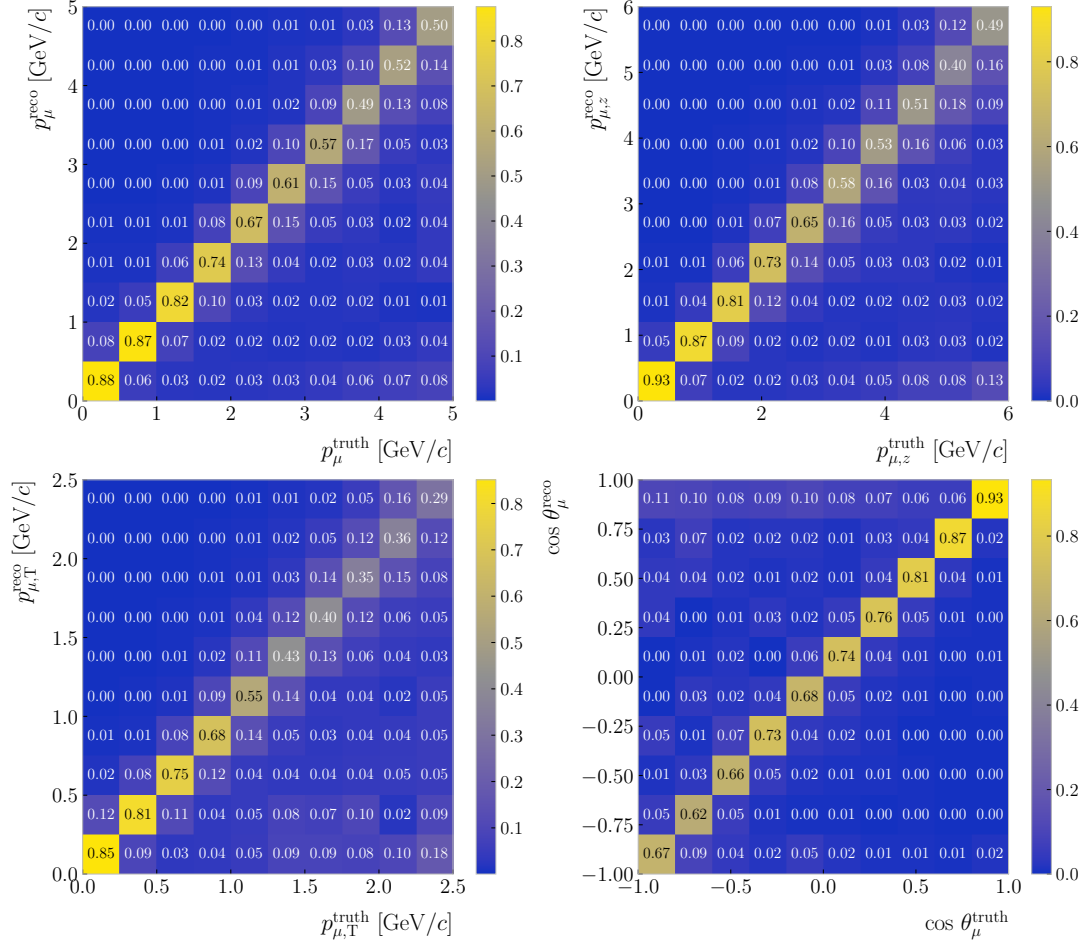


Figure 7.11: Distributions for the reconstructed versus truth generated primary muon momentum (top left panel), longitudinal momentum (top right panel), transverse momentum (bottom left panel), and beam angle (bottom right panel). The reconstructed values correspond to the selected primary muon candidate, whereas the truth values come from the true primary muon in the event.

3589 this that one can study the kinematics of these selected primary muons.

3590 Figure 7.11 shows a comparison between some of the reconstructed and truth primary
 3591 muon kinematic variables. From top to bottom, left to right, we have muon momentum,
 3592 longitudinal momentum, transverse momentum and beam angle. The histograms are
 3593 column-normalised, and so the diagonal entries give an idea of the resolution for the
 3594 different variables. The match between truth and reconstructed values can only be done
 3595 for the selected true ν_{μ} CC events, as the others do not have a primary muon. However,
 3596 for this comparison I do not require the events to start inside the FV.

7.2. ν_μ CC SELECTION

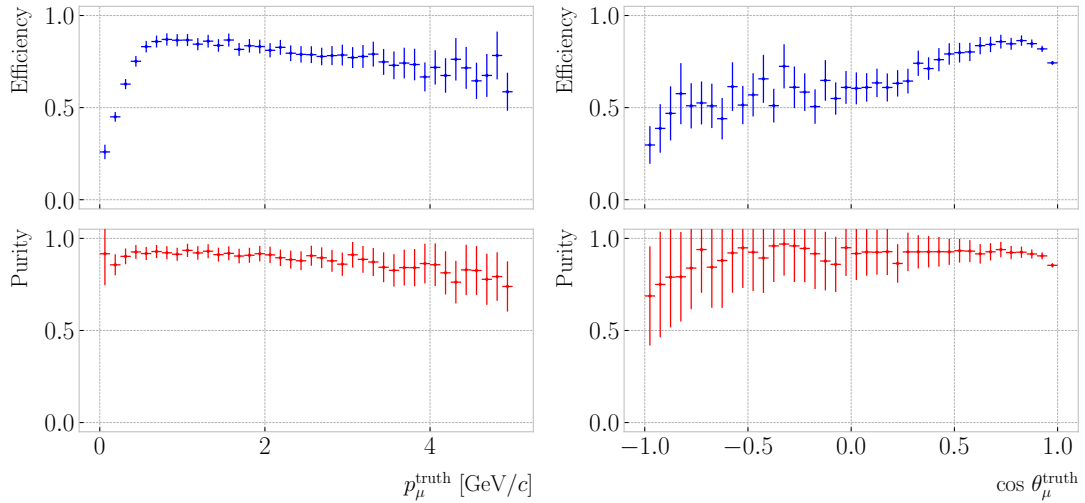


Figure 7.12: Efficiency (blue) and purity (red) of the ν_μ CC selection as a function of the primary muon true momentum (left panel) and beam angle (right panel).

3597 Notice that, for the reconstructed values, the variables do not necessarily come
 3598 from a reconstructed particle that matches the true primary muon. In other words,
 3599 sometimes, even though the event was correctly identified, the primary muon may have
 3600 been confused with another particle. That means that in these distributions include
 3601 both reconstruction and selection deficiencies.

3602 I also studied the performance of the ν_μ CC selection as a function of the kinematic
 3603 variables of the primary muon. As before, these metrics are only possible to compute for
 3604 true ν_μ CC events. The efficiency (top panels) and purity (bottom panels) as a function
 3605 of the truth muon momentum (left) and beam angle (right) are shown in Fig. 7.12. One
 3606 can see that there are some similarities in the behaviour of both metrics between the
 3607 true neutrino energy and the muon momentum cases. This is to be expected, as these
 3608 two variables are highly correlated. For the efficiency, there is a rapid increase at low
 3609 momentum values until it peaks at around 1 GeV/c, after which it starts decreasing
 3610 slowly. The purity remains relatively constant, with a slight drop towards high p_μ^{truth}
 3611 values. In the case of the muon angle, the decrease in efficiency at high $\theta_\mu^{\text{truth}}$ is more
 3612 noticeable. However, note that the number of events with backward-going muons is
 3613 much smaller than those aimed towards the forward direction, as can be seen from the

CHAPTER 7. EVENT SELECTION IN ND-GAR

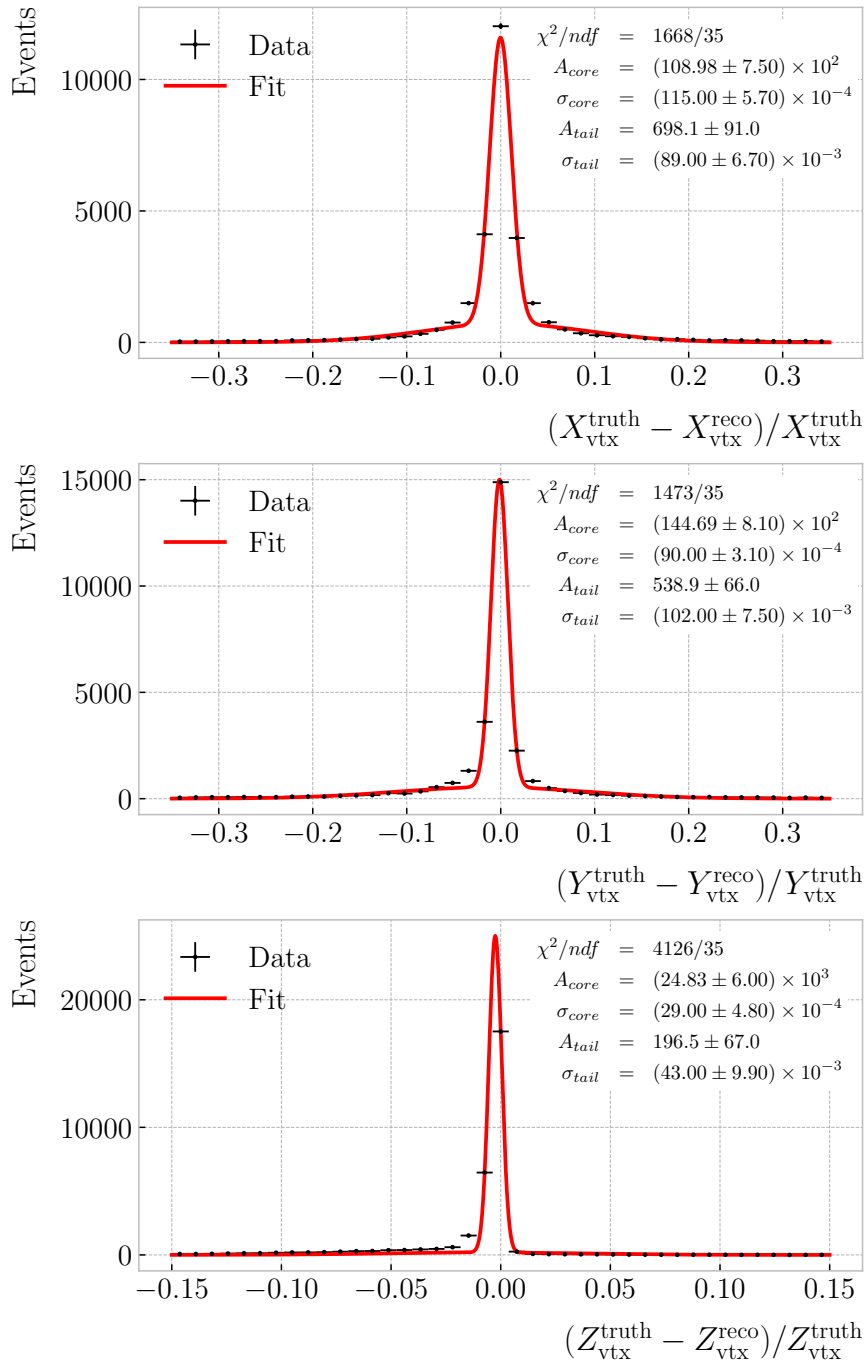


Figure 7.13: Fractional residual distributions for the position of the primary vertex in the ν_μ CC selection. The best fits to a double Gaussian function are also shown (red lines).

7.3. CHARGED PION IDENTIFICATION

size of the vertical error bars. There is also a decline in the purity with the beam angle, but this effect is much smaller.

A byproduct of selecting the primary lepton in the interaction is the position of the reconstructed neutrino vertex candidate. Checking how the position of the selected reconstructed primary vertex and the true vertex position compare is needed to understand the validity of our method. Figure 7.13 shows the distributions of fractional residuals between the truth and reconstructed vertex positions in the X (top panel), Y (middle panel), and Z (bottom panel) directions. Performing a double Gaussian fit to the distributions (red lines), I estimate the reconstructed vertex resolution achieved with this method to be $1.62 \pm 0.08\%$, $1.23 \pm 0.05\%$, and $0.32 \pm 0.05\%$ for the X , Y , and Z directions, respectively. As expected, the resolution along the drift direction. However, the significant difference in resolution between the two transverse directions is worth noting. Not only the resolution is better for the Z direction, but the layout of the residual distribution is highly asymmetrical. This may be related to the variability in the selection efficiency along that direction.

7.3 Charged pion identification

Now that I have checked the robustness of the proposed ν_μ CC selection, it can be used as a starting point for other, more convoluted, selections. One of the priorities of ND-GAr, as mentioned previously, is the identification of pions. With its lower tracking thresholds, ND-GAr is expected to do better regarding π^\pm identification than the traditional LArTPCs, like ND-LAr. Moreover, it can make use of the different detector subcomponents to tag the charged pions.

The ν_μ CC selection provides a starting point for the pion identification. The first thing one can do is rule out the selected primary muon candidate. Then, by looking at the properties of the rest of the reconstructed particles, one can start the counting of the charged pions.

The two proton scores, the one based on the dE/dx in the HPgTPC and the one

CHAPTER 7. EVENT SELECTION IN ND-GAR

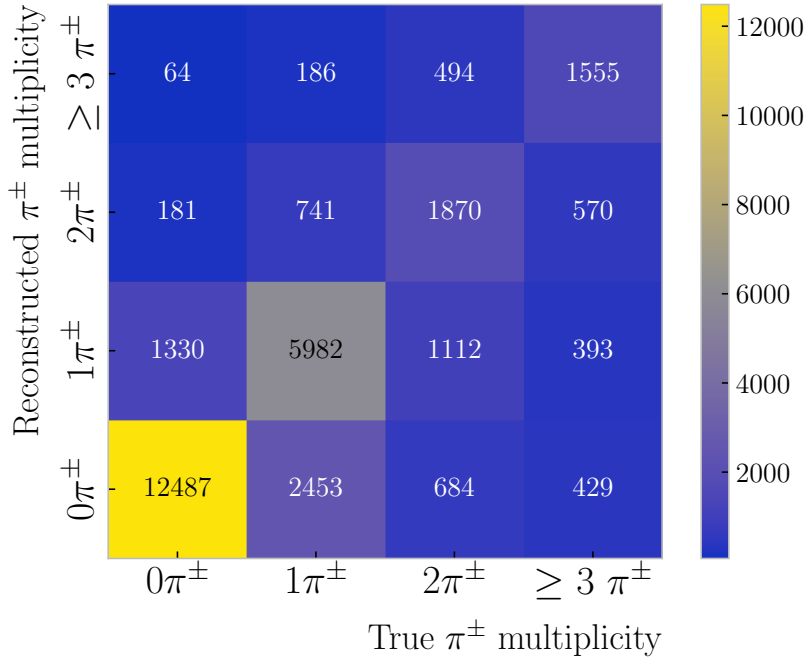


Figure 7.14: Distribution of events given their true and reconstructed π^\pm multiplicity, for the selection given by $p_{dE/dx}^{\text{cut}} = p_{\text{ToF}}^{\text{cut}} = 0.50$, $\Delta_{dE/dx}^{\pi^\pm} = 0.20$, and $d_\mu^{\text{cut}} = 50.0$ cm.

3641 obtained from the ToF measurement in the ECal, can be used to separate the protons
 3642 from the sample of charged pions. By providing appropriate cuts for these, a good
 3643 separation can be achieved.

3644 Another source of information available is the dE/dx of the track associated to the
 3645 reconstructed particle. To select the charged pions, we can require that the measured
 3646 mean dE/dx is compatible with the expectation for a true π^\pm , in other words:

$$\left\langle \frac{dE}{dx} \right\rangle_{\pi^\pm} \left(1 - \Delta_{dE/dx}^{\pi^\pm} \right) \leq \left\langle \frac{dE}{dx} \right\rangle_{\text{meas.}} < \left\langle \frac{dE}{dx} \right\rangle_{\pi^\pm} \left(1 + \Delta_{dE/dx}^{\pi^\pm} \right), \quad (7.6)$$

3647 where the parameter $\Delta_{dE/dx}^{\pi^\pm}$ measures the fractional variation one allows around the
 3648 theoretical expectation. To obtain the expected mean dE/dx of a charged pion with a
 3649 given momentum, I use the ALEPH parametrisation with the parameter values obtained
 3650 previously.

3651 Also, as we are only interested in the primary pions, and because these are by
 3652 definition close to the interaction vertex, one can apply an additional distance cut. Using

7.3. CHARGED PION IDENTIFICATION

3653 the start position of the muon candidate, we can restrict the starting point of pions to a
3654 certain volume around the vertex.

3655 Combining all these ideas, I propose the following procedure to identify the charged
3656 pions in an event:

- 3657 1. Apply ν_μ CC selection.
- 3658 2. Disregard particle selected as primary muon.
- 3659 3. Remove particles with momentum below threshold.
- 3660 4. Select particles with proton dE/dx score below threshold.
- 3661 5. Select particles with proton ToF score below threshold.
- 3662 6. Select particles with mean dE/dx around the expected value for a pion.
- 3663 7. Remove particles with a distance between the start of the track and the primary
3664 vertex greater than the cut.

3665 The remaining particles after all these cuts are taken to be charged pion candidates.

3666 This counting method depends on four cuts, denoted by $p_{dE/dx}^{\text{cut}}$, $p_{\text{ToF}}^{\text{cut}}$, $\Delta_{dE/dx}^{\pi^\pm}$, and
3667 d_μ^{cut} in order of appearance. The momentum threshold is necessary to compare with
3668 the true multiplicity. For values of the kinetic energy lower than 10 – 20 MeV, we
3669 do not expect to be able to tag individual pions. Such low energy particles just leave
3670 small traces in the TPC which, together with the busy environment of the neutrino
3671 interaction vertex, leaves one with no other option but to only account for their energy
3672 calorimetrically. As such, the true pion counting also features this momentum threshold.

3673 I performed an optimisation of the charged pion counting by scanning the space of
3674 possible cut configurations. For the two proton scores, I let them vary between 0.10 to
3675 0.90, in increments of 0.10. Similarly, the parameter $\Delta_{dE/dx}^{\pi^\pm}$ takes values in the range
3676 0.05 – 0.25, with a step size of 0.05. Finally, the distance cut changes in 10 cm steps,
3677 from 10 to 120 cm.

CHAPTER 7. EVENT SELECTION IN ND-GAR

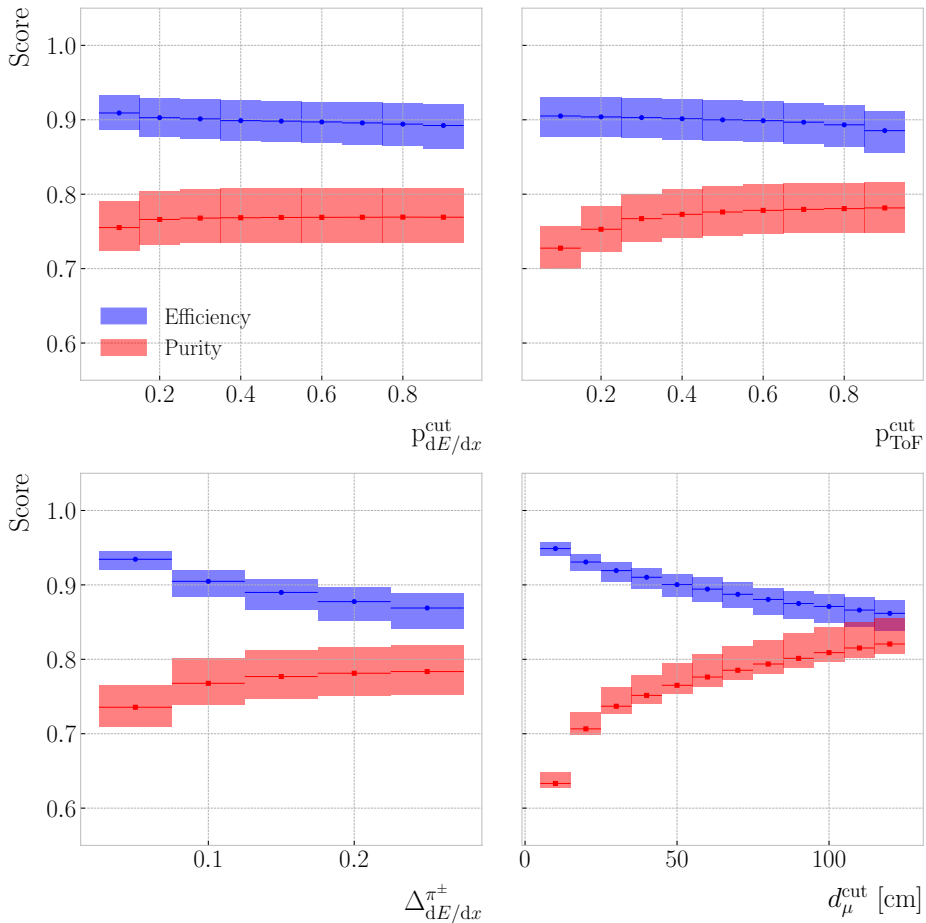


Figure 7.15: Efficiency (blue) and purity (red) for the ν_μ CC $0\pi^\pm$ selection as a function of the proton dE/dx score cut (top left panel), proton ToF score cut (top right panel), pion dE/dx cut (bottom left panel), and distance to muon cut (bottom right panel). The height of the boxes represents the IQR of the conditional distributions, whereas the line corresponds to the median.

3678 For each combination of selection cuts, I compare the true charged pion multiplicity
 3679 given by GENIE with the number of charged pion candidates I count with this method,
 3680 hereafter referred to as the reconstructed π^\pm multiplicity. The result of this comparison
 3681 is a matrix, with columns and rows indicating true and reconstructed charged pion
 3682 multiplicity, respectively. An example of one of these matrices, obtained for a certain
 3683 configuration of cuts, can be seen in Fig. 7.14. From these multiplicity matrices one can
 3684 extract performance metrics, like efficiency, purity, and significance.

3685 Given a multiplicity matrix \mathbf{M} , the efficiency for the i -th multiplicity value can be

7.3. CHARGED PION IDENTIFICATION

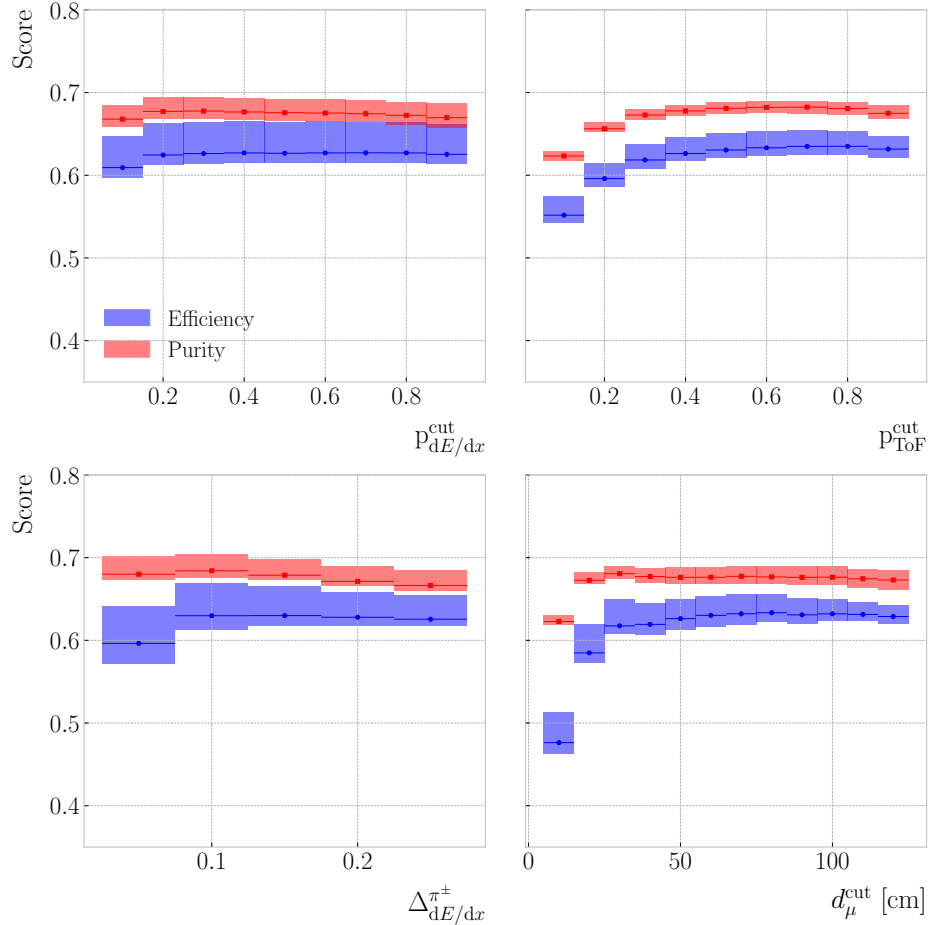


Figure 7.16: Efficiency (blue) and purity (red) for the ν_μ CC $1\pi^\pm$ selection as a function of the proton dE/dx score cut (top left panel), proton ToF score cut (top right panel), pion dE/dx cut (bottom left panel), and distance to muon cut (bottom right panel). The height of the boxes represents the IQR of the conditional distributions, whereas the line corresponds to the median.

3686 computed as:

$$\text{Efficiency}|_i = \frac{M_{ii}}{\sum_j M_{ij}}, \quad (7.7)$$

3687 or in other words, dividing the corresponding diagonal entry by the sum of all the entries

3688 in the same column. On the other hand, the purity is given by:

$$\text{Purity}|_i = \frac{M_{ii}}{\sum_j M_{ji}}, \quad (7.8)$$

3689 which is just the ratio between the diagonal entry and the sum of the entries in the

CHAPTER 7. EVENT SELECTION IN ND-GAR

3690 corresponding row. Similarly, the significance is obtained by taking the square root of
 3691 the denominator in the previous expression:

$$\text{Significance}|_i = \frac{S}{\sqrt{S+B}} \Big|_i = \frac{M_{ii}}{\sqrt{\sum_j M_{ji}}}. \quad (7.9)$$

3692 Figures 7.15 and 7.16 show the efficiency (blue) and the purity (red) for the ν_μ
 3693 CC $0\pi^\pm$ and $1\pi^\pm$ selections, respectively, as a function of the different cut values. In
 3694 the figures, each box represents the IQR of the conditional distribution for the fixed
 3695 value of the corresponding cut, and the horizontal lines correspond to the medians. The
 3696 first thing one notices is that the efficiency is always higher than the purity in the $0\pi^\pm$
 3697 selection, while the opposite is true for the $1\pi^\pm$ selection. Also, it is clear that the range
 3698 within these metrics fluctuate in the $0\pi^\pm$ selection is significantly higher than it is for
 3699 the $1\pi^\pm$ case. This shows that it is easier to assess that no charged pions are present in
 3700 the event than actually tagging them.

3701 For the ν_μ CC $0\pi^\pm$ selection, the performance metrics follow the expected tendency.
 3702 As the purity grows with a cut value, the efficiency decreases. Interestingly, this is not
 3703 the case for the $1\pi^\pm$ selection, where both efficiency and purity follow roughly the same
 3704 trends along the different cuts. This makes sense when one comprehends that this is not
 3705 a traditional cut-based selection, but more of a counting exercise. Some restrictive cut
 3706 configurations will not tag any particles as pions. On the contrary, loose cuts will render
 3707 every particle as a π^\pm . Therefore, when looking at a specific multiplicity, the relation
 3708 between the cut value and the performance metrics is not obvious. Thus, sometimes
 3709 efficiency and purity can both increase, as the cuts refine the definition of a reconstructed
 3710 pion.

3711 To have a working point for our studies, I chose the cut configuration that yields
 3712 the maximum significance for the ν_μ CC $1\pi^\pm$ selection. Of course, other cuts would be
 3713 more appropriate in certain scenarios. However, this provides us with a starting point
 3714 to understand the performance of the selection. A significance of 66 ± 7 for the $1\pi^\pm$
 3715 selection is achieved for the cut values $p_{dE/dx}^{\text{cut}} = 0.30$, $p_{\text{ToF}}^{\text{cut}} = 0.70$, $\Delta_{dE/dx}^{\pi^\pm} = 0.10$, and

7.3. CHARGED PION IDENTIFICATION

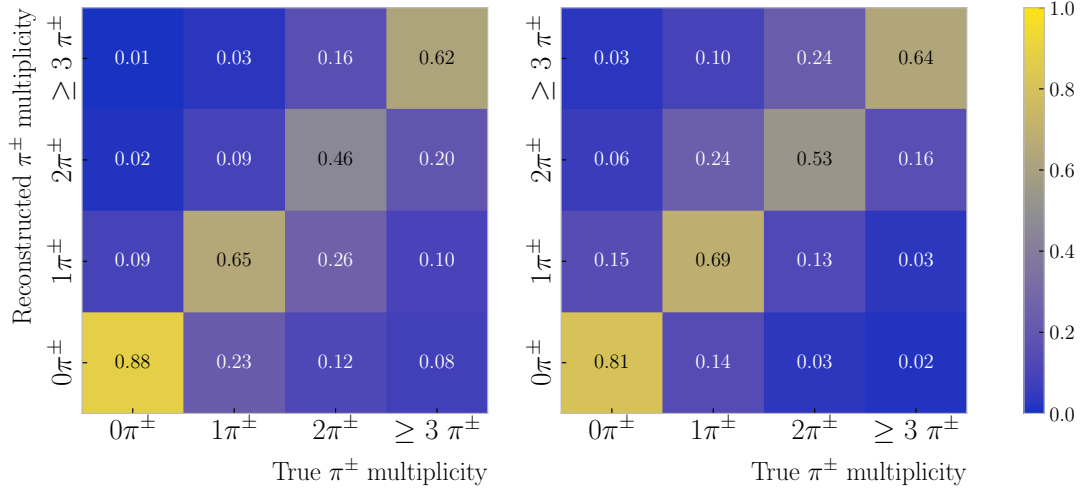


Figure 7.17: Distribution of events given their true and reconstructed π^\pm multiplicity, both column-wise (left panel) and row-wise (right panel) normalised, for the selection that maximises the significance of the ν_μ CC $1\pi^\pm$ selection. The column normalisation yields the efficiency in the diagonal entries, whereas the row normalisation reveals the purity.

3716 $d_\mu^{\text{cut}} = 110.0$ cm.

3717 Figure 7.19 shows the multiplicity matrices resulting from this optimised ν_μ CC $1\pi^\pm$
 3718 selection. Although both matrices are produced with the same selection cuts, one is
 3719 column normalised (left panel), whereas the other is row normalised (right panel). It
 3720 follows from the definitions in Eqs. (7.7) and ((7.8)) that the diagonal entries of these
 3721 matrices correspond to the efficiencies and the purities, respectively, for each of the
 3722 possible charged pion multiplicity selections.

3723 An additional check to make is understand how this configuration performs when
 3724 applied to the other selections, like ν_μ CC $0\pi^\pm$, and how it compares to the other
 3725 possible configurations. A comparison between the different pion multiplicity selections,
 3726 indicated with colours, in the purity versus efficiency space is shown in Fig. 7.18. For
 3727 each of the possible multiplicity choices, the performance obtained for the $1\pi^\pm$ optimised
 3728 selection is indicated by an outlined point. From this, one can see that the selected
 3729 configuration performs reasonably well, within the limits of what can be achieved in
 3730 each case, across the different multiplicities.

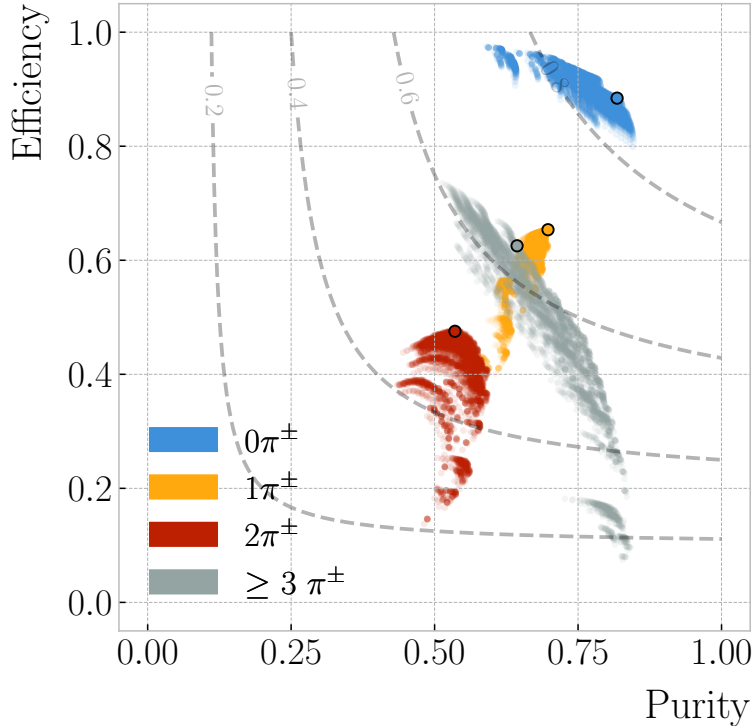


Figure 7.18: Purity versus efficiency achieved for the different cut configurations explored separated by the various ν_μ CC $N\pi^\pm$ selections. The outlined points indicate the state for each possible multiplicity when using the configuration that maximises the significance of the ν_μ CC $1\pi^\pm$ selection. The contours indicate the surfaces of equal F_1 -score.

³⁷³¹ **7.3.1 ν_μ CC $1\pi^\pm$ selection**

³⁷³² **7.4 Neutral pion identification**

³⁷³³ **7.5 Systematic uncertainties**

³⁷³⁴ **7.5.1 Flux uncertainties**

³⁷³⁵ The neutrino flux prediction is affected by systematic uncertainties arising from two
³⁷³⁶ sources: the uncertainties in the production of hadrons in the target and the uncertainties
³⁷³⁷ in the design parameters of the beamline itself. These fluxes and their uncertainties are
³⁷³⁸ generated with the G4LBNF simulation [85], a Geant4 implementation of the LBNF
³⁷³⁹ beamline, and the Package to Predict the Flux (PPFX) framework, originally developed

7.5. SYSTEMATIC UNCERTAINTIES

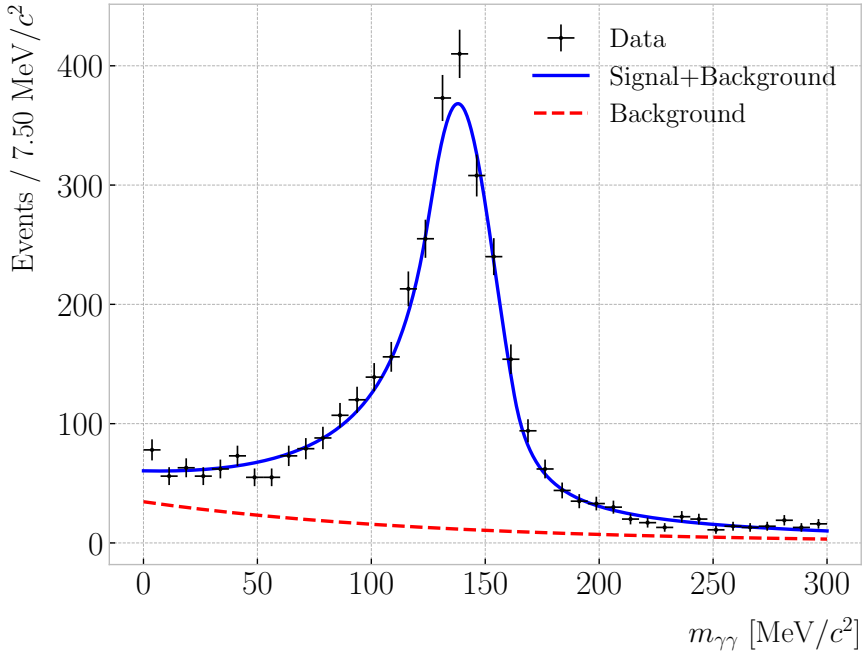


Figure 7.19: Invariant mass distribution obtained for the unassociated ECal cluster pair in the event with the value closest to the true π^0 mass. The best fits for signal plus background (solid blue line) and background only (dashed red line) are also shown.

3740 for MINERvA [167].

3741 The hadron production uncertainties are associated to the kinematic distributions
 3742 of the hadrons produced when the protons interact with the carbon target, as well
 3743 as the possible interactions of the hadrons with the beamline materials. The PPFX
 3744 package estimates these uncertainties by performing a number of random throws of the
 3745 production model parameters [168]. This way, different predictions of the LBNF flux
 3746 are generated, which can be compared to the nominal prediction to build a matrix of
 3747 the covariances between neutrino energies, flavours and running modes (either FHC or
 3748 RHC). The resulting hadron production uncertainties are described by the eigenvectors
 3749 associated to the largest eigenvalues in this matrix, obtained performing a PCA analysis.

3750 The other set of uncertainties affecting the neutrino flux prediction come from the
 3751 limited precision with which we know the parameters of the different components in the
 3752 beamline. These include the specifications of the target, the dimensions of the decay
 3753 pipe, and the current and alignment of the magnetic horns. The effects on the flux

CHAPTER 7. EVENT SELECTION IN ND-GAR

3754 predictions of these uncertainties are estimated using the G4LBNF simulation. For each
3755 of the parameters, the simulation runs with said parameter shifted by $\pm 1\sigma$ from the
3756 nominal value, and the resulting flux prediction is compared to the nominal one.

3757 7.5.2 Cross section uncertainties

3758 7.5.3 Detector uncertainties

Conclusion and outlook

3761 *Our plans miscarry because they have no aim. When a man does not know
3762 what harbour he is making for, no wind is the right wind.*

3763 – Lucio Anneo Seneca, *Epistulae morales ad Lucilium*

3764

A [REDACTED]

3765

An appendix

Bibliography

- 3767 [1] J.N. Bahcall, A.M. Serenelli and S. Basu, *New solar opacities, abundances,*
 3768 *helioseismology, and neutrino fluxes, Astrophys. J. Lett.* **621** (2005) L85
 3769 [[astro-ph/0412440](#)]. 22, 44, 126, 127, 128
- 3770 [2] R. Garani and S. Palomares-Ruiz, *Dark matter in the Sun: scattering off electrons*
 3771 *vs nucleons, JCAP* **05** (2017) 007 [[1702.02768](#)]. 22, 124, 125, 128, 129, 152
- 3772 [3] M. Honda, M. Sajjad Athar, T. Kajita, K. Kasahara and S. Midorikawa,
 3773 *Atmospheric neutrino flux calculation using the NRLMSISE-00 atmospheric model,*
 3774 *Phys. Rev. D* **92** (2015) 023004 [[1502.03916](#)]. 22, 133
- 3775 [4] M. Colom i Bernadich and C. Pérez de los Heros, *Limits on Kaluza-Klein dark*
 3776 *matter annihilation in the Sun from recent IceCube results, Eur. Phys. J. C,* **80** 2
 3777 (2020) 129 **80** (2019) [[1912.04585](#)]. 23, 137, 138
- 3778 [5] ANTARES collaboration, *Search for Dark Matter in the Sun with the ANTARES*
 3779 *Neutrino Telescope in the CMSSM and mUED frameworks, Nucl. Instrum. Meth.*
 3780 *A* **725** (2013) 76 [[1204.5290](#)]. 23, 137, 138
- 3781 [6] N. Deutschmann, T. Flacke and J.S. Kim, *Current LHC Constraints on Minimal*
 3782 *Universal Extra Dimensions, Phys. Lett. B* **771** (2017) 515 [[1702.00410](#)]. 23, 137,
 3783 138
- 3784 [7] ICECUBE collaboration, *Search for GeV-scale dark matter annihilation in the Sun*
 3785 *with IceCube DeepCore, Phys. Rev. D* **105** (2022) 062004 [[2111.09970](#)]. 24, 149,
 3786 150

BIBLIOGRAPHY

- 3787 [8] C.-S. Chen, F.-F. Lee, G.-L. Lin and Y.-H. Lin, *Probing Dark Matter*
3788 *Self-Interaction in the Sun with IceCube-PINGU*, *JCAP* **10** (2014) 049
3789 [1408.5471]. 24, 149, 150
- 3790 [9] N.F. Bell, M.J. Dolan and S. Robles, *Searching for dark matter in the Sun using*
3791 *Hyper-Kamiokande*, *JCAP* **11** (2021) 004 [2107.04216]. 24, 149, 150
- 3792 [10] E. Behnke et al., *Final Results of the PICASSO Dark Matter Search Experiment*,
3793 *Astropart. Phys.* **90** (2017) 85 [1611.01499]. 24, 149, 150
- 3794 [11] PICO collaboration, *Dark Matter Search Results from the Complete Exposure of*
3795 *the PICO-60 C₃F₈ Bubble Chamber*, *Phys. Rev. D* **100** (2019) 022001
3796 [1902.04031]. 24, 149, 150
- 3797 [12] DARKSIDE collaboration, *Constraints on Sub-GeV Dark-Matter–Electron*
3798 *Scattering from the DarkSide-50 Experiment*, *Phys. Rev. Lett.* **121** (2018) 111303
3799 [1802.06998]. 24, 154, 155
- 3800 [13] XENON collaboration, *Light Dark Matter Search with Ionization Signals in*
3801 *XENON1T*, *Phys. Rev. Lett.* **123** (2019) 251801 [1907.11485]. 24, 154, 155
- 3802 [14] P.F. de Salas, D.V. Forero, S. Gariazzo, P. Martínez-Miravé, O. Mena,
3803 C.A. Ternes et al., *2020 global reassessment of the neutrino oscillation picture*,
3804 *JHEP* **02** (2021) 071 [2006.11237]. 33, 57, 65
- 3805 [15] W. Pauli, *Dear radioactive ladies and gentlemen*, *Phys. Today* **31N9** (1978) 27. 39
- 3806 [16] F. Reines and C.L. Cowan, *Detection of the free neutrino*, *Phys. Rev.* **92** (1953)
3807 830. 39
- 3808 [17] S.L. Glashow, *Partial-symmetries of weak interactions*, *Nuclear Physics* **22** 579. 39
- 3809 [18] S. Weinberg, *A model of leptons*, *Physical Review Letters* **19** 1264. 39
- 3810 [19] A. Salam, *Weak and Electromagnetic Interactions*, *Conf. Proc. C* **680519** (1968)
3811 367. 39

BIBLIOGRAPHY

- 3812 [20] A. Pich, *The Standard Model of Electroweak Interactions*, in *2010 European
3813 School of High Energy Physics*, pp. 1–50, 1, 2012 [[1201.0537](#)]. 40
- 3814 [21] ALEPH, DELPHI, L3, OPAL, SLD, LEP ELECTROWEAK WORKING GROUP,
3815 SLD ELECTROWEAK GROUP, SLD HEAVY FLAVOUR GROUP collaboration,
3816 *Precision electroweak measurements on the Z resonance*, *Phys. Rept.* **427** (2006)
3817 257 [[hep-ex/0509008](#)]. 43
- 3818 [22] R. Davis, D.S. Harmer and K.C. Hoffman, *Search for neutrinos from the sun*,
3819 *Physical Review Letters* **20** 1205. 44
- 3820 [23] J.N. Bahcall, N.A. Bahcall and G. Shaviv, *Present Status of the Theoretical
3821 Predictions for the ^{37}Cl Solar-Neutrino Experiment*, . 44
- 3822 [24] B.T. Cleveland, T. Daily, R. Davis, Jr., J.R. Distel, K. Lande, C.K. Lee et al.,
3823 *Measurement of the solar electron neutrino flux with the Homestake chlorine
3824 detector*, *Astrophys. J.* **496** (1998) 505. 44
- 3825 [25] SAGE collaboration, *Measurement of the solar neutrino capture rate with gallium
3826 metal. III: Results for the 2002–2007 data-taking period*, *Phys. Rev. C* **80** (2009)
3827 015807 [[0901.2200](#)]. 44, 56
- 3828 [26] F. Kaether, W. Hampel, G. Heusser, J. Kiko and T. Kirsten, *Reanalysis of the
3829 GALLEX solar neutrino flux and source experiments*, *Phys. Lett. B* **685** (2010) 47
3830 [[1001.2731](#)]. 44, 56
- 3831 [27] Q.R. Ahmad, R.C. Allen, T.C. Andersen, J.D. Anglin, G. Bühler, J.C. Barton
3832 et al., *Measurement of the Rate of $\nu_e + d \rightarrow p + p + e^-$ Interactions Produced by
3833 ^8B Solar Neutrinos at the Sudbury Neutrino Observatory*, . 45
- 3834 [28] Q.R. Ahmad, R.C. Allen, T.C. Andersen, J. D. Anglin, J.C. Barton, E.W. Beier
3835 et al., *Direct Evidence for Neutrino Flavor Transformation from Neutral-Current
3836 Interactions in the Sudbury Neutrino Observatory*, . 45
- 3837 [29] T.K. Gaisser and M. Honda, *Flux of atmospheric neutrinos*, . 45

BIBLIOGRAPHY

- 3838 [30] K. Hirata, T. Kajita, M. Koshiba, M. Nakahata, S. Ohara, Y. Oyama et al.,
3839 *Experimental study of the atmospheric neutrino flux*, . 46
- 3840 [31] D. Casper, R. Becker-Szendy, C.B. Bratton, D.R. Cady, R. Claus, S.T. Dye et al.,
3841 *Measurement of atmospheric neutrino composition with the imb-3 detector*, . 46
- 3842 [32] M. Ambrosio, R. Antolini, C. Aramo, G. Auriemma, A. Baldini, G. C. Barbarino
3843 et al., *Measurement of the atmospheric neutrino-induced upgoing muon flux using*
3844 *macro*, . 46
- 3845 [33] W. Allison, G. Alner, D. Ayres, W. Barrett, C. Bode, P. Border et al.,
3846 *Measurement of the atmospheric neutrino flavour composition in soudan 2*, . 46
- 3847 [34] SUPER-KAMIOKANDE collaboration, *Evidence for oscillation of atmospheric*
3848 *neutrinos*, *Phys. Rev. Lett.* **81** (1998) 1562 [[hep-ex/9807003](#)]. 46
- 3849 [35] P. Minkowski, $\mu \rightarrow e\gamma$ at a Rate of One Out of 10^9 Muon Decays?, *Phys. Lett. B*
3850 **67** (1977) 421. 49
- 3851 [36] M. Gell-Mann, P. Ramond and R. Slansky, *Complex Spinors and Unified Theories*,
3852 *Conf. Proc. C* **790927** (1979) 315 [[1306.4669](#)]. 49
- 3853 [37] T. Yanagida, *Horizontal gauge symmetry and masses of neutrinos*, *Conf. Proc. C*
3854 **7902131** (1979) 95. 49
- 3855 [38] R.N. Mohapatra and G. Senjanovic, *Neutrino Mass and Spontaneous Parity*
3856 *Nonconservation*, *Phys. Rev. Lett.* **44** (1980) 912. 49
- 3857 [39] J. Schechter and J.W.F. Valle, *Neutrino Masses in $SU(2) \times U(1)$ Theories*, *Phys.*
3858 *Rev. D* **22** (1980) 2227. 49
- 3859 [40] B. Pontecorvo, *Mesonium and anti-mesonium*, *Sov. Phys. JETP* **6** (1957) 429. 49
- 3860 [41] M. Gell-Mann and A. Pais, *Behavior of neutral particles under charge conjugation*,
3861 . 49

BIBLIOGRAPHY

- 3862 [42] B. Pontecorvo, *Neutrino Experiments and the Problem of Conservation of*
 3863 *Leptonic Charge, Zh. Eksp. Teor. Fiz.* **53** (1967) 1717. 50
- 3864 [43] B. Pontecorvo, *Inverse beta processes and nonconservation of lepton charge, Zh.*
 3865 *Eksp. Teor. Fiz.* **34** (1957) 247. 51
- 3866 [44] Z. Maki, M. Nakagawa and S. Sakata, *Remarks on the unified model of elementary*
 3867 *particles, Prog. Theor. Phys.* **28** (1962) 870. 51
- 3868 [45] PARTICLE DATA GROUP collaboration, *Review of particle physics, Phys. Rev. D*
 3869 **110** (2024) 030001. 53
- 3870 [46] L. Wolfenstein, *Neutrino Oscillations in Matter, Phys. Rev. D* **17** (1978) 2369. 54
- 3871 [47] B.T. Cleveland, T. Daily, R. Davis, Jr., J.R. Distel, K. Lande, C.K. Lee et al.,
 3872 *Measurement of the solar electron neutrino flux with the Homestake chlorine*
 3873 *detector, Astrophys. J.* **496** (1998) 505. 56
- 3874 [48] G. Bellini et al., *Precision measurement of the ^{7}Be solar neutrino interaction rate*
 3875 *in Borexino, Phys. Rev. Lett.* **107** (2011) 141302 [[1104.1816](#)]. 56
- 3876 [49] SUPER-KAMIOKANDE collaboration, *Solar neutrino measurements in*
 3877 *super-Kamiokande-I, Phys. Rev. D* **73** (2006) 112001 [[hep-ex/0508053](#)]. 56
- 3878 [50] SNO collaboration, *Combined Analysis of all Three Phases of Solar Neutrino*
 3879 *Data from the Sudbury Neutrino Observatory, Phys. Rev. C* **88** (2013) 025501
 3880 [[1109.0763](#)]. 56
- 3881 [51] SUPER-KAMIOKANDE collaboration, *Atmospheric neutrino oscillation analysis*
 3882 *with external constraints in Super-Kamiokande I-IV, Phys. Rev. D* **97** (2018)
 3883 072001 [[1710.09126](#)]. 56, 157
- 3884 [52] ICECUBE collaboration, *Measurement of Atmospheric Neutrino Oscillations at*
 3885 *6–56 GeV with IceCube DeepCore, Phys. Rev. Lett.* **120** (2018) 071801
 3886 [[1707.07081](#)]. 56

BIBLIOGRAPHY

- 3887 [53] KamLAND collaboration, *Reactor On-Off Antineutrino Measurement with*
3888 *KamLAND*, *Phys. Rev. D* **88** (2013) 033001 [[1303.4667](#)]. 57
- 3889 [54] RENO collaboration, *Measurement of Reactor Antineutrino Oscillation Amplitude*
3890 *and Frequency at RENO*, *Phys. Rev. Lett.* **121** (2018) 201801 [[1806.00248](#)]. 57
- 3891 [55] DAYA BAY collaboration, *Measurement of the Electron Antineutrino Oscillation*
3892 *with 1958 Days of Operation at Daya Bay*, *Phys. Rev. Lett.* **121** (2018) 241805
3893 [[1809.02261](#)]. 57
- 3894 [56] K.J. Kelly, P.A.N. Machado, S.J. Parke, Y.F. Perez-Gonzalez and R.Z. Funchal,
3895 *Neutrino mass ordering in light of recent data*, *Phys. Rev. D* **103** (2021) 013004.
3896 57
- 3897 [57] P. Dunne, “Latest Neutrino Oscillation Results from T2K.” Jul, 2020. 57
- 3898 [58] MINOS collaboration, *Combined analysis of ν_μ disappearance and $\nu_\mu \rightarrow \nu_e$*
3899 *appearance in MINOS using accelerator and atmospheric neutrinos*, *Phys. Rev.*
3900 *Lett.* **112** (2014) 191801 [[1403.0867](#)]. 57
- 3901 [59] OPERA collaboration, *Final Results of the OPERA Experiment on ν_τ*
3902 *Appearance in the CNGS Neutrino Beam*, *Phys. Rev. Lett.* **120** (2018) 211801
3903 [[1804.04912](#)]. 57
- 3904 [60] K2K collaboration, *Measurement of Neutrino Oscillation by the K2K Experiment*,
3905 *Phys. Rev. D* **74** (2006) 072003 [[hep-ex/0606032](#)]. 57
- 3906 [61] DUNE collaboration, *Long-baseline neutrino oscillation physics potential of the*
3907 *DUNE experiment*, *Eur. Phys. J. C* **80** (2020) 978 [[2006.16043](#)]. 57
- 3908 [62] HYPER-KAMIOKANDE collaboration, *Physics potential of Hyper-Kamiokande for*
3909 *neutrino oscillation measurements*, *PoS NuFact2019* (2019) 040. 57
- 3910 [63] SUPERNEMO collaboration, *Probing New Physics Models of Neutrinoless Double*
3911 *Beta Decay with SuperNEMO*, *Eur. Phys. J. C* **70** (2010) 927 [[1005.1241](#)]. 58

BIBLIOGRAPHY

- 3912 [64] SNO+ collaboration, *Current Status and Future Prospects of the SNO+*
 3913 *Experiment, Adv. High Energy Phys.* **2016** (2016) 6194250 [[1508.05759](#)]. 58
- 3914 [65] NEXT collaboration, *Sensitivity of a tonne-scale NEXT detector for neutrinoless*
 3915 *double beta decay searches, JHEP* **2021** (2021) 164 [[2005.06467](#)]. 58
- 3916 [66] P. Coloma and P. Huber, *Impact of nuclear effects on the extraction of neutrino*
 3917 *oscillation parameters, Phys. Rev. Lett.* **111** (2013) 221802 [[1307.1243](#)]. 59
- 3918 [67] P. Coloma, P. Huber, C.-M. Jen and C. Mariani, *Neutrino-nucleus interaction*
 3919 *models and their impact on oscillation analyses, Phys. Rev. D* **89** (2014) 073015
 3920 [[1311.4506](#)]. 59
- 3921 [68] U. Mosel, *Neutrino Interactions with Nucleons and Nuclei: Importance for*
 3922 *Long-Baseline Experiments, Ann. Rev. Nucl. Part. Sci.* **66** (2016) 171
 3923 [[1602.00696](#)]. 59
- 3924 [69] J.A. Formaggio and G.P. Zeller, *From ev to eev: Neutrino cross sections across*
 3925 *energy scales, Rev. Mod. Phys.* **84** (2012) 1307 [[1305.7513](#)]. 60
- 3926 [70] L. Bathe-Peters, S. Gardiner and R. Guenette, *Comparing generator predictions*
 3927 *of transverse kinematic imbalance in neutrino-argon scattering,* [2201.04664](#). 61
- 3928 [71] R.A. Smith and E.J. Moniz, *Neutrino reactions on nuclear targets, Nucl. Phys. B*
 3929 **43** (1972) 605. 61
- 3930 [72] H. Nakamura and R. Seki, *Quasi-elastic neutrino-nucleus scattering and spectral*
 3931 *function, Nuclear Physics B - Proceedings Supplements* **112** 197. 61
- 3932 [73] V. Pandey, N. Jachowicz, T. Van Cuyck, J. Ryckebusch and M. Martini,
 3933 *Low-energy excitations and quasielastic contribution to electron-nucleus and*
 3934 *neutrino-nucleus scattering in the continuum random-phase approximation, Phys.*
 3935 *Rev. C* **92** (2015) 024606 [[1412.4624](#)]. 61

BIBLIOGRAPHY

- 3936 [74] A. Nikolakopoulos, R. González-Jiménez, N. Jachowicz, K. Niewczas, F. Sánchez
3937 and J.M. Udías, *Benchmarking intranuclear cascade models for neutrino*
3938 *scattering with relativistic optical potentials*, *Phys. Rev. C* **105** (2022) 054603
3939 [2202.01689]. 61
- 3940 [75] MINIBooNE collaboration, *First Measurement of the Muon Neutrino Charged*
3941 *Current Quasielastic Double Differential Cross Section*, *Phys. Rev. D* **81** (2010)
3942 092005 [1002.2680]. 62
- 3943 [76] MINERvA collaboration, *Measurements of the Inclusive Neutrino and*
3944 *Antineutrino Charged Current Cross Sections in MINERvA Using the Low- ν Flux*
3945 *Method*, *Phys. Rev. D* **94** (2016) 112007 [1610.04746]. 62
- 3946 [77] MICROBooNE collaboration, *First Measurement of Energy-Dependent Inclusive*
3947 *Muon Neutrino Charged-Current Cross Sections on Argon with the MicroBooNE*
3948 *Detector*, *Phys. Rev. Lett.* **128** (2022) 151801 [2110.14023]. 62
- 3949 [78] SBND collaboration, *Neutrino cross-section measurement prospects with SBND*,
3950 *PoS NuFact2017* (2018) 067. 62
- 3951 [79] NOvA collaboration, *Measurement of the double-differential muon-neutrino*
3952 *charged-current inclusive cross section in the NOvA near detector*, *Phys. Rev. D*
3953 **107** (2023) 052011 [2109.12220]. 62
- 3954 [80] T2K collaboration, *Measurement of the ν_μ charged-current cross sections on*
3955 *water, hydrocarbon, iron, and their ratios with the T2K on-axis detectors*, *PTEP*
3956 **2019** (2019) 093C02 [1904.09611]. 62
- 3957 [81] \$NU\$PRISM collaboration, *ν PRISM: A new way of probing neutrino*
3958 *interactions*, *PoS NUFACT2014* (2015) 046. 62
- 3959 [82] C. Hasnip, *DUNE-PRISM – A New Method to Measure Neutrino Oscillations*,
3960 Ph.D. thesis, Oxford U., 2023. 62

BIBLIOGRAPHY

- 3961 [83] DUNE collaboration, *Deep Underground Neutrino Experiment (DUNE), Far
3962 Detector Technical Design Report, Volume I Introduction to DUNE*, JINST **15**
3963 (2020) T08008 [2002.02967]. 63, 64, 65, 70, 71, 81, 82, 83, 84
- 3964 [84] DUNE collaboration, *Snowmass Neutrino Frontier: DUNE Physics Summary,*
3965 2203.06100. 65, 66
- 3966 [85] DUNE collaboration, *Deep Underground Neutrino Experiment (DUNE), Far
3967 Detector Technical Design Report, Volume II: DUNE Physics*, 2002.03005. 65, 67,
3968 68, 75, 133, 142, 146, 258
- 3969 [86] SUPER-KAMIOKANDE collaboration, *Search for Proton Decay via $p \rightarrow e^+ \pi_0$ and
3970 $p \rightarrow \mu^+ \pi_0$ in a Large Water Cherenkov Detector*, Phys. Rev. Lett. **102** (2009)
3971 141801 [0903.0676]. 66
- 3972 [87] S. Raby, *Grand Unified Theories*, in *2nd World Summit: Physics Beyond the
3973 Standard Model*, 8, 2006 [[hep-ph/0608183](#)]. 66
- 3974 [88] KAMIOKANDE-II collaboration, *Observation of a Neutrino Burst from the
3975 Supernova SN 1987a*, Phys. Rev. Lett. **58** (1987) 1490. 67
- 3976 [89] R.M. Bionta et al., *Observation of a Neutrino Burst in Coincidence with
3977 Supernova SN 1987a in the Large Magellanic Cloud*, Phys. Rev. Lett. **58** (1987)
3978 1494. 67
- 3979 [90] J. Strait, E. McCluskey, T. Lundin, J. Willhite, T. Hamernik, V. Papadimitriou
3980 et al., *Long-baseline neutrino facility (lbnf) and deep underground neutrino
3981 experiment (dune) conceptual design report volume 3: Long-baseline neutrino
3982 facility for dune june 24, 2015*, 1601.05823. 67, 68
- 3983 [91] DUNE collaboration, *Deep Underground Neutrino Experiment (DUNE) Near
3984 Detector Conceptual Design Report, Instruments* **5** (2021) 31 [2103.13910]. 69,
3985 71, 73, 74, 76, 77, 159

BIBLIOGRAPHY

- 3986 [92] DUNE collaboration, *DUNE Phase II: Scientific Opportunities, Detector*
3987 *Concepts, Technological Solutions*, 2408.12725. 72, 78
- 3988 [93] DUNE collaboration, *A Gaseous Argon-Based Near Detector to Enhance the*
3989 *Physics Capabilities of DUNE*, 2203.06281. 74
- 3990 [94] F. Sauli, *Gem: A new concept for electron amplification in gas detectors*, *Nuclear*
3991 *Instruments and Methods in Physics Research Section A: Accelerators,*
3992 *Spectrometers, Detectors and Associated Equipment* **386** 531. 76, 80
- 3993 [95] A. Ritchie-Yates et al., *First operation of an ALICE OROC operated in high*
3994 *pressure Ar-CO₂ and Ar-CH₄*, *Eur. Phys. J. C* **83** (2023) 1139 [2305.08822]. 79
- 3995 [96] ALICE TPC collaboration, *The upgrade of the ALICE TPC with GEMs and*
3996 *continuous readout*, *JINST* **16** (2021) P03022 [2012.09518]. 79
- 3997 [97] F. Sauli, *The gas electron multiplier (gem): Operating principles and applications*,
3998 *Nuclear Instruments and Methods in Physics Research Section A: Accelerators,*
3999 *Spectrometers, Detectors and Associated Equipment* **805** 2. 80
- 4000 [98] C. Lippmann, *A continuous read-out tpc for the alice upgrade*, *Nuclear*
4001 *Instruments and Methods in Physics Research Section A: Accelerators,*
4002 *Spectrometers, Detectors and Associated Equipment* **824** 543. 80
- 4003 [99] C. Calabria, *Large-size triple gem detectors for the cms forward muon upgrade*,
4004 *Nuclear and Particle Physics Proceedings* **273–275** 1042. 80
- 4005 [100] DUNE collaboration, *The DUNE Far Detector Vertical Drift Technology*,
4006 *Technical Design Report*, 2312.03130. 85, 86
- 4007 [101] DUNE collaboration, *Deep Underground Neutrino Experiment (DUNE), Far*
4008 *Detector Technical Design Report, Volume IV: Far Detector Single-phase*
4009 *Technology*, *JINST* **15** (2020) T08010 [2002.03010]. 87

BIBLIOGRAPHY

- 4010 [102] DUNE DAQ, “dtp-firmware.”
4011 <https://gitlab.cern.ch/dune-daq/readout/dtp-firmware>, 2020. 89
- 4012 [103] DUNE DAQ, “dtp-simulation.”
4013 <https://gitlab.cern.ch/dune-daq/readout/dtp-simulation>, 2020. 92
- 4014 [104] DUNE DAQ, “dtpe emulator.”
4015 https://github.com/DUNE-DAQ/dtpe emulator/tree/fmlopez/filter_ana,
4016 2022. 92
- 4017 [105] J. McClellan and T. Parks, *A personal history of the Parks-McClellan algorithm*,
4018 *IEEE Signal Processing Magazine* **22** (2005) 82. 93
- 4019 [106] G. Turin, *An introduction to matched filters*, *IEEE Transactions on Information*
4020 *Theory* **6** (1960) 311. 97
- 4021 [107] J.W. Goodman, *Statistical Optics*, Wiley (1985). 98
- 4022 [108] B. Dwork, *Detection of a pulse superimposed on fluctuation noise*, *Proceedings of*
4023 *the IRE* **38** (1950) 771. 99
- 4024 [109] L. Wainstein and V. Zubakov, *Extraction of Signals from Noise*, Prentice-Hall
4025 (1962). 99
- 4026 [110] E.D. Church, *Larsoft: A software package for liquid argon time projection drift*
4027 *chambers*, **1311.6774**. 103
- 4028 [111] S.V. Stehman, *Selecting and interpreting measures of thematic classification*
4029 *accuracy*, *Remote Sensing of Environment* **62** (1997) 77. 116
- 4030 [112] A.A. Taha and A. Hanbury, *Metrics for evaluating 3d medical image*
4031 *segmentation: analysis, selection, and tool*, *BMC Medical Imaging* **15** (2015) . 117
- 4032 [113] J. Silk, K.A. Olive and M. Srednicki, *The Photino, the Sun and High-Energy*
4033 *Neutrinos*, *Phys. Rev. Lett.* **55** (1985) 257. 123

BIBLIOGRAPHY

- 4034 [114] M. Srednicki, K.A. Olive and J. Silk, *High-Energy Neutrinos from the Sun and*
4035 *Cold Dark Matter*, *Nucl. Phys. B* **279** (1987) 804. 123
- 4036 [115] J.S. Hagelin, K.W. Ng and K.A. Olive, *A High-energy Neutrino Signature From*
4037 *Supersymmetric Relics*, *Phys. Lett. B* **180** (1986) 375. 123
- 4038 [116] T.K. Gaisser, G. Steigman and S. Tilav, *Limits on Cold Dark Matter Candidates*
4039 *from Deep Underground Detectors*, *Phys. Rev. D* **34** (1986) 2206. 123
- 4040 [117] N. Bernal, J. Martín-Albo and S. Palomares-Ruiz, *A novel way of constraining*
4041 *WIMPs annihilations in the Sun: MeV neutrinos*, *JCAP* **08** (2013) 011
4042 [1208.0834]. 123, 124, 130
- 4043 [118] C. Rott, J. Siegal-Gaskins and J.F. Beacom, *New Sensitivity to Solar WIMP*
4044 *Annihilation using Low-Energy Neutrinos*, *Phys. Rev. D* **88** (2013) 055005
4045 [1208.0827]. 123, 130
- 4046 [119] C. Rott, S. In, J. Kumar and D. Yaylali, *Dark Matter Searches for Monoenergetic*
4047 *Neutrinos Arising from Stopped Meson Decay in the Sun*, *JCAP* **11** (2015) 039
4048 [1510.00170]. 123
- 4049 [120] DUNE collaboration, *Searching for solar KDAR with DUNE*, *JCAP* **10** (2021)
4050 065 [2107.09109]. 123
- 4051 [121] G. Busoni, A. De Simone and W.-C. Huang, *On the Minimum Dark Matter Mass*
4052 *Testable by Neutrinos from the Sun*, *JCAP* **07** (2013) 010 [1305.1817]. 124
- 4053 [122] V.A. Bednyakov and F. Simkovic, *Nuclear spin structure in dark matter search:*
4054 *The Zero momentum transfer limit*, *Phys. Part. Nucl.* **36** (2005) 131
4055 [hep-ph/0406218]. 125
- 4056 [123] A. Gould, *WIMP Distribution in and Evaporation From the Sun*, *Astrophys. J.*
4057 **321** (1987) 560. 125

BIBLIOGRAPHY

- 4058 [124] J.N. Bahcall, M.H. Pinsonneault and S. Basu, *Solar models: Current epoch and*
 4059 *time dependences, neutrinos, and helioseismological properties*, *Astrophys. J.* **555**
 4060 (2001) 990 [[astro-ph/0010346](#)]. 128
- 4061 [125] T. Golan, J.T. Sobczyk and J. Zmuda, *NuWro: the Wroclaw Monte Carlo*
 4062 *Generator of Neutrino Interactions*, *Nucl. Phys. B Proc. Suppl.* **229-232** (2012)
 4063 499. 132
- 4064 [126] G. Cowan, K. Cranmer, E. Gross and O. Vitells, *Asymptotic formulae for*
 4065 *likelihood-based tests of new physics*, *Eur. Phys. J. C* **71** (2011) 1554 [[1007.1727](#)].
 4066 134
- 4067 [127] T. Kaluza, *Zum Unitätsproblem der Physik, Sitzungsber. Preuss. Akad. Wiss.*
 4068 *Berlin (Math. Phys.)* **1921** (1921) 966 [[1803.08616](#)]. 135
- 4069 [128] O. Klein, *Quantum Theory and Five-Dimensional Theory of Relativity. (In*
 4070 *German and English)*, *Z. Phys.* **37** (1926) 895. 135
- 4071 [129] T. Appelquist, H.-C. Cheng and B.A. Dobrescu, *Bounds on universal extra*
 4072 *dimensions*, *Phys. Rev. D* **64** (2001) 035002 [[hep-ph/0012100](#)]. 135
- 4073 [130] N. Arkani-Hamed, S. Dimopoulos and G.R. Dvali, *The Hierarchy problem and new*
 4074 *dimensions at a millimeter*, *Phys. Lett. B* **429** (1998) 263 [[hep-ph/9803315](#)]. 135
- 4075 [131] L. Randall and R. Sundrum, *A Large mass hierarchy from a small extra*
 4076 *dimension*, *Phys. Rev. Lett.* **83** (1999) 3370 [[hep-ph/9905221](#)]. 135
- 4077 [132] G. Servant and T.M.P. Tait, *Is the lightest Kaluza-Klein particle a viable dark*
 4078 *matter candidate?*, *Nucl. Phys. B* **650** (2003) 391 [[hep-ph/0206071](#)]. 136
- 4079 [133] H.-C. Cheng, K.T. Matchev and M. Schmaltz, *Radiative corrections to*
 4080 *Kaluza-Klein masses*, *Phys. Rev. D* **66** (2002) 036005 [[hep-ph/0204342](#)]. 136
- 4081 [134] M. Blennow, J. Edsjö and T. Ohlsson, *Neutrinos from WIMP annihilations using*
 4082 *a full three-flavor Monte Carlo*, *JCAP* **01** (2008) 021 [[0709.3898](#)]. 136, 139

BIBLIOGRAPHY

- 4083 [135] J. Edsjö, J. Elevant and C. Niblaeus, *WimpSim Neutrino Monte Carlo.* 136, 139
- 4084 [136] U. Haisch and A. Weiler, *Bound on minimal universal extra dimensions from*
4085 *anti- $B \rightarrow X(s)\gamma$,* *Phys. Rev. D* **76** (2007) 034014 [[hep-ph/0703064](#)]. 138
- 4086 [137] A. Freitas and U. Haisch, *Anti- $B \rightarrow X(s)\gamma$ in two universal extra*
4087 *dimensions,* *Phys. Rev. D* **77** (2008) 093008 [[0801.4346](#)]. 138
- 4088 [138] C. Rott, D. Jeong, J. Kumar and D. Yaylali, *Neutrino Topology Reconstruction at*
4089 *DUNE and Applications to Searches for Dark Matter Annihilation in the Sun,*
4090 *JCAP* **07** (2019) 006 [[1903.04175](#)]. 141
- 4091 [139] F. Pedregosa, G. Varoquaux, A. Gramfort, V. Michel, B. Thirion, O. Grisel et al.,
4092 *Scikit-learn: Machine learning in Python,* *Journal of Machine Learning Research*
4093 **12** (2011) 2825. 147
- 4094 [140] J. Kopp, V. Niro, T. Schwetz and J. Zupan, *DAMA/LIBRA and leptonically*
4095 *interacting Dark Matter,* *Phys. Rev. D* **80** (2009) 083502 [[0907.3159](#)]. 151
- 4096 [141] PARTICLE DATA GROUP collaboration, *Review of Particle Physics,* *PTEP* **2020**
4097 (2020) 083C01. 152
- 4098 [142] M. Beltran, D. Hooper, E.W. Kolb and Z.C. Krusberg, *Deducing the nature of*
4099 *dark matter from direct and indirect detection experiments in the absence of*
4100 *collider signatures of new physics,* *Phys. Rev. D* **80** (2009) 043509 [[0808.3384](#)].
4101 153
- 4102 [143] PLANCK collaboration, *Planck 2018 results. VI. Cosmological parameters,* *Astron.*
4103 *Astrophys.* **641** (2020) A6 [[1807.06209](#)]. 153
- 4104 [144] C. Principato, *An Indirect Search for Weakly Interacting Massive Particles in the*
4105 *Sun Using Upward-going Muons in NOvA*, Ph.D. thesis, Virginia U., 2021.
4106 10.18130/x5z2-1466. 156

BIBLIOGRAPHY

- 4107 [145] G. Wikström and J. Edsjö, *Limits on the wimp-nucleon scattering cross-section from neutrino telescopes*, 0903.2986. 156
- 4109 [146] SUPER-KAMIOKANDE collaboration, *Search for neutrinos from annihilation of captured low-mass dark matter particles in the Sun by Super-Kamiokande*, *Phys. Rev. Lett.* **114** (2015) 141301 [1503.04858]. 156
- 4112 [147] C. Rott, T. Tanaka and Y. Itow, *Enhanced sensitivity to dark matter self-annihilations in the sun using neutrino spectral information*, 1107.3182. 156
- 4114 [148] M.M. Boliev, S.V. Demidov, S.P. Mikheyev and O.V. Suvorova, *Search for muon signal from dark matter annihilations inthe Sun with the Baksan Underground Scintillator Telescope for 24.12 years*, *JCAP* **09** (2013) 019 [1301.1138]. 156, 157
- 4117 [149] M. Honda, T. Kajita, K. Kasahara, S. Midorikawa and T. Sanuki, *Calculation of atmospheric neutrino flux using the interaction model calibrated with atmospheric muon data*, *Phys. Rev. D* **75** (2007) 043006 [astro-ph/0611418]. 157
- 4120 [150] C. Green, J. Kowalkowski, M. Paterno, M. Fischler, L. Garren and Q. Lu, *The Art Framework*, *J. Phys. Conf. Ser.* **396** (2012) 022020. 160
- 4122 [151] H. Bethe, *Zur theorie des durchgangs schneller korpuskularstrahlen durch materie*, *Annalen der Physik* **397** (1930) 325. 165
- 4124 [152] E. Fermi, *The ionization loss of energy in gases and in condensed materials*, *Physical Review* **57** (1940) 485. 166
- 4126 [153] R. Sternheimer, M. Berger and S. Seltzer, *Density effect for the ionization loss of charged particles in various substances*, *Atomic Data and Nuclear Data Tables* **30** (1984) 261. 166
- 4129 [154] W.W.M. Allison and J.H. Cobb, *Relativistic Charged Particle Identification by Energy Loss*, *Ann. Rev. Nucl. Part. Sci.* **30** (1980) 253. 166

BIBLIOGRAPHY

- 4131 [155] W. Blum, L. Rolandi and W. Riegler, *Particle detection with drift chambers*,
4132 Particle Acceleration and Detection (2008), 10.1007/978-3-540-76684-1. 166
- 4133 [156] ALICE TPC collaboration, *Particle identification of the ALICE TPC via dE/dx*,
4134 *Nucl. Instrum. Meth. A* **706** (2013) 55. 166
- 4135 [157] L. Landau, *On the energy loss of fast particles by ionization*, *J. Phys. (USSR)* **8**
4136 (1944) 201. 169
- 4137 [158] W. Ulmer and E. Matsinos, *Theoretical methods for the calculation of Bragg*
4138 *curves and 3D distributions of proton beams*, *The European Physical Journal*
4139 *Special Topics* **190** (2010) 1. 170
- 4140 [159] E. Aprile, A.E. Bolotnikov, A.L. Bolozdynya and T. Doke, *Noble Gas Detectors*,
4141 Wiley (Oct., 2008), 10.1002/9783527610020. 173
- 4142 [160] D.S. Wilks, *Statistical Methods in the Atmospheric Sciences*, Academic Press. 210
- 4143 [161] ALICE collaboration, *Production of pions, kaons and protons in pp collisions at*
4144 $\sqrt{s} = 900 \text{ gev with alice at the lhc}$, **1101.4110**. 212
- 4145 [162] U. Einhaus, *Charged hadron identification with de/dx and time-of-flight at future*
4146 *higgs factories*, **2110.15115**. 212
- 4147 [163] R. Frühwirth, *Application of filter methods to the reconstruction of tracks and*
4148 *vertices in events of experimental high energy physics*, Ph.D. thesis, Technischen
4149 Universität Wien, 1988. 217
- 4150 [164] P. Astier, A. Cardini, R.D. Cousins, A. Letessier-Selvon, B.A. Popov and
4151 T. Vinogradova, *Kalman filter track fits and track breakpoint analysis*, *Nuclear*
4152 *Instruments and Methods in Physics Research Section A: Accelerators*,
4153 *Spectrometers, Detectors and Associated Equipment* **450** (2000) 138. 217
- 4154 [165] T2K UK collaboration, *The Electromagnetic Calorimeter for the T2K Near*
4155 *Detector ND280*, *JINST* **8** (2013) P10019 [1308.3445]. 226

BIBLIOGRAPHY

- ⁴¹⁵⁶ [166] J.E. Gaiser, *Charmonium Spectroscopy From Radiative Decays of the J/ψ and ψ' ,*
⁴¹⁵⁷ Ph.D. thesis, Stanford University, 1982. 231
- ⁴¹⁵⁸ [167] T. Golan, L. Aliaga and M. Kordosky, *Minerva's flux prediction*, in *Proceedings of*
⁴¹⁵⁹ *the 10th International Workshop on Neutrino-Nucleus Interactions in Few-GeV*
⁴¹⁶⁰ *Region (NuInt15)*, Journal of the Physical Society of Japan, DOI. 259
- ⁴¹⁶¹ [168] A. Bashyal, H. Schellman and L. Fields, *Ppx implementation in deep underground*
⁴¹⁶² *neutrino experiment*, . 259